Acta Pharmacologica Sinica (2011) 32: 1–2
 1671-4083/11 $32.00
www.nature.com/aps

Research Highlight

Erasing fear memories — key receptor and essential timeframe discovered

Shigenori KAWAHARA

Acta Pharmacologica Sinica (2011) 32: 1–2; doi: 10.1038/aps.2010.215; published online 20 Dec 2010

It is clinically important to suppress or inhibit traumatic memories, which are formed after fearful experiences. In animal models, fear memory is formed by repetitive presentation of a tone paired with an electrical foot-shock[1]. It is well known that an extinction protocol, in which the tone is repeatedly presented without the foot-shock, gradually decreases the pre-acquired fear response to the tone. However, this fear extinction protocol is not sufficient to erase the fear memory; fear responses may recover spontaneously or relapse under some conditions. If the fear memory is retrieved or reactivated by a single presentation of the tone without the shock 1 h before the extinction session, the fear responses are permanently removed by this retrieval–extinction protocol[2]. This suggests that a critical brain state is caused by the retrieval procedure, in which the fear memory becomes labile and can be destroyed by the subsequent extinction procedure. Clem and Huganir[3] have found a critical receptor for the permanent erasure of fear memories by this retrieval–extinction protocol. They focused on the Ca^{2+}-permeable type of α-amino-3-hydroxyl-5-methyl-4-isoxazole-propionate receptor (Ca^{2+}-permeable-AMPAR) located in the lateral amygdala, an essential region of the brain for learning. They suggested that removal of Ca^{2+}-permeable-AMPARs, the content of which in the synapses is elevated for a few days after fear conditioning, is responsible for the permanent erasure of the fear memory by that protocol.

Graduate School of Science and Engineering, University of Toyama, 3190 Gofuku, Toyama 930–8555, Japan
Correspondence: Prof Shigenori KAWAHARA (kawahara@eng.u-toyama.ac.jp)

First, they demonstrated an enhancement of Ca^{2+}-permeable-AMPAR mediated excitatory postsynaptic currents in fear-conditioned animals, suggesting an incorporation of Ca^{2+}-permeable-AMPARs or a change of subunit composition of AMPAR to the Ca^{2+}-permeable type. This increase of Ca^{2+}-permeable-AMPARs peaked at 24 h after conditioning and disappeared by d 7, whereas the total amount of AMPARs remained increased even after 7 d. These results suggest the presence of an important time window, during which AMPARs transiently change their subunit composition to the Ca^{2+}-permeable type. Increased Ca^{2+}-permeable-AMPARs at 24 h after fear conditioning was also supported by an enhancement of long-term depression (LTD), which is caused by selective removal of Ca^{2+}-permeable-AMPARs that become abundant at that time.

Next, they examined the effects of memory retrieval on Ca^{2+}-permeable-AMPARs measured after extinction. They found that reactivation of the fear memory before the extinction session significantly decreased AMPA-mediated current, indicating that memory reactivation followed by extinction attenuates the potentiated transmission caused by fear conditioning. Electrophysiological and pharmacological examinations suggested that this reversal change of synaptic transmission is due to the selective removal of Ca^{2+}-permeable-AMPARs, which are enriched 24 h after conditioning. Consistent with this, LTD induction was greatly reduced in the animals receiving the retrieval–extinction protocol, compared with those receiving extinction alone. This is because memory retrieval prior to the extinction removes the Ca^{2+}-permeable-AMPARs from the synapses, and so further reduction in synaptic transmission would not be observed. In addition, memory reactivation is not effective when carried out 7 d after the conditioning, when the Ca^{2+}-permeable-AMPARs return to the basal level, supporting the idea that successful erasure of the fear memory requires an abundance of Ca^{2+}-permeable-AMPARs at the time of the retrieval-extinction treatment.

Finally, they investigated the molecular mechanisms underlying the elevation of Ca^{2+}-permeable-AMPAR content after fear conditioning, which is a prerequisite for removal of Ca^{2+}-permeable-AMPARs by the retrieval–extinction protocol. It was reported that phosphorylation of the serine 845 (S845) residue of glutamate receptor 1 (GluR1) by protein kinase A (PKA) is required for stable expression

of Ca^{2+}-permeable-AMPARs[4]. Using mutant mice with an alanine substitution mutation of S845 (S845A), they showed that phosphorylation of Ca^{2+}-permeable-AMPARs by PKA is critical for the increase of Ca^{2+}-permeable-AMPAR current and the enhancement of LTD 24 h after fear conditioning. These results suggest the importance of phosphorylation of S845 for the synaptic incorporation of Ca^{2+}-permeable-AMPARs. In parallel with the deficits in the post-conditioning dynamics of Ca^{2+}-permeable-AMPARs, memory erasure by the retrieval-extinction protocol was impaired in these mutant mice. Because phosphorylation of Ca^{2+}-permeable-AMPARs by PKA is blocked throughout the brain in these mutant mice, there is a possibility that the lack of the erasure effect might be due to impairments in other regions outside the lateral amygdala. Combined with other data, however, it is suggested that the transient up-and-down change in the amount of Ca^{2+}-permeable-AMPARs in the lateral amygdala synapses has a crucial role in permanent erasure of the fear memory and that phosphorylation of Ca^{2+}-permeable-AMPARs by PKA is involved in their up-regulation. Interestingly, S845A mutant mice showed a significant post-conditioning synaptic potentiation in the lateral amygdala and learned as successfully as the wildtype mice. These results indicate that phosphorylation of S845 and its resulting Ca^{2+}-permeable-AMPAR dynamics are specifically related to the memory erasure processes triggered by the retrieval–extinction protocol.

In addition to molecular strategies for treatment of traumatic memories, these data also provide important information on the right timing of the treatment: there is a critical or effective period for the memory erasure. Because Ca^{2+}-permeable-AMPARs reach a maximum level 24 h after fear conditioning and then gradually decline within a few days, the treatment will only be effective within this time window. Further attempts to artificially induce Ca^{2+}-permeable-AMPAR accumulation might remove the time limit and make the treatment successful beyond this narrow timeframe.

1 Herry C, Ferraguti F, Singewald N, Letzkus JJ, Ehrlich I, Lüthi A. Neuronal circuits of fear extinction. Eur J Neurosci 2010; 31: 599–612.
2 Monfils MH, Cowansage KK, Klann E, LeDoux JE. Extinction-reconsolidation boundaries: key to persistent attenuation of fear memories. Science 2009; 324: 951–5.
3 Clem RL, Huganir RL. Calcium-permeable AMPA receptor dynamics mediate fear memory erasure. Science 2010; 330: 1108–12.
4 He K, Song L, Cummings LW, Goldman J, Huganir RL, Lee H-K. Stabilization of Ca^{2+}-permeable AMPA receptors at perisynaptic sites by GluR1-S845 phosphorylation. Proc Natl Acad Sci USA 2009; 106: 20033–8.

Acta Pharmacologica Sinica (2011) 32: 3–11

www.nature.com/aps

Review

The role of BDNF in depression on the basis of its location in the neural circuitry

Hui YU, Zhe-yu CHEN*

Department of Neurobiology, Shandong Provincial Key Laboratory of Mental Disorders, School of Medicine, Shandong University, Jinan 250012, China

Depression is one of the most prevalent and life-threatening forms of mental illnesses and the neural circuitry underlying depression remains incompletely understood. Most attention in the field has focused on hippocampal and frontal cortical regions for their roles in depression and antidepressant action. While these regions no doubt play important roles in the mental illness, there is compelling evidence that other brain regions are also involved. Brain-derived neurotrophic factor (BDNF) is broadly expressed in the developing and adult mammalian brain and has been implicated in development, neural regeneration, synaptic transmission, synaptic plasticity and neurogenesis. Recently BDNF has been shown to play an important role in the pathophysiology of depression, however there are controversial reports about the effects of BDNF on depression. Here, we present an overview of the current knowledge concerning BDNF actions and associated intracellular signaling in hippocampus, prefrontal cortex, nucleus accumbens (NAc) and amygdala as their relation to depression.

Keywords: BDNF; depression; antidepressant; neural circuitry

Acta Pharmacologica Sinica (2011) 32: 3–11; doi: 10.1038/aps.2010.184; published online 6 Dec 2010

Introduction

Depression is a clinically and biologically heterogeneous disease, with 10%–30% of women and 7%–15% of men likely to suffer from depression in their life-time[1]. The symptoms of depression are the loss of interest or pleasure in virtually all activities (anhedonia) and a long-lasting depressed mood, feelings of guilt, anxiety, and recurrent thoughts of death and suicide[2]. The genetic contribution to the manifestation of depression has been estimated as 40%–50%[3]. However, combinations of multiple genetic factors may be involved in the development of depression, because a defect in a single gene usually fails to induce the expression of multifaceted symptoms of depression[4]. Also, various non-genetic factors such as stress, affective trauma, viral infection, and neurodevelopmental abnormalities increase the complexity of the pathogenesis of the disease. Thus, extensive studies have led to a variety of hypotheses for the molecular mechanism of depression, but a definite pathogenic mechanism has yet to be defined. The objective of this review is to investigate the contribution of brain-derived neurotrophic factor (BDNF) and its intracellular signaling in different brain regions to depression and antidepressant treatments.

* To whom correspondence should be addressed.
E-mail zheyuchen@sdu.edu.cn
Received 2010-07-05 Accepted 2010-09-24

Neurobiology of depression

As a basic understanding of depression the monoamine hypothesis was formulated in the mid 1960s based on the antidepressant efficacy of the monoamine reuptake inhibitors, monoamine oxidase inhibitors and the depressogenic effects of reserpine as a monoamine depleter[5]. This hypothesis suggests a deficiency or imbalances in the monoamine neurotransmitters, such as serotonin (5-HT), dopamine and norepinephrine (NE), as the cause of depression. Among therapeutic agents, antidepressants including tricyclics, monoamine oxidase inhibitors and selective serotonin reuptake inhibitors (SSRIs) exert their therapeutic action through their ability to increase the synaptic content of monoamine neurotransmitters[6]. However, antidepressants exert their therapeutic action only after chronic treatment, indicating that enhanced 5-HT or NE neurotransmission *per se* is not responsible for the clinical actions of these drugs. Second, antidepressants are effective in less than 50% of patients[2], which suggests that additional biological substrates could provide potential therapeutic targets.

Based on clinical and animal studies it has been suggested that depression are associated with neuronal atrophy and neuronal cell loss, especially in the hippocampus and cerebral cortex[7]. Therefore the neurotrophic factors are recognized as an

important new lead in the quest for a deeper understanding of depression and the mechanisms of antidepressants effect[8]. The neurotrophic hypothesis of depression states that a deficiency in neurotrophic support may contribute to hippocampal pathology during the development of depression, and the reversal of this deficiency by antidepressant treatments may contribute to the resolution of depressive symptoms. Of various neurotrophins, most studies have focused on BDNF, one of the most prevalent neurotrophic factors in adult brain.

BDNF and depression

Studies in humans have shown decreased plasma levels of BDNF in bipolar disorder, manic and depressed patients[9, 10]. Many preclinical and clinical studies provide direct evidence suggesting that modulation in expression of BDNF could be involved in behavioral phenomenon associated with depression. Recently, a variant in the human BDNF gene, which leads to a valine to methionine change in the pro-domain of the BDNF protein (position 66), was found to decrease activity-dependent secretion of BDNF[11, 12] and be associated with increased susceptibility to neuropsychiatric disorders including depression, anxiety-related dysfunction and bipolar disorder[13–17]. People with the Met allele have been found to have a relatively small hippocampus and poor hippocampus-dependent memory function[18]. In our previous work, we have generated a BDNF knock-in mouse containing the BDNF Val66Met polymorphism, which provided a valuable tool to assess the *in vivo* consequence of $BDNF^{Met}$ polymorphism[19]. We found that $BDNF^{Met/Met}$ mice showed increased anxiety-related behaviors, which could not be reversed by fluoxetine treatment[19]. Furthermore, we found $BDNF^{Met/Met}$ mice had decreased ventromedial prefrontal cortex volume and displayed aversive memory extinction deficit[20]. These studies suggest that the BDNF Val66Met polymorphism might be at risk to develop smaller prefrontal cortex and hippocampus and thus lead to susceptibility to mood disorders, which strengthens the hypothesis that BDNF plays an important role in depression.

The role of BDNF in depression has also been supported by the hypothesis that BDNF mediates the action of antidepressant. The most widely accepted hypothesis assuming that antidepressants restore the compromised neurotransmission in mainly noradrenergic and serotoninergic system has dominated our thinking of antidepressant action. Indeed, speaking of depression, a key question has always been why therapeutic responses with antidepressants could only be achieved after at least 2–3 weeks of treatment, whereas antidepressants alter synaptic monoamine levels within hours. Since the monoaminergic hypothesis cannot fully explain this delay of antidepressant effect, it has been suggested that this delay is required in order to produce neuroadaptive mechanisms that may enhance neuronal plasticity and resilience[21, 22]. Along this line of reasoning, several studies have shown that BDNF may mediate the therapeutic action of antidepressants[23–25]. There is a plethora of evidence documenting that antidepressant treatments, including SSRIs and electroconvulsive shock (ECS) increase the expression of BDNF and tropomyosin receptor kinase B (TrkB) in the hippocampus in animal models. These effects are dependent on chronic administration of antidepressant therapy, consistent with the time course of antidepressant treatments[26, 27]. This suggests that the regulations of BDNF and TrkB are involved in the pathology and development of depression and antidepressant treatments.

However, although BDNF exerts antidepressant-like effects in hippocampus, its actions might be different or even opposite, in different brain regions. The best example is the ventral tegmental area-nucleus accumbens (NAc) dopaminergic reward circuit, in which chronic stress increases BDNF expression[28]. Local BDNF infusion into NAc exerts a prodepression-like effect in the forced swim test, and blockade of BDNF function in NAc exerts an antidepressant-like effect[28]. Thus the differential role of BDNF in depression might be attributed to its location in the depression neural circuits. In the following parts of the review, we would like to summarize the local contribution of BDNF/TrkB signaling to depression on the basis of its location in the neural circuitry.

Neural circuitry of depression

Disturbances in the detection of, response to, and interpretation of emotion are common in depression. The affective fronto-limbic circuitry including the prefrontal cortices, the cingulate cortex, several limbic structures including the hippocampus, amygdala, lower brainstem structures and the basal ganglia are highly involved in mediating these stages of emotion processing, and evidence indicates that these regions show structural and functional alterations in depression[29].

A greater understanding of the neural circuitry underlying normal mood and abnormalities in mood has been identified as one of the critical needs in the field of depression research. The hippocampus and frontal cortex are implicated in learning and memory, attention and impulse control, which suggests they may mediate cognitive aspects of depression, such as memory impairments and feelings of hopelessness, guilt, doom, and suicidality[2, 30]. The striatum (particularly the NAc) and amygdala, and related brain areas, are important in emotional memory, and could as a result mediate the anhedonia, anxiety, and reduced motivation that predominated in many patients[31]. Hypothalamic abnormalities likely contribute to altered appetite and autonomic symptoms. Thalamic and brainstem dysregulation contribute to altered sleep and arousal states[32]. Of course, these various brain areas cannot be thought of as distinct, they operate in a series of highly interacting parallel circuits, which perhaps begins to formulate a neural circuitry involved in depression.

Brain imaging studies of depressed patients indicate a significant reduction in hippocampal volume compared with healthy subjects[33, 34]. Magnetic resonance imaging (MRI) studies consistently show that the ventral prefrontal cortex is reduced in size in adult patients with major depressive disorder (MDD) compared with healthy controls. Postmortem data support this finding, and suggest that fewer glia cells may contribute to the overall reduced size of the region[35]. To the

striatum, MRI and postmortem studies showed volumetric reductions in the caudate and the ventral region of the striatum in individuals with depression[36], but other studies have found no differences[37]. In the amygdale, findings are not entirely consistent across studies. It has been reported that amygdala volumes were increased in patients during first episode with MDD, but patients with recurring MDD had smaller amygdala[38]. Other study reported that adult patients with MDD have increased amygdala volume than healthy comparison subjects[39]. Thus, inconsistencies in the data may relate to stage of the disorder. In summary, the anatomical data suggest that adult MDD is associated with reduced hippocampus, ventral prefrontal cortex volume and altered amygdala volume in comparison with healthy controls.

BDNF signaling in hippocampus involved in depression

The hippocampus, a key structure for the encoding of emotionally relevant data into memory, interacts with the amygdala to provide input regarding the context in which stimuli occur[40]. In addition, the hippocampus plays an inhibitory role in the regulation of the amygdala and hypothalamic– pituitary–adrenal (HPA) axis activity, which is the major mediator of systemic stress responses[41]. Evaluation of the mean changes of hippocampal volumes shows that the hippocampus is about 4%–5% smaller in patients with MDD than in healthy controls[42]. Using *in situ* DNA end-labeling demonstrated slightly increased rate of apoptosis in the dentate gyrus, CA1 and CA3 areas of the hippocampus in depressed patients[43]. In another postmortem study, Stockmeier *et al* found that hippocampal sections from depressed patients shrank more than sections from control subjects after histologic processing[44]. Hence, it suggests that both apoptosis and atrophy may occur in depression. BDNF clearly has a role in survival of neurons during hippocampal development, and this may relate to its putative role in depression. Decreased levels of BDNF may contribute to the atrophy of hippocampus that has been observed in depressed patients. Moreover, consistent data suggest that serum BDNF levels are reduced in depressed patients and are negatively correlated with depression severity while antidepressant treatment restores the basal level of serum BDNF[45, 46]. Decreased BDNF mRNA and protein levels, TrkB and cyclic adenosine monophosphate (cAMP) response element binding protein (CREB) have been found in postmortem brains of suicide victims[47]. Consistently, suicidal behavior has been associated with lower plasma BDNF level[48]. In postmortem hippocampal sections, BDNF expression has been observed to be increased in dentate gyrus and subgranular regions in subjects treated with antidepressants prior to death as compared with non-treated subjects[49].

Postmortem studies have a number of limitations in assessing depression-related molecular or cell turnover. Particularly, it is difficult to rule out the effects of antidepressant medication and other drugs or factors that are not known to investigators. Therefore, animal models were applied to investigate clear depression-induced hippocampal changes. Stress is widely used as a model for mood disorders in experimental animals. A summary of studies demonstrate that many different types of acute (single stress) and chronic (7 to 21 d) stress paradigms decrease the expression of BDNF in the hippocampus. In chronically stressed tree shrews, an animal model with high validity for depression, demonstrated reduced hippocampal volume and cell proliferation, and these alterations were prevented by tianeptine treatment[50]. Immobilization stress significant decreases BDNFmRNA expression in the major subfields of the hippocampus, with the greatest effects observed in the dentate gyrus granule cell layer. Subsequent work found that other types of stress, including unpredictable, footshock, swim stress, and maternal deprivation, also decreased the expression of BDNF in the hippocampus[51, 52]. Genetic studies support the role of BDNF Val66Met polymorphism in depression[13, 14]. In our previous study, $BDNF^{Met/Met}$ mice have smaller hippocampal volumes and increased anxiety-related behaviors[19]. Moreover, music treatment could decrease anxiety state in $BDNF^{Met/Met}$ mice by increasing BDNF levels in the hippocampus and prefrontal cortex[53].

In contrast to the actions of stress, different classes of antidepressants significantly increased the expression of BDNF in the major subfields of the hippocampus, including the granule cell layer and the CA1 and CA3 pyramidal cell layers[54]. Chronic pretreatment with antidepressants blocks the stress-induced decrease in BDNF mRNA expression in the hippocampus[55]. Distinct classes of antidepressants appear to regulate the BDNF gene through differential recruitment of individual BDNF promoters[56]. In addition, they appear to be capable of reversing the epigenetic shut down of the BDNF III and IV promoters caused by stress. Indeed, overexpression of histone deacetylases, which would derepress the epigenetic control of the BDNF promoters, is shown to upregulate hippocampal BDNF expression and exert antidepressant-like effects in animal models[57]. Furthermore, truncated TrkB overexpressing mice, which show reduced BDNF signaling, are resistant to the effects of antidepressants in the forced swim model of depression[58]. Several lines of evidence suggest that increased BDNF signaling is associated with antidepressant-like behaviors in rodent depression models. Specifically, Siuciak and colleagues were the first to report that short-term (6–7 d), microinfusion of BDNF into the dentate gyrus of hippocampus produces antidepressant-like effect in forced swim test (FST) and learned helpless (LH)[59]. Furthermore, a single intracerebroventricular injection of BDNF (10 μg) produces similar changes in the modified rat FST[60]. Compared with the classical antidepressants, the effects of BDNF on these behaviors are long lasting[60, 61]. Unfortunately, relatively high doses of BDNF need to be administered to achieve these behavioral responses. Taken together, these reports clearly implicate BDNF in both the pathogenesis of depression and as a target/mediator of antidepressant action.

Several studies have suggested that normal BDNF signaling is both necessary and sufficient for antidepressant drug action. Antidepressant-induced tyrosine phosphorylation of TrkB does not induce activity of the extracellular signal-regulated kinase pathway, but does activate phospholipase-Cγ signaling

and lead to the phosphorylation of CREB, a major transcription factor directing gene expression of plasticity-related molecules[62]. In the hippocampus, increased activity of the BDNF-CREB cascade results in antidepressive responses. Chronic, but not acute, administration of several different types of antidepressants, including SSRIs, a NE-selective reuptake inhibitor, a monoamine oxidase inhibitor, an atypical antidepressant, ECS, and lithium, increase the levels of CREB mRNA and immunoreactivity in hippocampus[55]. *In situ* hybridization and immunohistochemical analysis demonstrate that the expression of CREB is increased in the major cell layers of hippocampus (*ie*, CA3 and CA1 pyramidal and dentate gyrus granule cell layers). In contrast, chronic administration of nonantidepressant psychotropic drugs (*ie*, morphine, cocaine, and haloperidol) does not influence the expression of CREB in hippocampus, demonstrating the pharmacologic specificity of this effect for antidepressants. This does not imply that the cAMP system and CREB are not involved in the actions of these drugs. In fact, chronic opiate or psychostimulant treatments are reported to regulate CREB in striatum and locus coeruleus[63]. This demonstrates that CREB is regulated in a region-specific manner depending on the neurotransmitter systems influenced by these psychotropic drug treatments.

Hippocampal overexpression of BDNF or CREB is capable of mimicking both the structural consequences of sustained antidepressant treatment as well as exerting antidepressant-like behavioral effects[61, 64]. Indeed, activation of the cAMP-CREB cascade results in increased neurogenesis of dentate granule cell progenitors, and increased dendritic length and branching[65]. It is possible that CREB, a transcriptional activator of BDNF, recruits this neurotrophin to mediate its effects on structural plasticity. BDNF, in addition to being a target of CREB, can itself recruit this particular transcription factor by activating the mitogen-activated protein (MAP) kinase cascade[66], thus setting up a potential positive feed-back loop. Taken together, elevated BDNF-CREB, through their protective influences on vulnerable hippocampal neurons and their ability to directly promote structural reorganization, could result in repair of this region known to be damaged in depression. In addition, BDNF can alter neurotransmitter release and itself elicit an activation of postsynaptic neurons, and may thus have potential protective functional consequences on hippocampal circuitry known to be dysfunctional in depression[67]. A direct consequence of enhanced hippocampal function would be a restoration of the inhibitory control exerted on the stress response pathway of the HPA axis. In addition, the well-established role of BDNF and CREB in hippocampal-dependent learning and memory may play a critical role in ameliorating the cognitive symptoms associated with depression[67, 68]. Therefore, reduced BDNF levels result in neuronal atrophy and cell death in the hippocampus whereas enhanced BDNF levels are associated with neurogenesis, cell survival and dendritic arborization. Thus, changes in hippocampal BDNF levels and the resulting downstream signaling pathways may play an essential role in regulating depression related behaviors.

BDNF signaling in prefrontal cortex involved in depression

Several lines of evidence suggest that the prefrontal cortex (PFC) is involved in the neuropathology of depression and the response to stress. Perhaps the most widely accepted division of PFC, based on anatomical connectivity and functional specialization, is the dorsolateral and ventromedial sectors[69]. The ventromedial prefrontal cortex (vmPFC) includes the ventral portion of the medial prefrontal cortex and medial portion of the orbital surface. Targets of vmPFC projections include the hypothalamus and periaqueductal gray, which mediate the visceral autonomic activity associated with emotion, and the ventral striatum, which signals reward and motivational value. In addition, vmPFC has dense reciprocal connections with the amygdala, which is involved in threat detection and fear conditioning[29]. By contrast, the dorsolateral prefrontal cortex (DLPFC), which includes portions of the middle and superior frontal gyri on the lateral surface of the frontal lobes, receives input from specific sensory cortices, and has dense interconnections with premotor areas, the frontal eye fields, and lateral parietal cortex[70]. The distinct patterns of connectivity in these two regions of PFC suggest disparate functionality. Indeed, DLPFC has primarily been associated with "cognitive" or "executive" functions, whereas vmPFC is largely ascribed "emotional" or "affective" functions.

Volumetric changes in the PFC in depression are similar to those described in the human hippocampus. The earliest functional imaging studies of depression compared the resting state brain activity (*eg* blood flow or glucose metabolism) of depressed patients with that of non-depressed comparison subjects. Results from these studies associate depression with abnormally high levels of vmPFC activity[71], but abnormally low levels of DLPFC activity in resting brain activity[72]. Recent, a type of functional imaging study compares task-related brain activations (blood flow) of depressed patients to that of non-depressed comparison subjects. Data from these studies demonstrate that depressed patients exhibit greater task-related activation in DLPFC during tests of working memory and cognitive control when performance is matched to non-depressed subjects[73]. In light of the resting state data indicating DLPFC hypoactivity in depression, these results suggest dysfunction (or at least inefficiency) in the DLPFC of depressed patients. In sum, the functional imaging studies converge to suggest that depression is associated with seemingly opposite activity profiles in vmPFC and DLPFC. The vmPFC is hyperactive at rest, whereas the DLPFC is hypoactive at rest. These imaging data hint that an imbalance in vmPFC/DLPFC activity may contribute to depression. However, functional imaging data alone cannot adjudicate whether the abnormal activity profiles observed in vmPFC and DLPFC are a cause or consequence of the disorder.

In humans, postmortem studies have shown that both BDNF and TrkB levels are significantly decreased in the prefrontal cortex and hippocampus of suicide patients compared with controls and antidepressant therapy restores brain BDNF levels to the normal range[74]. In addition, there were signifi-

cant decreases in the phosphorylation of TrkA and TrkB in both PFC and hippocampus of suicide subjects, whereas the phosphorylation of TrkC was decreased only in hippocampus without any change in PFC[75]. Stress is used as a model to study alterations of molecules and brain structure because mood disorders are often precipitated or exacerbated by acute or chronic stressful life events[76]. Repeated stress causes dendritic shortening in medial prefrontal cortex, as well as in hippocampus[77]. As with in the hippocampus, stress decrease BDNF levels in the PFC. Prenatally stressed rats had significantly less BDNF protein than nonstressed rats in PFC by Western blotting analysis[78]. Furthermore, Roth showed that infant maltreatment results in methylation of *BDNF* DNA through the lifespan to adulthood that dovetails reduced *BDNF* gene expression in the adult PFC in rat[79].

Many different antidepressants produce a modest increase in BDNF mRNA levels in PFC after a few days of treatment. BDNF mRNA and protein levels, as well as TrkB mRNA levels, were increased significantly in post-natal day 13 rats in hippocampus and PFC after escitalopram treatment as compared to control, but desipramine failed to increase either BDNF or TrkB, which suggests that SSRIs are able to positively modulate BDNF and TrkB expression, whereas desipramine is not able to. The failure of desipramine to positively modulate BDNF and TrkB expression in postnatal day 13 rats is consistent with the lack of efficacy of desipramine in children and adolescents[80]. The BDNF gene consists of four 5′ noncoding exons (I–IV) each with a separate promotor and one 3′ exon (exon-V) encoding the mature BDNF protein. The exon-III and IV BDNF promoters are regulated as immediate early genes. Previous work showed that BDNF-LTP is associated with rapid upregulation of exon-III specific and exon-V (total) BDNF mRNA. In PFC exon-III and exon-V BDNF mRNA levels were significantly elevated about 3- and 2-fold, respectively, after chronic but not acute fluoxetine treatment. In hippocampus, chronic fluoxetine administration led to a 2.5-fold increase in exon-III expression, but no significant change in exon-V expression. These studies demonstrate that chronic administration of fluoxetine leads to brain region specific upregulation of BDNF in the adult brain, which suggests that chronically administered antidepressants could promote BDNF-induced gene expression and synaptic plasticity in multiple brain regions.

Animals work shows that stress decreases phosphorylated CREB and antidepressants treatment increases the expression of phosphorylated CREB specifically in the hippocampus and prefrontal cortex[81]. Experimental studies demonstrated that chronic forced swim stress decreased the expression of phosphorylated-extracellular signal-regulated kinase 2 (p-ERK2), ERK1 and ERK2 in the hippocampus and prefrontal cortex in rats; fluoxetine reversed the stress-induced disruption of the p-ERK2, which is indicated by the increased level of the p-ERK2 in the hippocampus and prefrontal cortex in stress-fluoxetine group compared to stress group, but exhibited no effect on the stress-induced decrease of the ERK1 and ERK2. It thus appears that the major effect of fluoxetine is to activate the ERK and CREB to increase the levels of p-ERK2 and p-CREB, but not to increase the ERK and CREB expression[82].

BDNF signaling in nucleus accumbens involved in depression

The NAc is a target of the mesolimbic dopamine system, which receives dopamine input from dopaminergic neurons in the ventral tegmental area (VTA) of the midbrain. Furthermore, the ventral striatum also has been noted to have extensive connections with the amygdala and the orbital, subgenual, and ventrolateral PFC[83]. The NAc, and its dopaminergic inputs, play critical roles in reward. Virtually all drugs of abuse increase dopaminergic transmission in the NAc, which partly mediates their rewarding effects[84]. On the other hand, the VTA neurons also innervate several other limbic structures, including the amygdala and limbic regions of neocortex. The relationship of VTA-NAc pathway to mood disorders requires further study, but it seems plausible that disturbances in this pathway would be related to abnormalities in hedonic tone and motivation[2], which are central features of mania and depression. This is supported by the finding of decreased striatal response to happy stimuli associated with level of anhedonia in depressed subjects as well as the observation of increased striatal activity in mania[85].

However, increasing BDNF levels in the NAc or VTA pathway produces depression-like phenotype and animals with a selective knockout of BDNF in the VTA are protected from the depressive effects produced by the social defeat stress[23]. At the same time, intra-VTA infusion of BDNF exerts a depression-like effect in the forced swim test, while blockade of BDNF action in the NAc, by use of viral-mediated overexpression of a dominant negative mutant of TrkB, causes an antidepressant-like effect in the same test[86]. These data suggest that BDNF plays opposite roles in the VTA-NAc circuit compared with in the hippocampal-prefrontal circuit.

While dysfunction of the VTA-NAc circuit is thought to be associated with depression, antidepressants have been postulated to reverse this dysfunction. In stark contrast to the effects of CREB-BDNF in the hippocampus, activation of the CREB-BDNF cascade in the VTA-NAc pathway results in pro-depressive like behavior[64]. Increased CREB activity in the NAc results in a phenotype characteristic of depression, including reduced reward experience or "anhedonia" and increased immobility in the forced swim test, symbolizing behavioral "despair"[87]. The effects of BDNF are thought to be mediated via up-regulating CREB expression, through activation of the MAPK/ERK pathway[66]. Thus BDNF, upstream of CREB, would recruit specific target genes with promoter CRE elements, and then affect the functioning of the VTA-NAc circuitry, resulting in a depression-like phenotype. CREB is known to positively modulate levels of dynorphin within the NAc[88], and this upregulation of the endogenous opioid dynorphin could mediate the pro-depressive effects of CREB. Although at present it is unknown if CREB induction in the NAc results in enhanced dynorphin release within the VTA, it has been hypothesized that such a change in the context of

the VTA-NAc pathway could result in dysphoria and lack of pleasure seeking[89]. This raises the possibility that enhanced BDNF-CREB in the NAc may, through a regulation of opioid signalling, result in an anhedonic state thus contributing to the pro-depressive effects, whereas an abrogation of BDNF-CREB signalling in this region could have beneficial consequences on behavior and exert an antidepressant-like effect. The opposite behavioral response for infusion BDNF to hippocampus versus NAc suggests that depression and antidepressant effects are related to the functional consequences of different downstream regulation in different neuronal networks.

BDNF signaling in amygdala involved in depression

Recent years, the amygdala has emerged as the key forebrain structure mediating inborn and acquired emotional responses, as well as processing, interpreting, and integrating various aspects of biologically and/or emotionally important information[90]. The amygdala is a complex structure that is comprised of many subnuclei. Two such units that have been particularly implicated in the control of emotional processes are the central nucleus (CeA) and the basolateral amygdala (BLA). A prevailing view is that the BLA is responsible for emotional learning; receiving sensory information and acts as a site of conditioned and unconditioned stimulus associations and uses this learned information to control the activity of the CeA. In turn, the CeA acts as a 'controller of the brainstem', by using its widespread projections to the hypothalamus, midbrain reticular formation and brainstem to orchestrate behavioral, autonomic, and neuroendocrine responses. Different regions within the amygdala are specialized, on the basis of connections with cortical, hippocampal, thalamic, hypothalamic, and other subcortical structures, to detect objects salient to the prevailing emotional state, and to modulate an appropriate response[91, 92]. Dysfunction in amygdala plasticity can be related theoretically to depression and bipolar disorder (BD)[91]. Neuroimaging studies of the amygdala in patients with BD are characterized by an interesting age-related dichotomy of findings. In adults, the predominant pattern is one of increased amygdala volume while in children and adolescents the reverse applies, which suggest that amygdala size may vary in relation to illness duration[93, 94]. Resting state functional analyses have been largely limited to the adult population and are indicative of increased baseline amygdala activity which correlates positively with severity of depression[95].

The link between stress and depression has long been observed, particularly at the clinical level, where chronic exposure to stressful life events has been associated with the development of depressive symptoms. Stress also causes structure changes in amygdala. Both acute and chronic stress increases spine synapse formation in amygdala[96] but chronic stress decreases it in hippocampus[97]. Moreover, chronic stress for 21 days or longer impairs hippocampal-dependent cognitive function and enhances amygdala-dependent unlearned fear and fear conditioning[98], which are consistent with the opposite effects of stress on hippocampal and amygdala structure and suggest that the effect of chronic stress on dendritic remodeling is regionally specific.

BDNF mRNA increased in the amygdala 1 h after the final exposure to intermittent water immersion stress. Consistent with this, repeated intermittent social stress increased BDNF mRNA in the BLA and CeA but not in the medial amygdala (MeA) 2 h after termination of social stress. However, repeated restraint or acute social stress exposure reduced amygdala BDNF mRNA 24 h later[99, 100]. This suggests that stress-induced changes in BDNF are transient in the amygdala. BDNF-overexpressing transgenic mice showed increased BLA spine density and increase anxiety-like behavior in open field test and elevated-plus maze test[101]. Furthermore, previous studies have reported that chronic stress-induced anxiety is accompanied by increases in dendritic area and spine density in the BLA[102, 103]. This increase in the BLA spine density may be a reason for the increased amygdala size and functional output.

The amygdala has been the focus of a great deal of work in the anxiety, post-traumatic stress disorder (PTSD), and drug addiction fields, but has received relatively little attention in depression. It would be interesting to use behavioral tests that focus on the amygdala, as well as direct manipulations of specific proteins in the amygdala (*eg*, CREB and BDNF, among many others), to explore the role played by these circuits in depression and antidepressant action.

Conclusions and future directions

In summary, the data herein reviews the role of BDNF in critical neural networks underlying depression/stress and antidepressant treatment (Table 1). The main studies suggest four points: First, depression or stress could reduce BDNF levels in the hippocampus and PFC; Second, depression or stress induces dentritic atrophy in the hippocampus and PFC, while leads to increased spine density in the BLA; Third, successful antidepressant treatments increase BDNF levels in the hippocampus and PFC and inhibit depression-like behavior; Fourth, BDNF levels increase in the BLA and NAc produce anxiety-like or depression-like phenotype. Thus the diverse roles of BDNF in depression depend on its location in the neural circuitry, namely, in the hippocampus and PFC BDNF inhibits depressive symptoms and whereas in the NAc and amygdala facilitates depression-like or anxiety-like symptoms.

Regardless of the role of BDNF in the etiology of depression

Table 1. Regulation of BDNF by depression/stress, and antidepressant treatment in different brain regions.

Brain regions	Depression/Stress	Antidepressant
Hippocampus	BDNF↓	BDNF↑
PFC	BDNF↓	BDNF↑
NAc	BDNF↑	BDNF↓
Amygdala (BLA)	BDNF↑	—

Symbols: ↓, decrease; ↑, increase; —, inconsistent.

and in the mechanism of action of current antidepressants, advances in understanding how specific molecular mechanisms within the hippocampus, PFC, NAc, amygdala, and other brain regions regulate mood will provide novel avenues. A major need of future research is to better define the detailed circuitry of the numerous and diverse molecular pathways in these brain regions.

Acknowledgements

This study was supported by National Natural Science Foundation of China (No 30725020 and 30700258), China Postdoctoral Science Foundation (No 20090461232 and 200901006) and Independent Innovation Foundation of Shandong University (No 2009TS126 and 2010TS088).

References

1 Briley M, Moret C. Present and future anxiolytics. IDrugs 2000; 3: 695–9.
2 Nestler EJ, Barrot M, DiLeone RJ, Eisch AJ, Gold SJ, Monteggia LM. Neurobiology of depression. Neuron 2002; 34: 13–25.
3 Fava M, Kendler KS. Major depressive disorder. Neuron 2000; 28: 335–41.
4 Burmeister M. Basic concepts in the study of diseases with complex genetics. Biol Psychiatry 1999; 45: 522–32.
5 Belmaker RH, Agam G. Major depressive disorder. N Engl J Med 2008; 358: 55–68.
6 Morilak DA, Frazer A. Antidepressants and brain monoaminergic systems: a dimensional approach to understanding their behavioural effects in depression and anxiety disorders. Int J Neuropsychopharmacol 2004; 7: 193–218.
7 Duman RS, Malberg J, Nakagawa S, D'Sa C. Neuronal plasticity and survival in mood disorders. Biol Psychiatry 2000; 48: 732–9.
8 Altar CA. Neurotrophins and depression. Trends Pharmacol Sci 1999; 20: 59–61.
9 Cunha AB, Frey BN, Andreazza AC, Goi JD, Rosa AR, Goncalves CA, *et al.* Serum brain-derived neurotrophic factor is decreased in bipolar disorder during depressive and manic episodes. Neurosci Lett 2006; 398: 215–9.
10 Palomino A, Vallejo-Illarramendi A, Gonzalez-Pinto A, Aldama A, Gonzalez-Gomez C, Mosquera F, *et al.* Decreased levels of plasma BDNF in first-episode schizophrenia and bipolar disorder patients. Schizophr Res 2006; 86: 321–2.
11 Chen ZY, Patel PD, Sant G, Meng CX, Teng KK, Hempstead BL, *et al.* Variant brain-derived neurotrophic factor (BDNF) (Met66) alters the intracellular trafficking and activity-dependent secretion of wild-type BDNF in neurosecretory cells and cortical neurons. J Neurosci 2004; 24: 4401–11.
12 Egan MF, Kojima M, Callicott JH, Goldberg TE, Kolachana BS, Bertolino A, *et al.* The BDNF val66met polymorphism affects activity-dependent secretion of BDNF and human memory and hippocampal function. Cell 2003; 112: 257–69.
13 Post RM. Role of BDNF in bipolar and unipolar disorder: clinical and theoretical implications. J Psychiatr Res 2007; 41: 979–90.
14 Monteggia LM, Luikart B, Barrot M, Theobold D, Malkovska I, Nef S, *et al.* Brain-derived neurotrophic factor conditional knockouts show gender differences in depression-related behaviors. Biol Psychiatry 2007; 61: 187–97.
15 Lang UE, Hellweg R, Kalus P, Bajbouj M, Lenzen KP, Sander T, *et al.* Association of a functional BDNF polymorphism and anxiety-related personality traits. Psychopharmacology (Berl) 2005; 180: 95–9.
16 Kunugi H, Ueki A, Otsuka M, Isse K, Hirasawa H, Kato N, *et al.* A novel polymorphism of the brain-derived neurotrophic factor (BDNF) gene associated with late-onset Alzheimer's disease. Mol Psychiatry 2001; 6: 83–6.
17 Mirowska-Guzel D, Mach A, Gromadzka G, Czlonkowski A, Czlonkowska A. BDNF A196G and C270T gene polymorphisms and susceptibility to multiple sclerosis in the Polish population. Gender differences. J Neuroimmunol 2008; 193: 170–2.
18 Duman RS, Monteggia LM. A neurotrophic model for stress-related mood disorders. Biol Psychiatry 2006; 59: 1116–27.
19 Chen ZY, Jing D, Bath KG, Ieraci A, Khan T, Siao CJ, *et al.* Genetic variant BDNF (Val66Met) polymorphism alters anxiety-related behavior. Science 2006; 314: 140–3.
20 Yu H, Wang Y, Pattwell S, Jing D, Liu T, Zhang Y, *et al.* Variant BDNF Val66Met polymorphism affects extinction of conditioned aversive memory. J Neurosci 2009; 29: 4056–64.
21 Kozisek ME, Middlemas D, Bylund DB. Brain-derived neurotrophic factor and its receptor tropomyosin-related kinase B in the mechanism of action of antidepressant therapies. Pharmacol Ther 2008; 117: 30–51.
22 Pittenger C, Duman RS. Stress, depression, and neuroplasticity: a convergence of mechanisms. Neuropsychopharmacology 2008; 33: 88–109.
23 Berton O, Nestler EJ. New approaches to antidepressant drug discovery: beyond monoamines. Nat Rev Neurosci 2006; 7: 137–51.
24 Groves JO. Is it time to reassess the BDNF hypothesis of depression? Mol Psychiatry 2007; 12: 1079–88.
25 Martinowich K, Manji H, Lu B. New insights into BDNF function in depression and anxiety. Nat Neurosci 2007; 10: 1089–93.
26 Castren E, Voikar V, Rantamaki T. Role of neurotrophic factors in depression. Curr Opin Pharmacol 2007; 7: 18–21.
27 Russo-Neustadt AA, Chen MJ. Brain-derived neurotrophic factor and antidepressant activity. Curr Pharm Des 2005; 11: 1495–510.
28 Berton O, McClung CA, Dileone RJ, Krishnan V, Renthal W, Russo SJ, *et al.* Essential role of BDNF in the mesolimbic dopamine pathway in social defeat stress. Science 2006; 311: 864–8.
29 Ongur D, Price JL. The organization of networks within the orbital and medial prefrontal cortex of rats, monkeys and humans. Cereb Cortex 2000; 10: 206–19.
30 Chamberlain SR, Sahakian BJ. The neuropsychology of mood disorders. Curr Psychiatry Rep 2006; 8: 458–63.
31 Davidson RJ, Abercrombie H, Nitschke JB, Putnam K. Regional brain function, emotion and disorders of emotion. Curr Opin Neurobiol 1999; 9: 228–34.
32 Ressler KJ, Nemeroff CB. Role of serotonergic and noradrenergic systems in the pathophysiology of depression and anxiety disorders. Depress Anxiety 2000; 12: 2–19.
33 Sheline YI, Wang PW, Gado MH, Csernansky JG, Vannier MW. Hippocampal atrophy in recurrent major depression. Proc Natl Acad Sci USA 1996; 93: 3908–13.
34 Sheline YI, Gado MH, Kraemer HC. Untreated depression and hippocampal volume loss. Am J Psychiatry 2003; 160: 1516–8.
35 Ongur D, Drevets WC, Price JL. Glial reduction in the subgenual prefrontal cortex in mood disorders. Proc Natl Acad Sci USA 1998; 95: 13290–5.
36 Baumann B, Danos P, Krell D, Diekmann S, Leschinger A, Stauch R, *et al.* Reduced volume of limbic system-affiliated basal ganglia in mood disorders: preliminary data from a postmortem study. J Neuropsychiatry Clin Neurosci 1999; 11: 71–8.
37 Lacerda AL, Nicoletti MA, Brambilla P, Sassi RB, Mallinger AG, Frank

E, *et al.* Anatomical MRI study of basal ganglia in major depressive disorder. Psychiatry Res 2003; 124: 129–40.
38 Frodl T, Meisenzahl EM, Zetzsche T, Born C, Jager M, Groll C, *et al.* Larger amygdala volumes in first depressive episode as compared to recurrent major depression and healthy control subjects. Biol Psychiatry 2003; 53: 338–44.
39 Siegle GJ, Konecky RO, Thase ME, Carter CS. Relationships between amygdala volume and activity during emotional information processing tasks in depressed and never-depressed individuals: an fMRI investigation. Ann N Y Acad Sci 2003; 985: 481–4.
40 LaBar KS, Cabeza R. Cognitive neuroscience of emotional memory. Nat Rev Neurosci 2006; 7: 54–64.
41 Jacobson L, Sapolsky R. The role of the hippocampus in feedback regulation of the hypothalamic-pituitary-adrenocortical axis. Endocr Rev 1991; 12: 118–34.
42 Videbech P, Ravnkilde B. Hippocampal volume and depression: a meta-analysis of MRI studies. Am J Psychiatry 2004; 161: 1957–66.
43 Lucassen PJ, Muller MB, Holsboer F, Bauer J, Holtrop A, Wouda J, *et al.* Hippocampal apoptosis in major depression is a minor event and absent from subareas at risk for glucocorticoid overexposure. Am J Pathol 2001; 158: 453–68.
44 Stockmeier CA, Mahajan GJ, Konick LC, Overholser JC, Jurjus GJ, Meltzer HY, *et al.* Cellular changes in the postmortem hippocampus in major depression. Biol Psychiatry 2004; 56: 640–50.
45 Aydemir C, Yalcin ES, Aksaray S, Kisa C, Yildirim SG, Uzbay T, *et al.* Brain-derived neurotrophic factor (BDNF) changes in the serum of depressed women. Prog Neuropsychopharmacol Biol Psychiatry 2006; 30: 1256–60.
46 Lee BH, Kim H, Park SH, Kim YK. Decreased plasma BDNF level in depressive patients. J Affect Disord 2007; 101: 239–44.
47 Dwivedi Y, Rao JS, Rizavi HS, Kotowski J, Conley RR, Roberts RC, *et al.* Abnormal expression and functional characteristics of cyclic adenosine monophosphate response element binding protein in postmortem brain of suicide subjects. Arch Gen Psychiatry 2003; 60: 273–82.
48 Kim YK, Lee HP, Won SD, Park EY, Lee HY, Lee BH, *et al.* Low plasma BDNF is associated with suicidal behavior in major depression. Prog Neuropsychopharmacol Biol Psychiatry 2007; 31: 78–85.
49 Chen B, Dowlatshahi D, MacQueen GM, Wang JF, Young LT. Increased hippocampal BDNF immunoreactivity in subjects treated with antidepressant medication. Biol Psychiatry 2001; 50: 260–5.
50 Czeh B, Michaelis T, Watanabe T, Frahm J, de Biurrun G, van Kampen M, *et al.* Stress-induced changes in cerebral metabolites, hippocampal volume, and cell proliferation are prevented by antidepressant treatment with tianeptine. Proc Natl Acad Sci USA 2001; 98: 12796–801.
51 Rasmusson AM, Shi L, Duman R. Downregulation of BDNF mRNA in the hippocampal dentate gyrus after re-exposure to cues previously associated with footshock. Neuropsychopharmacology 2002; 27: 133–42.
52 Roceri M, Cirulli F, Pessina C, Peretto P, Racagni G, Riva MA. Postnatal repeated maternal deprivation produces age-dependent changes of brain-derived neurotrophic factor expression in selected rat brain regions. Biol Psychiatry 2004; 55: 708–14.
53 Li WJ, Yu H, Yang JM, Gao J, Jiang H, Feng M, *et al.* Anxiolytic effect of music exposure on BDNFMet/Met transgenic mice. Brain Res 2010; 1347: 71–9.
54 Russo-Neustadt AA, Alejandre H, Garcia C, Ivy AS, Chen MJ. Hippocampal brain-derived neurotrophic factor expression following treatment with reboxetine, citalopram, and physical exercise. Neuropsychopharmacology 2004; 29: 2189–99.
55 Nibuya M, Morinobu S, Duman RS. Regulation of BDNF and trkB mRNA in rat brain by chronic electroconvulsive seizure and antidepressant drug treatments. J Neurosci 1995; 15: 7539–47.
56 Dias BG, Banerjee SB, Duman RS, Vaidya VA. Differential regulation of brain derived neurotrophic factor transcripts by antidepressant treatments in the adult rat brain. Neuropharmacology 2003; 45: 553–63.
57 Tsankova NM, Berton O, Renthal W, Kumar A, Neve RL, Nestler EJ. Sustained hippocampal chromatin regulation in a mouse model of depression and antidepressant action. Nat Neurosci 2006; 9: 519–25.
58 Saarelainen T, Hendolin P, Lucas G, Koponen E, Sairanen M, MacDonald E, *et al.* Activation of the TrkB neurotrophin receptor is induced by antidepressant drugs and is required for antidepressant-induced behavioral effects. J Neurosci 2003; 23: 349–57.
59 Siuciak JA, Lewis DR, Wiegand SJ, Lindsay RM. Antidepressant-like effect of brain-derived neurotrophic factor (BDNF). Pharmacol Biochem Behav 1997; 56: 131–7.
60 Hoshaw BA, Malberg JE, Lucki I. Central administration of IGF-I and BDNF leads to long-lasting antidepressant-like effects. Brain Res 2005; 1037: 204–8.
61 Shirayama Y, Chen AC, Nakagawa S, Russell DS, Duman RS. Brain-derived neurotrophic factor produces antidepressant effects in behavioral models of depression. J Neurosci 2002; 22: 3251–61.
62 Duman RS. Pathophysiology of depression: the concept of synaptic plasticity. Eur Psychiatry 2002; 17: 306–10.
63 Widnell KL, Russell DS, Nestler EJ. Regulation of expression of cAMP response element-binding protein in the locus coeruleus *in vivo* and in a locus coeruleus-like cell line *in vitro*. Proc Natl Acad Sci USA 1994; 91: 10947–51.
64 Malberg JE, Blendy JA. Antidepressant action: to the nucleus and beyond. Trends Pharmacol Sci 2005; 26: 631–8.
65 Fujioka T, Fujioka A, Duman RS. Activation of cAMP signaling facilitates the morphological maturation of newborn neurons in adult hippocampus. J Neurosci 2004; 24: 319–28.
66 Arthur JS, Fong AL, Dwyer JM, Davare M, Reese E, Obrietan K, *et al.* Mitogen- and stress-activated protein kinase 1 mediates cAMP response element-binding protein phosphorylation and activation by neurotrophins. J Neurosci 2004; 24: 4324–32.
67 Tyler WJ, Perrett SP, Pozzo-Miller LD. The role of neurotrophins in neurotransmitter release. Neuroscientist 2002; 8: 524–31.
68 Mizuno K, Giese KP. Hippocampus-dependent memory formation: do memory type-specific mechanisms exist? J Pharmacol Sci 2005; 98: 191–7.
69 Zald DH. Orbital versus dorsolateral prefrontal cortex: anatomical insights into content versus process differentiation models of the prefrontal cortex. Ann N Y Acad Sci 2007; 1121: 395–406.
70 Barbas H. Connections underlying the synthesis of cognition, memory, and emotion in primate prefrontal cortices. Brain Res Bull 2000; 52: 319–30.
71 Greicius MD, Flores BH, Menon V, Glover GH, Solvason HB, Kenna H, *et al.* Resting-state functional connectivity in major depression: abnormally increased contributions from subgenual cingulate cortex and thalamus. Biol Psychiatry 2007; 62: 429–37.
72 Galynker II, Cai J, Ongseng F, Finestone H, Dutta E, Serseni D. Hypofrontality and negative symptoms in major depressive disorder. J Nucl Med 1998; 39: 608–12.
73 Wagner G, Sinsel E, Sobanski T, Kohler S, Marinou V, Mentzel HJ, *et al.* Cortical inefficiency in patients with unipolar depression: an event-related FMRI study with the Stroop task. Biol Psychiatry 2006; 59: 958-65.

74 Castren E. Neurotrophic effects of antidepressant drugs. Curr Opin Pharmacol 2004; 4: 58–64.
75 Dwivedi Y, Rizavi HS, Zhang H, Mondal AC, Roberts RC, Conley RR, *et al.* Neurotrophin receptor activation and expression in human postmortem brain: effect of suicide. Biol Psychiatry 2009; 65: 319–28.
76 Brown J, Cooper-Kuhn CM, Kempermann G, Van Praag H, Winkler J, Gage FH, *et al.* Enriched environment and physical activity stimulate hippocampal but not olfactory bulb neurogenesis. Eur J Neurosci 2003; 17: 2042–6.
77 Brown SM, Henning S, Wellman CL. Mild, short-term stress alters dendritic morphology in rat medial prefrontal cortex. Cereb Cortex 2005; 15: 1714–22.
78 Burton CL, Chatterjee D, Chatterjee-Chakraborty M, Lovic V, Grella SL, Steiner M, *et al.* Prenatal restraint stress and motherless rearing disrupts expression of plasticity markers and stress-induced corticosterone release in adult female Sprague-Dawley rats. Brain Res 2007; 1158: 28–38.
79 Roth TL, Lubin FD, Funk AJ, Sweatt JD. Lasting epigenetic influence of early-life adversity on the BDNF gene. Biol Psychiatry 2009; 65: 760–9.
80 Kozisek ME, Middlemas D, Bylund DB. The differential regulation of BDNF and TrkB levels in juvenile rats after four days of escitalopram and desipramine treatment. Neuropharmacology 2008; 54: 251–7.
81 Sairanen M, O'Leary OF, Knuuttila JE, Castren E. Chronic antidepressant treatment selectively increases expression of plasticity-related proteins in the hippocampus and medial prefrontal cortex of the rat. Neuroscience 2007; 144: 368–74.
82 Qi X, Lin W, Li J, Li H, Wang W, Wang D, *et al.* Fluoxetine increases the activity of the ERK-CREB signal system and alleviates the depressive-like behavior in rats exposed to chronic forced swim stress. Neurobiol Dis 2008; 31: 278–85.
83 Price JL, Carmichael ST, Drevets WC. Networks related to the orbital and medial prefrontal cortex; a substrate for emotional behavior? Prog Brain Res 1996; 107: 523–36.
84 Koob GF, Sanna PP, Bloom FE. Neuroscience of addiction. Neuron 1998; 21: 467–76.
85 Keedwell PA, Andrew C, Williams SC, Brammer MJ, Phillips ML. The neural correlates of anhedonia in major depressive disorder. Biol Psychiatry 2005; 58: 843–53.
86 Eisch AJ, Bolanos CA, de Wit J, Simonak RD, Pudiak CM, Barrot M, *et al.* Brain-derived neurotrophic factor in the ventral midbrain-nucleus accumbens pathway: a role in depression. Biol Psychiatry 2003; 54: 994–1005.
87 Pliakas AM, Carlson RR, Neve RL, Konradi C, Nestler EJ, Carlezon WA, Jr. Altered responsiveness to cocaine and increased immobility in the forced swim test associated with elevated cAMP response element-binding protein expression in nucleus accumbens. J Neurosci 2001; 21: 7397–403.
88 Carlezon WA Jr, Thome J, Olson VG, Lane-Ladd SB, Brodkin ES, Hiroi N, *et al.* Regulation of cocaine reward by CREB. Science 1998; 282: 2272–5.
89 Nestler EJ, Carlezon WA Jr. The mesolimbic dopamine reward circuit in depression. Biol Psychiatry 2006; 59: 1151–9.
90 Phelps EA, LeDoux JE. Contributions of the amygdala to emotion processing: from animal models to human behavior. Neuron 2005; 48: 175–87.
91 Quiroz JA, Singh J, Gould TD, Denicoff KD, Zarate CA, Manji HK. Emerging experimental therapeutics for bipolar disorder: clues from the molecular pathophysiology. Mol Psychiatry 2004; 9: 756–76.
92 Yaniv D, Desmedt A, Jaffard R, Richter-Levin G. The amygdala and appraisal processes: stimulus and response complexity as an organizing factor. Brain Res Brain Res Rev 2004; 44: 179–86.
93 Brambilla P, Harenski K, Nicoletti M, Sassi RB, Mallinger AG, Frank E, *et al.* MRI investigation of temporal lobe structures in bipolar patients. J Psychiatr Res 2003; 37: 287–95.
94 Frangou S. The maudsley bipolar disorder project. Epilepsia 2005; 46: 19–25.
95 Mah L, Zarate CA Jr, Singh J, Duan YF, Luckenbaugh DA, Manji HK, *et al.* Regional cerebral glucose metabolic abnormalities in bipolar II depression. Biol Psychiatry 2007; 61: 765–75.
96 Vyas A, Mitra R, Shankaranarayana Rao BS, Chattarji S. Chronic stress induces contrasting patterns of dendritic remodeling in hippocampal and amygdaloid neurons. J Neurosci 2002; 22: 6810–8.
97 Pawlak R, Rao BS, Melchor JP, Chattarji S, McEwen B, Strickland S. Tissue plasminogen activator and plasminogen mediate stress-induced decline of neuronal and cognitive functions in the mouse hippocampus. Proc Natl Acad Sci USA 2005; 102: 18201–6.
98 Conrad CD, LeDoux JE, Magarinos AM, McEwen BS. Repeated restraint stress facilitates fear conditioning independently of causing hippocampal CA3 dendritic atrophy. Behav Neurosci 1999; 113: 902–13.
99 Pizarro JM, Lumley LA, Medina W, Robison CL, Chang WE, Alagappan A, *et al.* Acute social defeat reduces neurotrophin expression in brain cortical and subcortical areas in mice. Brain Res 2004; 1025: 10–20.
100 Fanous S, Hammer RP Jr, Nikulina EM. Short- and long-term effects of intermittent social defeat stress on brain-derived neurotrophic factor expression in mesocorticolimbic brain regions. Neuroscience 2010; 167: 598–607.
101 Govindarajan A, Rao BS, Nair D, Trinh M, Mawjee N, Tonegawa S, *et al.* Transgenic brain-derived neurotrophic factor expression causes both anxiogenic and antidepressant effects. Proc Natl Acad Sci USA 2006; 103: 13208–13.
102 Vyas A, Pillai AG, Chattarji S. Recovery after chronic stress fails to reverse amygdaloid neuronal hypertrophy and enhanced anxiety-like behavior. Neuroscience 2004; 128: 667–73.
103 Mitra R, Jadhav S, McEwen BS, Vyas A, Chattarji S. Stress duration modulates the spatiotemporal patterns of spine formation in the basolateral amygdala. Proc Natl Acad Sci USA 2005; 102: 9371–6.

Acta Pharmacologica Sinica (2011) 32: 12–20
 1671-4083/11 $32.00
www.nature.com/aps

Review

Hepatocyte growth factor in lung repair and pulmonary fibrosis

Ronald Allan M PANGANIBAN, Regina M DAY*

Department of Pharmacology, Uniformed Services University of the Health Sciences, Bethesda, MD 20852, USA

Pulmonary remodeling is characterized by the permanent and progressive loss of the normal alveolar architecture, especially the loss of alveolar epithelial and endothelial cells, persistent proliferation of activated fibroblasts, or myofibroblasts, and alteration of extracellular matrix. Hepatocyte growth factor (HGF) is a pleiotropic factor, which induces cellular motility, survival, proliferation, and morphogenesis, depending upon the cell type. In the adult, HGF has been demonstrated to play a critical role in tissue repair, including in the lung. Administration of HGF protein or ectopic expression of HGF has been demonstrated in animal models of pulmonary fibrosis to induce normal tissue repair and to prevent fibrotic remodeling. HGF-induced inhibition of fibrotic remodeling may occur via multiple direct and indirect mechanisms including the induction of cell survival and proliferation of pulmonary epithelial and endothelial cells, and the reduction of myofibroblast accumulation.

Keywords: hepatocyte growth factor; myofibroblast; alveolar epithelial cell; pulmonary fibrosis

Acta Pharmacologica Sinica (2011) 32: 12–20; doi: 10.1038/aps.2010.90; published online 6 Dec 2010

Pathophysiology of pulmonary fibrosis

Pulmonary fibrosis is a disease characterized by the replacement of the lung tissue with scar tissue, resulting in the permanent loss of the normal alveolar architecture. The disease is usually progressive, and death is often the direct result of either respiratory insufficiency or right heart failure due to pulmonary hypertension. Pulmonary fibrosis can be directly induced by a variety of insults to lung tissue including exposure to drugs, organic or inorganic particles, bacterial or viral infection, or clinical irradiation for the treatment of cancer[1, 2]. The condition may also occur idiopathically[1]. Treatments for pulmonary fibrosis consist of anti-inflammatory and immunomodulatory agents, cytotoxic agents (*eg*, methotrexate, cyclophosphamide), antioxidants (*eg*, *N*-acetylcycteine), antifibrotic agents (*eg*, pirfenidone, colchicine), interferon-gamma 1β, and/or lung transplantation[3, 4]. The pulmonary fibrosis patient's response to treatment often depends on the etiology of the disease. However, currently available treatments are largely ineffective in halting the progression of the disease.

The progression of pulmonary fibrosis is believed to involve a failed or dysregulated injury response, which may be accompanied by inflammation[5]. An emerging view of lung remodeling suggests that the disease may develop as the result of repeated stimuli, with early cycles of injury to alveolar epithelial and endothelial cells, followed by inflammation and attempted repair, ultimately leading to aberrant wound healing and fibrosis[2, 6].

Cellular alterations in pulmonary fibrosis

In pulmonary remodeling, the loss of the normal pulmonary architecture is characterized by: 1) the loss of alveolar epithelial and endothelial cells; 2) the persistent proliferation of activated fibroblasts, or myofibroblasts; and 3) the extensive alteration of the extracellular matrix (Figure 1). Two primary animal models have been developed for the study of experimentally-induced pulmonary fibrosis: thoracic irradiation and the profibrotic chemotherapy drug bleomycin. Both of these agents induce pulmonary fibrosis in humans with similar pathophysiology.

Studies of lung fibrosis have demonstrated the presence of extensive and apparently progressive epithelial cell apoptosis, especially in regions adjacent to fibrotic foci[7–10]. Endothelial cell apoptosis has been less studied but has also been identified as a prominent event in fibrotic human lung tissue[9]. In rodent models of experimental lung fibrosis, extensive apoptosis occurs, similarly to that observed in human lung fibrosis patients[11, 12]. Rodent models have also demonstrated lung microvascular and pulmonary artery endothelial cell injury and apoptosis[11, 13, 14].

Pro-apoptotic factors are upregulated in fibrotic lung tissue.

* To whom correspondence should be addressed.
E-mail rday@usuhs.mil
Received 2010-03-30 Accepted 2010-06-23

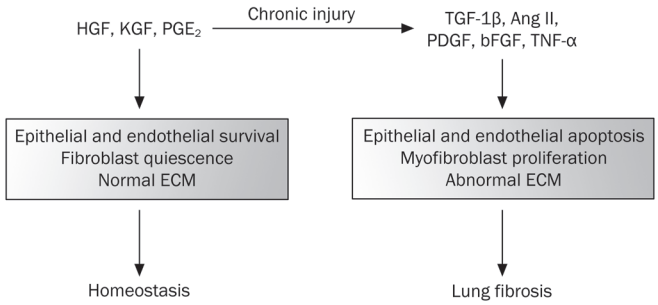

Figure 1. Schematic diagram depicting the development of lung fibrosis following irreparable damage to lung cells. A number of pro-survival factors including HGF, KGF and Cox-2 normally promote survival of epithelial and endothelial cells, fibroblasts quiescence and normal regulation of extracellular matrix (ECM) which altogether results in homeostasis in the lung. Injuries such as bleomycin, radiation, and pro-fibrotic factors may cause epithelial and endothelial apoptosis as well as fibroblast activation and myofibroblast proliferation – events observed in the development of lung fibrosis.

Lung fibrosis patient samples have increased levels of transforming growth factor β1 (TGF-β1) and angiotensin II (Ang II)[15–17] that induce apoptosis and/or growth arrest in epithelial and endothelial cells[18]. Tumor necrosis factor-α (TNF-α), a ligand for the death receptors, as well as death receptors themselves, are increased in the lung tissue of patients with IPF[19–21]. Data indicate many of the same factors identified in human lung fibrosis are also increased in animal models of the disease[22–29]. The imbalance of homeostatic factors created by increased production of pro-apoptotic factors is further exacerbated by a decrease in the production of factors that sustain epithelial and endothelial cell survival, including hepatocyte growth factor (HGF) and keratinocyte growth factor (KGF)[30–34]. The inhibition of cellular apoptosis by a caspase inhibitor or by blocking Ang II signaling significantly mitigated fibrotic remodeling in mice treated with bleomycin[35, 36]. Specific inhibition of endothelial cell death was also demonstrated to prevent TGF-β1-induced fibrosis in a rat model of lung fibrosis[14].

Activated fibroblasts, or myofibroblasts, a central topic in pulmonary fibrosis research, are thought to be a primary causative cell type in the progression of the disease[37–39]. Lung tissue from IPF patients contain increased levels in specific factors that support fibroblasts and/or mesenchymal cell growth including TGF-β1, basic fibroblast growth factor (bFGF), platelet-derived growth factor (PDGF), TNFα, interleukins-1β and -8, and insulin-like growth factor[15–17, 21, 25, 40–44]. At the same time, IPF lung tissue has reduced levels of factors that suppress fibroblast growth, such as cyclooxygenase-2 (COX-2) and its downstream product prostaglandin E_2 (PGE_2)[45, 46]. Myofibroblasts, either from patient sample, or from animal models of pulmonary fibrosis, have pathophysiological characteristics consistent with their key role in affecting alterations associated with fibrotic remodeling[47]. 1) They exhibit rapid proliferation and secrete autocrine factors including bFGF, PDGF, and TGF-β1[48, 49]. 2) They display significant resistance to apoptosis, including that mediated by Fas[50–52]. 3) They are contractile and express α-smooth muscle actin, and these cells are highly motile[38]. And finally, 4) they significantly alter the extracellular milieu of the lung by secreting extracellular matrix proteins, including collagen types I and III, and by producing reactive oxygen species that contribute to the oxidative state of the lung in fibrosis and to the cross-linking of the extracellular matrix[53–56]. Unlike normal fibroblasts that provide a supportive environment to the resident epithelial and endothelial tissues of the lung, myofibroblasts create a toxic environment for other lung cells. Myofibroblasts are a primary source of many pro-apoptotic factors that induce epithelial and endothelial cell death in lung fibrosis. Data from *in vitro* experiments using myofibroblasts cultured from fibrotic tissue indicate that these cells induce growth arrest and apoptosis in primary lung epithelial and endothelial cells[35, 47].

Multiple cellular origins of myofibroblasts have been identified in pulmonary fibrosis. Originally, it was thought that resident lung fibroblasts provided the sole source for this pathological cell type. Myofibroblasts can be derived from fibroblasts through the process of transdifferentiation, believed to be driven by sustained over-expression of TGF-β1 in fibrotic tissue[4, 38, 57]. Myofibroblasts can also derive from alveolar type II pneumocytes through epithelial-mesenchymal transformation (EMT)[58–60]; this process, like transdifferentiation, is also induced by TGF-β1[2]. A third potential source of myofibroblasts are the mesenchymal stem cells from adult bone marrow, which can be recruited to the injured lung[61–63]. Circulating fibrocytes are increased in IPF patients compared to healthy control subjects[64, 65], and studies tracking bone marrow-derived fibroblasts suggest that fibrocytes may migrate to the lung and contribute to remodeling[61, 63, 66]. The inhibition of factors that induce myofibroblast transdifferentiation and EMT processes, such as TGF-β1 and Ang II, significantly attenuates the development of pulmonary fibrosis in animal models[17, 26, 36, 67–69]. Likewise, the inhibition of fibrocyte extravasation to the lungs, for instance by inhibiting CXCL12 signaling, was shown to reduce collagen deposition and fibrosis in mouse models[2, 70].

Hepatocyte growth factor in normal and fibrotic tissue repair

HGF is a paracrine factor produced by cells of mesenchymal origin (*eg*, fibroblasts and macrophages), while the HGF receptor, Met, is expressed by epithelial and endothelial cells[71]. HGF is a heterodimeric protein comprised of a 55–60 kDa α chain and a 32–34 kDa β chain linked by a single disulfide bond[71]. The Met receptor is a tyrosine kinase receptor with a single transmembrane spanning region and a conserved tyrosine kinase domain. Met is translated as a single polypeptide chain which is proteolytically cleaved to form a ~145 kDa β heavy chain and a ~35 kDa α light chain linked by a single disulfide bond[71]. The exclusion of Met expression from fibroblasts provides specificity for HGF-induced survival and proliferative activities on epithelial and endothelial cell

types. Met contains a number of critical tyrosine residues that are phosphorylated in response to HGF binding (Figure 2)[72]. A juxtamembrane tyrosine (Y1001) is involved in down-regulation of Met following activation[72]. Two tyrosines in the kinase domain (Y1234 and Y1235) are required for kinase activity of the receptor[73]. Two other critical tyrosines (Y1349 and Y1356) are found in the carboxy terminal domain of Met, in the "multifunctional docking region"[74]. These latter phosphorylation sites are required for the association with multiple adaptor proteins and signaling molecules[75].

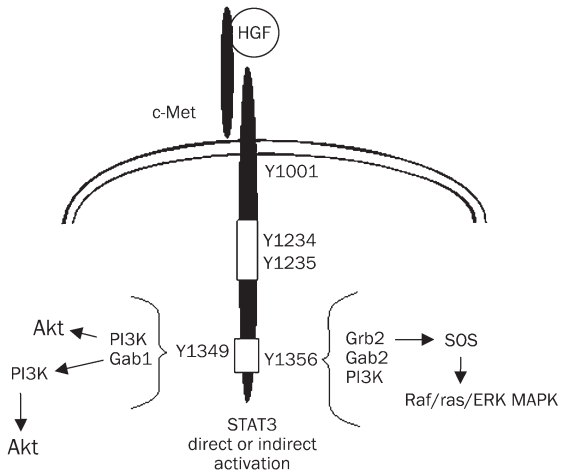

Figure 2. HGF/c-Met signal transduction. Two tyrosine phosphorylation sites (Y1349/Y1356) in the multi-functional docking domain interact with multiple adaptor proteins and signal transduction enzymes. STAT3 has been shown to bind directly to c-Met in some cell types, but the site has not been defined.

Signal transduction by HGF leads to a variety of biological responses including migration, proliferation and morphogenesis, especially branching tubulogenesis in specific cell types[71]. HGF is required for normal embryogenesis and development[76, 77], including for the lung[78]. However, in the adult a primary function of HGF is tissue repair[79]. HGF promotes normal tissue regeneration and prevents fibrotic remodeling in the lung, heart, kidney, and liver[80–84]. HGF is expressed locally in response to injury in a number of tissues, including the lung, kidney, and liver[82, 83, 85–88]. HGF is also produced in the lung in response to distal injuries, suggesting an endocrine function for tissue repair[89].

The role of HGF in lung tissue repair has been well established[82, 90]. Studies indicate that HGF is elevated in the lung following injury. HGF mRNA levels are elevated in damaged lung tissue[82, 91], and HGF protein levels are increased in bronchoalveolar fluid extracted from injured lungs[92]. The time course of HGF induction following lung injury correlates with proliferation of the alveolar epithelial cells[82, 93] and lung vascular endothelial cells[94]. Administration of HGF neutralizing antibodies resulted in reduced DNA synthesis in alveolar epithelial cells after ischemia-reperfusion lung injury in rats[95].

Although HGF is increased in response to tissue injury, an inverse correlation has been identified for HGF expression during the development and/or progression of fibrosis in several tissues including the lung[31, 96, 97]. Lung tissue from patients with pulmonary fibrosis has reduced expression of factors that sustain epithelial and endothelial cell growth and survival, including HGF[31]. Lung fibroblasts isolated from IPF patients have decreased HGF expression and activation relative to fibroblasts from control patients[30]. In cell culture and animal models, suppression of HGF synthesis occurs in response to treatment with the pro-fibrotic factors TGF-β and Ang II[98–101].

Studies in animal models have provided strong evidence that HGF-induced lung repair prevents the induction of fibrotic remodeling. *In vivo* studies have shown that HGF potently mitigates the effects of acute and chronic lung injuries caused by oxidative stress and inflammation. Administration of HGF protein or adenoviral expression of HGF prevents fibrotic remodeling in several animal models of lung fibrosis[91, 102–104]. Transient *in vivo* expression of HGF, using non-viral plasmids, also prevents fibrotic lung remodeling. Using albumin-derived particles to transfect lung endothelial cells, *in vivo* transient transfection of HGF increased repair and prevented collagen deposition and remodeling in mice[105, 106]. Because HGF is secreted, it was reasoned that "nondiseased-organ-targeting gene transfer" could also be used to produce HGF protein, which would then reach the lung through the circulatory system[107]. Electrotransfer of an HGF-encoding plasmid into muscle tissue was also demonstrated to suppress bleomycin-induced fibrotic remodeling in mice[107]. Importantly, studies show that HGF has protective activity when given either simultaneously with or 7 d after administration of a pro-fibrotic treatment, suggesting that HGF is effective during both the initiation phase and the progressive phase of the disease[102].

Because human patients are usually diagnosed only during the progressive phase of pulmonary fibrosis, the identification of factors effective during this phase of the disease is critical for development of treatments and cures.

HGF signaling to induce epithelial and endothelial survival and growth

Regeneration of normal epithelium and endothelium is critical to healthy repair following tissue injury. Thus, normal tissue repair requires factors, such as HGF, that specifically support growth in epithelial and endothelial cells, but not in myofibroblasts, may be required for antifibrotic tissue repair[93, 108]. HGF is mitogenic, motogenic, and induces survival in pulmonary endothelial and alveolar type II epithelial cells[71, 109–114]. HGF also releases lung epithelial and capillary endothelial cells from growth arrest induced by the profibrotic factor TGF-β1[115].

HGF blocks apoptosis in lung epithelial and endothelial cells. The cell survival activities by HGF have been attributed to the activation of a number of anti-apoptotic signaling pathways[112, 116–119] although the specific anti-apoptotic mecha-

nisms of HGF appear to differ among cell types[118, 120]. Three predominant pathways implicated in survival by HGF are ERK/MAPK, PI3K/Akt, and signal transducer and activator of transcription 3 (STAT3) (Figure 2)[121]. Although much of the research on HGF signaling for proliferation and survival has been performed on cancer cell types, some studies have investigated the mechanisms for HGF-induced survival and proliferation in primary lung cells.

In murine lung endothelial cells subjected to hypoxic stress followed by reoxygenation, a procedure that activates the extrinsic apoptotic pathway through the death inducing signaling complex (DISC) and caspase-8. HGF confers protection against extrinsic apoptosis through PI3K/Akt-dependent up-regulation of the caspase-8 inhibitor FLICE-like inhibiting protein (FLIP) and through down-regulation of DISC formation[122]. This report additionally showed that HGF inhibited Bax translocation into the mitochondria, also in an Akt-dependent manner[122]. An investigation of the effects of HGF on H_2O_2- and TNF-α-induced apoptosis in pulmonary epithelial cells demonstrated that survival of epithelial cells by HGF involved the activation of nuclear factor-kappa B (NF-κB) [118]. The mechanism by which HGF activates NF-κB in these cells is unknown.

Both cell culture and *in vivo* studies provide evidence that HGF regulates gene expression of the anti-apoptotic members of the Bcl-2 protein family. Studies of hypoxia-reoxygenation injury to endothelial cells demonstrate that HGF exerts Akt-dependent anti-apoptotic activity by enhancement of the expression of anti-apoptotic protein Bcl-x_L[118, 122]. Investigation of HGF treatment prevented cellular apoptosis and increased Bcl-x_L expression in mice following ischaemic reperfusion injury to the lung[123].

HGF may also block fibrotic remodeling through indirect mechanisms, including the regulation of pro-fibrotic factors. As stated above, Ang II is a potent inducer of epithelial and endothelial cell apoptosis in lung fibrosis, and studies suggest that *de novo* generation of Ang II is required for FAS- and TNF-α induced apoptosis of alveolar epithelial cells in cell culture[124, 125]. The enzyme angiotensin converting enzyme (ACE) is required for the proteolytic activation of Ang II from its inactive precursor angiotensin I (Ang I), and bleomycin-induced fibrosis can be blocked *in vivo* using an ACE inhibitor or an Ang II receptor antagonist[35]. Our laboratory demonstrated that HGF reduces ACE expression in lung endothelial cell culture[126]. The down-regulation of ACE might provide a potential indirect mechanism for HGF reduction of lung cell apoptosis through Ang II suppression.

HGF inhibition of myofibroblast accumulation

Rodent models for lung fibrosis indicate that HGF treatment restricts myofibroblast recruitment. Three potential mechanisms for this effect of HGF are: 1) the induction of quiescence in lung fibroblasts and inhibition of transdifferentiation; 2) the inhibition of EMT of lung epithelial cells; and 3) induction of apoptosis in myofibroblasts. Direct inhibition of fibroblast transdifferentiation by HGF has not been demonstrated, but regulation of myofibroblast development may occur through indirect mechanism(s).

HGF reduces fibroblast activation to the myofibroblast phenotype. HGF may affect fibroblast activation indirectly through the regulation of lung endothelial cell expression of cyclooxygenase 2 (COX-2), a potent activator of prostaglandin E_2 (PGE_2) synthesis[127, 128]. PGE_2 is secreted by pulmonary endothelial cells, induces fibroblast quiescence and is a potent inhibitor TGF-β1-induced fibroblast transdifferentiation[57, 129]. Our laboratory has shown that HGF regulates COX-2 expression in primary lung epithelial cells through Akt- and beta catenin-dependent up-regulation of COX-2 mRNA[127]. This suggests a possible mechanism for HGF-mediated COX-2 inhibition of fibroblast transdifferentiation.

EMT is an important process during development and organogenesis, and HGF has been demonstrated to induce EMT under specific cellular conditions[130, 131]. However, EMT associated with fibrotic remodeling is negatively modulated by HGF[96]. Rat alveolar epithelial cells that were treated with TGF-β to induce EMT, HGF inhibits the expression of myofibroblast markers such as α-SMA, collagen type I, and fibronectin[132]. The inhibitory activity of HGF on EMT requires upregulation of Smad7 expression and its export from the nucleus to the cytoplasm. The export of Smad-7 to cytoplasmic compartment results in the inhibition of signal transduction by the TGF-β receptor[132]. HGF may also indirectly affect EMT processes. Endothelial nitric oxide attenuates EMT[133]. Increased nitric oxide results in the retention of epithelial morphology while inhibition of NOS leads to increased α-SMA expression and fibroblast-like morphology in TGF-β1-treated alveolar epithelial cells[133]. HGF stimulates activity of endothelial nitric oxide synthase (eNOS) via a PI3K/Akt-dependent pathway in endothelial cells[134, 135].

Finally, it has been shown recently that HGF affects the viability of myofibroblasts through direct mechanisms. Although normal fibroblasts lack the HGF receptor Met, myofibroblasts taken from the fibrotic lungs of experimental animals have been shown to express Met[136]. In the Met-expressing myofibroblasts, HGF was shown to induce apoptosis in a caspase-dependent manner[136]. This apoptotic activity of HGF is associated with increased degradation of the extracellular matrix. Treatment of myofibroblasts with HGF increases in the activities of predominant enzymes involved in fibronectin degradation and a decrease in a fibronectin central cell binding domain which is involved in FAK phosphorylation; both of these activities lead to decreased survival of myofibroblasts[136].

Conclusion

Findings from animal models of pulmonary fibrosis show that HGF can inhibit both the initiation and progression of lung fibrosis (Figure 3). However, the critical mechanism(s) for HGF protection of the lung from fibrotic remodeling and promotion of normal tissue regeneration remains poorly understood. HGF directly induces epithelial and endothelial proliferation and survival, and may indirectly modulate myofibroblast accumulation in the lung after injury. Despite the

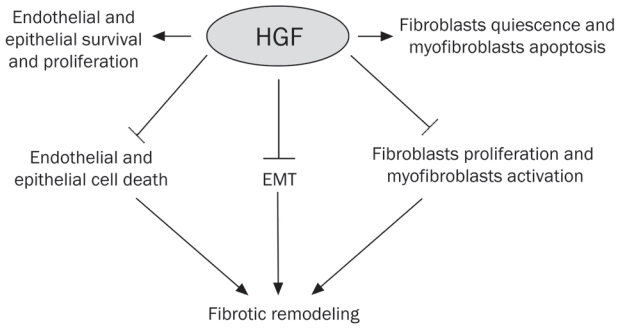

Figure 3. HGF actions for the inhibition of fibrotic remodeling.

potential clinical applications for HGF for wound repair and prevention of fibrotic remodeling, its complex structure has precluded its development for clinical use. The future development and study of HGF mimetics and/or Met agonists may aid in the understanding of HGF mechanisms of tissue repair as well as provide potential therapies for treatment of lung fibrosis.

Acknowledgements

We thank Dr Usamah KAYYALI for critical reading of this article. Some of the authors are employees of the US Government, and this manuscript was prepared as part of their official duties. Title 17 USC §105 provides that 'Copyright protection under this title is not available for any work of the United States Government.' Title 17 USC §101 defined a US Government work as a work prepared by a military service member or employees of the US Government as part of that person's official duties. The views in this article are those of the authors and do not necessarily reflect the views, official policy, or position of the Uniformed Services University of the Health Sciences, Department of the Navy, Department of Defense, or the US Federal Government.

References

1 Streiter R, Keane M, Stadiford T, Kunkel SL. Cytokine biology and the pathogenesis of interstitial lung disease. London: BC Decker, Inc; 1998.
2 Strieter RM, Mehrad B. New mechanisms of pulmonary fibrosis. Chest 2009; 136: 1364–70.
3 Walter N, Collard HR, King TE Jr. Current perspectives on the treatment of idiopathic pulmonary fibrosis. Proc Am Thorac Soc 2006; 3: 330–8.
4 Selman M, Thannickal VJ, Pardo A, Zisman DA, Martinez FJ, Lynch JP 3rd. Idiopathic pulmonary fibrosis: pathogenesis and therapeutic approaches. Drugs 2004; 64: 405–30.
5 Selman M, Pardo A. Idiopathic pulmonary fibrosis: an epithelial/fibroblastic cross-talk disorder. Respir Res 2002; 3: 3.
6 Gross T, Hunninghake G. Idiopathic pulmonary fibrosis. N Engl J Med 1996; 345: 517–25.
7 Uhal BD. Apoptosis in lung fibrosis and repair. Chest 2002; 122: 293S–98S.
8 Penny DP, Rubin P. Specific early fine structural changes in the lung following irradiation. Int J Rad Oncology Biol Phys 1977; 2: 1123–32.
9 Yoshida K, Kuwano K, Hagimoto N, Watanabe K, Matsuba T, Fujita M, *et al*. MAP kinase activation and apoptosis in lung tissues from patients with idiopathic pulmonary fibrosis. J Pathol 2002; 198: 388–96.
10 Uhal BD, Gidea C, Bargout R, Bifero A, Ibarra-Sunga O, Papp M, *et al*. Captopril inhibits apoptosis in human lung epithelial cells: a potential antifibrotic mechanism. Am J Physiol 1998; 275: L1013–7.
11 Ward WF, Molteni A, Solliday NH, Jones GE. The relationship between endothelial dysfunction and collagen accumulation in irradiated rat lung. Int J Radiat Oncol Biol Phys 1985; 11: 1985–90.
12 Li X, Zhang H, Soledad-Conrad V, Zhuang J, Uhal B. Bleomycin-induced apoptosis of alveolar epithelial cells requires angiotensin synthesis *de novo*. Am J Physiol Lung Cell Mol Physiol 2003; 284: L501–7.
13 Zhang H, Lawson WE, Polosukhin VV, Pozzi A, Blackwell TS, Litingtung Y, *et al*. Inhibitor of differentiation 1 promotes endothelial survival in a bleomycin model of lung injury in mice. Am J Pathol 2007; 171: 1113–26.
14 Farkas L, Farkas D, Ask K, Moller A, Gauldie J, Margetts P, *et al*. VEGF ameliorates pulmonary hypertension through inhibition of endothelial apoptosis in experimental lung fibrosis in rats. J Clin Invest 2009; 119: 1298–311.
15 Border WA, Noble NA. Transforming growth factor β in tissue fibrosis. N Engl J Med 1994; 331: 1286–92.
16 Broekelmann T, Limper A, Colby T, McDonald J. Transfomring growth factor β1 is present at sites of extracellular matrix gene expression in human pulmonary fibrosis. Proc Natl Acad Sci USA 1991; 88: 6642–46.
17 Marshall RP, Gohlke P, Chambers RC, Howell DC, Bottoms SE, Unger T, *et al*. Angiotensin II and the fibroproliferative response to acute lung injury. Am J Physiol Lung Cell Mol Physiol 2004; 286: L156–64.
18 Lee YH, Mungunsukh O, Tutino RL, Marquez AP, Day RM. Angiotensin II-induced apoptosis requires SHP-2 regulation of nucleolin and Bcl-x_L in primary lung endothelial cells. J Cell Sci 2010; 123: 1634–43.
19 Ziegenhagen MW, Schrum S, Zissel G, Zipfel PF, Schlaak M, Muller-Quernheim J. Increased expression of proinflammatory chemokines in bronchoalveolar lavage cells of patients with progressing idiopathic pulmonary fibrosis and sarcoidosis. J Investig Med 1998; 46: 223–31.
20 Homolka J, Ziegenhagen MW, Gaede KI, Entzian P, Zissel G, Muller-Quernheim J. Systemic immune cell activation in a subgroup of patients with idiopathic pulmonary fibrosis. Respiration 2003; 70: 262–9.
21 Piguet PF, Ribaux C, Karpuz V, Grau GE, Kapanci Y. Expression and localization of tumor necrosis factor-alpha and its mRNA in idiopathic pulmonary fibrosis. Am J Pathol 1993; 143: 651–5.
22 Kuwano K, Miyazaki H, Hagimoto N, Kawasaki M, Fujita M, Kunitake R, *et al*. The involvement of Fas-Fas ligand pathway in fibrosing lung diseases. Am J Respir Cell Mol Biol 1999; 20: 53–60.
23 Cavarra E, Carraro F, Fineschi S, Naldini A, Bartalesi B, Pucci A, *et al*. Early response to bleomycin is characterized by different cytokine and cytokine receptor profiles in lungs. Am J Physiol Lung Cell Mol Physiol 2004; 287: L1186–92.
24 Coker RK, Laurent GJ, Shahzeidi S, Lympany PA, du Bois RM, Jeffery PK, *et al*. Transforming growth factors-beta 1, -beta 2, and -beta 3 stimulate fibroblast procollagen production *in vitro* but are differentially expressed during bleomycin-induced lung fibrosis. Am J Pathol 1997; 150: 981–91.
25 Liu JY, Sime PJ, Wu T, Warshamana GS, Pociask D, Tsai SY, *et al*. Transforming growth factor-beta(1) overexpression in tumor necrosis factor-alpha receptor knockout mice induces fibroproliferative lung disease. Am J Respir Cell Mol Biol 2001; 25: 3–7.

26 Li X, Zhuang J, Rayford H, Zhang H, Shu R, Uhal BD. Attenuation of bleomycin-induced pulmonary fibrosis by intratracheal administration of antisense oligonucleotides against angiotensinogen mRNA. Curr Pharm Des 2007; 13: 1257–68.
27 Fujita M, Shannon JM, Irvin CG, Fagan KA, Cool C, Augustin A, *et al*. Overexpression of tumor necrosis factor-alpha produces an increase in lung volumes and pulmonary hypertension. Am J Physiol Lung Cell Mol Physiol 2001; 280: L39–49.
28 Fujita M, Shannon JM, Morikawa O, Gauldie J, Hara N, Mason RJ. Overexpression of tumor necrosis factor-alpha diminishes pulmonary fibrosis induced by bleomycin or transforming growth factor-beta. Am J Respir Cell Mol Biol 2003; 29: 669–76.
29 Kuwano K, Hagimoto N, Tanaka T, Kawasaki M, Kunitake R, Miyazaki H, *et al*. Expression of apoptosis-regulatory genes in epithelial cells in pulmonary fibrosis in mice. J Pathol 2000; 190: 221–9.
30 Marchand-Adam S, Fabre A, Mailleux AA, Marchal J, Quesnel C, Kataoka H, *et al*. Defect of pro-hepatocyte growth factor activation by fibroblasts in idiopathic pulmonary fibrosis. Am J Respir Crit Care Med 2006; 174: 58–66.
31 Marchand-Adam S, Marchal J, Cohen M, Soler P, Gerard B, Castier Y, *et al*. Defect of hepatocyte growth factor secretion by fibroblasts in idiopathic pulmonary fibrosis. Am J Respir Crit Care Med 2003; 168: 1156–61.
32 Marchand-Adam S, Plantier L, Bernuau D, Legrand A, Cohen M, Marchal J, *et al*. Keratinocyte growth factor expression by fibroblasts in pulmonary fibrosis: poor response to interleukin-1beta. Am J Respir Cell Mol Biol 2005; 32: 470–7.
33 Zhang F, Nielsen LD, Lucas JJ, Mason RJ. Transforming growth factor-beta antagonizes alveolar type II cell proliferation induced by keratinocyte growth factor. Am J Respir Cell Mol Biol 2004; 31: 679–86.
34 Skibinski G, Elborn JS, Ennis M. Bronchial epithelial cell growth regulation in fibroblast cocultures: the role of hepatocyte growth factor. Am J Physiol Lung Cell Mol Physiol 2007; 293: L69–76.
35 Wang R, Ibarra-Sunga O, Verlinski L, Pick R, Uhal B. Abrogation of bleomycin-induced epithelial apoptosis and lung fibrosis by captopril or by a caspase inhibitor. Am J Physiol Lung Cell Mol Physiol 2000; 279: L143–51.
36 Chen FP, Gong LK, Zhang L, Wang H, Qi XM, Wu XF, *et al*. Early lung injury contributes to lung fibrosis via AT1 receptor in rats. Acta Pharmacol Sin 2007; 28: 227–37.
37 Phan SH. Role of the myofibroblast in pulmonary fibrosis. Kidney Int Suppl 1996; 54: S46–8.
38 Zhang HY, Gharaee-Kermani M, Zhang K, Karmiol S, Phan SH. Lung fibroblast alpha-smooth muscle actin expression and contractile phenotype in bleomycin-induced pulmonary fibrosis. Am J Pathol 1996; 148: 527–37.
39 Kisseleva T, Brenner DA. Fibrogenesis of parenchymal organs. Proc Am Thorac Soc 2008; 5: 338–42.
40 Pan LH, Yamauchi K, Uzuki M, Nakanishi T, Takigawa M, Inoue H, *et al*. Type II alveolar epithelial cells and interstitial fibroblasts express connective tissue growth factor in IPF. Eur Respir J 2001; 17: 1220–7.
41 Pan LH, Ohtani H, Yamauchi K, Nagura H. Co-expression of TNF alpha and IL-1 beta in human acute pulmonary fibrotic diseases: an immunohistochemical analysis. Pathol Int 1996; 46: 91–9.
42 Martinet Y, Menard O, Vaillant P, Vignaud JM, Martinet N. Cytokines in human lung fibrosis. Arch Toxicol Suppl 1996; 18: 127–39.
43 Martinet Y, Rom WN, Grotendorst GR, Martin GR, Crystal RG. Exaggerated spontaneous release of platelet-derived growth factor by alveolar macrophages from patients with idiopathic pulmonary fibrosis. N Engl J Med 1987; 317: 202–9.
44 Zhuo Y, Zhang J, Laboy M, Lasky JA. Modulation of PDGF-C and PDGF-D expression during bleomycin-induced lung fibrosis. Am J Physiol Lung Cell Mol Physiol 2004; 286: L182–8.
45 Petkova DK, Clelland CA, Ronan JE, Lewis S, Knox AJ. Reduced expression of cyclooxygenase (COX) in idiopathic pulmonary fibrosis and sarcoidosis. Histopathology 2003; 43: 381–6.
46 Wilborn J, Crofford LJ, Burdick MD, Kunkel SL, Strieter RM, Peters-Golden M. Cultured lung fibroblasts isolated from patients with idiopathic pulmonary fibrosis have a diminished capacity to synthesize prostaglandin E2 and to express cyclooxygenase-2. J Clin Invest 1995; 95: 1861–8.
47 Phan SH. The myofibroblast in pulmonary fibrosis. Chest 2002; 122: 286S–289S.
48 Ramos C, Montano M, Garcia-Alvarez J, Ruiz V, Uhal BD, Selman M, *et al*. Fibroblasts from idiopathic pulmonary fibrosis and normal lungs differ in growth rate, apoptosis, and tissue inhibitor of metalloproteinases expression. Am J Respir Cell Mol Biol 2001; 24: 591–8.
49 Uhal BD, Kim JK, Li X, Molina-Molina M. Angiotensin-TGF-beta 1 crosstalk in human idiopathic pulmonary fibrosis: autocrine mechanisms in myofibroblasts and macrophages. Curr Pharm Des 2007; 13: 1247–56.
50 Horowitz JC, Lee DY, Waghray M, Keshamouni VG, Thomas PE, Zhang H, *et al*. Activation of the pro-survival phosphatidylinositol 3-kinase/AKT pathway by transforming growth factor-beta1 in mesenchymal cells is mediated by p38 MAPK-dependent induction of an autocrine growth factor. J Biol Chem 2004; 279: 1359–67.
51 Moodley YP, Caterina P, Scaffidi AK, Misso NL, Papadimitriou JM, McAnulty RJ, *et al*. Comparison of the morphological and biochemical changes in normal human lung fibroblasts and fibroblasts derived from lungs of patients with idiopathic pulmonary fibrosis during FasL-induced apoptosis. J Pathol 2004; 202: 486–95.
52 Moodley YP, Misso NL, Scaffidi AK, Fogel-Petrovic M, McAnulty RJ, Laurent GJ, *et al*. Inverse effects of interleukin-6 on apoptosis of fibroblasts from pulmonary fibrosis and normal lungs. Am J Respir Cell Mol Biol 2003; 29: 490–8.
53 Mastruzzo C, Crimi N, Vancheri C. Role of oxidative stress in pulmonary fibrosis. Monaldi Arch Chest Dis 2002; 57: 173–6.
54 Day RM, Suzuki YJ. Cell proliferation, reactive oxygen and cellular glutathione. Dose Response 2005; 3: 425–42.
55 Thannickal VJ, Fanburg BL. Activation of an H_2O_2-generating NADH oxidase in human lung fibroblasts by transforming growth factor beta 1. J Biol Chem 1995; 270 : 30334–8.
56 Larios JM, Budhiraja R, Fanburg BL, Thannickal VJ. Oxidative protein cross-linking reactions involving *L*-tyrosine in transforming growth factor-beta1-stimulated fibroblasts. J Biol Chem 2001; 276: 17437–41.
57 Thannickal VJ, Lee DY, White ES, Cui Z, Larios JM, Chacon R, *et al*. Myofibroblast differentiation by transforming growth factor-beta1 is dependent on cell adhesion and integrin signaling via focal adhesion kinase. J Biol Chem 2003; 278: 12384–9.
58 Kasai H, Allen JT, Mason RM, Kamimura T, Zhang Z. TGF-beta1 induces human alveolar epithelial to mesenchymal cell transition (EMT). Respir Res 2005; 6: 56.
59 Yao HW, Xie QM, Chen JQ, Deng YM, Tang HF. TGF-beta1 induces alveolar epithelial to mesenchymal transition *in vitro*. Life Sci 2004; 76: 29–37.
60 Willis BC, Liebler JM, Luby-Phelps K, Nicholson AG, Crandall ED, du Bois RM, *et al*. Induction of epithelial-mesenchymal transition in alveolar epithelial cells by transforming growth factor-beta1: potential role in idiopathic pulmonary fibrosis. Am J Pathol 2005; 166: 1321–

32.
61 Epperly MW, Guo H, Gretton JE, Greenberger JS. Bone marrow origin of myofibroblasts in irradiation pulmonary fibrosis. Am J Respir Cell Mol Biol 2003; 29: 213–24.
62 Hashimoto N, Jin H, Liu T, Chensue SW, Phan SH. Bone marrow-derived progenitor cells in pulmonary fibrosis. J Clin Invest 2004; 113: 243–52.
63 Trotman W, Beckett T, Goncz KK, Beatty BG, Weiss DJ. Dual Y chromosome painting and *in situ* cell-specific immunofluorescence staining in lung tissue: an improved method of identifying donor marrow cells in lung following bone marrow transplantation. Histochem Cell Biol 2004; 121: 73–9.
64 Andersson-Sjoland A, de Alba CG, Nihlberg K, Becerril C, Ramirez R, Pardo A, *et al*. Fibrocytes are a potential source of lung fibroblasts in idiopathic pulmonary fibrosis. Int J Biochem Cell Biol 2008; 40: 2129–40.
65 Moeller A, Gilpin SE, Ask K, Cox G, Cook D, Gauldie J, *et al*. Circulating fibrocytes are an indicator of poor prognosis in idiopathic pulmonary fibrosis. Am J Respir Crit Care Med 2009; 179: 588–94.
66 Dunsmore SE, Shapiro SD. The bone marrow leaves its scar: new concepts in pulmonary fibrosis. J Clin Invest 2004; 113: 180–2.
67 Azuma A, Li YJ, Abe S, Usuki J, Matsuda K, Henmi S, *et al*. Interferon-{beta} inhibits bleomycin-induced lung fibrosis by decreasing transforming growth factor-{beta} and thrombospondin. Am J Respir Cell Mol Biol 2005; 32: 93–8.
68 Horan GS, Wood S, Ona V, Li DJ, Lukashev ME, Weinreb PH, *et al*. Partial inhibition of integrin alpha(v)beta6 prevents pulmonary fibrosis without exacerbating inflammation. Am J Respir Crit Care Med 2008; 177: 56–65.
69 Daniels CE, Wilkes MC, Edens M, Kottom TJ, Murphy SJ, Limper AH, *et al*. Imatinib mesylate inhibits the profibrogenic activity of TGF-beta and prevents bleomycin-mediated lung fibrosis. J Clin Invest 2004; 114: 1308–16.
70 Phillips R, Burdick M, Hong K, Lutz M, Murray L, Xue Y, *et al*. Circulating fibrocytes traffic to the lungs in response to CXCL12 and mediate fibrosis. J Clin Invest 2004; 114: 438–46.
71 Rubin JS, Bottaro DP, Aaronson SA. Hepatocyte growth factor/scatter factor and its receptor, the c-met proto-oncogene product. Biochim Biophys Acta 1993; 1155: 357–71.
72 Weidner KM, Sachs M, Riethmacher D, Birchmeier W. Mutation of juxtamembrane tyrosine residue 1001 suppresses loss-of-function mutations of the met receptor in epithelial cells. Proc Natl Acad Sci USA 1995; 92: 2597–601.
73 Rodrigues GA, Park M. Autophosphorylation modulates the kinase activity and oncogenic potential of the Met receptor tyrosine kinase. Oncogene 1994; 9: 2019–27.
74 Schaeper U, Gehring NH, Fuchs KP, Sachs M, Kempkes B, Birchmeier W. Coupling of Gab1 to c-Met, Grb2, and SHP-2 mediates biological responses. J Cell Biol 2000; 149: 1419–32.
75 Ponzetto C, Bardelli A, Zhen Z, Maina F, dalla Zonca P, Giordano S, *et al*. A multifunctional docking site mediates signaling and transformation by the hepatocyte growth factor/scatter factor receptor family. Cell 1994; 77: 261–71.
76 Sonnenberg E, Weidner KM, Birchmeier C. Expression of the met-receptor and its ligand, HGF-SF during mouse embryogenesis. EXS 1993; 65: 381–94.
77 Birchmeier C, Gherardi E. Developmental roles of HGF/SF and its receptor, the c-Met tyrosine kinase. Trends Cell Biol 1998; 8: 404–10.
78 Yamamoto H, Yun EJ, Gerber HP, Ferrara N, Whitsett JA, Vu TH. Epithelial-vascular cross talk mediated by VEGF-A and HGF signaling directs primary septae formation during distal lung morphogenesis. Dev Biol 2007; 308: 44–53.
79 Matsumoto K, Nakamura T. Roles of HGF as a pleiotropic factor in organ regeneration. EXS 1993; 65: 225–49.
80 Matsuda Y, Matsumoto K, Yamada A, Ichida T, Asakura H, Komoriya Y, *et al*. Preventive and therapeutic effects in rats of hepatocyte growth factor infusion on liver fibrosis/cirrhosis. Hepatology 1997; 26: 81–9.
81 Schaper W, Kubin T. Is hepatocyte growth factor a protein with cardioprotective activity in the ischemic heart? Circulation 1997; 95: 2471–72.
82 Yanagita K, Matsumoto K, Sekiguchi K, Ishibashi H, Niho Y, Nakamura T. Hepatocyte growth factor may act as a pulmotrophic factor on lung regeneration after acute lung injury. J Biol Chem 1993; 268: 21212–7.
83 Igawa T, Matsumoto K, Kanda S, Saito Y, Nakamura T. Hepatocyte growth factor may function as a renotropic factor for regeneration in rats with acute renal injury. Am J Physiol 1993; 265: F61–9.
84 Panos RJ, Patel R, Bak PM. Intratracheal administration of hepatocyte growth factor/scatter factor stimulates rat alveolar type II cell proliferation *in vivo*. Am J Respir Cell Mol Biol 1996; 15: 574–81.
85 Ono K, Matsumori A, Shioi T, Furukawa Y, Sasayama S. Enhanced expression of hepatocyte growth factor/c-Met by myocardial ischemia and reperfusion in a rat model. Circulation 1997; 95: 2552–58.
86 Yamazaki H, Matsumoto K, Inoue T, Nose T, Murayama S, Teshima T, *et al*. Induction of hepatocyte growth factor in the liver, kidney and lung following total body irradiation in rat. Cytokine 1996; 8: 927–32.
87 Maeda J, Ueki N, Hada T, Higashino K. Elevated serum hepatocyte growth factor/scatter factor levels in inflammatory lung disease. Am J Respir Crit Care Med 1995; 152: 1587–91.
88 Hamanoue M, Kawaida K, Takao S, Shimazu H, Noji S, Matsumoto K, *et al*. Rapid and marked induction of hepatocyte growth factor during liver regeneration after ischemic or crush injury. Hepatology 1992; 16: 1485–92.
89 Yanagita K, Nagaike M, Ishibashi H, Niho Y, Matsumoto K, Nakamura T. Lung may have an endocrine function producing hepatocyte growth factor in response to injury of distal organs. Biochem Biophys Res Commun 1992; 182: 802–9.
90 Adamson Y, Bakowska J. Relationship of keratinocyte growth factor an hepatocyte growth factor levels in rat lung lavage fluid to epithelial cell regneration after bleomycin. Am J Pathol 1999; 155: 949–54.
91 Liu XL, Sato S, Dai W, Yamanaka N. The protective effect of hepatocyte growth-promoting factor (pHGF) against hydrogen peroxide-induced acute lung injury in rats. Med Electron Microsc 2001; 34: 92–102.
92 Stern JB, Fierobe L, Paugam C, Rolland C, Dehoux M, Petiet A, *et al*. Keratinocyte growth factor and hepatocyte growth factor in bronchoalveolar lavage fluid in acute respiratory distress syndrome patients. Crit Care Med 2000; 28: 2326–33.
93 Sakamaki Y, Matsumoto K, Mizuno S, Miyoshi S, Matsuda H, Nakamura T. Hepatocyte growth factor stimulates proliferation of respiratory epithelial cells during postpneumonectomy compensatory lung growth in mice. Am J Respir Cell Mol Biol 2002; 26: 525–33.
94 Ishizawa K, Kubo H, Yamada M, Kobayashi S, Suzuki T, Mizuno S, *et al*. Hepatocyte growth factor induces angiogenesis in injured lungs through mobilizing endothelial progenitor cells. Biochem Biophys Res Commun 2004; 324: 276–80.
95 Yamada T, Hisanaga M, Nakajima Y, Mizuno S, Matsumoto K, Nakamura T, *et al*. Enhanced expression of hepatocyte growth factor by pulmonary ischemia-reperfusion injury in the rat. Am J Respir Crit

Care Med 2000; 162: 707–15.
96 Yang J, Dai C, Liu Y. Hepatocyte growth factor gene therapy and angiotensin II blockade synergistically attenuate renal interstitial fibrosis in mice. J Am Soc Nephrol 2002; 13: 2464–77.
97 Taniyama Y, Morishita R, Nakagami H, Moriguchi A, Sakonjo H, Shokei K, *et al*. Potential contribution of a novel antifibrotic factor, hepatocyte growth factor, to prevention of myocardial fibrosis by angiotensin II blockade in cardiomyopathic hamsters. Circulation 2000; 102: 246–52.
98 Harrison P, Bradley L, Bomford A. Mechanism of regulation of HGF/SF gene expression in fibroblasts by TGF-beta1. Biochem Biophys Res Commun 2000; 271: 203–11.
99 Matsumoto K, Tajima H, Okazaki H, Nakamura T. Negative regulation of hepatocyte growth factor gene expression in human lung fibroblasts and leukemic cells by transforming growth factor-beta 1 and glucocorticoids. J Biol Chem 1992; 267: 24917–20.
100 Matsumoto K, Morishita R, Moriguchi A, Tomita N, Yo Y, Nishii T, *et al*. Prevention of renal damage by angiotensin II blockade, accompanied by increased renal hepatocyte growth factor in experimental hypertensive rats. Hypertension 1999; 34: 279–84.
101 Matsumoto K, Morishita R, Tomita N, Moriguchi A, Komai N, Aoki M, *et al*. Improvement of endothelial dysfunction by angiotensin II blockade accompanied by induction of vascular hepatocyte growth factor system in diabetic spontaneously hypertensive rats. Heart Vessels 2003; 18: 18–25.
102 Yaekashiwa M, Nakayama S, Ohnuma K, Sakai T, Abe T, Satoh K, *et al*. Simultaneous or delayed administration of hepatocyte growth factor equally represses the fibrotic changes in murine lung injury induced by bleomycin. A morphologic study. Am J Respir Crit Care Med 1997; 156: 1937–44.
103 Dohi M, Hasegawa T, Yamamoto K, Marshall BC. Hepatocyte growth factor attenuates collagen accumulation in a murine model of pulmonary fibrosis. Am J Respir Crit Care Med 2000; 162: 2302–7.
104 Ebina M, Shimizukawa M, Narumi K, Miki M, Koinuma D, Watabe M, *et al*. Towards an effective gene therapy for idiopathic pulmonary fibrosis. Chest 2002; 121: 32S–33S.
105 Gazdhar A, Fachinger P, van Leer C, Pierog J, Gugger M, Friis R, *et al*. Gene transfer of hepatocyte growth factor by electroporation reduces bleomycin-induced lung fibrosis. Am J Physiol Lung Cell Mol Physiol 2007; 292: L529–36.
106 Watanabe M, Ebina M, Orson FM, Nakamura A, Kubota K, Koinuma D, *et al*. Hepatocyte growth factor gene transfer to alveolar septa for effective suppression of lung fibrosis. Mol Ther 2005; 12: 58–67.
107 Umeda Y, Marui T, Matsuno Y, Shirahashi K, Iwata H, Takagi H, *et al*. Skeletal muscle targeting *in vivo* electroporation-mediated HGF gene therapy of bleomycin-induced pulmonary fibrosis in mice. Lab Invest 2004; 84: 836–44.
108 Chi CH, Liu IL, Lo WY, Liaw BS, Wang YS, Chi KH. Hepatocyte growth factor gene therapy prevents radiation-induced liver damage. World J Gastroenterol 2005; 11: 1496-502.
109 Nakagami H, Morishita R, Yamamoto K, Taniyama Y, Aoki M, Matsumoto K, *et al*. Mitogenic and antiapoptotic actions of hepatocyte growth factor through ERK, STAT3, and AKT in endothelial cells. Hypertension 2001; 37: 581–6.
110 Day RM, Soon L, Breckenridge D, Bridges B, Patel BK, Wang LM, *et al*. Mitogenic synergy through multilevel convergence of hepatocyte growth factor and interleukin-4 signaling pathways. Oncogene 2002; 21: 2201–11.
111 Day RM, Cioce V, Breckenridge D, Castagnino P, Bottaro DP. Differential signaling by alternative HGF isoforms through c-Met: activation of both MAP kinase and PI 3-kinase pathways is insufficient for mitogenesis. Oncogene 1999; 18: 3399–406.
112 Bardelli A, Longati P, Albero D, Goruppi S, Schneider C, Ponzetto C, *et al*. HGF receptor associates with the anti-apoptotic protein BAG-1 and prevents cell death. EMBO J 1996; 15: 6205–12.
113 Shiratori M, Michalopoulos G, Shinozuka H, Singh G, Ogasawara H, Katyal SL. Hepatocyte growth factor stimulates DNA synthesis in alveolar epithelial type II cells *in vitro*. Am J Respir Cell Mol Biol 1995; 12: 171–80.
114 Singh-Kaw P, Zarnegar R, Siegfried JM. Stimulatory effects of hepatocyte growth factor on normal and neoplastic human bronchial epithelial cells. Am J Physiol 1995; 268: L1012–20.
115 Taipale J, Keski-Oja J. Hepatocyte growth factor releases epithelial and endothelial cells from growth arrest induced by transforming growth factor-β1. J Biol Chem 1996; 271: 4342–48.
116 Fan S, Gao M, Meng Q, Laterra JJ, Symons MH, Coniglio S, *et al*. Role of NF-kappaB signaling in hepatocyte growth factor/scatter factor-mediated cell protection. Oncogene 2005; 24: 1749–66.
117 Fan S, Ma YX, Gao M, Yuan RQ, Meng Q, Goldberg ID, *et al*. The multisubstrate adapter Gab1 regulates hepatocyte growth factor (scatter factor)-c-Met signaling for cell survival and DNA repair. Mol Cell Biol 2001; 21: 4968–84.
118 Okada M, Sugita K, Inukai T, Goi K, Kagami K, Kawasaki K, *et al*. Hepatocyte growth factor protects small airway epithelial cells from apoptosis induced by tumor necrosis factor-alpha or oxidative stress. Pediatr Res 2004; 56: 336–44.
119 Moumen A, Ieraci A, Patane S, Sole C, Comella JX, Dono R, *et al*. Met signals hepatocyte survival by preventing Fas-triggered FLIP degradation in a PI3k-Akt-dependent manner. Hepatology 2007; 45: 1210–7.
120 Liu Y. Hepatocyte growth factor promotes renal epithelial cell survival by dual mechanisms. Am J Physiol 1999; 277: F624–33.
121 Crosby LM, Waters CM. Epithelial repair mechanisms in the lung. Am J Physiol Lung Cell Mol Physiol 2010; 298: L715–31.
122 Wang X, Zhou Y, Kim HP, Song R, Zarnegar R, Ryter SW, *et al*. Hepatocyte growth factor protects against hypoxia/reoxygenation-induced apoptosis in endothelial cells. J Biol Chem 2004; 279: 5237–43.
123 Makiuchi A, Yamaura K, Mizuno S, Matsumoto K, Nakamura T, Amano J, *et al*. Hepatocyte growth factor prevents pulmonary ischemia-reperfusion injury in mice. J Heart Lung Transplant 2007; 26: 935–43.
124 Wang R, Alam G, Zagariya A, Gidea C, Pinillos H, Lalude O, *et al*. Apoptosis of lung epithelial cells in response to TNF-alpha requires angiotensin II generation *de novo*. J Cell Physiol 2000; 185: 253–9.
125 Wang R, Zagariya A, Ang E, Ibarra-Sunga O, Uhal BD. Fas-induced apoptosis of alveolar epithelial cells requires ANG II generation and receptor interaction. Am J Physiol 1999; 277: L1245–50.
126 Day RM, Thiel G, Lum J, Chevere RD, Yang Y, Stevens J, *et al*. Hepatocyte growth factor regulates angiotensin converting enzyme expression. J Biol Chem 2004; 279: 8792–801.
127 Lee YH, Suzuki YJ, Griffin AJ, Day RM. Hepatocyte growth factor regulates cyclooxygenase-2 expression via beta-catenin, Akt, and p42/p44 MAPK in human bronchial epithelial cells. Am J Physiol Lung Cell Mol Physiol 2008; 294: L778–86.
128 Moore AE, Greenhough A, Roberts HR, Hicks DJ, Patsos HA, Williams AC, *et al*. HGF/Met signalling promotes PGE(2) biogenesis via regulation of COX-2 and 15-PGDH expression in colorectal cancer cells. Carcinogenesis 2009; 30: 1796–804.
129 Thomas PE, Peters-Golden M, White ES, Thannickal VJ, Moore BB. PGE(2) inhibition of TGF-beta1-induced myofibroblast differentiation is Smad-independent but involves cell shape and adhesion-depend-

ent signaling. Am J Physiol Lung Cell Mol Physiol 2007; 293: L417–28.

130 Leroy C, Deheuninck J, Reveneau S, Foveau B, Ji Z, Villenet C, *et al*. HGF/SF regulates expression of apoptotic genes in MCF-10A human mammary epithelial cells. Ann N Y Acad Sci 2006; 1090: 188–202.

131 Grotegut S, von Schweinitz D, Christofori G, Lehembre F. Hepatocyte growth factor induces cell scattering through MAPK/Egr-1-mediated upregulation of Snail. EMBO J 2006; 25 : 3534–45.

132 Shukla MN, Rose JL, Ray R, Lathrop KL, Ray A, Ray P. Hepatocyte growth factor inhibits epithelial to myofibroblast transition in lung cells via Smad7. Am J Respir Cell Mol Biol 2009; 40: 643–53.

133 Vyas-Read S, Shaul PW, Yuhanna IS, Willis BC. Nitric oxide attenuates epithelial-mesenchymal transition in alveolar epithelial cells. Am J Physiol Lung Cell Mol Physiol 2007; 293: L212–21.

134 Makondo K, Kamikawa A, Ahmed M, Terao A, Saito M, Kimura K. Geldanamycin enhances hepatocyte growth factor stimulation of eNOS phosphorylation in endothelial cells. Eur J Pharmacol 2008; 582: 110–5.

135 Makondo K, Kimura K, Kitamura N, Kitamura T, Yamaji D, Jung BD, *et al*. Hepatocyte growth factor activates endothelial nitric oxide synthase by Ca(2+)- and phosphoinositide 3-kinase/Akt-dependent phosphorylation in aortic endothelial cells. Biochem J 2003; 374: 63–9.

136 Mizuno S, Matsumoto K, Li MY, Nakamura T. HGF reduces advancing lung fibrosis in mice: a potential role for MMP-dependent myofibroblast apoptosis. FASEB J 2005; 19: 580–2.

Acta Pharmacologica Sinica (2011) 32: 21–30
 1671-4083/11 $32.00
www.nature.com/aps

Review

In vitro models for the evaluation of angiogenic potential in bone engineering

Elisabetta CENNI[1, *], Francesca PERUT[1], Nicola BALDINI[1, 2, 3]

[1]*Laboratorio di Fisiopatologia Ortopedica e Medicina Rigenerativa, Istituto Ortopedico Rizzoli, Bologna, Italy;* [2]*Clinica Ortopedica e Traumatologica I, Istituto Ortopedico Rizzoli, Bologna, Italy;* [3]*Dipartimento di Scienze Anatomiche Umane e Fisiopatologia dell'Apparato Locomotore, Università di Bologna-Alma Mater Studiorum, Bologna, Italy*

Blood vessels have a fundamental role both in skeletal homeostasis and in bone repair. Angiogenesis is also important for a successful bone engineering. Therefore, scaffolds should be tested for their ability to favour endothelial cell adhesion, proliferation and functions. The type of endothelial cell to use for *in vitro* assays should be carefully considered, because the properties of these cells may depend on their source. Morphological and functional relationships between endothelial cells and osteoblasts are evaluated with co-cultures, but this model should still be standardized, particularly for distinguishing the two cell types. Platelet-rich plasma and recombinant growth factors may be useful for stimulating angiogenesis.

Keywords: endothelial cells; bone; angiogenesis; scaffold; osteoblasts; vascular endothelial growth factors

Acta Pharmacologica Sinica (2011) 32: 21–30; doi: 10.1038/aps.2010.143; published online 1 Nov 2010

Role of angiogenesis in bone engineering

In bone, the connection between cells and blood vessels is required to maintain skeletal integrity. In tissue engineering, a vessel network is an essential pre-requisite for scaffolds to survive and integrate with existing host tissue.

Activators and inhibitors of angiogenesis

Vascular development is a co-ordinated process through three major steps, regulating (1) sprouting of endothelial cells (ECs) from mature vessels, (2) assembly of vessels to vascular structures and (3) vessel maturation and subsequent induction of quiescence[1]. Each of these steps is regulated by molecules acting on specific vascular receptors. Sprouting is induced by vascular endothelial growth factor (VEGF)[2], which is produced by monocytes and macrophages migrated to the site of the tissue lesion and stimulated by hypoxia. Vessel cells become sensitive to VEGF after the hypoxia-induced bond of angiopoietin-2 to the endothelial receptor tyrosine kinase Tie-2. VEGF binds to receptors VEGFR-1 (Flt-1) and VEGFR-2 (Flk-1/KDR) on EC membrane. Assembly of vessels to vascular structures is regulated by the ephrin ligands and ephrin receptor tyrosine kinases, which mediate cell-contact-dependent signalling[3]. Angiopoietins[4] and Tie-1 and -2 receptors[5] regulate blood vessel maturation too. Angiogenesis is also modulated by other growth factors (GFs), cytokines, enzymes and integrins, such as fibroblast growth factor 2 (FGF-2)[6], hepatocyte growth factor/scatter factor[7], platelet derived growth factor (PDGF)[8], interluekin-8 (IL-8)[9], IL-3[10], $\alpha_v\beta_3$-integrin[11] and matrix metalloproteinases (MMPs)[12], which degrade extracellular matrix (ECM) facilitating EC migration.

Angiogenesis and bone

In bone, microvessels are essential for bone formation, metabolism, healing and remodelling. Osteoprogenitors are always located near blood vessels. Sinusoids surrounded by reticular cells secrete high amounts of chemokine CXCL12 or stromal cell-derived factor-1 (SDF-1), which is required for the maintenance of human stem cells[13]. Both intramembraneous and endochondral bone ossification occur in close proximity to vascular ingrowth. In intramembranous ossification there is an invasion of capillaries that transport marrow stromal cells (MSCs), which differentiate into osteoblasts and in turn deposit bone matrix. In endochondral ossification the avascular cartilage template is replaced by highly vascularized bone tissue. The immature and proliferating chondrocytes secrete angiogenic inhibitors, while hypertrophic chondrocytes produce angiogenic stimulators, such as VEGF, fibroblast growth factor (FGF)-1 and FGF-2, thus providing a target for capillary invasion and angiogenesis. Hypertrophic chondrocytes and migrating cells from the newly formed bone marrow secrete

* To whom correspondence should be addressed.
E-mail ecenni70@gmail.com
Received 2010-05-26 Accepted 2010-07-23

metalloproteinases (MMPs), which in turn degrade extracellular matrix (ECM), thus permitting vessel invasion. MMP-9 regulates also the release of VEGF-A bound to the hypertrophic cartilage matrix. Once released, VEGF-A binds to its receptors on endothelial cells, osteoclasts and osteoblasts[14]. The new vasculature supplies a conduit for the recruitment of cells involved in cartilage resorption and bone deposition[15]. ECs produce GFs which contribute to recruit stem cells and to address them towards osteoblast differentiation.

Blood vessels play a crucial role in both phases of bone remodelling. In bone resorption, vessels transport osteoclast precursors to the sites of remodelling[16]. In bone deposition, vessels transport osteoprogenitor cells[17]. According to their phenotype, ECs produce molecules modulating bone remodelling, such as RANKL, osteoprotegerin (OPG), IL-6, PDGF, transforming growth factor-β (TGF-β), and others.

Angiogenesis is fundamental for fracture repair. One of the earliest events during bone healing is the reconstruction of intraosseous circulation[18]. Following trauma, disruption of vessels leads to acute hypoxia of the surrounding tissue, as well as to clotting activation. The inflammatory response activates cytokines and GFs that recruit MSCs and ECs to the fracture site. The latter produce PDGF-BB, which contributes to MSC recruitment[19]. Lack of angiogenesis is considered as a pathogenetic cause of non-unions[20].

Angiogenic GFs also play roles in bone formation. VEGF seems to play a key role in endochondral ossification[21], where its functions are mediated by cbfa-1/runx-2[22]. VEGF production is increased by BMP-2, -4, and -6[23], and by TGF-β1[24]. VEGF-A binds to VEGFR-1 on osteoclasts and induce osteoclast recruitment and bone-resorption[25]. FGF-2 stimulates the proliferation and differentiation of osteoblasts[26] and accelerates fracture repair when added to the early healing stage[27].

Relationships between endothelial cells and osteoblasts

ECs and osteoblasts (OBs) communicate through three mechanisms[28]:

1. Direct interaction between membrane molecules of the two adjacent cells (tight junctions);

2. Gap junction communications that form direct cytoplasmic connections between adjacent cells;

3. Secretion of diffusible factors that diffuse freely in the extracellular environment and interact with the target cells through specific receptors.

Gap junction communications are mediated by Cx43 on OBs and ECs, and by Cx40 on ECs[29, 30].

Some diffusible factors secreted by ECs favour bone deposition, such as PDGF-AB, TGF-β1, TGF–β2, FGF-2, epidermal growth factor (EGF), OPG, and bone morphogenetic protein 2 (BMP-2)[31]. When ECs are incubated with a proinflammatory stimulus, such as TNF, IL-1β, or endotoxin, they synthesize both substances inducing bone healing, such as endothelin-1[32], and molecules favouring bone resorption, such as IL-6 and RANK-L[33]. Moreover, ECs may stimulate osteoblasts to express ALP[34].

In turn, MSCs produce angiogenic GFs, such as VEGF, particularly under hypoxic conditions, FGF-2, insulin-like growth factors (IGF), PDGF, and TGF-β. VEGF-stimulated ECs release prostaglandins that strongly promote VEGF release by osteoblasts[35]. ECs co-cultured with OBs show an increased production of collagen type I[36].

The interaction between ECs and OBs is variable with time, as it was shown in co-cultures onto a scaffold made of starch and polycaprolactone. At early time points ECs formed monolayer patches above OBs. At 21 days, ECs had organized into microcapillary-like structures, which were established among OBs. The concentration profile of VEGF during 35 days *in vitro* was characterized by 3 distinct phases: (1) from day 7 to 14 a steep increase in VEGF concentration; (2) between day 14 and day 28 a plateau phase and (3) from day 28 until day 35 a pronounced decrease of VEGF concentration. In hOB monoculture, the VEGF concentration curve exhibited a steady increase at lower magnitude as compared to co-culture until day 28 followed by a decrease[37].

The sonic hedgehog (Shh) pathway is involved both in bone repair and in neoangiogenesis. Hedgehog morphogens play a pivotal role in embryonic development[38]. There is increasing evidence that the Shh pathway plays a significant role in adults both in angiogenesis[39, 40] and in endochondral bone formation[41].

Endothelial cells

ECs are classified into macrovascular and microvascular, according to the vessel type.

Human umbilical vein endothelial cells and other macrovascular endothelial cells

HUVEC are the most known among macrovascular ECs. Other macrovascular ECs were isolated from human saphena or from human, bovine or swine aorta or pulmonary artery. However, the latter EC types have been scarcely used for the evaluation of scaffolds for bone engineering. Moreover, non-human ECs show a different behaviour than human cells[42].

Microvascular endothelial cells

There is evidence that ECs from different organs exhibit different responses to stimulants - particularly, macrovascular ECs have different properties from microvascular ECs.

Microvascular endothelial cells (HMVEC) were isolated from adipose tissue (ADEC)[43], derma (HDMEC)[44] or lung microvessels (HPMEC)[45]. The advantages of ADEC or HDMEC consist in more similar properties to bone microvessels than HUVEC. Moreover, in light of a possibile clinical application, they may be easily isolated from the same patient who will receive the scaffold.

Endothelial progenitor cells

EPCs are adult progenitor cells that can differentiate into mature ECs[46] and therefore play a physiological role in vessel homeostasis[47]. EPCs may be identified through the expression of three cell markers (CD133, CD34, and VEGFR-2)[48]. EPCs are mainly located in bone marrow and can be mobilized

into peripheral blood[49], where they are present from 0.01% to 0.0001% of mononuclear cells (MNCs) in healthy subjects[50]. In culture, two distinct types of EPCs develop. The first type, named early EPCs[51], appears after 3–5 days, is formed by spindle-shaped cells and dies after 4 weeks. The second type, named late EPCs[52] or outgrowth endothelial cells (OECs) [51], appears after 2–3 weeks, forms a cobblestone monolayer and lives for about 12 weeks. Early EPCs, which derive from $CD14^+$ MNCs, are myeloid cells with some endothelial properties, which stimulate neovascularization by paracrine factors but are not incorporated in the endothelial lining. OECs derive from $CD14^-$ MNCs, have similar properties to mature ECs but a higher proliferative ability[53], and are incorporated into the endothelial lining of new blood vessels[54].

One of the most therapeutically interesting features of EPCs is their apparently enhanced ability to be incorporated into newly forming microvasculature. Although their concentration in blood is low, they have been detected in newly formed vasculature, contributing about 5%–35% of the endothelial cells in new capillaries[55]. In fact, EPCs are mobilized by tissue ischemia and cytokines from the bone marrow into peripheral blood, migrate to regions of neovascularization, differentiate into mature endothelial cells and promote vasculogenesis[56]. The most known application of EPCs is the promotion of the therapeutic neovascularization in myocardial infarction[57] and liver disorders[58]. Moreover, it was shown that EPCs develop a favorable environment for fracture healing via angiogenesis and osteogenesis, through two mechanisms. One is the osteogenic and endothelial differentiation potential of CD34+ cells, and the other one is the paracrine effect of CD34+ cells, which secrete VEGF[59]. For this reason, EPCs were investigated to specifically address the problem of delayed and atrophic nonunions[60].

Endothelial cell continuous cell lines

Typically, EC cultures are primary cultures and the proliferative potiential gradually decreases during passages. Therefore continuous cell lines were generated from angiosarcomas, or through cell immortalization with viral transfection or with fusion with neoplastic lines. Examples of tumour-derived endothelial cell lines are ISO-HAS from human haemangiosarcoma[61] and HAEND derived from hepatic angiosarcoma[62]. Transfection may be obtained with SV40 virus or with the introduction of human telomerase reverse transcriptase (hTERT)[63]. Examples of lines obtained with transfection are EVLC2, derived from HUVEC[64], HMEC-1, developed by transfection of HDMEC with SV-40 large T-antigen[65], and HPMEC-ST1.6R, developed by transfection of HPMEC with plasmids encoding the SV-40 large T-antigen and human telomerase[66].

A line obtained from the fusion of ECs with neoplastic cells is EA.hy926, which was developed from the fusion of HUVEC with human pulmonary adenocarcinoma A549[67].

The changes resulting in the capacity of cells to replicate indefinitely may be accompanied by changes in the expression of specific endothelial properties, such as the induction of inter-cellular adhesion molecule 1 (ICAM-1), vascular cell adhesion molecule 1 (VCAM-1) or E-selectin with an inflammatory stimulus[68]. Among EA.hy926, EVLC2, HAEND, HMEC-1, ISOHAS-1, only HPMEC-ST1.6R exhibited the major constitutive and inducible endothelial cell characteristics and showed an angiogenic response on Matrigel[69].

A continuous EC line was isolated from the microvessels of bovine foetal sternus[70]. The endothelial phenotype was shown by the presence of von Willebrand factor and by the ability to form tubular-like structures on Matrigel. These cells display own distinctive characteristics, particularly they possess the receptor for estrogens and are able to respond to estrogens and parathyroid hormone (PTH)[71–73].

Evaluation of the angiogenic potential of the scaffold

Upon graft implantation, inflammation, which represents the first phase of tissue repair, favours a vascular response, but angiogenesis is generally limited to less than 1 mm from the interface implant-host tissue[74]. Moreover, the capillary network induced by the inflammatory process is transient and regress within a few weeks[75]. Neoformed vessels of the implant must anastomose to the systemic circulation[76]. In the absence of a vascular supply, the transport of nutrients occurs mainly by diffusion, which is only efficient for distances from 100 to 200 micron or for tissues with a low metabolic activity, such as cartilage[77]. The insufficient vascularization compromises the supply of oxygen and nutrients to the new-formed tissue and does not remove the waste products of cells[78]. The local accumulation of toxic substances may trigger an inflammatory reaction[79].

Therefore the scaffold must not only support the growth of the cells that will replace the specific tissue *in vivo*, but it must also support EC adhesion and proliferation, and develop an effectively functioning vasculature to supply the cells with oxygen and nutrients. The success of this strategy requires a series of consecutive events: a) EC migration to the outer surface of the scaffold, b) EC migration from the outer surface to the inner pores of the scaffold, c) EC adhesion to the foreign surface and proliferation, d) ECM synthesis, e) tubular structures formation, f) recruitment of further cell types (smooth muscle cells, pericytes, fibroblasts) forming the vessel wall and g) anastomosis with the vessels of the surrounding tissue (Figure 1). Moreover, endothelial cells growing on the scaffold should maintain normal functions and should not exhibit a pro-inflammatory phenotype. In order to obtain stable and durable vascular networks, ECs require the cooperation with perivascular cells. It was shown that a network of stable and functional blood vessels was formed in mice by co-implantation of vascular ECs and mesenchymal precursor cells[80].

In the light of the critical role of angiogenesis, a preliminary step in the evaluation of the scaffold properties should predict its vascularization potential through the assessment of its interaction with ECs.

Endothelial cell seeding

ECs are seeded on the scaffold, which may be pre-condition-

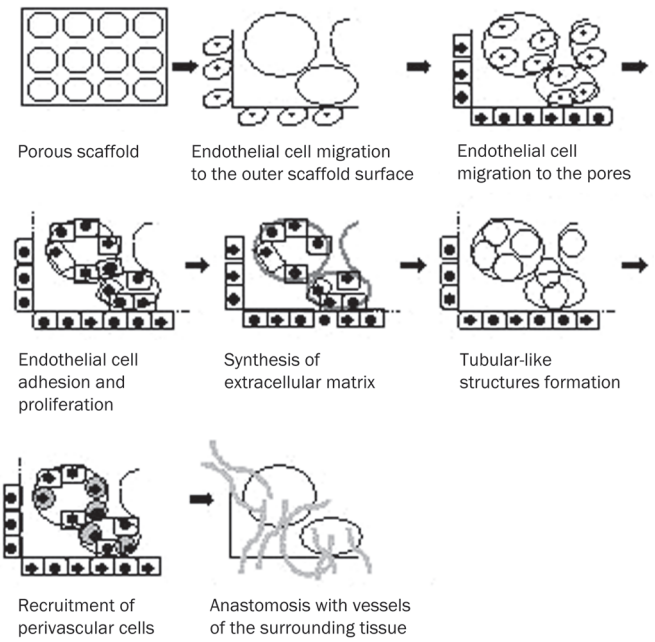

Figure 1. Neoangiogenesis on a porous scaffold.

ated by immersion in culture medium for a few hours. This treatment leads to protein adsorption on the artificial surface, and purposes to reproduce the ECM layer to which the cells usually adhere to live on. Cell seeding is favoured by the following technique: to apply a drop of cell suspension on the scaffold, to incubate at 37 °C for 15–30 min in a wet chamber to allow initial cell attachment, then to add culture medium. The scaffold may be coated with gelatin or fibronectin or collagen or pooled serum to favour cell adhesion.

Endothelial cell morphology

Cell morphology can be evaluated before or after staining. Immunofluorescence for specific antigens, such as von Willebrand factor or CD31, or stain with fluorescent molecules, such as calcein-acetoxymethylester[81] or acridine orange, may be used. Cytoskeleton is shown by F-actin stain (Figure 2A)

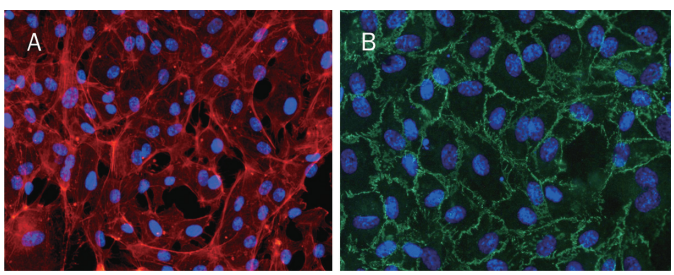

Figure 2. Immunofluorescent staining of endothelial cells for proteins specific for cytoskeleton or for adhesion molecules. (A) F-actin stain of HUVEC. Actin was stained using rhodamine-phalloidin fluorescent dye. Nuclei were stained with Hoechst 33258. Magnification (×20). (B) Immunofluorescent staining for VE-cadherin. Nuclei were stained with Hoechst 33258. Magnification (×20).

or by immunofluorescence for vimentin[82]. VE-cadherin is an adhesion molecule that mediates cell-to-cell contact between endothelial cells and plays a relevant role in the maintenance of vascular integrity[83] (Figure 2B). The maintenance of VE-cadherin expression on a scaffold is a good indicator of the proper interaction between endothelial cells and the material. Fluorescent staining of intracellular organelles may be evaluated by confocal microscopy. With fluorescence microscopy and scanning electron microscopy the relationships between cells and scaffold may be investigated, but no information is obtained on the biomaterial effects on the synthesis of specific molecules.

Adhesion and spreading

The scaffold could affect the synthesis of molecules for homotypic adhesion (CD31, VE-cadherin) or of integrin for the adhesion to substratum[84]. To favour EC and osteoblast adhesion, RGD-peptides were bound to the scaffold. These peptides are formed by the arginine, glutammic acid and aspartic acid sequence, which is common to the integrin $\alpha_v\beta_3$ ligands[85]. Moreover, the scaffold could decrease the expression of adhesion molecules for leukocytes (E-selectin, ICAM and VCAM) in response to inflammatory stimula or, *vice versa*, could induce their expression also on basal conditions[86]. Cell adhesion to the substratum and adhesion molecules are evaluated at fluorescence and confocal microscopy with immunofluorescence staining[87].

A quantitative method to evaluate the expression of adhesion molecules is an enzyme immunoassay performed directly on the cells adherent to the substratum (CAM-EIA)[88]. Flow cytometry is another quantitative assay for adhesion molecules and integrins, but it requires cell detachment, which could affect their expression[89]. Moreover, adhesion molecules and integrins may be indirectly evaluated with RT-PCR for their specific mRNA[90].

Cell proliferation

The proliferation of endothelial cells on artificial scaffolds may be directly determined with vital stains, such as blue alamar[91] or calcein-acetoxymethylester[92], without detaching cells. Alamar changes from blue to pink in proportion to the amount of reactions of oxide-reduction of the cells and therefore in proportion to the cell number. Through a standard curve with known cell numbers, the cell number of the unknown sample grown on the scaffold can be obtained with a good approximation[93]. Calcein-acetoxymethylester becomes fluorescent when taken up by viable cells and the fluorescence is spread throughout the cell. Alternatively the cell number can be evaluated with tritiated thymidine[94], MTT[95], or crystal violet[96] assays.

Tubulogenesis

EC grown on the scaffold can be evaluated for their ability to form tubular-like structures. ECs are seeded on an inducing matrix, with or without GFs. This matrix can be used also to coat the scaffold. After a few hours, tubular-like structure

formation is observed, eventually after vital staining with calcein-acetoxymethylester and nuclear staining with Hoechst 33342[97]. The tube number, length and bifurcations may be quantificated with image analysis, in order to appreciate differences among scaffolds. Matrigel (Becton Dickinson), formed by EMC proteins, is a well-known matrix. Also type I collagen was used, which determined after 20 h the formation of tubular-like structures similar to capillaries[97].

Expression of proteins acting on bone remodelling

For the evaluation of scaffolds for bone engineering, the assay of GFs, cytokines and other proteins produced by endothelium and acting on bone remodelling could be useful. Both specific mRNA expression[98] and the concentration of these substances in the conditioned medium are determined[99]. Proinflammatory markers should be assayed both on basal conditions and after incubation with LPS, because the biomaterial could affect the cell response to the proinflammatory stimulus[100].

Co-cultures

The different co-culture systems take the different interactions among ECs and OBs into account (Figure 3):

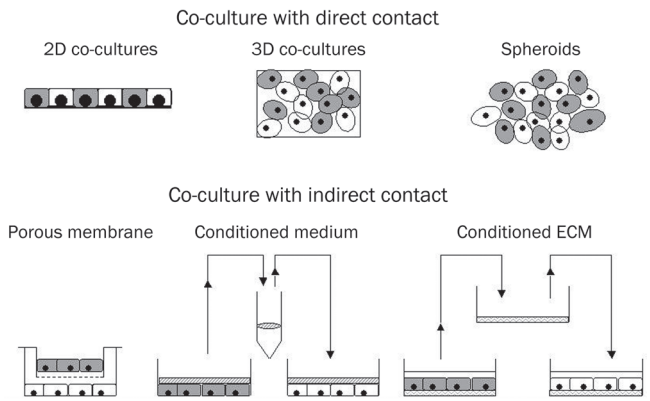

Figure 3. Cell co-culture systems. In the direct contact model, cells are seeded together in 2D supports or 3D scaffolds or as 3-D multicellular spheroids. In the indirect contact model, a porous membrane can be used, with appropriate pore size which let the conditioned medium pass but not cells. Alternatively, the culture of one type of cells is supplemented with the conditioned medium of the other type. In the third method, one cell type is seeded on the ECM of the other type, which has been discharged after grown.

- Co-cultures with direct contact can be initiated on a 2-D surface or on a 3D scaffold or with spheroid systems. With direct contact all the mechanisms of cell-to-cell interaction are evaluated (direct interaction through tight junctions, gap junction communications and secretion of paracrine factors)[28];

- Co-cultures with indirect contact evaluate only communications through paracrine soluble factors. The two cell types may be put in indirect contact through a porous membrane with a such pore size which lets the conditioned medium pass but not cells[101]. Other methods consist in culturing one cell type in the conditioned medium of the other type or in seeding a cell type over the ECM that has been produced by the other cell type.

The indirect contact methods allow to easily quantificate the reciprocal metabolic influences, but do not give any information on the reciprocal spatial relationships.

With the direct contact method the relationships between cells into the living tissue are simulated. 2D studies provide detailed information of the molecular basis of cell-to-cell contacts, and knowledge of cellular events governing the differentiation of OBs that are in contact with ECs. Conversely, 3D co-cultures offer a physiologically optimized environment for cell survival which favors the formation of functional blood vessels. Spheroids formed when a cellular suspension in medium containing 20% methyl cellulose (Methocel, Dow Chemical Co, USA) was seeded in nonadhesive wells with U shape[102]. HUVECs were grown as 3-D multicellular spheroids in a collagen matrix. Direct cell contact between hOBs and HUVECs was established by incorporating hOBs into the EC spheroids, thus forming heterogeneous cospheroids. Co-culture spheroids differentiated spontaneously to organize into a core of OBs and a surface layer of ECs[103].

Direct contact method requires the standardization of a) the choice of culture medium, b) the choice to seed the cell types at the same time or successively, and which type should be seeded as the first; c) the ratio between cell types, d) the separation of the cell types during and at the end of the co-cultures. As culture medium, the medium of ECs, which have higher nutrition requirements, is usually chosen. Both cell types may be seeded at the same time or ECs are seeded before OBs. The optimal ratio between HDMVEC and OBs was shown to be 5:1 or 10:1[92]. The evaluation of the relationships between the cell types is based on differential staining with quantum dots incorporated by cells before seeding and the evaluation at fluorescence or confocal microscopy. Also staining for von Willebrand factor or CD31, specific for ECs, and ALP, specific for OBs, were used. Time-lapse microscopy showed the formation of a tubular-like network through the movement of HUVEC along hOB and their philopodia[104].

With morphological methods the relationships between cells are investigated, but no information on the reciprocal metabolic influences is obtained. The latter is examined with the assay of specific genes and protein of each cell type. ECs produce VEGFR-1, VEGFR-2, CD31, Tie-1, Tie-2, but do not synthesize collagen I, ALP and osteocalcin. ECs co-cultured with hOB stimulated ALP activity and mineralization[105], but down-regulated runx2, osteocalcin and Cx43[106]. The most serious problem is the evaluation of the relative synthesis of proteins because the total protein content of each cell type cannot be distinguished. Also gene expression cannot be normalized because housekeeping genes are common to hECs and hOB, unless human and animal cells are co-cultured. Therefore it is fundamental to separate the two cell types at the end of co-culture. Magnetic immunoseparation with anti-CD31 antibodies showed upregulation of 79 genes and downregula-

tion of 62 genes in OBs and, particularly, the downregulation of the gene of *PDGF receptor* α after co-culture with ECs[101].

Direct co-culture of ECs and OBs prevented the precoating of biomaterials with gelatin or fibronectin. Moreover, ECs formed an extensive network of capillary-like structures with lumina only when they were co-cultured with OBs, but not when they were cultured on biomaterials alone even in the presence of an exogenously supplied angiogenic stimulus. Thus, a prevascularization can take place *in vitro* only in the presence of OBs[92].

Local delivery of angiogenic growth factors

Biomaterial vascularization can be promoted or by seeding mature ECs or their progenitors directly on scaffolds[107], or by locally delivering angiogenic GFs[108], which may induce ECs to migrate, proliferate, and produce molecules acting on bone remodelling. Particularly, it was shown that VEGF-A increased mRNA specific for FGF-2 and decreased mRNA specific for IL-6[19], and increased both mRNA expression and surface protein expression of RANK[109].

Delivery of recombinant growth factors

The ability of biodegradable scaffolds to locally deliver GFs mimicks the conditions of tissue repair *in vivo*. A combination of PDGF-BB and VEGF-165 initiated formation and maturation of a significant number of blood vessels[110]. When calvarial defects of rats were treated with scaffolds in poly(*D*,*L*-lactide-co-glycolide) (PLGA) bound to rhVEGF-A, a significant increase of blood vessel formation, bone coverage, and bone mineral density was observed in comparison with defects treated with simple PLGA[111]. The use of rhVEGF-A in bone defect models showed that new blood vessel formation preceded the osteogenic front and that an increased angiogenesis corresponded to an increased bone formation[112]. However, the local application of VEGF-A to rabbit tibia during distraction osteogenesis increased the blood flow in the distracted limb, but failed to influence bone mineral content and histomorphometric indices of bone regeneration[113]. A possible explanation was that a high level of endogenous VEGF-A had already been secreted during osteogenesis, reaching an optimal local concentration, and therefore the additional delivery of VEGF-A had little or no effect[114].

Platelet-rich plasma (PRP)

A more feasible way to administer angiogenic GFs consists in the application of PRP. In fact, activated platelets release osteogenic and angiogenic GFs from α-granules, such as PDGF, TGF-β, IGF, EGF, and VEGF. Therefore autologous platelets activated with thrombin were used as a source of GFs to stimulate tissue repair. PRP could also favour proliferation and differentiation of the cells seeded on scaffolds, ECs included[115], also when they were co-cultured with hOB[116].

Gene therapy

Ex vivo gene therapy, which consists in the transplantation of genetically modified MSCs secreting angiogenic GFs[117], could overcome the limits of conventional GF delivery. When adipose-derived stem cells (ADSCs) were transfected with adenovirus encoding the cDNA of VEGF, the combination of VEGF releasing cells and ECs resulted in a higher vascular growth within PLGA scaffolds[118].

Discussion

In the last forty years, the new knowledge in cellular and molecular biology and the possibility of the synthesis of innovative materials have determined a shift from the concept of an "inert" material, *ie* non-toxic for cells and tissues of the body, to the concept of a "bioactive" material, which favours cellular adhesion, proliferation and functions. At the same time, it has been understood that angiogenesis was necessary not only for the treatment of obstructive vasculopathies, but also for the repair of most tissues and organs. Consequently, it has been understood that the successful clinical outcome of an implanted cell-construct is dependent on the establishment of a functional vascular network. Therefore, scaffolds should be tested for their angiogenic potential before implantation. Particularly, the ability to favour EC adhesion, proliferation and functions should be assayed with *in vitro* and *in vivo* tests.

The choice of the EC type is crucial, because they may have different properties according to their source. For the evaluation of scaffolds intended for bone engineering, cells with similar characteristics to ECs of bone vasculature should be chosen. Olfactory ensheathing cells (OECs), which can be isolated from the patients without invasive methods, seem to be the most suitable in the formation of functional vessels anastomosed to the host's vascular system[119].

Among the different models of *in vitro* evaluation of the angiogenic potential, the co-cultures between ECs and OBs are the closest to the *in vivo* situation. However, they allow to appreciate the reciprocal relationships between these cell types, but still need to be standardized for the quantitative evaluation of specific gene expression and protein synthesis.

At present, *in vitro* models alone cannot predict if the capillary-like structures pre-formed in the scaffold will establish connections *in vivo* with the host microvascular system. A co-culture of EPCs and MSCs on a scaffold followed by implantation in animal demonstrated improved osteogenesis and angiogenesis when the scaffold had been seeded with the two cell types, without ischemic necrosis at the center of the graft, while impaired osteogenesis and progressive necrosis were observed when the scaffold had been seeded with only OBs[120].

At present, efforts are mainly focused on stabilizing neovasculature and thus promoting the formation of lasting blood vessels. Perivascular cells such as pericytes and smooth muscle cells contribute to the remodelling and maturation of the primitive vascular network and therefore are fundamental agents in the construction of a durable engineered vasculature. In this line of thought, the actual co-culture systems will be upgraded with tri-cultures among OBs, ECs and perivascular cells.

In conclusion, blood vessels, which are necessary to skel-

etal homeostasis and bone repair, have a fundamental role to assure the incorporation of a cells-scaffold construct into the body. Therefore, the ability of the scaffolds to favour EC adhesion and proliferation, without affecting their functions, should be assayed. In *in vitro* tests, the source of ECs should be carefully considered, because it may affect their properties. Morphological and functional relationships between ECs and OBs should be evaluated with appropriate models, such as co-cultures. PRP and recombinant GFs may be useful for stimulating neoangiogenesis.

Acknowledgements

This study was supported by the Istituto Ortopedico Rizzoli, "Ricerca corrente" and by the Emilia-Romagna district (Italy) "Progetto di Ricerca Regione-Università: Regenerative Medicine in Osteo-articular Diseases." The authors thank Ms. Lucy Scioscia for her help in editing English.

Author contribution

Elisabetta CENNI wrote the manuscript; Francesca PERUT contributed to the sections Endothelial progenitor cells, Evaluation of the angiogenic potential of the scaffold, and Local delivery of angiogenic growth factors, and to the photographs at fluorescence microscopy; Nicola BALDINI supervised the paper.

References

1 Polykandriotis, Arkudas A, Horch RE, Stürzl M, Kneser U. Autonomously vascularized cellular constructs in tissue engineering: opening a new perspective for biomedical science. J Cell Mol Med 2007; 11: 6–20.
2 Ferrara N, Gerber HP, LeCouter J. The biology of VEGF and its receptors. Nat Med 2003; 9: 669–76.
3 Heroult M, Schaffner F, Augustin HG. Eph receptor and ephrin ligand-mediated interactions during angiogenesis and tumor progression. Exp Cell Res 2006; 312: 642–50.
4 Thurston G. Role of angiopoietins and Tie receptor tyrosine kinases in angiogenesis and lymphangiogenesis. Cell Tissue Res 2003; 314: 61–8.
5 Peters KG, Kontos CD, Lin PC, Wong AL, Rao P, Huang L, *et al*. Functional significance of Tie2 signaling in the adult vasculature. Recent Prog Horm Res 2004; 59: 51–71.
6 Przybylski M. A review of the current research on the role of bFGF and VEGF in angiogenesis. J Wound Care 2009; 18: 516–9.
7 You WK, McDonald DM. The hepatocyte growth factor/c-Met signaling pathway as a therapeutic target to inhibit angiogenesis. BMB Rep 2008; 41: 833–9.
8 Andrae J, Gallini R, Betsholtz C. Role of platelet-derived growth factors in physiology and medicine. Genes Dev 2008; 22: 1276–312.
9 Waugh DJ, Wilson C. The interleukin-8 pathway in cancer. Clin Cancer Res 2008; 14: 6735–41.
10 Zeoli A, Dentelli P, Rosso A, Togliatto G, Trombetta A, Damiano L, *et al*. Interleukin-3 promotes expansion of hemopoietic-derived $CD45^+$ angiogenic cells and their arterial commitment via STAT5 activation. Blood 2008; 112: 350–61.
11 Robinson SD, Reynolds LE, Kostourou V, Reynolds AR, da Silva RG, Tavora B, *et al*. Alphav beta3 integrin limits the contribution of neuropilin-1 to vascular endothelial growth factor-induced angiogenesis. J Biol Chem 2009; 284: 33966–81.
12 Davis GE, Senger DR. Endothelial extracellular matrix: biosynthesis, remodeling, and functions during vascular morphogenesis and neovessel stabilization. Circ Res 2005; 97: 1093–107.
13 Sugiyama T, Kohara H, Noda M, Nagasawa T. Maintenance of the hematopoietic stem cell pool by CXCL12-CXCR4 chemokine signaling in bone marrow stromal cell niches. Immunity 2006; 25: 977–88.
14 Nakagawa M, Kaneda T, Arakawa T, Morita S, Sato T, Yomada T, *et al*. Vascular endothelial growth factor (VEGF) directly enhances osteoclastic bone resorption and survival of mature osteoclasts. FEBS Lett 2000; 473: 161–4.
15 Harper J, Klagsbrun M. Cartilage to bone-angiogenesis leads the way. Nat Med 1999; 5: 617–8.
16 Kanczler JM, Oreffo RO. Osteogenesis and angiogenesis: the potential for engineering bone. Eur Cell Mater 2008; 15: 100–14.
17 Barou O, Mekraldi S, Vico L, Boivin G, Alexandre C, Lafage-Proust MH. Relationships between trabecular bone remodeling and bone vascularization: a quantitative study. Bone 2002; 30: 604–12.
18 Schindeler A, McDonald MM, Bokko P, Little DG. Bone remodeling during fracture repair: the cellular picture. Semin Cell Dev Biol 2008; 19: 459–66.
19 Cenni E, Ciapetti G, Granchi D, Fotia C, Perut F, Giunti A, *et al*. Endothelial cells incubated with platelet-rich plasma express PDGF-B and ICAM-1 and induce bone marrow stromal cell migration. J Orthop Res 2009; 27: 1493–8.
20 Fang TD, Salim A, Xia W, Nacamuli RP, Guccione S, Song HM, *et al*. Angiogenesis is required for successful bone induction during distraction osteogenesis. J Bone Mineral Res 2005; 20: 1114–24.
21 Gerber HP, Vu TH, Ryan AM, Kowalski J, Werb Z, Ferrara N. VEGF couples hypertrophic cartilage remodeling, ossification and angiogenesis during endochondral bone formation. Nat Med 1999; 5: 623–8.
22 Zelzer E, Glotzer DJ, Hartmann C, Thomas D, Fukai N, Soker S, *et al*. Tissue specific regulation of VEGF expression during bone development requires Cbfa1/Runx2. Mech Dev 2001; 106: 97–106.
23 Deckers MM, Karperien M, van der Bent C, Yamashita T, Papapoulos SE, Lowik CW. Expression of vascular endothelial growth factors and their receptors during osteoblast differentiation. Endocrinology 2000; 141: 1667–74.
24 Chang SC, Chuang HL, Chen YR, Chen JK, Chung HY, Lu YL, *et al*. *Ex vivo* gene therapy in autologous bone marrow stromal stem cells for tissue-engineered maxillofacial bone regeneration. Gene Ther 2003; 10: 2013–9.
25 Niida S, Kondo T, Hiratsuka S, Hayashi S, Amizuka N, Noda T, *et al*. VEGF receptor 1 signaling is essential for osteoclast development and bone marrow formation in colony-stimulating factor 1-deficient mice. Proc Natl Acad Sci USA 2005; 102: 14016–21.
26 Pun S, Dearden RL, Ratkus AM, Liang H, Wronski TJ. Decreased bone anabolic effect of basic fibroblast growth factor at fatty marrow sites in ovariectomized rats. Bone 2001; 28: 220–6.
27 Chen WJ, Jingushi S, Aoyama I, Anzai J, Hirata G, Tamura M, *et al*. Effects of FGF-2 on metaphyseal fracture repair in rabbit tibiae. J Bone Miner Metab 2004; 22: 303–9.
28 Grellier M, Bordenave L, Amédée J. Cell-to-cell communication between osteogenic and endothelial lineages: implications for tissue engineering. Trends Biotechnol 2009; 27: 562–71.
29 Yeh HI, Lee PY, Su CH, Tian TY, Ko YS, Tsai CH. Reduced expression of endothelial connexins 43 and 37 in hypertensive rats is rectified after 7-day carvedilol treatment. Am J Hypertens 2006; 19: 129–35.
30 Villars F, Guillotin B, Amedee T, Dutoya S, Bordenave L, Bareille R, *et al*. Effect of HUVEC on human osteoprogenitor cell differentiation

needs heterotypic gap junction communication. Am J Physiol Cell Physiol 2002; 282: C775–C785.
31 Bouletreau PJ, Warren SM, Spector JA, Peled ZM, Gerrets RP, Greenwald JA, *et al*. Hypoxia and VEGF up-regulate BMP-2 mRNA and protein expression in microvascular endothelial cells: implications for fracture healing. Plast Reconstr Surg 2002; 109: 2384–97.
32 von Schroeder HP, Veillette CJ, Payandeh J, Qureshi A, Heersche JN. Endothelin-1 promotes osteoprogenitor proliferation and differentiation in fetal rat calvarial cell cultures. Bone 2003; 33: 673–84.
33 Collin-Osdoby P, Rothe L, Anderson F, Nelson M, Maloney W, Osdoby P. Receptor activator of NF-kappa B and osteoprotegerin expression by human microvascular endothelial cells, regulation by inflammatory cytokines, and role in human osteoclastogenesis. J Biol Chem 2001; 276: 20659–72.
34 Rouwkema J, De Boer J, van Blitterswijk CA. Endothelial cells assemble into a 3-dimensional prevascular network in a bone tissue engineering construct. Tissue Eng 2006; 12: 2685–93.
35 Clarkin CE, Emery RJ, Pitsillides AA, Wheeler-Jones CP. Evaluation of VEGF mediated signaling in primary human cells reveals a paracrine action for VEGF in osteoblast-mediated crosstalk to endothelial cells. J Cell Physiol 2008; 214: 537–44.
36 Fuchs S, Jiang X, Schmidt H, Dohle E, Ghanaati S, Orth C, *et al*. Dynamic processes involved in the pre-vascularization of silk fibroin constructs for bone regeneration using outgrowth endothelial cells. Biomaterials 2009; 30: 1329–38.
37 Santos MI, Unger RE, Sousa RA, Reis RL, Kirkpatrick CJ. Crosstalk between osteoblasts and endothelial cells co-cultured on a polycaprolactone-starch scaffold and the *in vitro* development of vascularization. Biomaterials 2009; 30: 4407–15.
38 Nagase T, Nagase M, Machida M, Yamagishi M. Hedgehog signaling: a biophysical or biomechanical modulator in embryonic development? Ann N Y Acad Sci 2007; 1101: 412–38.
39 Pola R, Ling LE, Silver M, Corbley MJ, Kearney M, Blake Pepinsky R, *et al*. The morphogen sonic hedgehog is an indirect angiogenic agent upregulating two families of angiogenic growth factors. Nat Med 2001; 7: 706–11.
40 Dohle E, Fuchs S, Kolbe M, Hofmann A, Schmidt H, Kirkpatrick CJ. Sonic hedgehog promotes angiogenesis and osteogenesis in a coculture system consisting of primary osteoblasts and outgrowth endothelial cells. Tissue Eng Part A 2010; 16: 1235–7.
41 van der Horst G, Farih-Sips H, Lowik CW, Karperien M. Hedgehog stimulates only osteoblastic differentiation of undifferentiated KS483 cells. Bone 2003; 33: 899–910.
42 Pasquinelli G, Freyrie A, Preda P, Curti T, D'Addato M, Laschi R. Healing of prosthetic arterial grafts. Scanning Microsc 1990; 4: 351–62.
43 Perego G, Preda P, Pasquinelli G, Curti T, Freyrie A, Cenni E. Functionalization of poly-(*L*-lactic-co-epsilon-caprolactone): effects of surface modification on endothelial cell proliferation and hemocompatibility. J Biomater Sci Polym Ed 2003; 14: 1057–75.
44 Rouwkema J, Westerweel PE, de Boer J, Verhaar MC, van Blitterswijk CA. The use of endothelial progenitor cells for prevascularized bone tissue engineering. Tissue Eng Part A 2009; 15: 2015–27.
45 Krump-Konvalinkova V, Bittinger F, Unger RE, Peters K, Lehr HA, Kirkpatrick CJ. Generation of human pulmonary microvascular endothelial cell lines. Lab Invest 2001; 81: 1717–27.
46 Asahara T, Murohara T, Sullivan A, Silver M, van der Zee R, Li T, *et al*. Isolation of putative progenitor endothelial cells for angiogenesis. Science 1997; 275: 964–7.
47 Sirker AA, Astroulakis ZMJ, Hill MJ. Vascular progenitor cells and translational research: the role of endothelial and smooth muscle progenitor cells in endogenous arterial remodelling in the adult. Clin Sci 2009; 116: 283–99.
48 Peichev M, Naiyer AJ, Pereira D, Zhu Z, Lane WJ, Williams M, *et al*. Expression of VEGFR-2 and AC133 by circulating human CD34(+) cells identifies a population of functional endothelial precursors. Blood 2000; 95: 952–8.
49 Korbling M, Reuben JM, Gao H, Lee BN, Harris DM, Cogdell D, *et al*. Recombinant human granulocyte-colony-stimulating factor-mobilized and apheresis-collected endothelial progenitor cells: a novel blood cell component for therapeutic vasculogenesis. Transfusion 2006; 46: 1795–802.
50 Khan SS, Solomon MA, McCoy JP Jr. Detection of circulating endothelial cells and endothelial progenitor cells by flow cytometry. Cytometry B Clin Cytom 2005; 64: 1–8.
51 Gulati R, Jevremovic D, Peterson TE, Chatterjee S, Shah V, Vile RG, *et al*. Diverse origin and function of cells with endothelial phenotype obtained from adult human blood. Circ Res 2003; 93: 1023–5.
52 Hur J, Yoon CH, Kim HS, Choi JH, Kang HJ, Hwang KK, *et al*. Characterization of two types of endothelial progenitor cells and their different contributions to neovasculogenesis. Arterioscler Thromb Vasc Biol 2004; 24: 288–93.
53 Yoon CH, Hur J, Park KW, Kim JH, Lee CS, Oh IY, *et al*. Synergistic neovascularization by mixed transplantation of early endothelial progenitor cells and late outgrowth endothelial cells: the role of angiogenic cytokines and matrix metalloproteinases. Circulation 2005; 112: 1618–27.
54 Verloop RE, Koolwijk P, Zonneveld AJ, Hinsbergh VW. Proteases and receptors in the recruitment of endothelial progenitor cells in neovascularization. Eur Cytokine Netw 2009; 20: 207–19.
55 Murayama T, Tepper OM, Silver M, Ma H, Losordo DW, Isner JM, *et al*. Determination of bone marrow-derived endothelial progenitor cell significance in angiogenic growth factor-induced neovascularization in vivo. Exp Hematol 2002; 30: 967–72.
56 Takahashi T, Kalka C, Masuda H, Chen D, Silver M, Kearney M, et al. Ischemia- and cytokine-induced mobilization of bone marrow-derived endothelial progenitor cells for neovascularization. Nat Med 1999; 5: 434–8.
57 Kocher AA, Schuster MD, Szabolcs MJ, Takuma S, Burkhoff D, Wang J, *et al*. Neovascularization of ischemic myocardium by human bone-marrow-derived angioblasts prevents cardiomyocyte apoptosis, reduces remodeling and improves cardiac function. Nat Med 2001; 7: 430–6.
58 Lemoli RM, Catani L, Talarico S, Loggi E, Gramenzi A, Baccarani U, *et al*. Mobilization of bone marrow-derived hematopoietic and endothelial stem cells after orthotopic liver transplantation and liver resection. Stem Cells 2006; 24: 2817–25.
59 Matsumoto T, Kawamoto A, Kuroda R, Ishikawa M, Mifune Y, Iwasaki H, *et al*. Therapeutic potential of vasculogenesis and osteogenesis promoted by peripheral blood CD34-positive cells for functional bone healing. Am J Pathol 2006; 169: 1440–57.
60 Matsumoto T, Kuroda R, Mifune Y, Kawamoto A, Shoji T, Miwa M, *et al*. Circulating endothelial/skeletal progenitor cells for bone regeneration and healing. Bone 2008; 43: 434–9.
61 Masuzawa M, Fujimura T, Hamada Y, Fujita Y, Hara H, Nishiyama S, *et al*. Establishment of a human hemangiosarcoma cell line (ISO-HAS). Int J Cancer 1999; 81: 305–8.
62 Hoover ML, Vetvicka V, Hoffpauir JM, Tamburro CH. Human endothelial cell line from an angiosarcoma. *In Vitro* Cell Dev Biol 1993; 29A: 199–202.
63 Shao R, Guo X. Human microvascular endothelial cells immortalized with human telomerase catalytic protein: a model for the study of

in vitro angiogenesis. Biochem Biophys Res Commun 2004; 321: 788–94.
64 van Leeuwen EB, Veenstra R, van Wijk R, Molema G, Hoekstra A, Ruiters MH, *et al*. Characterization of immortalized human umbilical and iliac vein endothelial cell lines after transfection with SV40 large T-antigen. Blood Coagul Fibrinolysis 2000; 11: 15–25.
65 Ades EW, Candal FJ, Swerlick RA, George VG, Summers S, Bosse DC, *et al*. HMEC-1: Establishment of an immortalized human microvascular endothelial cell line. J Invest Dermatol 1992; 99: 683–90.
66 Krump V, Bittinger F, Unger RE, Peters K, Lehr HA, Kirkpatrick CJ. Generation of human pulmonary microvascular endothelial cell lines. Lab Invest 2001; 81: 1717–27.
67 Edgell CJ, Haizlip JE, Bagnell CR, Packenham JP, Harrison P. Wilbourn B, *et al*. Endothelium specific Weibel–Palade bodies in a continuous human cell line, EA.hy926. *In Vitro* Cell Dev Biol 1990; 26: 1167–72.
68 Brown J, Reading SJ, Jones S, Fitchett CJ, Howl J, Martin A, *et al*. Critical evaluation of ECV304 as a human endothelial cell model defined by genetic analysis and functional responses: A comparison with the human bladder cancer derived epithelial cell line T24/83. Lab Invest 2000; 80: 37–45.
69 Unger RE, Krump-Konvalinkova V, Peters K, Kirkpatrick CJ. *In vitro* expression of the endothelial phenotype: comparative study of primary isolated cells and cell lines, including the novel cell line HPMEC-ST1.6R. Microvasc Res 2002; 64: 384–97.
70 Streeten EA, Ornberg R, Curcio F, Sakaguchi K, Marx S, Aurbach GD *et al*. Cloned endothelial cells from fetal bovine bone. Proc Natl Acad Sci USA 1989; 86: 916–20.
71 Streeten EA, Brandi ML. Biology of bone endothelial cells. Bone Miner 1990; 10: 85–94.
72 Brandi ML, Crescioli C, Tanini A, Frediani U, Agnusdei D, Gennari C. Bone endothelial cells as estrogen targets. Calcif Tissue Int 1993; 53: 312–7.
73 Fiorelli G, Orlando C, Benvenuti S, Franceschelli F, Bianchi S, Pioli P, *et al*. Characterization, regulation, and function of specific cell membrane receptors for insulin-like growth factor I on bone endothelial cells. J Bone Miner Res 1994; 9: 329–37.
74 Colton CK. Implantable biohybrid artificial organs. Cell Transplant 1995; 4: 415–36.
75 Sieminski AL, Gooch KJ. Biomaterial-microvasculature interactions. Biomaterials 2000; 21: 2232–41.
76 Scheufler O, Schaefer DJ, Jaquiery C, Braccini A, Wendt DJ, Gasser JA, *et al*. Spatial and temporal patterns of bone formation in ectopically pre-fabricated, autologous cell-based engineered bone flaps in rabbits. J Cell Mol Med 2008; 12: 1238–49.
77 Rouwkema J, Rivron NC, van Blitterswijk CA. Vascularization in tissue engineering. Trends Biotechnol 2008; 26: 434–41.
78 Hutmacher DW. Scaffolds in tissue engineering bone and cartilage. Biomaterials 2000; 21: 2529–43.
79 Taylor MS, Daniels AU, Andriano KP, Heller J. Six bioabsorbable polymers: *in vitro* acute toxicity of accumulated degradation products. J Appl Biomater 1994; 5: 151–7.
80 Koike N, Fukumura D, Gralla O, Au P, Schechner JS, Jain RK. Tissue engineering: creation of long-lasting blood vessels. Nature 2004; 428: 138–9.
81 Thimm BW, Unger RE, Neumann HG, Kirkpatrick CJ. Biocompatibility studies of endothelial cells on a novel calcium phosphate/SiO_2-xerogel composite for bone tissue engineering. Biomed Mater 2008; 3: 015007.
82 Silva Marques JM, Gomes PS, Silva MA, Silvério Cabrita AM, Santos JD, Fernandes MH. Growth and phenotypic expression of human endothelial cells cultured on a glass-reinforced hydroxyapatite. J Mater Sci Mater Med 2009; 20: 725–31.
83 Mochizuki N. Vascular integrity mediated by vascular endothelial cadherin and regulated by sphingosine 1-phosphate and angiopoietin-1. Circ J 2009; 73: 2183–91
84 Amato I, Ciapetti G, Pagani S, Marletta G, Satriano C, Baldini N, *et al*. Expression of cell adhesion receptors in human osteoblasts cultured on biofunctionalized poly-(epsilon-caprolactone) surfaces. Biomaterials 2007; 28: 3668–78.
85 Marletta G, Ciapetti G, Satriano C, Pagani S, Baldini N. The effect of irradiation modification and RGD sequence adsorption on the response of human osteoblasts to polycaprolactone. Biomaterials 2005; 26: 4793–804.
86 Campillo-Fernández AJ, Unger RE, Peters K, Halstenberg S, Santos M, Salmerón Sánchez M, *et al*. Analysis of the biological response of endothelial and fibroblast cells cultured on synthetic scaffolds with various hydrophilic/hydrophobic ratios: influence of fibronectin adsorption and conformation. Tissue Eng Part A 2009; 15: 1331–41.
87 Jabbarzadeh E, Jiang T, Deng M, Nair LS, Khan YM, Laurencin CT. Human endothelial cell growth and phenotypic expression on three dimensional poly(lactide-co-glycolide) sintered microsphere scaffolds for bone tissue engineering. Biotechnol Bioeng 2007; 98: 1094–102.
88 Perut F, Cenni E, Unger RE, Kirkpatrick CJ, Giunti A, Baldini N. Immunogenic properties of renal cell carcinoma and the pathogenesis of osteolytic bone metastases. Int J Oncol 2009; 34: 1387–93.
89 Cenni E, Granchi D, Verri E, Remiddi G, Cavedagna D, Di Leo A. Evaluation of endothelial cell integrins after *in vitro* contact with polyethylene terephthalate. J Mater Sci Mater Med 2001; 12: 345–9.
90 Williamson MR, Woollard KJ, Griffiths HR, Coombes AG. Gravity spun polycaprolactone fibers for applications in vascular tissue engineering: proliferation and function of human vascular endothelial cells. Tissue Eng 2006; 12: 45–51.
91 Deb S, Mandegaran R, Di Silvio L. A porous scaffold for bone tissue engineering/45S5 Bioglass derived porous scaffolds for co-culturing osteoblasts and endothelial cells. J Mater Sci Mater Med 2010; 21: 893–905.
92 Unger RE, Sartoris A, Peters K, Motta A, Migliaresi C, Kunkel M, *et al*. Tissue-like self-assembly in cocultures of endothelial cells and osteoblasts and the formation of microcapillary-like structures on three-dimensional porous biomaterials. Biomaterials 2007; 28: 3965–76.
93 Larson EM, Doughman DJ, Gregerson DS, Obritsch WF. A new, simple, nonradioactive, nontoxic *in vitro* assay to monitor corneal endothelial cell viability. Invest Ophthalmol Vis Sci 1997; 38: 1929–33.
94 Hopper RA, VerHalen JP, Tepper O, Mehrara BJ, Detch R, Chang EI, *et al*. Osteoblasts stimulated with pulsed electromagnetic fields increase HUVEC proliferation via a VEGF-A independent mechanism. Bioelectromagnetics 2009; 30: 189–97.
95 Qian YF, Zhang KH, Chen F, Ke QF, Mo XM. Cross-linking of gelatin and chitosan complex nanofibers for tissue-engineering scaffolds. J Biomater Sci Polym Ed 2010 doi: 10.1163/092050610x499447.
96 Lippert C, Seeger H, Wallwiener D, Mueck AO. Comparison of the effects of 17alpha-ethinylestradiol and 17beta-estradiol on the proliferation of human breast cancer cells and human umbilical vein endothelial cells. Clin Exp Obstet Gynecol 2002; 29: 87–90.

97 Peters K, Schmidt H, Unger RE, Otto M, Kamp G, Kirkpatrick CJ. Software-supported image quantification of angiogenesis in an *in vitro* culture system: application to studies of biocompatibility. Biomaterials 2002; 23: 3413–9.
98 Cenni E, Granchi D, Ciapetti G, Savarino L, Corradini A, Di Leo A. Cytokine expression *in vitro* by cultured human endothelial cells in contact with polyethylene terephthalate coated with pyrolytic carbon and collagen. J Biomed Mater Res 2000; 50: 483–9.
99 Cenni E, Granchi D, Ciapetti G, Cavedagna D, Corradini A, Di Leo A. Interleukin-6 expression by cultured human endothelial cells in contact with carbon coated polyethylene terephthalate. J Mater Sci Mater Med 2001; 12: 365–9.
100 Unger RE, Peters K, Wolf M, Motta A, Migliaresi C, Kirkpatrick CJ. Endothelialization of a non-woven silk fibroin net for use in tissue engineering: growth and gene regulation of human endothelial cells. Biomaterials 2004; 25: 5137–46.
101 Finkenzeller G, Arabatzis A, Geyer M, Wenger A, Bannasch H, Stark GB. Gene expression profiling reveals platelet-derived growth factor receptor alpha as a target of cell contact dependent gene regulation in an endothelial cell-osteoblast co-culture model. Tissue Eng 2006; 12: 2889–903.
102 Korff T, Augustin HG. Integration of endothelial cells in multicellular spheroids prevents apoptosis and induces differentiation. J Cell Biol 1998; 143: 1341–52.
103 Wenger A, Stahl A, Weber H, Finkenzeller G, Augustin HG, Stark GB, *et al*. Modulation of *in vitro* angiogenesis in a three-dimensional spheroidal coculture model for bone tissue engineering. Tissue Eng 2004; 10: 1536–47.
104 Grellier M, Ferreira-Tojais N, Bourget C, Bareille R, Guillemot F, Amédée J. Role of vascular endothelial growth factor in the communication between human osteoprogenitors and endothelial cells. J Cell Biochem 2009; 106: 390–8.
105 Guillotin B, Bourget C, Remy-Zolgadri M, Bareille R, Fernandez P, Conrad V, *et al*. Human primary endothelial cells stimulate human osteoprogenitor cell differentiation. Cell Physiol Biochem 2004; 14: 325–32.
106 Guillotin B, Bareille R, Bourget C, Bordenave L, Amédée J. Interaction between human umbilical vein endothelial cells and human osteoprogenitors triggers pleiotropic effect that may support osteoblastic function. Bone 2008; 42: 1080–91.
107 Rafii S, Lyden D. Therapeutic stem and progenitor cells transplantation for organ vascularization and regeneration. Nat Med 2003; 9: 702–12.
108 Perets A, Baruch Y, Weisbuch F, Shoshany G, Neufeld G, Cohen S. Enhancing the vascularization of three-dimensional porous scaffolds by incorporating controlled release basic fibroblast growth factors microspheres. J Biomed Mater Res 2003; 65: 489–97.
109 Min JK, Kim YM, Kim YM, Kim EC, Gho YS, Kang IJ, *et al*. Vascular endothelial growth factor up-regulates expression of receptor activator of NF-kappa B (RANK) in endothelial cells. Concomitant increase of angiogenic responses to RANK ligand. J Biol Chem 2003; 278: 39548–57.
110 Richardson TP, Peters MC, Ennett AB, Mooney DJ. Polymeric system for dual growth factor delivery. Nat Biotechnol 2001; 19: 1029–34.
111 Orlandini M, Spreafico A, Bardelli M, Rocchigiani M, Salameh A, Nucciotti S, *et al*. Vascular endothelial growth factor-D activates VEGFR-3 expressed in osteoblasts inducing their differentiation. J Biol Chem 2006; 281: 17961–7.
112 Kleinheinz J, Stratmann U, Joos U, Wiesmann HP. VEGF-activated angiogenesis during bone regeneration. J Oral Maxillofac Surg 2005; 63: 1310–6.
113 Eckardt H, Bundgaard KG, Christensen KS, Lind M, Hansen ES, Hvid I. Effects of locally applied vascular endothelial growth factor (VEGF) and VEGF-inhibitor to the rabbit tibia during distraction osteogenesis. J Orthop Res 2003; 21: 335–40.
114 Dai J, Rabie AB. VEGF: an essential mediator of both angiogenesis and endochondral ossification. J Dent Res 2007; 86; 937–50.
115 Kandler B, Fischer MB, Watzek G, Gruber R. Platelet-released supernatant increases matrix metalloproteinase-2 production, migration, proliferation and tube formation of human umbilical vascular endothelial cells. J Periodontol 2004; 75: 1255–61.
116 Hofmann A, Ritz U, Verrier S, Eglin D, Alini M, Fuchs S, *et al*. The effect of human osteoblasts on proliferation and neo-vessel formation of human umbilical vein endothelial cells in a long-term 3D co-culture on polyurethane scaffolds. Biomaterials 2008; 29: 4217–26.
117 Iwaguro H, Yamaguchi J, Kalka C, Murasawa S, Masuda H, Hayashi S, *et al*. Endothelial progenitor cell vascular endothelial growth factor gene transfer for vascular regeneration. Circulation 2002; 105: 732–8.
118 Jabbarzadeh E, Starnes T, Khan YM, Jiang T, Wirtel AJ, Deng M, *et al*. Induction of angiogenesis in tissue-engineered scaffolds designed for bone repair: A combined gene therapy– cell transplantation approach. Proc Natl Acad Sci USA 2008; 105: 11099–104.
119 Au P, Daheron LM, Duda DG, Cohen KS, Tyrrell JA, Lanning RM, *et al*. Differential *in vivo* potential of endothelial progenitor cells from human umbilical cord blood and adult peripheral blood to form functional long-lasting vessels. Blood 2008; 111: 1302–5.
120 Yu H, Vandevord PJ, Gong W, Wu B, Song Z, Matthew HW, *et al*. Promotion of osteogenesis in tissue-engineered bone by pre-seeding endothelial progenitor cells-derived endothelial cells. J Orthop Res 2008; 26: 1147–52.

Acta Pharmacologica Sinica (2011) 32: 31–37
 1671-4083/11 $32.00
www.nature.com/aps

Original Article

Effect of intravenous anesthetic propofol on synaptic vesicle exocytosis at the frog neuromuscular junction

Luciana Ferreira LEITE[1], Renato Santiago GOMEZ[2, *], Matheus de Castro FONSECA[1], Marcus Vinicius GOMEZ[3], Cristina GUATIMOSIM[1, §]

[1]Department of Morphology, Federal University of Minas Gerais, Belo Horizonte, Minas Gerais, Brazil; [2]Department of Surgery, School of Medicine, Federal University of Minas Gerais, Belo Horizonte, Minas Gerais, Brazil; [3]Graduate Program of Santa Casa, Belo Horizonte, Minas Gerais, Brazil

Aim: To investigate the presynaptic effects of propofol, a short-acting intravenous anesthetic, in the frog neuromuscular junction.
Methods: Frog cutaneous pectoris nerve muscle preparations were prepared. A fluorescent tool (FM1-43) was used to visualize the effect of propofol on synaptic vesicle exocytosos in the frog neuromuscular junction.
Results: Low concentrations of propofol, ranging from 10 to 25 μmol/L, enhanced spontaneous vesicle exocytosis monitored by FM1-43 in a Ca^{2+}-dependent and Na^{+}-independent fashion. Higher concentrations of propofol (50, 100, and 200 μmol/L) had no effect on spontaneous exocytosis. By contrast, higher concentrations of propofol inhibited the Na^{+}-dependent exocytosis evoked by 4-aminopyridine but did not affect the Na^{+}-independent exocytosis evoked by KCl. This action was similar and non-additive with that observed by tetrodotoxin, a Na^{+} channel blocker.
Conclusion: Our data suggest that propofol has a dose-dependent presynaptic effect at the neuromuscular transmission which may help to understand some of the clinical effects of this agent on neuromuscular function.

Keywords: propofol; neuromuscular junction; frog; FM1-43; synaptic vesicle; general anesthetic

Acta Pharmacologica Sinica (2011) 32: 31–37; doi: 10.1038/aps.2010.175; published online 29 Nov 2010

Introduction

During the last decade, there was a significant progress related to the knowledge of the mechanism of action of general anesthetic. Cellular and molecular mechanisms underlying general anesthesia are not yet fully elucidated but general anesthetics seems to act in both presynaptic and postsynaptic molecular targets[1–4]. There is now a great body of evidences that clinical concentrations of most general anesthetics act on specific ligand-gated ion channels like GABA and glutamate receptors and/or other important ion channels, such as voltage gated sodium channels, potassium channels and HCN-pacemaker channels[3]. Nevertheless, characterizing the molecular targets of general anesthetics has challenged many research groups over the years.

Propofol is one of the most widely used general anesthetic agent for induction and maintenance of anesthesia. Previous works performed in central nervous system (CNS) synapses have shown an inhibition of calcium channels by propofol[5–7]. Other works showed that propofol inhibited calcium-dependent glutamate release evoked by veratridine and 4-AP with greater potency than Na^{+} channel-independent release evoked by KCl[8, 9]. In addition, there were evidences in the literature suggesting that high doses of propofol might have a direct effect on Na^{+} channels[9–13].

It is well described the sedative and hypnotic effects of propofol on CNS. Nevertheless, there are few studies investigating its effect on neuromuscular transmission. Indeed, it has been proposed that propofol has a dual effect on the neuromuscular junction. Low concentrations of propofol stimulate skeletal muscle contractions elicited direct and indirectly[14] but high concentrations of this agent inhibit skeletal muscle contractions evoked direct and indirectly[15, 16]. The mechanisms underlying the neuromuscular effects of propofol include reduction of muscular blood flow, a direct effect on the post-junctional membrane receptors, and reduction on acetylcholine (ACh) release on the neuromuscular junction[17–23].

§ Now in Center for Brain Sciences and Department of Molecular and Cellular Biology, Harvard University, 52 Oxford Street, Cambridge, MA 02138, USA.
* To whom correspondence should be addressed.
E-mail renatogomez2000@yahoo.com.br
Received 2010-07-13 Accepted 2010-09-14

FM1-43 is a fluorescent tool that has been used to study synaptic vesicle recycling at the neuromuscular junction[24–26]. The molecular characteristics of this fluorescent marker allow its internalization during synaptic vesicle endocytosis as well as its release during exocytosis[25]. In the present work, we investigated the effect of propofol on synaptic vesicle exocytosis, a crucial step for neurotransmitter release. We used FM1-43 to visualize the effect of several concentrations of propofol on spontaneous and evoked exocytosis at frog neuromuscular junction.

Materials and methods

Reagents

FM1-43 was purchased from Molecular Probes (Eugene, OR, USA), *d*-tubocurarine, 4-aminopyridine (4AP), tetrodotoxin (TTX), 2APB, dantrolene and omega-conotoxin GVIA were purchased from Sigma-Aldrich (St Louis, MO, USA). Propofol was obtained from Fresenius (Uppsala, Sweden) and azumolene was obtained from Proctor & Gamble (Norwich, NY, USA). All other chemicals and reagents were of analytical grade. All procedures were approved by the local animal care committee (CETEA-UFMG).

Staining and destaining with FM1-43

The frog neuromuscular junction has been an invaluable experimental model for elucidating many aspects of neurotransmission which is the basis of neuronal communication. Two decades ago, Betz and colleagues have introduced the use of the fluorescent dye FM1-43 to visualize synaptic vesicles recycling in motor nerve terminals of the frog neuromuscular junction[24, 25, 27]. Using this powerful tool, it was possible to elucidate the mechanisms that governed synaptic vesicle recycling and consequently neurotransmitter release in several neuronal cell types[28].

In the present work, frog cutaneous pectoris nerve muscle preparations were dissected from Rana catesbeiana (about 60 g) and mounted in a sylgard-lined chamber containing frog Ringer solution (115 mmol/L NaCl, 2.5 mmol/L KCl, 1.8 mmol/L $CaCl_2$, 5 mmol/L HEPES, pH 7.2). FM1-43 (4 μmol/L) was used to stain the recycling pool of synaptic vesicles[25]. This dye presents a hydrophobic tail that reversibly binds to membranes and a polar head that impairs it to fully permeate the plasma membrane[24–28]. Therefore, FM1-43 binds to synaptic membrane and when the nerve terminal is submitted to a stimulus that causes exocytosis of synaptic vesicles and, consequently, a compensatory endocytosis, the fluorescent dye is incorporated, resulting in a typical pattern of staining[25]. After a new round of stimulation, in the absence of FM1-43 in the external medium, the dye is released to the hydrophilic medium, resulting in a decrease of fluorescence intensity, reflecting the exocytosis of synaptic vesicle[24–26]. In our experiments, the muscles were incubated with *d*-tubocurarine (16 μmol/L) to prevent contractions during stimulation. The muscles were stimulated for 10 min with modified Ringer solution (57.5 mmol/L NaCl, 60 mmol/L KCl, 1.8 mmol/L $CaCl_2$, 5 mmol/L HEPES, pH 7.2) in the presence of FM1-43 (4 μmol/L). Thereafter, the preparation was kept resting for 15 min to guarantee FM1-43 uptake. The excess of FM1-43 adhered to the muscle membranes was removed during an one hour washing period in frog Ringer solution. Images were acquired in intervals of 5 min until the end of the experiments. The destaining at the absence of stimulus (photobleaching) was used as a control.

After labeling with FM1-43, neuromuscular preparations were exposed to different concentrations of propofol during 30 min to evaluate its effect on spontaneous exocytosis. Experiments were also performed to investigate the effect of propofol on Na^+-dependent exocytosis evoked by 4AP. After labeling neuromuscular preparations with FM1-43, muscles were exposed to 4AP (1 mmol/L) during 30 min. To test the role of extracellular Na^+ on 4AP-evoked exocytosis, the neuromuscular preparation was initially incubated for 30 min in frog Ringer containing 1.0 μmol/L TTX and, thereafter, it was exposed to 4AP for 30 min. The propofol effect on 4AP-induced exocytosis was investigated by pre-incubation in propofol (100 μmol/L) solution during 10 min before 4AP exposure. Similar protocols were applied to investigate the effects of propofol and TTX on Na^+-independent exocytosis evoked by 60 mmol/L KCl.

Experiments that investigated the role of extracellular Ca^{2+} on the vesicular release induced by propofol were performed in modified Ringer solution without Ca^{2+} but containing EGTA (2.0 mmol/L), an extracellular Ca^{2+} chelator. The preparations were incubated in modified Ringer during 30 min before application of propofol. In experiments performed with the calcium channel blocker omega-conotoxin GVIA, the preparations were pre-incubated in Ringer containing toxin for 30 min before propofol. The participation of intracellular Ca^{2+} stores on the exocytosis evoked by propofol was also investigated. For this purpose, preparations were incubated for 30 min in Ringer containing 2APB (100 μmol/L), an IP_3 receptor blocker, or azumolene (100 μmol/L), a ryanodine receptors blocker before the addition of propofol.

Fluorescence microscopy and imaging analyses

Images were acquired using a fluorescence microscope (Zeiss Axioskop) coupled to a CCD camera (Micromax) and visualized in a computer. The microscope was equipped with water immersion objectives (63×, 0.95 NA and 40×, 0.75 NA). Excitation light came from a 100 W Hg lamp and passed through filters (505/530 nm) to select the fluorescence spectrum. The experimental parameters for collection of images were always identical in control and test contralateral muscles in a given trial.

Statistical analysis

Image analysis was performed using the softwares Image J and Microsoft Excel. The mean fluorescence intensity was determined for each group of spots and plotted against the time as percentage of its mean initial fluorescence using the software Sigma Plot 9.0. Statistical analysis was performed using paired Student's *t*-Test or ANOVA. $P<0.05$ values were

considered statistically significant.

Results

FM1-43 staining and destaining of nerve terminals

Frog cutaneous-pectoris neuromuscular junctions were stained with FM1-43 as previously described[25]. The nerve terminal that was stained with FM1-43 shows fluorescent spots corresponding to clusters of synaptic vesicles that were able to pick up the dye (Figure 1A, upper panel). When this previously labeled terminal was submitted to a new depolarizing stimulus by modified Ringer containing 60 mmol/L KCl, in the absence of FM1-43 in external medium, we observed a significant reduction in fluorescence (Figure 1A, lower panel). The loss of fluorescence was due to dye release to external medium, that correspond to synaptic vesicle exocytosis[25]. Exposure of nerve terminals to illumination without any depolarizing stimulus resulted in a small decrease on fluorescence (maximum 10%) attributable to dye photobleaching[28]. A representative image of the terminal before (upper panel) and after illumination (lower panel), in the absence of stimulus, is shown in Figure 1B. To quantify the decrease in fluorescence that occurs after stimulation with 60 mmol/L KCl and photobleaching, the mean fluorescence intensity for each synaptic vesicle cluster was measured and plotted as gray levels against time (Figure 1C). The small reduction in fluorescence observed corresponds to photobleaching whereas the larger destaining curve obtained during depolarization stimulus corresponds to synaptic vesicle exocytosis.

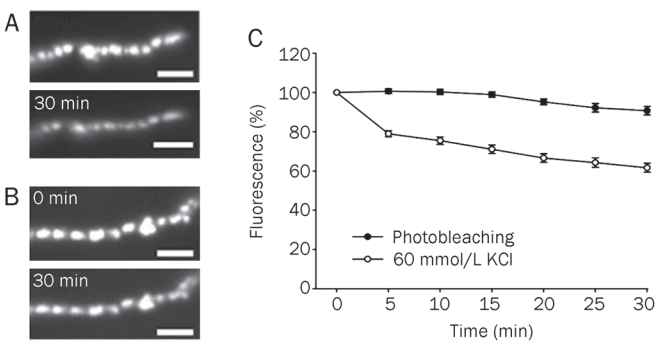

Figure 1. Synaptic vesicles recycling visualized by the fluorescent dye FM1-43. (A) Upper panel: Representative nerve terminal that was incubated in modified Ringer containing 60 mmol/L KCl for 10 min in the presence of FM1-43. Note the formation of fluorescent spots, corresponding to clusters of synaptic vesicles that were able to pick up dye. Lower panel: The same terminal after a second round of depolarization with modified Ringer containing 60 mmol/L KCl, now in the absence of extracellular dye. Note a pronounced destaining of fluorescent spots, corresponding to exocytosis of synaptic vesicles and dye release to the external medium. (B) Representative image of fluorescence loss due to photobleaching during illumination for 30 min. Upper panel: before illumination. Lower panel: after 30 min of illumination. (C) Quantification of FM1-43 fluorescence loss due to photobleaching and KCl fluorescence loss due to exocytosis of synaptic vesicles. The results are mean±SEM of 65 spots from 8 nerve terminals of 4 animals. Scale Bar=10 μm.

Effect of low concentrations of propofol on spontaneous synaptic vesicle exocytosis

Nerve terminals labeled with FM1-43 were bathed in different concentrations of propofol (10 to 200 μmol/L) for 30 min (Figure 2). Fluorescence of representative terminals before and after photobleaching (Figure 2A); propofol 10 μmol/L (Figure 2B), and propofol 200 μmol/L (Figure 2C) were obtained. Low concentrations of propofol ranging from 10 to 25 μmol/L significantly reduced FM1-43 fluorescence, corresponding to exocytosis of previously labeled vesicular clusters (**P*<0.01 compared to photobleaching) (Figure 2D). On the other hand, high doses of propofol (50–200 μmol/L) had no effect on FM1-43 destaining from motor nerve terminals (Figure 2D), suggesting a dose-dependent effect of the anesthetic agent.

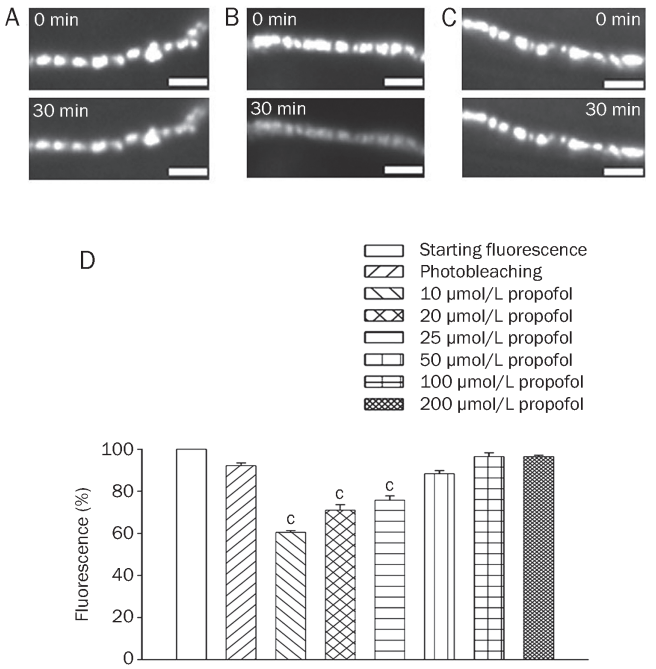

Figure 2. Dose-response curve of exocytosis induced by propofol. (A) Representative image of fluorescence loss due to photobleaching during illumination for 30 min. Upper panel: before illumination. Lower panel: after 30 min of illumination. (B) Representative image of fluorescence loss before (upper panel) and after (lower panel) 30 min in the presence of propofol 10 μmol/L. (C) Representative image of fluorescence loss before (upper panel) and after (lower panel) 30 min in the presence of propofol 200 μmol/L. (D) Quantification of exocytosis evoked by different concentrations of propofol. The results are mean±SEM of 131 fluorescent spots from 15 nerve terminals of 8 animals. ^{c}P<0.01 compared to the second bar (photobleaching). Scale Bar=10 μm.

The next set of experiments was performed to identify the mechanism(s) by which low doses of propofol induced exocytosis of synaptic vesicles. Pre-incubation of nerve terminals with TTX (1.0 μmol/L), a voltage-gated Na^+-channel blocker, did not affect the vesicle exocytosis evoked by propofol (data not shown). By contrast, the effect of low doses of propofol

on spontaneous exocytosis monitored by FM1-43 destaining was Ca^{2+}-dependent (Figure 3A). Indeed, we observed a statistically significant inhibition of exocytosis evoked by low doses of propofol in the presence of the external Ca^{2+} chelator EGTA (2.0 mmol/L) or in the presence of omega-toxin GVIA (5 μmol/L), that blocks N-type calcium channels (Figure 3A). The FM1-43 destaining in the presence of GVIA was not significantly different from that due to photobleaching ($P>0.05$). In addition, we observed that the effect of low doses of propofol on synaptic vesicles exocytosis was independent on intracellular Ca^{2+} stores (Figure 3B). Our data suggest that FM1-43 destaining induced by propofol (10 μmol/L) was Ca^{2+} dependent and Na^+-independent.

Effects of high concentrations of propofol on exocytosis evoked by depolarizing stimuli

It has been shown that propofol at concentrations around 100 μmol/L inhibits skeletal muscle evoked contractions[15, 16]. We therefore tested in our system if this concentration of propofol could alter with 4AP-evoked FM1-43 destaining, which is dependent on extracellular Na^+. The incubation of nerve terminals with 4AP (1.0 mmol/L) during 30 min induced a significant FM1-43 destaining (Figure 4A). The destaining evoked by 4AP was reduced by TTX ($P<0.01$ compared to 4AP alone). Pre-incubation of FM1-43 stained nerve terminals with propofol (100 μmol/L) also reduced the 4AP-evoked exocytosis (Figure 4A; $P<0.01$ compared to 4AP alone). Moreover, the simultaneous pre-incubation with propofol (100 μmol/L) and TTX (1.0 μmol/L) produced a significant inhibition of 4AP evoked FM1-43 destaining without any additive effect (Figure 4A), suggesting that propofol reduces the 4AP-induced vesicle exocytosis by blocking Na^+ channels sensitive to TTX.

We next tested the effect of high doses of propofol on Na^+-independent exocytosis evoked by modified Ringer containing 60 mmol/L KCl. Nerve terminals were stained with FM1-43

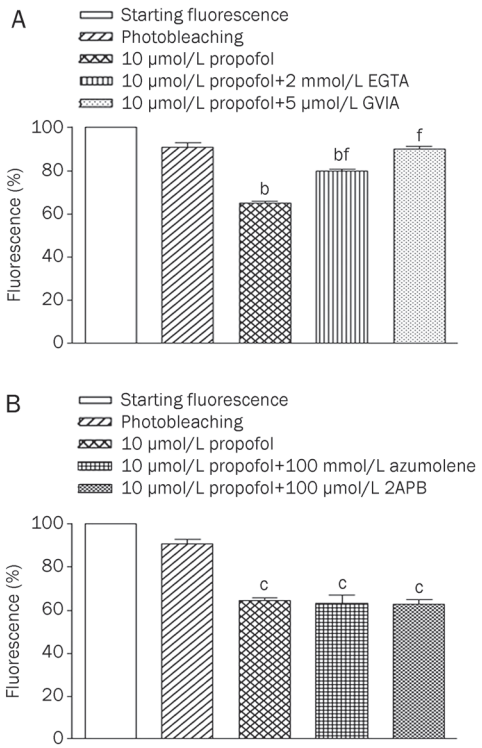

Figure 3. Low doses of propofol evoke synaptic vesicles exocytosis that is dependent on external calcium. (A) FM1-43 destaining evoked by photobleaching (second bar), propofol (10 μmol/L) (third bar), propofol (10 μmol/L)+EGTA (2 mmol/L) (fourth bar), propofol (10 μmol/L)+GVIA (5 μmol/L) (fifth bar). Note that even though EGTA was apparently slightly less effective than GVIA, both agents inhibited the propofol-evoked destaining. The results are mean±SEM of 192 fluorescent spots from 20 nerve terminals of 10 animals. $^bP<0.05$ compared to the second bar (photobleaching). $^fP<0.01$ compared to propofol (10 μmol/L). (B) FM1-43 destaining evoked by photobleaching (second bar), propofol (10 μmol/L) (third bar), propofol (10 μmol/L)+azumolene (100 μmol/L) (fourth bar), propofol (10 μmol/L)+2APB (100 μmol/L) (fifth bar). The results are mean±SEM of 237 fluorescent spots from 18 nerve terminals of 9 animals. $^cP<0.01$ compared to the second bar (photobleaching).

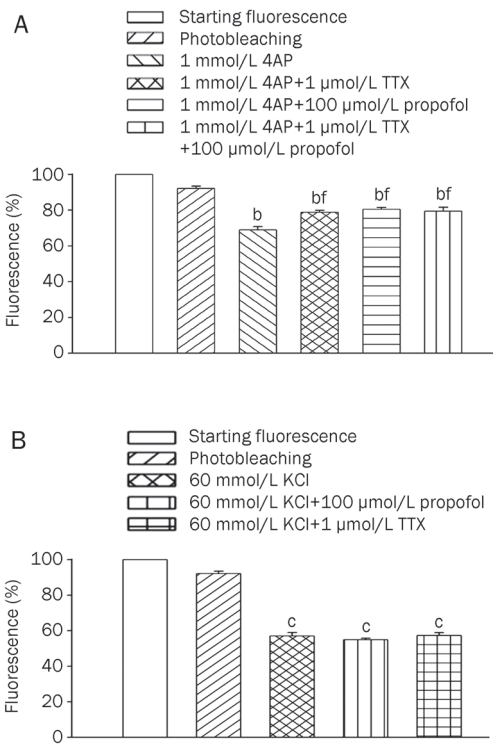

Figure 4. High doses of propofol inhibit synaptic vesicles exocytosis by a Na^+-dependent manner. (A) Graphic comparing FM1-43 destaining evoked by photobleaching (second bar), 4AP (1 mmol/L, third bar), 4AP (1 mmol/L)+TTX (1 μmol/L) (fourth bar), 4AP (1 mmol/L)+propofol (100 μmol/L) (fifth bar) and 4AP (1 mmol/L)+propofol (100 μmol/L)+TTX (1 μmol/L) (sixth bar). The results are mean±SEM of 114 fluorescent spots from 10 nerve terminals of 5 animals. $^bP<0.05$ compared to the second bar (photobleaching). $^fP<0.01$ compared to 4AP (1 mmol/L). (B) Quantification of exocytosis evoked by photobleaching (second bar), KCl (60 mmol/L) (third bar); KCl (60 mmol/L)+propofol (100 μmol/L) (fourth bar); KCl (60 mmol/L)+TTX (1 μmol/L) (fifth bar). The results are mean±SEM of 120 fluorescent spots from 10 nerve terminals of 5 animals. $^cP<0.01$ compared to the second bar (photobleaching).

and we observed a significant reduction on fluorescence after incubation with KCl for 30 min (Figure 4B). Pre-incubation of terminals with TTX had no effect on KCl-evoked reduction in fluorescence, confirming the data that depolarization induced by high concentration of K^+ is independent of extracellular Na^+ [29] (Figure 4B). In addition, pre-incubation with high doses of propofol did not inhibit KCl-evoked Na^+-independent exocytosis (Figure 4B). Taken together, these results suggest that high doses of propofol inhibit synaptic vesicles exocytosis on the neuromuscular junction by a Na^+-dependent manner.

Discussion

Propofol is widely used during general anesthesia, as well as for sedation in the intensive care unit. However, fatigue of the respiratory muscles, especially the diaphragm, may cause respiratory failure. Indeed, it has been demonstrated that volatile (halothane, enflurane, isoflurane, and sevoflurane) and intravenous (propofol and midazolam) anesthetics cause diaphragmatic contractile dysfunction which may probably contributes to acute respiratory failure[19–21, 30–32]. Studies *in vivo* suggested that several mechanisms such as reduction of blood flow, failure of neuromuscular transmission, and impairment of membrane excitation and excitation-contraction (E–C) coupling may be responsible for the neuromuscular effects of propofol. However, *in vivo* studies preclude any specification regarding the mechanism involved on the anesthetic effect and the use of the fluorescent probe FM1-43 enabled us to assess specifically a presynaptic effect of this agent on the neuromuscular junction. Hemmings *et al*[30] had already performed a pioneer study on cultured hippocampal neurons using this fluorescent dye to probe synaptic vesicles exocytosis in the presence of isoflurane and they showed that isoflurane depresses exocytosis evoked by multiple presynaptic targets.

In the present work, we examined the effect of propofol on spontaneous and evoked synaptic vesicle exocytosis at the neuromuscular junction, an experimental model that provides a direct way to investigate neurotransmitter release in an isolated synapse. We found that propofol, at low concentrations ranging from 10 to 25 μmol/L, induced synaptic vesicles exocytosis monitored by FM1-43 destaining on a Ca^{2+}-dependent and Na^+-independent manner. By contrast, high concentrations of propofol ranging from 50 to 200 μmol/L were ineffective to induce synaptic vesicle exocytosis.

It is well known that exocytosis depends on external Ca^{2+}[23] and we observed that in the absence of this ion, there was a significant reduction on FM1-43 destaining evoked by low doses of propofol, suggesting that synaptic vesicles exocytosis evoked by propofol is Ca^{2+}-dependent. In addition, we investigated which calcium channel subtype could be the target of low doses of propofol at the frog neuromuscular junction and we observed an inhibition of propofol evoked exocytosis in the presence of the *N*-type inhibitor omega-conotoxin GVIA. Because the FM1-43 destaining evoked by propofol in the presence of GVIA was similar to that due to photobleaching ($P>0.05$) , we suggest that propofol might act on N-type calcium channels promoting calcium influx that is coupled to synaptic vesicles exocytosis. Different from our data, previous works performed in CNS synapses have shown a predominant inhibition of calcium channels by propofol[5–7]. However, none of them have shown evidences that *N*-type calcium channels could be a target for propofol action. This discrepancy might be due to the fact that these studies were performed in brain slices that maintain intact neuronal circuitry whereas in the present work we were looking at nerve terminals without connection with motor neuron cell bodies. Therefore, we cannot rule out the possibility that propofol may exert an inhibitory effect on calcium channels located at motor neurons' cell bodies that are located at the spinal cord. Because we are looking at events that take place exclusively at the synaptic nerve terminal, such inhibition would not be detected in our experimental model. Nonetheless, our data provide direct evidences that low doses of propofol might act through *N*-type calcium channel that are directly coupled to synaptic vesicle exocytosis at motor nerve terminals. Moreover, we showed that propofol and KCl-evoked exocytosis were not affected by TTX suggesting that both conditions did not increase the synaptic vesicle exocytosis by interfering with Na^+ channels. Therefore, propofol and KCl can induce exocytosis in a Ca^{2+}-dependent and Na^+-independent fashion suggesting that this anesthetic may act directly on Ca^{2+} entry through *N*-type voltage-gated Ca^{2+} channels.

In agreement with our data, it has been observed that low concentrations of propofol increased the amplitude of the indirectly-elicited twitch and tetanic contractions in chick biventer cervices skeletal muscle, indicating that, in low concentrations, this anesthetic may stimulate skeletal muscle[14].

Previous work showed that propofol, at concentrations of 42 and 112 μmol/L, inhibited contraction of isolated rat diaphragm by decreasing ACh release on neuromuscular junction[16]. These authors also observed that this agent inhibited muscle contraction evoked by electrical field stimulation, suggesting that propofol, at this concentration range, may act by inhibiting Ca^{2+} entry through presynaptic voltage-gated Ca^{2+} channels. In the present work high doses of propofol inhibited Na^+-dependent exocytosis evoked by 4AP but did not have any significant effect on Na^+-independent exocytosis evoked by KCl. The decrease on vesicle exocytosis induced by 4AP in the presence of high doses of propofol is in correspondence with data showing a decreasing on the contractility of fatigued canine diaphragm with propofol in a dose-related fashion[21]. Previous studies in rat brain synaptosomes showed that propofol inhibits Ca^{2+}-dependent glutamate release evoked by veratridine and 4-AP with greater potency than Na^+ channel-independent release evoked by KCl[33–36]. In addition, it has been observed that high concentrations of propofol selectively inhibited 4AP-evoked but not KCl-evoked [^{3}H]norepinephrine release[37]. Considering that high doses of propofol inhibited 4AP-evoked synaptic vesicles exocytosis in a similar manner to TTX and did not interfere with KCl-evoked exocytosis, we could suggest that the effect of propofol on neuromuscular junction is thus caused primarily by inhibition of action potential-evoked synaptic vesicle exocytosis at a step upstream of

Ca^{2+} entry through voltage-gated Ca^{2+} channels, possibly as a result of Na^+ channel blockade. In addition, there are evidences in the literature suggesting that high doses of propofol might have a direct effect on Na^+ channels[10, 12, 13]. Finally, experiments in dogs show that administration of propofol decreases diaphragm contractility in a dose-dependent manner and that high dose of this anesthetic produces a progressive decrease in contractility[18]. Based on the data presented here, we could speculate that such diaphragmatic dysfunction might be due to a presynaptic effect of high doses of propofol. In addition, propofol and midazolam seems to cause diaphragm dysfunction through mechanisms other than E–C coupling failure[23]. However, the clinical importance of the present data requires further investigations and we are unable to extrapolate our *in vitro* findings to the clinical practice.

It is difficult to correlate the concentrations of anesthetics used *in vitro* experiments with those used during clinical anesthesia and it has been shown that the doses of intravenous anesthetics required in the case of experimental animals are 10-100 times higher than those used for humans[38]. Plasma concentrations of propofol during anesthesia in humans are estimated to range between 70 and 106 μmol/L[35, 39–41]. Because of the high protein binding (98%), the half-maximal effect free concentration of propofol is around 2.0 μmol/L[35, 42, 43]. It has been suggested that brain concentrations of propofol are about eight-fold higher than plasma free concentrations[44] but there is no estimative of the concentrations on neuromuscular junction. Moreover, the propofol concentration producing loss of righting reflex in Rana pipiens tadpoles ranged between 1 and 10 μmol/L[45] an end point that usually occurs at a lower concentration than surgical anesthesia. Finally, it has been argued that clinically relevant concentrations are difficult to estimate[1-4] and it is important to mention that clinically relevant concentrations of anesthetic are important to examine the integrated responses in the intact animal but their relevance to *in vitro* studies should be taken with care due to our lack of understanding of how to integrate *in vitro* systems into the anesthesia model[46].

In conclusion, we showed that propofol has a dual effect on the exocytosis of cholinergic synaptic vesicles from the neuromuscular transmission and the present results may contribute to understanding some of the clinical effects observed with this agent on neuromuscular function.

Acknowledgements

This work was supported by grants from CNPq, FAPEMIG and CAPES. We thank Dr Hugh C HEMMINGS Jr for valuable comments on this manuscript.

Author contribution

Luciana Ferreira LEITE and Matheus de Castro FONSECA performed research and analysed data; Renato Santiago GOMEZ designed research and wrote the paper; Marcus Vinicius GOMEZ wrote the paper; Cristina GUATIMOSIM design research and analysed data.

References

1 Franks NP, Lieb WR. Molecular and cellular mechanisms of general anaesthesia. Nature 1994; 367: 607–14.
2 Yamakura T, Bertaccini E, Trudell JR, Harris RA. Anesthetics and ion channels: molecular models and sites of action. Annu Rev Pharmacol Toxicol 2001; 41: 23–51.
3 Hemmings HC Jr, Akabas MH, Goldstein PA, Trudell JR, Orser BA, Harrison NL. Emerging molecular mechanisms of general anesthetic action. Trends Pharmacol Sci 2005; 26: 503–10.
4 Franks NP. Molecular targets underlying general anaesthesia. Br J Pharmacol 2006; 147: S72–81.
5 Inoue Y, Shibuya I, Kabashima N, Noguchi J, Harayama N, Ueta Y, *et al*. The mechanism of inhibitory actions of propofol on rat supraoptic neurons. Anesthesiology. 1999; 91: 167-78.
6 Shirasaka T, Yoshimura Y, Qiu DL, Takasaki M. The effects of propofol on hypothalamic paraventricular nucleus neurons in the rat. Anesth Analg 2004; 98: 1017–23.
7 Martella G, De Persis C, Bonsi P, Natoli S, Cuomo D, Bernardi G, *et al*. Inhibition of persistent sodium current fraction and voltage-gated *L*-type calcium current by propofol in cortical neurons: implications for its antiepileptic activity. Epilepsia 2005; 46: 624–35.
8 Ratnakumari L, Hemmings HC Jr. Effects of propofol on sodium channel-dependent sodium influx and glutamate release in rat cerebrocortical synaptosomes. Anesthesiology 1997; 86: 428–39.
9 Lingamaneni R, Birch ML Hemmings HC Jr. Widespread inhibition of sodium channel-dependent glutamate release from isolated nerve terminals by isoflurane and propofol. Anesthesiology 2001; 95: 1460–6.
10 Frenkel C, Urban BW. Human brain sodium channels as one of the molecular target sites for the new intravenous anaesthetic propofol (2,6-diisopropylphenol). Eur J Pharmacol 1991; 208: 75–9.
11 Frenkel C, Duch DS, Urban BW. Effects of iv anaesthetics on human brain sodium channels. Br J Anaesth 1993; 71: 15–24.
12 Lingamaneni R, Hemmings HC Jr. Differential interaction of anaesthetics and antiepileptic drugs with neuronal Na^+ channels, Ca^{2+} channels, and GABA(A) receptors. Br J Anaesth 2003; 90: 199–211.
13 Martella G, De Persis C, Bonsi P, Natoli S, Cuomo D, Bernardi G, *et al*. Inhibition of persistent sodium current fraction and voltage-gated *L*-type calcium current by propofol in cortical neurons: implications for its antiepileptic activity. Epilepsia 2005; 46: 624–35.
14 Wali FA. Effects of some intravenous anaesthetics on the contractile responses produced in the chick biventer cervicis skeletal muscle. Pharmacol Res Commun 1985; 17: 361–76.
15 Lebeda MD, Wegrzynowicz ES, Wachtel RE. Propofol potentiates both pre- and postsynaptic effects of vecuronium in the rat hemidiaphragm. Br J Anaesth 1992; 68: 282–5.
16 Abdel-Zaher AO, Askar FG. The myoneural effects of propofol emulsion (Diprivan) on the nerve-muscle preparations of rats. Pharmacol Res 1997; 36: 323–32.
17 Robertson EN, Fragen RJ, Booij LH, van Egmond J, Crul JF. Some effects of diisopropylphenol (ICI35868) on the pharmacodynamics of atracurium and vecuronium in anaesthetized man. Br J Anaesth 1983; 55: 723–8.
18 Fujii Y, Hoshi T, Takahashi S, Toyooka H. Propofol decreases diaphragmatic contractility in dogs. Anesth Analg 1999; 89: 1557–60.
19 Fujii Y, Hoshi T, Takahashi S, Toyooka H. The effect of sedative drugs on diaphragmatic contractility in dogs: propofol versus midazolam. Anesth Analg 2000; 91: 1035–7.
20 Fujii Y, Uemura A, Toyooka H. The dose-range effects of propofol on the contractility of fatigued diaphragm in dogs. Anesth Analg 2001;

93: 1194–8.
21 Fujii Y, Toyooka H. Midazolam versus propofol for reducing contractility of fatigued canine diaphragm. Br J Anaesth 2001; 86: 879–81.
22 Bouhemad B, Langeron O, Orliaguet G, Coriat P, Riou B. Effects of halothane and isoflurane on the contraction, relaxation and energetics of rat diaphragmatic muscle. Br J Anaesth 2002; 89: 479–85.
23 Nishina K, Mikawa K, Kodama S-I, Kagawa T, Uesugi T, Obara H. The effects of enflurane, isoflurane, and intravenous anesthetics on rat diaphragmatic function and fatigability. Anesth Analg 2003; 96: 1674–8.
24 Betz WJ, Bewick GS. Optical analysis of synaptic vesicle recycling at the frog neuromuscular junction. Science 1992; 255: 200–3.
25 Betz WJ, Mao F, Bewick GS. Activity-dependent fluorescent staining and destaining of living vertebrate motor nerve terminals. J Neurosci 1992; 12: 363–75.
26 Gaffield MA, Betz WJ. Imaging synaptic vesicle exocytosis and endocytosis with FM dyes. Nat Protoc 2006; 1: 2916–21.
27 Guatimosim C, Romano-Silva MA, Gomez MV, Prado MAM. Use of fluorescent probes to follow membrane traffic in nerve terminals. Braz J Med Biol Res 1998; 31: 1491–500.
28 Rizzoli SO, Richards DA, Betz WJ. Monitoring synaptic vesicle recycling in frog motor nerve terminals with FM dyes. J Neurocytol 2003; 32: 539–49.
29 Nicholls DG. The glutamatergic nerve terminal. Eur J Biochem 1993; 212: 613–31.
30 Hemmings HC Jr, Yan W, Westphalen RI, Ryan TA. The general anesthetic isoflurane depresses synaptic vesicle exocytosis. Mol Pharmacol 2005; 67: 1591–9.
31 Kochi T, Ide T, Isono S, Mizuguchi T, Nishino T. Different effects of halothane and enflurane on diaphragmatic contractility *in vivo*. Anesth Analg 1990; 70: 362–8.
32 Ide T, Kochi T, Isono S, Mizuguchi T. Diaphragmatic activity during isoflurane anaesthesia in dogs. Acta Anaesthesiol Scand 1993; 37: 253–7.
33 Kagawa T, Maekawa N, Mikawa K, Nishina K, Yaku H, Obara H. The effect of halothane and sevoflurane on fatigue-induced changes in hamster diaphragmatic contractility. Anesth Analg 1998; 86: 392–7.
34 Südhof TC. The synaptic vesicle cycle: a cascade of protein-protein interactions. Nature 1995; 375: 645–53.
35 Ratnakumari L, Hemmings HC Jr. Effects of propofol on sodium channel-dependent sodium influx and glutamate release in rat cerebrocortical synaptosomes. Anesthesiology 1997; 86: 428–39.
36 Lingamaneni R, Birch ML, Hemmings HC Jr. Widespread inhibition of sodium channel-dependent glutamate release from isolated nerve terminals by isoflurane and propofol. Anesthesiology 2001; 95: 1460–6.
37 Pashkov VN, Hemmings HC Jr. The effects of general anesthetics on norepinephrine release from isolated rat cortical nerve terminals. Anesth Analg 2002; 95: 1274–81.
38 Wakasugi M, Hirota K, Roth SH, Ito Y. The effects of general anesthetics on excitatory and inhibitory synaptic transmission in area CA1 of the rat hippocampus *in vitro*. Anesth Analg 1999; 88: 676–80.
39 Smith C, McEwan AI, Jhaveri R, Wilkinson M, Goodman D, Smith R, *et al*. The interaction of fentanyl on the CP50 of propofol for loss of consciousness and skin incision. Anesthesiology 1994; 81: 820–8.
40 Kazama T, Ikeda K, Morita K. The pharmacodynamic interaction between propofol and fentanyl with respect to the suppression of somatic or hemodynamic responses to skin incision, peritoneum incision, and abdominal wall retraction. Anesthesiology 1998; 89: 894–06.
41 Haeseler G, Störmer M, Bufler J, Dengler R, Hecker H, Piepenbrock S, *et al*. Propofol blocks human skeletal muscle sodium channels in a voltage-dependent manner. Anesth Analg 2001; 92: 1192–8.
42 Servin F, Desmonts JM, Haberer JP, Cockshott ID, Plummer GF, Farinotti R. Pharmacokinetics and protein binding of propofol in patients with cirrhosis. Anesthesiology 1988; 69: 887–91.
43 Rehberg B, Duch DS. Suppression of central nervous system sodium channels by propofol. Anesthesiology 1999; 91: 512–20.
44 Shyr MH, Tsai TH, Tan PP, Chen CF, Chan SH. Concentration and regional distribution of propofol in brain and spinal cord during propofol anesthesia in the rat. Neurosci Lett 1995; 184: 212–5.
45 Tonner PH, Poppers DM, Miller KW. The general anesthetic potency of propofol and its dependence on hydrostatic pressure. Anesthesiology 1992; 77: 926–31.
46 Eckenhoff RG, Johansson JS. On the relevance of "clinically relevant concentrations" of inhaled anesthetics in *in vitro* experiments. Anesthesiology 1999; 91: 856–60.

Acta Pharmacologica Sinica (2011) 32: 38–44
 1671-4083/11 $32.00
www.nature.com/aps

Original Article

Salvianolic acid B inhibits autophagy and protects starving cardiac myocytes

Xiao HAN, Jian-xun LIU*, Xin-zhi LI

Research Center, Xiyuan Hospital, China Academy of Chinese Medical Sciences, Beijing 100091, China

Aim: To investigate the protective or lethal role of autophagy and the effects of Salvianolic acid B (Sal B) on autophagy in starving myocytes.

Methods: Cardiac myocytes were incubated under starvation conditions (GD) for 0, 1, 2, 3, and 6 h. Autophagic flux in starving cells was measured via chloroquine (3 μmol/L). After myocytes were treated with Sal B (50 μmol/L) in the presence or absence of chloroquine (3 μmol/L) under GD 3 h, the amount of LC3-II, the abundance of LC3-positive fluorescent dots in cells, cell viability and cellular ATP levels were determined using immunoblotting, immunofluorescence microscopy, MTT assay and luminometer, respectively. Moreover, electron microscopy (EM) and immunofluorescent duel labeling of LC3 and Caspase-8 were used to examine the characteristics of autophagy and apoptosis.

Results: Immunoblot analysis showed that the amount of LC3-II in starving cells increased in a time-dependent manner accompanied by increased LC3-positive fluorescence and decreased cell viability and ATP content. Sal B (50 μmol/L) inhibited the increase in LC3-II, reduced the abundance of LC3 immunofluorescence and intensity of Caspase-8 fluorescence, and enhanced cellular viability and ATP levels in myocytes under GD 3 h, regardless of whether chloroquine was present.

Conclusion: Autophagy induced by starvation for 3 h led to cell injury. Sal B protected starving cells by blocking the early stage of autophagic flux and inhibiting apoptosis that occurred during autophagy.

Keywords: Salvianolic acid B; autophagy; apoptosis; cardiac myocyte; starvation

Acta Pharmacologica Sinica (2011) 32: 38–44; doi: 10.1038/aps.2010.182; published online 29 Nov 2010

Introduction

Autophagy is a highly conserved cellular mechanism that plays a key role in the turnover of long-lived proteins, RNA, and dysfunctional organelles. In starvation or stress conditions, autophagy represents an adaptive strategy by which cells clear damaged organelles and survive nutritional, bioenergetic stress[1]. It is becoming clear that autophagy might be more important in terminally differentiated cell types, such as cardiac myocytes[2].

Basal autophagy activity is essential for the heart to maintain homeostasis[3]; however, increasing evidence suggests that autophagy constitutes a second mode of programmed cell death (Type II PCD) that is distinct from apoptosis (Type I PCD)[4]. Autophagy has been observed in both hypertrophied myocardium and failing myocardium, which is caused by dilated cardiomyopathy, vascular disease and ischemic heart disease[5]. Therefore, the regulation of autophagy by pharmacological approaches is a potential therapeutic strategy to treat heart diseases.

The autophagy-related genes (Atg) have been isolated and characterized in yeast and mammals[6]. In mammalian cells, LC3, one of the homologues of yeast Atg8, is modified via an ubiquitylation-like system. The carboxy-terminal region of LC3 is cleaved, generating a soluble form known as LC3-I and exposing a carboxy-terminal glycine essential for additional activity. LC3-I, in turn, is modified to a membrane-bound form, LC3-II (an LC3-phospholipid conjugate), by mammalian Atg7 and Atg3 homologues, prompting its localization to autophagosomes[7]. Thereafter, autophagosomes fuse with lysosomes, forming autolysosomes, to degrade engulfed cytosolic components. Thus, the amount of LC3-II in mammalian cells is a good early marker for the formation of autophagosomes[7].

The cellular level of LC3-II and the presence of numerous autophagosomes are generally considered to be synonymous with increased autophagic activity. But autophagy is a dynamic process that reflects the formation of autophagosomes and their clearance subsequent to lysosomal fusion. The presence of numerous autophagosomes can reflect two

* To whom correspondence should be addressed.
E-mail liujx0324@sina.com
Received 2010-04-29 Accepted 2010-09-15

different conditions: an increase in autophagosome formation or a decrease in autophagosome clearance due to frustrated autophagy. Frustrated autophagy is characterized by failure of lysosomal fusion, leading to the accumulation of autophagosomes, which may eventually cause catastrophic leakage of lysosomal proteases and cell death[8].

We therefore used the lysosomal inhibitor chloroquine to measure autophagic flux, which reflected the dynamic process of autophagy and could help to estimate whether autophagy is frustrated during the process.

It has been reported that Sal B protects cardiac myocytes against ischemia-reperfusion injury through inhibition of platelet activation in cardiovascular endothelial cells[9], regulation of the balance of the ET/NO[10] and TXA_2/PGI_2 systems[11] in coronary arteries, raising SOD activity[12], and inhibition of calcium overload[13], but not through the regulation of autophagy. To our knowledge, this study is the first to explore the potential mechanism by which Sal B mediates autophagy.

The goals of our study were the following: (1) to investigate the protective or lethal role of autophagy in starvation-induced cardiac myocytes using a time-course experiment; (2) to verify the effects of Sal B on autophagy in starving myocytes; and (3) to observe whether apoptosis occurs in myocytes during autophagy and determine the effect of Sal B on these autophagic myocytes, because there is crosstalk between the autophagic and apoptotic pathways[14].

Materials and methods

Primary culture of neonatal rat ventricular myocytes

Primary cultures of ventricular cardiac myocytes were prepared from 1-day-old SD rats (Vital River Laboratory Animal Technology Co Ltd, China). Cells were cultured in Dulbecco's modified Eagle's medium (DMEM, GIBCO) with 10% fetal bovine serum (FBS, GIBCO). Most cells beat spontaneously in a confluent monolayer 48–72 h after plating.

Starvation and drug treatment of cells

To obtain starvation conditions, cardiac myocytes were washed three times with phosphate-buffered saline and incubated in glucose-free, serum-free DMEM (GD, Invitrogen) at 37 °C for 0, 1, 2, 3, and 6 h, with cells cultured in nutrient-rich medium as a control. For drug treatment study, cells were treated with Sal B (50 μmol/L, National Institute for the Control of Pharmaceutical and Biological Products) with or without chloroquine (3 μmol/L, Sigma) under GD condition for 3 h. After treatment, cells were analyzed as described below. Incubation of cardiac myocytes with chloroquine (3 μmol/L) and/or Sal B (50 μmol/L) for 24 h under normal culture conditions did not result in cytotoxicity (data not shown).

Electron microscopy (EM)

Cardiac myocytes were centrifuged for collection, fixed with 4% glutaraldehyde, post-fixed with 1% osmium tetroxide, stained with uranyl acetate, and embedded in Epon. Ultrathin sections were observed using an electron microscope (Hitachi, H7500, Japan).

Cell viability of cardiac myocytes

Cell viability was measured by MTT [3-(4,5-dimethylthiazol-2-yl)-2,5-diphenyl tetrazolium bromide, Amersco] assay. In brief, cardiac myocytes (1×10^5 per 100 μL) were seeded in 96-well plates. After treatment, 20 μL of MTT solution (5 mg/mL) was added to each well and incubated (37 °C, 5% CO_2) for 4 h. Next, the media was removed and the wells were allowed to dry. The MTT metabolic product was resuspended in 200 μL of DMSO and placed on a shaking table for 5 min. At this point, the absorbance (optical density) was measured at 560 nm using a microplate reader.

Measurement of intracellular ATP content

Intracellular ATP content was measured using an ATP bioluminescent assay kit (Beyotime Institute of Biotechnology, China). Cells were lysed directly in somatic cell ATP-releasing agent, and the lysates were assayed according to the manufacturer's instructions using a 1:25 dilution of the ATP assay mix. Light emitted was measured using a luminometer. ATP content was calculated by comparison with a standard curve derived from known concentrations of ATP.

Immunoblot analyses

Following treatment, cells were lysed in RIPA lysis buffer (Beyotime Institute of Biotechnology, China). Protein concentrations were determined using the BCA protein assay reagent (Beyotime Institute of Biotechnology, China). Equal protein amounts (10 μg) were electrophoresed in an sodium dodecyl sulfate (SDS) polyacrylamide gel and transferred to a polyvinylidene fluoride membrane, which was blocked with 3% BSA and incubated with rabbit anti-LC3 antibody (Sigma, St Louis, MO, USA) or rabbit anti-α-actin antibody (Beijing Biosynthesis Biotechnology, China) overnight at 4 °C. Membranes were then incubated with HRP-conjugated anti-rabbit IgG (Sigma, St Louis, MO, USA) for 1 h at room temperature. All primary antibodies were used at a dilution of 1:2000 and the secondary antibody was used at a dilution of 1:40 000. Blots were developed with ECL reagent (Thermo, USA) and exposed to film. Bands were analyzed using BIO-RAD Quantity One-4.6.2.

Immunofluorescence analysis

Cardiac myocytes growing on gelatinized coverslips were fixed with 100% ethanol for 30 min and blocked in immunostaining blocking buffer for 1 h at room temperature. The fixed cells were incubated with rabbit anti-LC3 antibody (1:100) at 4 °C overnight. Cellular LC3 protein was stained by incubating with FITC conjugated anti-rabbit IgG (1:150) (Zhongshan Goldbridge Biotechnology Co Ltd, China) for 1 h at room temperature. Nuclei were dyed with DAPI (Roche).

For dual labeling studies, LC3 (1:100) and Caspase-8 (1:300) (Santa Cruz) primary antibodies were simultaneously added to cells followed by incubation with secondary antibodies labeled with FITC (1:150) for LC3 and Cy3 (1:500) (CW Biotechnology Co LTD, China) for Caspase-8.

Immunofluorescence of cells was visualized using an immunofluorescence microscope (Olympus IX81, Japan). Images

were captured with a CCD camera (ROLERA-MGi PLUS), and image contrast was adjusted using Image-Pro Analyzer 6.3 software.

Statistical analysis

Data were expressed as means±SD. ANOVA was performed, and significance was assumed when the *P* value was less than 0.05.

Results

Endogenous LC3-II accumulation in starving cardiac myocytes led to cell injury in a time-dependent manner

To investigate the starvation condition, cardiac myocytes were cultured under GD for 1, 2, 3, and 6 h, with myocytes cultured in nutrient-rich conditions (GD 0 h) serving as a control. Immunoblot analysis showed that the amount of LC3-II increased in a time-dependent manner in myocytes under starvation conditions (Figure 1A, 1B).

It was not evident whether the observed increase in LC3-II was due to active autophagy or low autophagic flux (*ie* impaired fusion with lysosomes). Therefore, we used chloroquine, a lysosomal inhibitor that inhibits lysosome-autophagosome fusion, to measure autophagic flux. In the presence of chloroquine (3 μmol/L), endogenous LC3-II dramatically increased in starving cells (Figure 1A, 1B). The amount of LC3-II in cells treated with chloroquine was about 1.5-fold higher than in untreated control cells at 3 h. These results suggest that autophagy was successfully induced, and LC3-II was rapidly degraded by lysosomal hydrolases, indicating high autophagic flux under starvation conditions.

We also examined cell viability over a time-course. As shown in Figure 1C, the viability of cells subjected to 1-h starvation was similar to that of cells in nutrient-rich conditions. However, 2-h starvation resulted in a slight decrease in cell viability, and 3-h starvation resulted in cell viability that was obviously decreased, indicating that starving for 3 h could be lethal to myocytes. Chloroquine interrupted the autophagy process by inhibiting autophagosome-lysosome fusion and led to more serious cell injury.

In the following experiments, we investigated the effects of Sal B on autophagy regulation in cardiac myocytes subjected to starvation for 3 h.

Sal B inhibited the accumulation of LC3-II and LC3-positive fluorescence dots in starving cardiac myocytes

Based on the results of the time-course experiment above, we investigated the regulatory effects of Sal B on autophagy in myocytes subjected to 3-h starvation (Figure 2). In this experiment, immunoblot analysis showed that starvation caused an increase in endogenous LC3-II. This increase was augmented by coadministration of chloroquine, indicating that the increase in LC3-II under starvation conditions was due to increased flux, not diminished clearance. The increased flux resulting from starvation could be blocked by Sal B (Figure 2A).

Although the accumulation of endogenous LC3-II under starvation was confirmed, its intracellular localization was not evident. Using immunofluorescence microscopy, we examined the intracellular localization of endogenous LC3 in cardiac myocytes during starvation-induced autophagy in the presence or absence of chloroquine. As shown in Figure 2B, the immunofluorescence of LC3-FITC was seen as weak and diffuse cytoplasmic staining in cells cultured in nutrient-rich conditions. Strong punctate staining of LC3-FITC was induced in cells under starvation conditions. This staining appeared as multiple distinct dots connected together, localized more abundantly in the cytoplasm than in the nucleus. Because chloroquine inhibits autophagosome-lysosome fusion during

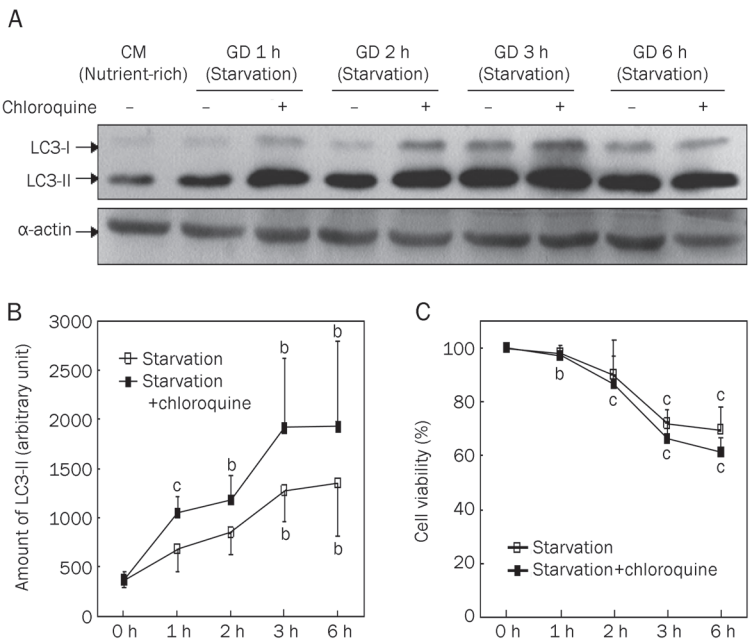

Figure 1. The accumulation of LC3-II in cardiac myocytes under starvation condition led to cell injury in a time-dependent manner. For nutrient-rich condition, cells were cultured in completed medium (CM). For starvation condition, cells were incubated for 1, 2, 3, and 6 h in glucose-free, serum-free DMEM medium (GD) in presence (+) or absence (–) of lysosomal inhibitor chloroquine (3 μmol/L). The cells were lysed and endogenous LC3 in the lysates was recognized by immunoblotting with an anti-LC3 or anti-α-actin antibody (WB: anti-LC3 or anti-α-actin). A) Representative immunoblots of LC3. LC3-I, soluble form of LC3; LC3-II, membrane-bound form of LC3. Western blotting of α-actin showed equal loading of the samples. B) Densitometric analyses of endogenous LC3-II in cardiac myocytes (A). The relative amount of LC3-II was shown. C) Cell viability of cardiac myocytes under starvation conditions in time-course experiment. Data are mean of three culture preparations. $^{b}P<0.05$, $^{c}P<0.01$ *vs* CM/Starvation 0 h.

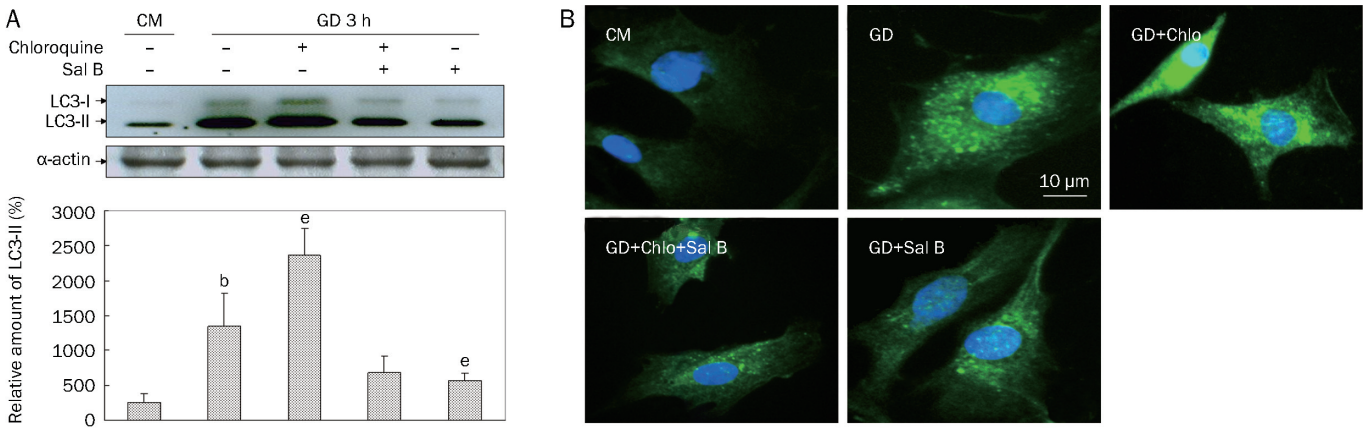

Figure 2. Sal B decreased the accumulation of LC3-II and LC3-positive fluorescence dots in starving cardiac myocyes. Cells were cultured in GD 3 h in presence (+) or absence (–) of chloroquine (Chlo, 3 μmol/L) or Sal B (50 μmol/L) with cells in CM as control. Cell lysates were subjected to immunoblots for detection of LC3-I, LC3-II, and α-actin. (A) Representative immunoblots of LC3 and the relative amount of LC3-II were shown. Western blotting of α-actin showed equal loading of the samples. (B) Representative images of LC3-positive fluorescence. Green fluorescence presented LC3-FITC staining of autophagosomes. Blue fluorescence indicated DAPI-stained nucleus. Data are mean of three culture preparations. $^{b}P<0.05$ *vs* CM, $^{e}P<0.05$ *vs* GD.

autophagy, we observed that LC3-positive punctate staining was significantly increased under starvation conditions. Sal B-treated starving myocytes presented fewer fluorescent LC3 dots in the presence or absence of chloroquine, indicating that Sal B blocked the autophagic flux.

Together with the decrease of immunofluorescent LC3 puncta in the cells, the reduction of endogenous LC3-II observed by immunoblot indicated that Sal B blocked the autophagic flux in cardiac myocytes and inhibited autophagy induced by starvation.

Sal B enhanced cell viability and cellular ATP content of starving myocytes

To verify the protective role of Sal B on autophagy-induced myocytes, cell viability and cellular ATP content were assayed. Under starvation conditions, cell viability and ATP content were significantly decreased in the presence of chloroquine. Sal B increased the ATP content and viability of starving cells regardless of the presence or absence of chloroquine (Figure 3).

Our findings indicate that Sal B protected starving cardiac myocytes by inhibiting autophagy.

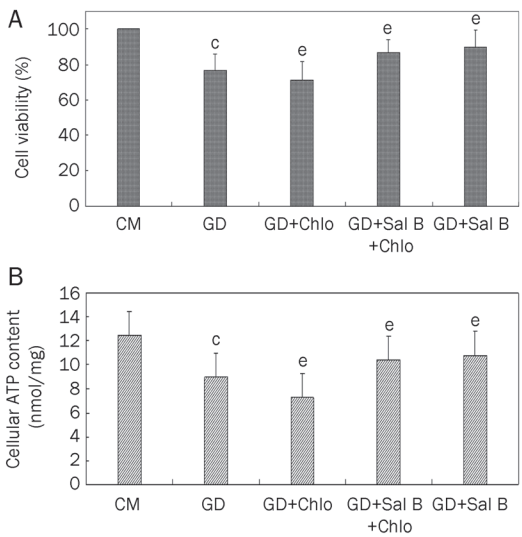

Figure 3. Sal B enhanced cell viability and cellular ATP content of starving myocytes. Cells were treated with CM or GD for 3 h in presence or absence of chloroquine (Chlo, 3 μmol/L) or Sal B (50 μmol/L). (A) Cell viability. Percentage of viability was shown. (B) Cellular ATP content. Data shown are from three independent experiments. $^{c}P<0.01$ *vs* CM; $^{e}P<0.05$ *vs* GD.

Evidence of autophagy and apoptosis in starving cardiac myocytes

Given the molecular connections between autophagy and apoptosis, we used EM to evaluate these two processes by examining characteristic structures. As shown in Figure 4A, different types of autophagosomes, which contained heterogeneous organelles ranging from mitochondria to multivesicular bodies surrounded by a sequestering membrane, were observed in myocytes under GD for 3 h (Figure 4, Ac–Ad). In addition to autophagosomes, apoptosis was observed in starving cardiac myocytes (Figure 4, Ab) with altered nuclear morphology, including chromatin condensation and fragmentation and cell shrinkage.

Dual fluorescent labeling of LC3 and Caspase-8 demonstrated the presence of autophagy and apoptosis in starving cardiac myocytes (Figure 4B, 4C). In control myocytes, green fluorescent staining of LC3 was diffusely localized to the cytoplasm, with or without weak Caspase-8 fluorescence. However, 3 h after GD, punctuate LC3 fluorescence was present, with some of these dots connected together, accompanied by intense Caspase-8 fluorescence in the cytoplasm and the nucleus. LC3 and caspase-8 exhibited a positive correlation. Chloroquine enhanced the number of fluorescent LC3 puncta

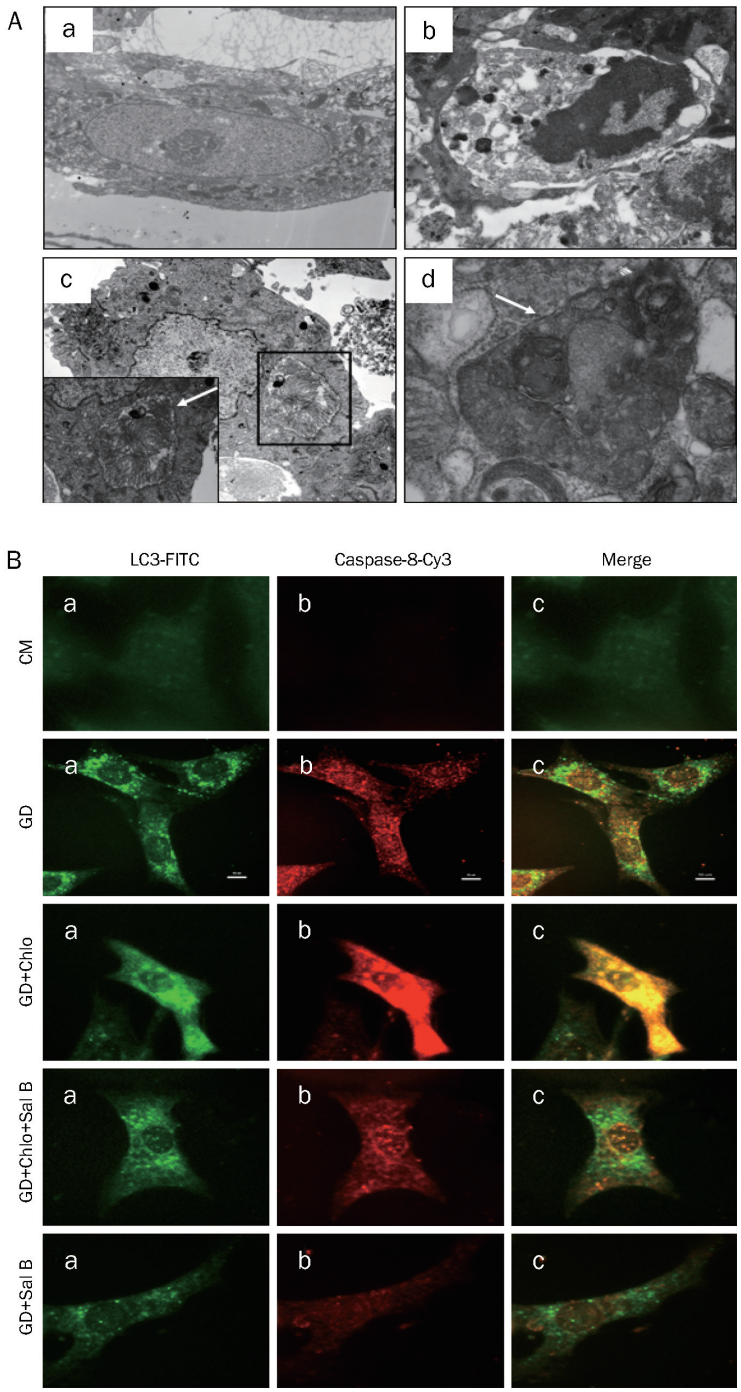

Figure 4. Evidences of autophagy and apoptosis in starving cardiac myocytes. (A) Representative electron micrograph image of autophagy and apoptosis. Cells were cultured in CM or GD for 3 h. (a) Cardiac myocyte under CM (×20000). (b) Apoptosis morphology in myocyte under GD for 3 h (×8000). (c) Autophagosome, dysfunctional mitochondrias are sequestrated in a doubl emembrane-bound vesicle (×4000). (d) Autophagosome, cytoplasmic proteins and dysfunctional mitochondrias are sequestrated in a doublemembrane-bound vesicle (×10000). Autophagosomes are indicated by arrows. (B) Representative images of LC3-Capase-8 dual labeling. Myocytes were cultured in CM or GD for 3 h in presence or absence of chloroquine (Chlo, 3 μmol/L) or Sal B (50 μmol/L) as indicated. The cells were fixed and permeabilized with digitonin, and endogenous LC3 and Caspase-8 were recognized using FITC-conjugated or Cy3-conjugated antibody respectively.

and the intensity of Caspase-8 signal. Starving myocytes treated with Sal B alone or co-treated with chloroquine exhibited fewer LC3 puncta and less intense Capase-8 fluorescence (Figure 4B).

Together, these data indicate that apoptosis occurred in autophagy-induced myocytes. Sal B demonstrated inhibitive effects on autophagy and apoptosis.

Discussion

Whether autophagy plays a protective role or a lethal role in ischemic myocardium remains controversial. Several studies reported a role for autophagy in programmed cell death type II (nonapoptotic death) in heart disease[15, 16] and indicated that excessive autophagy could lead to cell death. Valentim *et al*[17] showed that inhibition of autophagy, by both genetic and pharmacological inhibition of Beclin 1, reduced cell death in cardiomyocytes subjected to simulated ischemia-reperfusion. In line with this evidence, heterozygous Beclin $1^{+/-}$ mice exhibited a reduction in autophagy and apoptosis and reduced infarct size in the heart after ischemia-reperfusion injury[18]. Matsui *et al*[18] found that autophagy might be protective during ischemia, but might play a detrimental role during reper-

fusion. Taken together, these studies suggest that autophagy is typically stimulated by nutrient starvation and has dual roles in the heart. The conditions under which autophagy provides protection or induces cell death depend on the intensity of insult and duration of autophagy[19].

In our study, we used nutrient starvation in cultured cardiac myocytes to mimic myocardium ischemia *in vitro*. In this model, we first studied autophagy intensity over four timepoints. According to immunoblot analysis, the amount of LC3-II was markedly increased in a time-dependent manner.

Increased levels of LC3-II alone do not constitute conclusive evidence of autophagy without considering lysosomal turnover of LC3-II. An increase in the amount of endogenous LC3-II could be due either to active autophagy or to frustrated autophagy. In the setting of frustrated autophagy, autophagosomes form and engulf targets but cannot fuse with lysosomes and clear their contents. This may elicit an acute and significant inflammatory response, or it may induce self-digestion and cell death[8].

In order to distinguish active autophagy and frustrated autophagy from each other, we assayed autophagic flux using lysosomal inhibitors. Flux reflects the dynamic process of autophagosome formation, engulfment, and lysosomal fusion. Chloroquine, a lysosomal inhibitor, is used to verify that increased numbers of autophagosomes reflect increased flux[20]. Comparing the number of autophagosomes in the presence and absence of chloroquine enables one to distinguish between increased autophagosome formation and decreased clearance; thus, it can provide a quantitative index of autophagic flux. In our time-course experiment, the amount of LC3-II increased in a time-dependent manner during autophagy. Administration of chloroquine to starving cardiac myocytes further enhanced the accumulation of LC3-II, indicating high autophagic flux in cells under starvation without chloroquine, in which autophagy was successfully induced and the LC3-II was rapidly degraded by lysosomal hydrolases.

To investigate whether the accumulation of LC3-II is beneficial or harmful to starving cells, cell viability was measured. We found that cells subjected to starvation for 1 or 2 h could maintain relatively high viability; however, when the insult of starving lasted 3 h, cell viability dramatically decreased, indicating that autophagy had surpassed its capacity to protect cardiac myocytes against starvation stress.

Next we examined the effect of Sal B on autophagy under starvation conditions lasting 3 h. The amount of LC3-II in starving myocytes increased, reflecting the activation of autophagy. The coadministration of chloroquine provided us with additional information about high autophagic flux in cells. Sal B decreased the amount of LC3-II in starving myocytes in the presence or absence of chloroquine, which could be interpreted to mean that Sal B inhibited the early stage of autophagy and blocked autophagic flux because Sal B inhibited the formation of autophagosomes. If this were the case, the accumulation of LC3 would not have occurred, even in the presence of chloroquine.

Starving cells presented many distinct puncta of LC3 fluorescence, which increased in abundance in the presence of chloroquine. After Sal B treatment, starving cells exhibited a diminished pattern of LC3 fluorescence. These results, consistent with our immunoblot results, suggest that Sal B may have suppressive effects on autophagy. Thereafter, we investigated the protective role of Sal B on starving cells. We showed that Sal B improved the cell viability and ATP content of starving cells in the presence or absence of chloroquine.

As previously reported, there is crosstalk between autophagic and apoptotic pathways[14]. The interplay between autophagic and apoptotic pathways is emerging as a crucial decision-making process in determining the initiation of programmed cell death[14]. Therefore, we attempted to determine whether apoptosis occurs in autophagy-induced cardiac myocytes. First, autophagy and apoptosis features were observed by EM in cardiac myocytes under starvation conditions. Next, we studied the effects of Sal B on cardiac myocytes under starvation conditions. To the best of our knowledge, we are the first to demonstrate the coexistence of autophagy and apoptosis by using immunofluorescent dual labeling. The results of co-labeling with LC3 and Caspase-8 confirm that cells underwent apoptosis during starvation-induced autophagy. Sal B reduced the accumulation of LC3 fluorescence and suppressed the expression of Caspase-8 in starving cells, indicating that Sal B inhibited both autophagy and apoptosis in starving cells.

Thus, our results demonstrate that autophagy overcomes the capacity of cardiac myocytes to maintain homeostasis when subjected to starvation for 3 h, and Sal B protected starving cells by blocking the early stage of autophagic flux and inhibiting autophagy.

As for autophagy and apoptosis observed in starving myocytes, this work was merely a primary study. Future experiments are needed to determine the relationship of autophagy and apoptosis in starvation conditions and the mechanism of Sal B suppressive effects on both autophagy and apoptosis.

Acknowledgements

This work was supported by the Key Project of the National Natural Science Foundation of China (No 30830118); Key Projectof the China Ministry of Science & Technology (No 2009ZX09301-005-2-11 and 2009ZX09303-003).

Author contribution

Xiao HAN, Jian-xun LIU and Xin-zhi LI designed the research and revised the manuscript; Xiao HAN performed the research and analyzed the data.

References

1 Glick D, Barth S, Macleod KF. Autophagy: cellular and molecular mechanisms. J Pathol 2010; 221: 3–12.

2 Bao XH, Naomoto Y, Hao HF, Watanabe N, Sakurama K, Noma K, *et al*. Autophagy: Can it become a potential therapeutic target? Int J Mol Med 2010; 25: 493–503.

3 Matsui Y, Kyoi S, Takagi H, Hsu CP, Hariharan N, Ago T, *et al*. Molecular mechanisms and physiological significance of autophagy during myocardial ischemia and reperfusion. Autophagy 2008; 4:

409–15.
4 Pattingre S, Tassa A, Qu X, Garuti R, Liang XH, Mizushima N, *et al*. Bcl-2 antiapoptotic proteins inhibit Beclin 1-dependent autophagy. Cell 2005; 122: 927–39.
5 Nishida K, Yamaguchi O, Otsu K. Crosstalk between autophagy and apoptosis in heart disease. Circ Res 2008; 103: 343–51.
6 Ohsumi Y. Molecular dissection of autophagy: Two ubiquitin-like systems. Nat Rev Mol Cell Biol 2001; 2: 211–6.
7 Kabeya Y, Mizushima N, Ueno T, Yamamoto A, Kirisako T, Noda T, *et al*. LC3, a mammalian homologue of yeast Apg8p, is localized in autophagosome membranes after processing. EMBO J 2000; 19: 5720–8.
8 Gottlieb RA, Mentzer RM. Autophagy during cardiac stress: joys and frustrations of autophagy. Annu Rev Physiol 2010; 72: 45–59.
9 Wang BH, Fu W, Li Z. Protective mechanism of Salviol acid B against acute myocardial ischemia/reperfusion injury in rats. J Tianjin Univ Tradit Chin Med 2004; 23: 132–3.
10 Zhang L, Yuan DP, Xu L, Jiang BP, Fang TH. Protective mechanism of Salvianolic acid B on myocardial ischemia-reperfusion injury of rats. Tradit Chin Drug Res Clin Pharmacol 2008; 19: 467–9.
11 Jin SM, Zhao GF, Fan YC. Effect of salvianolic acid B on endothel in release and TXA2-PGI2 system in myocardial ischemia reperfusion injury in rats. Chin J Gerontol 2004; 24: 127–8.
12 Zhao GF, Zhang HX. Protective effects of Salviol acid B against myocardial ischemia/reperfusion injury in rats. J Liaoning Univ Tradit Chin Med 2004; 6: 55–6.
13 Zhao GF, Li ZT, Fan YC. Effect of Salvianolic acid B on free calcium concentration in hypoxia and reoxygenation cardiac muscle cell. Mod J Integr Tradit Chin West Med 2004; 13: 19–20.
14 Kazuhiko N, Osamu Y, Kinya O. Crosstalk between autophagy and apotosis in heart disease. Circ Res 2008; 103: 343–51.
15 Whelan RS, Kaplinskiy V, Kitsis RN. Cell death in the pathogenesis of heart disease: mechanisms and significance. Annu Rev Physiol 2010; 72: 19–44.
16 Dorn GW 2nd. Apoptotic and non-apoptotic programmed cardiomyocyte death in ventricular remodeling. Cardiovasc Res 2009; 81: 465–73.
17 Valentim L, Laurence KM, Townsend PA, Carrol CJ, Soond S, Scarabelli TM, *et al*. Urocortin inhibits Beclin1-mediated autophagic cell death in cardiac myocytes exposed to ischaemia/reperfusion injury. J Mol Cell Cardiol 2006; 40: 846–52.
18 Matsui Y, Takagi H, Qu X, Abdellatif M, Sakoda H, Asano T, *et al*. Distinct roles of autophagy in the heart during ischemia and reperfusion: roles of AMP-activated protein kinase and Beclin 1 in mediating autophagy. Circ Res 2007; 100: 914–22.
19 Kang C, Avery L. To be or not to be, the level of autophagy is the question: dual roles of autophagy in the survival response to starvation. Autophagy 2008; 4: 82–4.
20 Iwai-Kanai E, Yuan H, Huang C, Sayen MR, Perry-Garza CN, Kim L, *et al*. A method to measure cardiac autophagic flux *in vivo*. Autophagy 2008; 4: 322–9.

Acta Pharmacologica Sinica (2011) 32: 45–51
 1671-4083/11 $32.00
www.nature.com/aps

Original Article

Angiopoietin-1 protects myocardial endothelial cell function blunted by angiopoietin-2 and high glucose condition

Qin-hui TUO[1, 2], Guo-zuo XIONG[3], Heng ZENG[1], Hei-di YU[1], Shao-wei SUN[2], Hong-yan LING[2], Bing-yang ZHU[2], Duan-fang LIAO[2, 4, *], Jian-xiong CHEN[1, *]

[1]Department of Pediatrics, Division of Neonatology, Vanderbilt University Medical Center, Nashville, TN 37232, USA; [2]Division of Pharmacoproteomics, School of Life Science and Technology, University of South China, Hengyang 421001, China; [3]Department of General Surgery, the Second Affiliated Hospital in University of South China, Hengyang 421001, China; [4]Department of Traditional Chinese Diagnotics,School of Pharmacy, Hunan University of Chinese Medicine, Changsha 410208, China

Aim: To evaluate the effects of angiopoietin-1 (Ang-1) on myocardial endothelial cell function under high glucose (HG) condition.
Methods: Mouse heart myocardial endothelial cells (MHMECs) were cultured and incubated under HG (25 mmol/L) or normal glucose (NG, 5 mmol/L) conditions for 72 h. MTT was used to determine cellular viability, and TUNEL assay and caspase-3 enzyme linked immunosorbent assays were used to assay endothelial apoptosis induced by serum starvation. Immunoprecipitation and Western blot analysis were used to analyze protein phosphorylation and expression. Endothelial tube formation was used as an *in vitro* assay for angiogenesis.
Results: Exposure of MHMECs to HG resulted in dramatic decreases in phosphorylation of the Tie-2 receptor and its downstream signaling partners, Akt/eNOS, compared to that under NG conditions. Ang-1 (250 ng/mL) increased Tie-2 activation, inhibited cell apoptosis, and promoted angiogenesis. Ang-1-mediated protection of endothelial function was blunted by Ang-2 (25 ng/mL).
Conclusion: Ang-1 activates the Tie-2 pathway and restores hyperglycemia-induced myocardial microvascular endothelial dysfunction. This suggests a protective role of Ang-1 in the ischemic myocardium, particularly in hearts affected by hyperglycemia or diabetes.

Keywords: angiopoietin; Tie-2; myocardial endothelial cells; hyperglycemia; diabetic

Acta Pharmacologica Sinica (2011) 32: 45–51; doi: 10.1038/aps.2010.183; published online 29 Nov 2010

Introduction

Angiopoietin-1 (Ang-1) has been shown to protect the heart against acute myocardial infarction under hyperglycemic conditions[1]. Hyperglycemic exacerbation of ischemic myocardial injury is strongly associated with high glucose-induced endothelial dysfunction[2]. Studies have also shown that Ang-1 has a protective effect on endothelial cells injured by hypoxia[3], arsenite toxicity[4, 5]. However, few published data are available on the effects of Ang-1 on cardiac microvascular endothelium cultured under hyperglycemic conditions.

Our previous study demonstrated that diabetes or hyperglycemia disrupts Ang-1/Tie-2 signaling and attenuates Ang-1-induced angiogenesis in mouse models[1]. Forced overexpression of Ang-1 shifts the ratio of Ang-2 to Ang-1 and conveys protection from ischemic myocardial injury normally exacerbated by hyperglycemia[6, 7]. However, the protective mechanism of Ang-1 in ischemic myocardium under hyperglycemic conditions remains unclear. Here we hypothesize that Ang-1 may restore angiopoietin/Tie-2 balance and protect myocardial endothelial cells under high glucose (HG) conditions. To test our hypothesis, we characterized the activation of the Tie-2 pathway in mouse heart myocardial endothelial cells (MHMECs) under HG conditions. We also examined apoptosis and angiogenic responses to Ang-1 and Ang-2 stimulation. Our data indicate that Ang-1 increases Tie-2 activation and restores MHMEC function in HG conditions. Furthermore, increased Ang-2 attenuates the protective effects of Ang-1 under HG conditions.

* To whom correspondence should be addressed.
E-mail Jian-xiong.chen@vanderbilt.edu (Jian-xiong CHEN);
dfliao66@yahoo.com.cn (Duan-fang LIAO)
Received 2010-05-06 Accepted 2010-09-16

Materials and methods

Materials

Endothelial cell growth medium (EGM-2) and fetal bovine serum (FBS) were purchased from Clonetics Co (MA, USA).

The following primary antibodies were used: anti-phosphotyrosine (Upstate Co, NJ, USA), mouse anti-phospho-eNOS, mouse anti-eNOS (BD Co, CA, USA), rabbit anti-Ang-1 (Santa Cruz, CA, USA), rabbit anti-phospho-AKT, rabbit anti-Akt, mouse anti-cleaved caspase-3, mouse anti-Tie-2, and rabbit anti-β-actin (Cell Signaling, MA, USA). All reagents were of analysis grade.

Culture of MHMECs

Hearts were excised from 4-week-old mice (n=6) under aseptic conditions. Cardiac ventricles were cleaned by sterilized Hank's solution and then cut into pieces. A homogenate of ventricles was suspended and filtered by sequential 200-μm and 60-μm microfiltration. The filtered cells were washed twice with EGM-2, moved to a dish, and cultured in EGM-2 supplemented with 10% FBS, 2 mmol/L glutamine, 50 U penicillin G, and 0.05 mg/mL streptomycin at 37 °C in a humidified 95% air/5% CO_2 incubator. Each of the endothelial lines used in these experiments had a typical cobblestone morphology, showed uptake of acetylated low-density lipoprotein, and exhibited factor VIII-related antigen. Primary cultures of MHMECs between passages 4 and 10 were used in all experiments.

Cell viability assay

MHMECs were cultured with either HG (25 mmol/L) or NG (5 mmol/L) media for 72 h and then transferred to 96-well plates with 1×10^5 cells/mL per well. MHMECs attached to the plates after 6-8 h and were starved in serum-free media for 48 h in the presence or absence of Ang-1 (250 ng/mL, R&D Systems, Inc, CA, USA). After treatment, MHMECs were washed twice with PBS, and MTT (final concentration of 500 mg/mL) was added to each well. MHMECs were incubated at 37 °C for 4 h, and then 100 mL of DMSO was added to dissolve the formed crystals. The absorbance measured at 570 nm was used to calculate the relative cell viability ratio.

Western blot analysis

MHMECs were washed with PBS, and 0.5 mL of TME lysis buffer [10 mmol/L Tris (pH 7.5), 5 mmol/L $MgCl_2$, 1 mmol/L EDTA, and 25 mmol/L NaF] containing fresh 100 μmol/L Na_3VO_4, 20 μg/mL leupeptin, 1 μg/mL pepstatin A, 4 μg/mL aprotinin, and 1 mmol/L DTT was added. Cell lysates were prepared by freezing, thawing on ice, scraping, sonicating for 30 s, and centrifuging for 30 min at 15 000×g. Protein concentration was determined using a bicinchoninic acid (BCA) protein assay kit. For Western blot analysis, 20 μg of protein was subjected to SDS-PAGE under reducing conditions, and proteins were then transferred to a polyvinylidene difluoride membrane as described previously[8]. The membrane was blocked for 2 h with a commercial blocking buffer from Life Technologies, Inc. The blots were incubated for 1 h with primary antibodies (1:1000 dilution), followed by a 1-h incubation with a secondary horseradish peroxidase-conjugated antibody. The presence of target proteins was revealed by a chemiluminescent assay (Amersham-Pharmacia Biotech).

Immunoprecipitation for Tie-2 phosphorylation

Each sample consisting of 1000 μg protein was incubated with 10 μL anti-Tie-2 antibody for 6-8 h at 4 °C, followed by the addition of 20 μL of protein G-Sepharose. The samples were then incubated overnight at 4 °C and centrifuged for 5 min at 1000×g at 4 °C. Protein-antibody complexes were washed once with buffer solution [10 mmol/L Tris (pH 7.4), 0.25 mmol/L EDTA, and 0.1% SDS], suspended in 30 μL loading buffer, heated for 5 min at 90-100 °C, and then centrifuged for 10 min at 12 000×g at 4 °C. The supernatant was subjected to immunoblot analysis. Tie-2 phosphorylation was revealed with an anti-phosphotyrosine antibody (1:1000).

Caspase-3 enzyme linked immunosorbent assay (ELISA)

MHMECs were cultured in either HG media or NG media for 72 h and then starved for 48 h to induce endothelial apoptosis in the presence or absence of Ang-1 or Ang-2 (R&D systems, Inc, CA, USA). Cell culture supernatants were collected and analyzed using commercial caspase-3 enzyme-linked immunosorbent assay kits (Sigma, MO, USA). The optical density of the wells was determined by spectrophotometry at a wavelength of 450 nm.

TUNEL assay

MHMECs were cultured with either HG or NG media for 72 h and then transferred to two-well chamber slides with a cell density of 2×10^5 cells/mL per well. MHMECs were attached to the slides after 6-8 h and were cultured in serum-free media for 48 h in the presence or absence of Ang-1 or Ang-2. Slides were fixed with 10% formaldehyde for 30 min. Cells were then submitted to terminal deoxynucleotidyltransferase-mediated dUTP nick end labeling (TUNEL) according to the manufacturer's instructions (Promega, CA, USA). The apoptotic cells were stained green. Nuclei were counterstained with DAPI in blue. Apoptosis was quantified by counting TUNEL-positive cells per 100 DAPI cells[9].

Endothelial tubular formation assay

MHMECs were plated on 48-well (1×10^5 cells/well) chamber slides (BD Falcon). After 6–8 h, the cells were washed with appropriate serum-free media and overlaid with matrigel (Sigma, St Louis, MO, USA) diluted 1:1 in EGM-2 media supplemented with 10% FBS. After a 30-min gel formation at 37 °C in the incubator, the gels were overlaid with 0.5 mL of culture media. The culture medium was supplemented with Ang-1 or Ang-2 in either HG or NG media. The cells were incubated for 24 h at 37 °C for full development of capillary-like network structures. The gels were photographed using a phase-contrast microscope. Endothelial tube formation was quantified by counting the number and cumulative length of tubular structures in six fields of each well with image acquisition and analysis software (Image Pro-express software, CA, USA). Each assay was performed in duplicate.

Adenovirus transfection

Ad-Ang-1 encodes mouse Ang-1. Adenoviruses (Adenovirus

Co, CA, USA) were amplified using a human embryonic kidney cell line (HEK 293) as a host. The titers of the lysates were 1×10^9 pfu/mL for Ad-Ang-1 and Ad-β-gal (adenovirus-β-galactosidase). MHMECs were transfected with 20 pfu/cell of Ad-Ang-1 or Ad-β-gal in serum-free medium for 24 h. Then the infection medium was removed, and cells were incubated with HG or NG media for 72 h.

Statistical analysis

The values are expressed as the mean±SE. Statistical analysis of the data was performed using Student's *t*-tests and ANOVA where appropriate. Values of $P<0.05$ were considered statistically significant.

Results

Ang-1-induced activation of Tie-2 is impaired by high glucose

We used immunoprecipitation to assay the activation of Tie-2. A Tie-2 antibody was used to precipitate the protein, and a phospho-tyrosine antibody was used to blot and assay the activation of Tie-2 because phosphorylated Tie-2 antibodies were unavailable. Exposure of MHMECs to HG for 72 h dramatically decreased the activation of Tie-2 receptors compared that under NG conditions (Figure 1A). Furthermore, HG significantly inhibited Akt/eNOS phosphorylation (Figure 1B), the major downstream event of the Ang-1/Tie-2 signaling pathway. Previously, we showed that Ang-1 activates Ang-1/Tie-2/Akt signaling, which is blunted by hyperglycemia in diabetic mouse models[1]. After MHMECs were incubated under HG or NG conditions for 72 h, we treated MHMECs with 250 ng/mL Ang-1 for 15 min. Consistent with our previous findings[6], our data show that Ang-1 significantly increased Tie-2 phosphorylation under both NG and HG conditions. Furthermore, our present study reveals that Ang-1-induced Tie-2 phosphorylation is attenuated in HG conditions compared to NG conditions (Figure 1C).

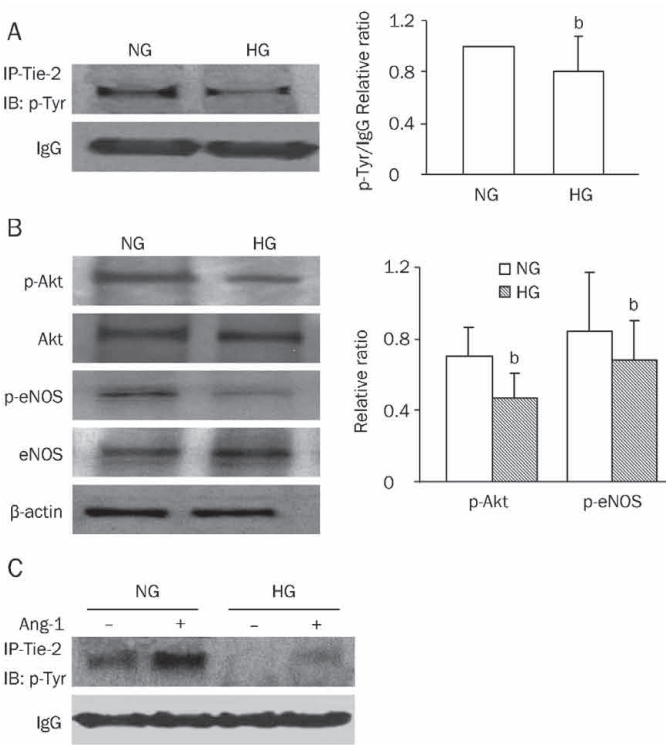

Figure 1. Changes in Tie-2/Akt/eNOS signaling pathways under HG conditions. (A) Tie-2 phosphorylation was decreased under HG conditions in MHMECs (n=3). (B) HG inhibited phosphorylation of Akt and eNOS in MHMECs compared with NG groups (n=5). (C) Ang-1 increased Tie-2 phosphorylation in MHMECs, which was dampened under HG conditions (n=3). $^bP<0.05$ compared with NG groups.

Ang-1 attenuated HG-induced endothelial cell dysfunction in MHMECs

After MHMECs were incubated under either HG or LG conditions for 72 h, we treated the MHMECs with serum-free media in the presence or absence of 250 ng/mL Ang-1 for 48 h. We then examined the effects of Ang-1 on apoptosis of MHMECs using MTT, caspase-3, and TUNEL assays. Our MTT results show that Ang-1 increased cellular viability from 88.56%±3.90% to 112.43%±9.28% under HG conditions (Figure 2A). This was accompanied by a significant suppression of caspase-3 activation under HG conditions (Figure 2B). Serum starvation-induced apoptosis was revealed by green staining in the TUNEL assay and was observed in a significantly higher proportion of non-Ang-1-treated cells ($P<0.01$) compared to cells treated with Ang-1 (14.03%±3.44% *vs* 6.25%±0.48%, respectively, $P<0.05$) under HG conditions (Figure 2C).

Angiogenesis is another important function of endothelial cells[10]. Our data clearly show that Ang-1 significantly promoted myocardial endothelial tubular formation that was significantly impaired by HG conditions (Figure 3).

Ang-2 exacerbated MHMEC dysfunction induced by HG

Ang-2, which is increased in diabetic patients, is a natural antagonist of Ang-1. However, few published data are available on the effects of Ang-2 on endothelial cells under HG conditions. After MHMECs were incubated under HG or NG conditions for 72 h, we treated the MHMECs continuously with serum-free media in the presence or absence of Ang-2 (25 ng/mL) for 48 h. We observed that increased Ang-2 exacerbated the endothelial apoptosis induced by HG (Figure 4). When we used Ang-2 siRNA to knock down Ang-2 protein expression, MHMEC apoptosis was decreased significantly under HG conditions (Figure 5).

Ang-1-mediated protection of MHMEC function is impaired by Ang-2 under HG conditions

MHMECs were incubated in HG media for 72 h and then sequentially supplemented with both Ang-2 (25 ng/mL) and Ang-1 (250 ng/mL) or Ang-1 alone[6]. MHMEC apoptosis and tubular formation were analyzed by the methods listed above. Exposure of MHMECs to Ang-2 led to increased activation of caspase-3 and an increased apoptotic ratio in HG conditions, whereas Ang-1 suppressed these effects (Figure 6A, 6B). Intriguingly, increased Ang-2 significantly delayed Ang-1-induced tubular formation in MHMECs under HG conditions

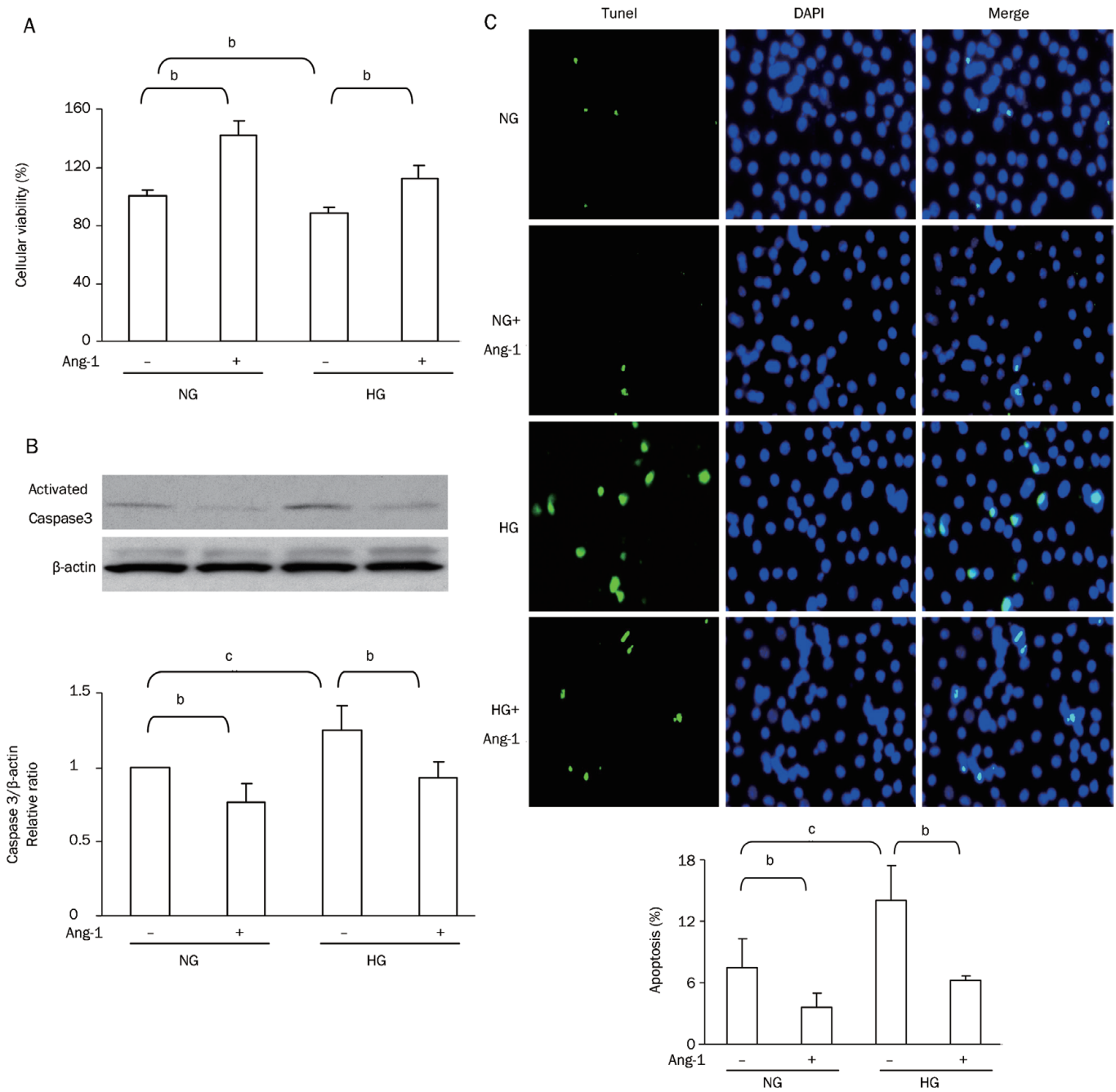

Figure 2. Ang-1 inhibited myocardial endothelial apoptosis induced by HG. (A) Ang-1 increased cellular viability under HG conditions, as observed by MTT assays. (B) Representative Western blot and densitometry analysis of caspase-3 activation. (C) Representative images of a TUNEL assay showing that Ang-1 significantly decreased MHMEC apoptosis induced by HG (n=3, 400× magnification). $^{b}P<0.05$, $^{c}P<0.01$.

(Figure 6C).

MHMECs do not express detectable Ang-1[1] and were thus transfected with Ad-Ang-1 to over-express Ang-1 (Figure 7A). The transfected MHMECs were incubated with HG or NG media for 72 h and then treated with serum-free media for 48 h in the presence or absence of Ang-2. The activation of caspase-3 in all Ad-Ang-1 groups was lower than that of Ad-β-gal groups in both HG and LG conditions. However, Ang-2 increased the activation of caspase-3 (Figure 7B).

Discussion

The risk of morbidity and mortality associated with cardiovascular disease is significantly increased in patients who are diabetic compared to patients who are non-diabetic[11]. This increase in risk may be related to vascular endothelial cell dysfunction that occurs under diabetic and hyperglycemic

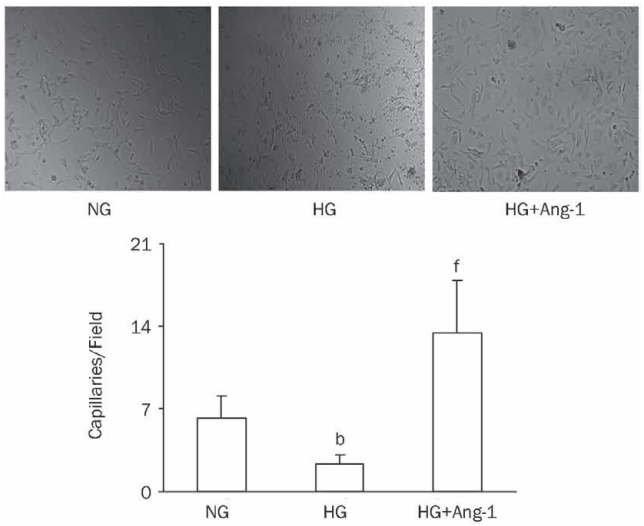

Figure 3. Representative images and quantitative analysis of tubular formation induced by Ang-1 under HG conditions (n=3, 100× magnification). [b]P<0.05 compared with NG groups. [f]P<0.01 compared with HG groups.

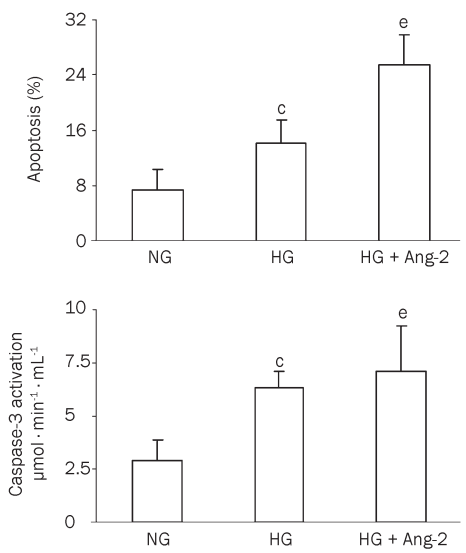

Figure 4. Ang-2 exacerbated myocardial endothelial apoptosis under HG conditions. (A) Quantification of the relative apoptosis of MHMECs determined by TUNEL staining (400× magnification). (B) Caspase-3 activation assayed by ELISA (n=3). [c]P<0.01 compared with NG groups; [e]P<0.05 compared with HG groups.

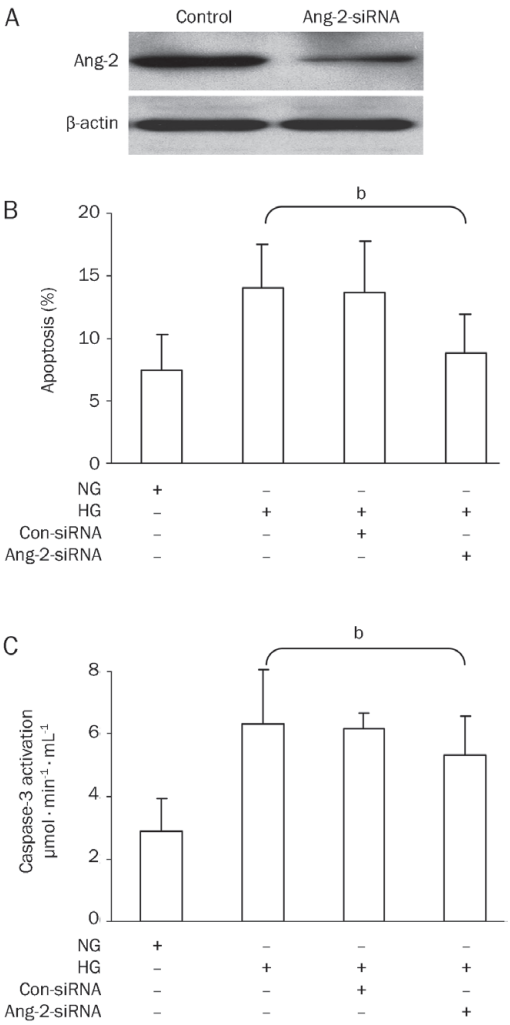

Figure 5. RNA interference of Ang-2 inhibited endothelial cell apoptosis induced by HG. (A) Western blot analysis shows that the expression of Ang-2 was significantly inhibited by RNA interference in endothelial cells 24 h after the transfer of Ang-2 siRNA. (B) Quantification of endothelial apoptosis by TUNEL staining. (C) Caspase-3 activation was assayed by ELISA (n=3). [b]P<0.05.

conditions. The angiopoietin system plays a critical role in maintaining vascular integrity and endothelial function in diabetic patients[12, 13]. Angiopoietins comprised of the ligands Ang-1/-2/-3/-4 represent a new family of angiogenic factors. Ang-1 and Ang-2 are the two key ligands for the Tie-2 receptor[14]. Tie-2 is a receptor tyrosine kinase that is expressed in the vascular endothelium. Ang-1 binds to the Tie-2 receptor and induces Tie-2 phosphorylation, thus promoting endothelial cell survival and angiogenesis by activating the PI3 kinase-Akt-eNOS pathway[15]. Therefore, we examined the Tie-2 signaling pathway under HG conditions. Our immunoprecipitation and Western blot data show that exposure of MHMECs to HG resulted in a dramatic decrease in phosphorylation of the Tie-2/Akt/eNOS signaling pathway compared to MHMECs exposed to NG conditions.

Because Ang-1-mediated protection of endothelial cells involves the Ang-1/Tie-2/Akt pathways[15–17], we observed the effects of Ang-1 on MHMECs under HG conditions. Our data show that Ang-1 significantly increased Tie-2 phosphorylation, which was inhibited by HG, and suppressed serum starvation-induced caspase-3 activation and endothelial cell apoptosis under HG conditions. Our data suggest that Ang-1 inhibits microvascular endothelial apoptosis, which may be responsible for the protection of Ang-1 in the ischemic heart, particularly in a hyperglycemic environment.

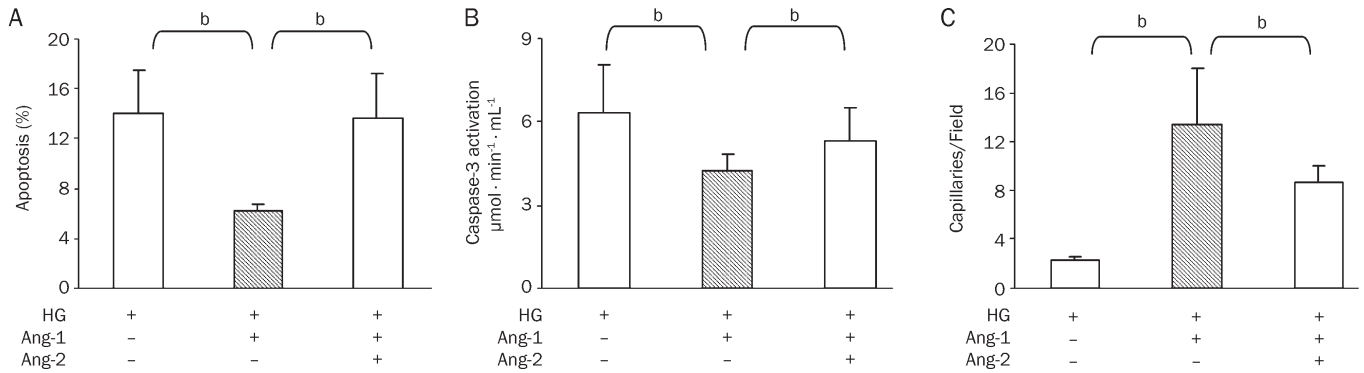

Figure 6. Ang-1 protected the function of MHMECs impaired by Ang-2 under HG conditions. (A) Quantification of endothelial apoptosis by TUNEL staining. (B) Caspase-3 activation was assayed by ELISA. (C) Ang-1-induced tubular formation was blunted in the presence of Ang-2 under HG conditions (n=3). ^{b}P<0.05.

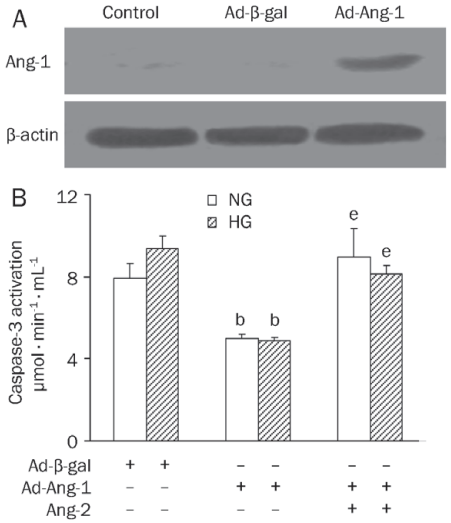

Figure 7. Ang-2 increased the activation of caspase-3 inhibited by Ang-1 in MHMECs. (A) Western blot analysis shows that the expression of Ang-1 was significantly increased in endothelial cells transfected with Ad-Ang-1 after 24 h. Control: untransfected cells; Ad-β-gal: cells were transfected with control adenovirus vector; Ad-Ang-1: cells were transfected with an adenovirus vector encoding mouse Ang-1. (B) Ang-2 increased caspase-3 activation, as assayed by ELISA (n=3). ^{b}P<0.05 compared with the Ad-β-gal groups; ^{e}P<0.05 compared with the Ad-Ang-1 groups.

Angiogenesis is an important function of the cardiac microvascular endothelium, which is impaired in diabetes[10]. Capillary tube formation, which depends on endothelial migration and proliferation[18, 19], is the primary mechanism of angiogenesis. In the present study, we also investigated the effect of Ang-1 on angiogenesis in the cardiac microvascular endothelium with tubular formation *in vitro*. Our data reveal that Ang-1 promoted myocardial endothelial tubular formation that was dampened by hyperglycemia. These data further suggest that Ang-1 can increase angiogenesis, benefiting ischemic hearts, particularly those in a hyperglycemic environment.

Ang-2 has been identified as a natural antagonist of Ang-1, inhibiting Ang-1-mediated Tie-2 phosphorylation in the presence of Ang-1[1, 6, 20, 21]. Our previous studies have shown that exposure of MHMECs to HG led to a significant increase in Ang-2 expression and a decrease in Tie-2 expression compared to NG conditions[6]. However, the functional roles of Ang-2 on myocardial endothelial cells under HG conditions were not explored. In the present study, we found that increased Ang-2 strikingly exacerbated myocardial endothelial apoptosis and delayed tubular structure formation of MHMECs under HG conditions. The endothelial protection mediated by Ang-1 was diminished in the presence of increased Ang-2 under HG conditions, which is consistent with our *in vivo* data[1, 6]. Additionally, our data suggest that Ang-1 shifts the ratio of Ang-2 to Ang-1 and protects myocardial endothelial cells under hyperglycemic conditions.

In the present study, we have demonstrated that Ang-1 can inhibit microvascular endothelial apoptosis and increase angiogenesis under HG conditions, possibly playing a role in protecting ischemic hearts in hyperglycemic or diabetic individuals.

Acknowledgements

This work was supported by grants from the American Heart Association (0565196B) and the NIH (DK074995 and R01HL102042), the National Natural Science Foundation of China (No 30971170, 30770868, 30971267, and 30600249), and the Outstanding Youth Foundation of Education Department in Hunan Province (09B089).

Author contribution

Jian-xiong CHEN and Duan-fang LIAO designed the studies; Qin-hui TUO conducted the experiments and wrote the paper. Drs Guo-zuo XIONG, Heng ZENG, and Hei-di YU performed MHMEC isolation, cell culture, and immunoprecipitation; Hong-yan LING, Bing-yang ZHU, and Shao-wei SUN assisted with data analysis.

References

1 Tuo QH, Zeng H, Stinnett A, Yu H, Aschner JL, Liao DF, *et al*. Critical role of angiopoietins/Tie-2 in hyperglycemic exacerbation of myocardial infarction and impaired angiogenesis. Am J Physiol Heart Circ Physiol 2007; 292: H1664–74.

2 Farhangkhoee H, Khan ZA, Kaur H, Xin X, Chen S, Chakrabarti S. Vascular endothelial dysfunction in diabetic cardiomyopathy: pathogenesis and potential treatment targets. Pharmacol Ther 2006; 111: 384–99.

3 Wang YL, Hui YN, Guo B, Ma JX. Strengthening tight junctions of retinal microvascular endothelial cells by pericytes under normoxia and hypoxia involving angiopoietin-1 signal way. Eye (Lond) 2007; 21: 1501–10.

4 Kugathasan L, Ray JB, Deng Y, Rezaei E, Dumont DJ, Stewart DJ. The angiopietin-1-Tie2 pathway prevents rather than promotes pulmonary arterial hypertension in transgenic mice. J Exp Med 2009; 206: 2221–34.

5 Park JS, Seo J, Kim YO, Lee HS, Jo I. Coordinated regulation of angiopoietin-1 and vascular endothelial growth factor by arsenite in human brain microvascular pericytes: implications of arsenite-induced vascular dysfunction. Toxicology 2009; 264: 26–31.

6 Chen JX, Stinnett A. Disruption of Ang-1/Tie-2 signaling contributes to the impaired myocardial vascular maturation and angiogenesis in type II diabetic mice. Arterioscler Thromb Vasc Biol 2008; 28: 1606–13.

7 Tuo QH, Liao DF. The ratio of Ang-1/Ang-2 in vessel diseases. Chin J Arterioscler 2009; 17: 414–6.

8 QH Tuo, C Wang, FX Yan, DF Liao. MAPK pathway mediates the protective effects of onychin on oxidative stress-induced apoptosis in ECV304 endothelial cells. Life Sci 2004; 76: 487–97.

9 Tuo QH, Liang L, Zhu BY, Cao X, Liao DF. The effect of Daxx on the cholesterol accumulation in hepatic cells. World J Gastroenterol 2008; 14: 435–40.

10 Lovren F, Pan Y, Shukla PC, Quan A, Teoh H, Szmitko PE, *et al*. Visfatin activates eNOS via Akt and MAP kinases and improves endothelial cell function and angiogenesis *in vitro* and *in vivo*: translational implications for atherosclerosis. Am J Physiol Endocrinol Metab 2009; 296: E1440–9.

11 Coutinho M, Gerstein HC, Wang Y, Yusuf S. The relationship between glucose and incident cardiovascular events. A metaregression analysis of published data from 20 studies of 95,783 individuals followed for 12.4 years. Diabetes Care 1999; 22: 233–40.

12 Singh H, Brindle NP, Zammit VA. High glucose and elevated fatty acids suppress signaling by the endothelium protective ligand angiopoietin-1. Microvasc Res 2010; 79: 121–7.

13 Minhas N, Xue M, Fukudome K, Jackson CJ. Activated protein C utilizes the angiopoietin/Tie2 axis to promote endothelial barrier function. FASEB J 2010; 24: 873–81.

14 Gomei Y, Nakamura Y, Yoshihara H, Hosokawa K, Iwasaki H, Suda T, *et al*. Functional differences between two Tie2 ligands, angiopoietin-1 and -2, in regulation of adult bone marrow hematopoietic stem cells. Exp Hematol 2010; 38: 82–9.

15 Fujikawa K, de Aos Scherpenseel I, Jain SK, Presman E, Christensen RA, Varticovski L. Role of PI 3-kinase in angiopoietin-1-mediated migration and attachment-dependent survival of endothelial cells. Exp Cell Res 1999; 253: 663–72.

16 Huang J, Bae JO, Tsai JP, Kadenhe-Chiweshe A, Papa J, Lee A, *et al*. Angiopoietin-1/Tie-2 activation contributes to vascular survival and tumor growth during VEGF blockade. Int J Oncol 2009; 34: 79–87.

17 Chen JX, Lawrence ML, Cunningham G, Christman BW, Meyrick B. HSP90 and Akt modulate Ang-1-induced angiogenesis via NO in coronary artery endothelium. J Appl Physiol 2004; 96: 612–20.

18 Risau W. Mechanisms of angiogenesis. Nature 1997; 386: 671–4.

19 Kern J, Bauer M, Rychli K, Wojta J, Ritsch A, Gastl G, *et al*. Alternative splicing of vasohibin-1 generates an inhibitor of endothelial cell proliferation, migration, and capillary tube formation. Arterioscler Thromb Vasc Biol 2008; 28: 478–84.

20 Maisonpierre PC, Suri C, Jones PF, Bartunkova S, Wiegand SJ, Radziejewski C, *et al*. Angiopoietin-2, a natural antagonist for Tie2 that disrupts *in vivo* angiogenesis. Science 1997; 277: 55–60.

21 Yang M, Zhang M, Chen J, Mukherjee R, Zhang L, Lin S, *et al*. Angiopoietin-1 inhibits mouse glomerular endothelial cell senescence via Tie2 receptor-modulated ERK1/2 signaling. Am J Nephrol 2010; 31: 490–500.

Acta Pharmacologica Sinica (2011) 32: 52–61
 1671-4083/11 $32.00
www.nature.com/aps

Original Article

Ouabain facilitates cardiac differentiation of mouse embryonic stem cells through ERK1/2 pathway

Yee-ki LEE[1, #], Kwong-man NG[1, #], Wing-hon LAI[1], Cornelia MAN[3], Deborah K LIEU[2], Chu-pak LAU[1], Hung-fat TSE[1, *], Chung-wah SIU[1, *]

[1]Cardiology Division, Department of Medicine, Queen Mary Hospital, the University of Hong Kong and Research Center of Heart, Brain, Hormone and Healthy Aging, Li Ka Shing Faculty of Medicine, the University of Hong Kong, Hong Kong, China; [2]Division of Cardiovascular Medicine, Department of Internal Medicine, University of California, Davis, CA, USA; [3]Department of Applied Biology and Chemical Technology, the Hong Kong Polytechnic University, Hong Kong, China

Aim: To investigate the effects of the cardiotonic steroid, ouabain, on cardiac differentiation of murine embryonic stem cells (mESCs).
Methods: Cardiac differentiation of murine ESCs was enhanced by standard hanging drop method in the presence of ouabain (20 μmol/L) for 7 d. The dissociated ES derived cardiomyocytes were examined by flow cytometry, RT-PCR and confocal calcium imaging.
Results: Compared with control, mESCs treated with ouabain (20 μmol/L) yielded a significantly higher percentage of cardiomyocytes, and significantly increased expression of a panel of cardiac markers including Nkx 2.5, α-MHC, and β-MHC. The α1 and 2- isoforms Na^+/K^+-ATPase, on which ouabain acted, were also increased in mESCs during differentiation. Among the three MAPKs involved in the cardiac hypertrophy pathway, ouabain enhanced ERK1/2 activation. Blockage of the Erk1/2 pathway by U0126 (10 μmol/L) inhibited cardiac differentiation while ouabain (20 μmol/L) rescued the effect. Interestingly, the expression of calcium handling proteins, including ryanodine receptor (RyR2) and sacroplasmic recticulum Ca^{2+} ATPase (SERCA2a) was also upregulated in ouabain-treated mESCs. ESC-derived cardiomyocyes (CM) treated with ouabain appeared to have more mature calcium handling. As demonstrated by confocal Ca^{2+} imaging, cardiomyocytes isolated from ouabain-treated mESCs exhibited higher maximum upstroke velocity ($P<0.01$) and maximum decay velocity ($P<0.05$), as well as a higher amplitude of caffeine induced Ca^{2+} transient ($P<0.05$), suggesting more mature sarcoplasmic reticulum (SR).
Conclusion: Ouabain induces cardiac differentiation and maturation of mESC-derived cardiomyocytes via activation of Erk1/2 and more mature SR for calcium handling.

Keywords: ouabain; embryonic stem cells; cardiac differentiation

Acta Pharmacologica Sinica (2011) 32: 52–61; doi: 10.1038/aps.2010.188; published online 13 Dec 2010

Introduction

Embryonic stem cells (ESCs) have the ability to self-renew and differentiate into virtually all cell types of the three embryonic germ layers including cardiomyocytes. They thus represent an unlimited *ex vivo* cell source for cardiac regenerative therapy[1–4] as well as an ideal *in vitro* model to investigate complex developmental processes. Spontaneous differentiation of ESCs towards cardiac lineage is generally poor[1, 5, 6]. To date, protocols have exploited transcription factors involved in embryonic heart development to direct ESC differentiation into cardiomyocytes[5–8]. In contrast, transcription pathways crucially involved in post-natal hypertrophic growth of cardiomyocytes have not been investigated to improve the efficacy of cardiac differentiation of ESCs.

The cardiotonic glycoside ouabain is a specific inhibitor of the ubiquitous Na^+/K^+-ATPase that is responsible for the active transport of Na^+ and K^+ across the plasma membrane of most animal cells. In adult cardiomyocytes, Na^+/K^+-ATPase inhibition results in a modest increase in intracellular Na^+, sufficient to affect the sarcolemmal Na^+/Ca^{2+} exchange and cardiac contractility[9–11]. Alterations in concentrations of endogenous cardiotonic glycosides have been reported in various human conditions such as essential hypertension[12], asymptomatic left ventricular dysfunction[13] and dilated cardiomyopathy[14]. In experimental models, cardiotonic glycoside has cardioprotective effects against ischemia not associated

# The two authors contributed equally to this work.
* To whom correspondence should be addressed.
E-mail cwdsiu@hkucc.hku.hk (Chung-wah SIU);
hftse@hkucc.hku.hk (Hung-fat TSE)
Received 2010-06-09 Accepted 2010-09-24

with Na^+/K^+-ATPase inhibition[15, 16]. They also cause transcriptional regulation of several cardiac-growth related genes resulting in hypertrophy of adult cardiomyocytes[17]. Extensive subsequent studies of various cell types have revealed that binding of cardiotonic glycosides to Na^+/K^+-ATPase in fact activates multiple pathways including cytoplasmic tyrosine kinase Src/epidermal growth factor receptor (EGFR)[18], phosphatidylinositol 3-kinase (PI3K)-Akt[19], phospholipase C kinase, and increased mitochondrial production of reactive oxygen species[20]. The downstream signaling pathway nonetheless appears to be cell-type specific. A previous report demonstrated the functional expression of Na^+/K^+-ATPase in undifferentiated ESCs as well as ESC-derived cardiomyocytes[5] although the effect of ouabain on cardiac differentiation and maturation of ESCs remains unclear. The aims of the present study were thus to determine whether ouabain, the prototypic Na^+/K^+-ATPase inhibitor and potent hypertrophic stimulus of adult cardiomyocytes, affects cardiac differentiation and maturity of ESCs. In order to validate the cardiac differentiation of ESCs, we quantified the number of troponin-positive cells using flow cytometry and the expression of a panel of cardiac specific markers in differentiated ESCs. We also studied the effects of ouabain on the extracellular signal-regulated kinase (ERK), c-Jun NH_2-terminal protein kinase (JNK), and p38 mitogen activated protein kinase (MAPK) during cardiac differentiation of ESCs. Treatment with a specific MAPK inhibitor would be useful to investigate the specific role of MAPK in cardiac differention. In addition, the maturity of calcium handling properties of differentiated ESCs was assessed using confocal calcium imaging.

Materials and methods

Murine embryonic stem cell culture and *in vitro* cardiac differentiation

Murine (m) ES cell-line D3 (CRL-1934, American Type Culture Collection, Manassas, VA) was used and cultured as previously described[21]. Briefly, undifferentiated mESCs were cultured on an irradiation-inactivated monolayer of mouse embryonic fibroblast feeders in Dulbecco's modified Eagle's minimal essential medium (DMEM, Gibco BRL, Karlsruhe, Germany), supplemented with 15% fetal bovine serum (FBS, Gibco BRL, Karlsruhe, Germany), 0.1 mmol/L mercaptoethanol (Sigma-Aldrich, St Louis, MO), non-essential amino acids (stock solution diluted 1:100; Hyclone, Logan, UT) and 1000 U/mL of recombinant mouse leukemia inhibitory factor (LIF) (Chemicon, Hofheim, Germany). To induce cardiac differentiation, embryoid bodies (EBs) were generated from hanging drops of approximately 800 mESCs in 20 μl of culture medium in the absence of leukemia inhibitory factor and feeder cells for two days and then grown in suspension or five more days[21].

Effect of cardiotonic glycoside, ouabain, on cardiac differentiation

Embryoid bodies were plated on gelatin-coated plate following five day suspension and cultured with 20 μmol/L ouabain dissolved in phosphate-buffered saline (PBS) at a stock concentration of 10 mmol/L (Sigma-Aldrich, St Louis, MO) for a further seven days. No drug or vehicle was added in the control group. When counting the number of beating EBs, number of day refers to time from plating of EBs onto gelation-coated plates. For Erk1/2 inhibitory experiments, EBs were treated with U0126 in combination with ouabain for 7 days before FACS counting of cardiomycytes. Some EBs pretreated with 20 μmol/L ouabain for 7 days were further incubated with 10 μmol/L U0126 (Cell-Signaling Technology, Danvers, MA) (dissolved in DMSO) in serum-free condition for 2 h prior to harvest for Western blotting. All experiments were performed using EBs generated from different passages of <10. Medium with corresponding drug was refreshed every 2 to 3 days.

Cell viability

Cell viability was assessed using the 3-(4,5-dimethylthiazol-2-y)-2,5–diphenyl-tetrazolium bromide (MTT) staining method described by Mosmann T and Hansen in a 96-well microtiter plate[22]. This method is based on the ability of viable, but not dead cells, to convert MTT to a blue colored formazan. Stock MTT solution (5 mg/mL) was prepared in PBS. Ten EBs were plated onto each 96-well coated plate with 0.1% gelatin following 5-day suspension and differentiation medium served as control. At the end of incubation, 20 μL of MTT solution was added to each well containing 180 μL medium with various concentrations of ouabain. Following 4 h incubation at 37 °C, dark crystals formed and the reaction was stopped by adding 100 μL of DMSO. The optical density (OD) of each well was read on a Bio-Rad 550 Microplate Reader (Bio-Rad Laboratories, Hercules, CA) at 570 nm. The viability values obtained in the presence of various dosages of ouabain were subsequently normalized against control values.

Isolation of beating mESC-derived cardiomyocytes

The beating outgrowths were microsurgically dissected with a glass knife from D3 mESC-derived 7-day differentiated EBs, and incubated in collagenase B (1 mg/mL) with DNase I (60 U/mL, Roche Applied Sciences Penzberg, Germany) at 37 °C for 30 min with occasional dispersion by pipetting up and down. Isolated cells were recovered in Kraftbrühe (KB) solution containing (mmol/L) 85 KCl, 30 K_2HPO_4, 5 $MgSO_4$, 1 EGTA, 2 Na_2-ATP, 5 pyruvic acid, 5 creatine, 20 taurine, and 20 *D*-glucose at room temperature for 1 h. The cells were subsequently plated on 0.1% gelatin coated glass cover slips in 24-well culture plates with corresponding differentiation medium. Calcium imaging of isolated cells or cell clusters was performed within 2 days; some of the cells were fixed in 4% paraformaldehyde for immunocytological staining at 4 °C.

Immunocytological staining

The 7-day differentiated EBs were microdissected and fixed with 2% paraformaldehyde for 20 min at 4 °C, followed by washing with wash buffer [DPBS with 0.1% Triton X-100 (Sigma-Aldrich, St Louis, MO)] once for 5 min. Cells were incubated overnight at 4 °C with anti-troponin-T (1:100, Lab

Vision, Fremont, CA) primary antibodies, then rinsed three times for five minutes with wash buffer. Further incubation for one hour at room temperature was performed with secondary antibodies, goat anti-mouse FITC antibodies (1:100, Molecular Probes), diluted in wash buffer. The cells were rinsed three times, counterstained and mounted with SlowFade® Gold antifade reagent with DAPI (Invitrogen, Life Technologies, Carlsbad, CA). Fluorescent immunostaining for troponin-T was examined and photographed under a fluorescent microscope (green). The images of troponin-T positive cells were captured by Laser Scanning Systems LSM 510 (Carl Zeiss, Inc, Oberkochen, Germany).

Assessment of cardiac differentiation using reverse transcription-polymerase chain reaction

Total RNA from 7-day old EBs was extracted with Trizol® reagent (Invitrogen, life technologies, Carlsbad, CA). Reverse transcription was then performed using 1 μg of total RNA in a final volume of 20 μL, using the QuantiTect® reverse transcription kit (Qiagen, Hilden, Germany) according to the manufacturer's instructions. Cardiac-specific genes, alpha isoforms of sodium-potassium ATPase and calcium handling proteins were compared in EBs in the presence or absence of ouabain with quantitative real-time polymerase chain reaction (qPCR). Primer sequence and annealing temperature are depicted in Table 1. GAPDH served as an internal control. Quantitative PCR analysis was performed with a real-time PCR Detector (Opticon 2 DNA Engine, MJ Research, MN, USA) using the iQ SYBR Green Supermix (Bio-Rad Laboratories, Hercules, CA). For amplification, after initial holds for 5 min at 95 °C, 50 cycles of 95 °C for 15 s followed by 57 °C for 30 s and 72 °C for 30 s, melt curve analysis was performed. The relative quantification of PCR products was performed according to the $2^{-\Delta\Delta Ct}$ method, using mouse GAPDH as an internal control. Where $\Delta\Delta Ct=[(Ct_{\text{target gene}}-Ct_{GAPDH})_{\text{control group}}-(Ct_{\text{target gene}}-Ct_{GAPDH})_{\text{ouabain group}}]$.

Confocal calcium imaging

mESC-derived cardiomyocytes were loaded with 1:1 (*v/v*) amount of 20% Pluronic®-F127 (Invitrogen, Life Technologies) and 5 μmol/L Fluo-3 AM (Sigma-Aldrich, St Louis, MO) dissolved in DMSO with stock concentration of 5 mmol/L for 45 min at 37 °C in Tyrode solution consisting of (mmol/L): 140 NaCl, 5 KCl, 1 $MgCl_2$, 1.8 $CaCl_2$, 10 glucose and 10 HEPES

Table 1. PCR primers and PCR conditions.

Gene	Accession No	Forward/reverse (5′–3′)	Annealing temperature (°C)	Reference
Nkx2.5	NM_008700	5′-GCTACAAGTGCAAGCGACAG-3′ 5′-GGGTAGGCGTTGTAGCCATA-3′	60	Designed by Primer3
GATA 4	NM_008092	5′-TCTCCCAGGAACATCAAAACC-3′ 5′-GTGTGAAGGGGTGAAAAGG-3′	60	Designed by Primer3
GATA 6	NM_010258.3	5′-CAAAAGCTTGCTCCGGTAAC-3′ 5′-TGAGGTGGTCGCTTGTGTAG-3′	60	Designed by Primer3
MLC2V	NM_010861	5′-GACCCAGATCCAGGAGTTCA-3′ 5′-AATTGGACCTGGAGCCTCTT-3′	60	Designed by Primer3
α-MHC	GI 191623	5′-GATGCCCAGATGGCTGACTT-3′ 5′-GGTCAGCATGGCCATGTCCT-3′	57	[38]
β-MHC	NM_080728.2	5′-GCCAACACCAACCTGTCCAAGTTC-3′ 5′-TGCAAAGGCTCCAGGTCTGAGGGC-3′	64	[39]
Na^+/K^+ ATPase α1	BC021496	5′-CTCCAGCAACAGGACCCGGCG-3′ 5′-GATCTCAGCGGCCCTTGCAGG-3′	57	[5]
Na^+/K^+ ATPase α2	BC013561	5′-GAATGGGTTTCTACCATCGCG-3′ 5′-GCACAGAACCACCACGTGAC-3′	57	[5]
Na^+/K^+ ATPase α3	BC020177	5′-GGCAGCCCAGGAACCCACGC-3′ 5′-AGGACAGGAAGGCAGCGAGG-3′	57	[5]
RyR2	NM_023868.2	5′-TGAGTTCCTGCTGTCCTGTG-3′ 5′-CTCTGCCAACTCCAAGAAGG-3′	60	Designed by Primer3
NCX-1	NM_011406	5′-TGTGTTTACGTGGTCCCTGA-3′ 5′-CTCCACAACTCCAGGAGAGC-3′	60	Designed by Primer3
SERCA-2a	NM_001110140	5′-AAGCTATGGGAGTGGTGGTG-3′ 5′-GCAATGCAAATGAGGGAGAT-3′	60	Designed by Primer3
GAPDH	NM_011406	5′-ACATCAAGAAGGTGGTGAAGCAGG-3′ 5′-CTCTTGCTCTCAGATCCTTGCTGG-3′	60	Designed by Primer3

Abbreviation: Nkx2.5, NK2 transcription factor related, locus 5; GATA 4, GATA binding protein 4; GATA 6, GATA binding protein 6; MLC-2v, myosin light chain 2v; α-MHC, alpha-myosin heavy chain; β-MHC, beta-myosin heavy chain; Na^+/K^+ ATPase, sodium potassion ATPase; RyR2, ryanodine receptor 2; NCX, sodium calcium exchanger; SERCA-2a, sarcoplasmic reticulum Calcium ATPase 2a; GAPDH, Glyceraldehyde 3-phosphate dehydrogenase.

at pH 7.4. The calcium transient of single ESC-derived cardiomyocytes was recorded with a confocal imaging system (Olympus Fluoview System version 4.2 FV300 TIEMPO) mounted on an upright Olympus microscope (IX71) with temporal resolution of the line scan at 274 frames per second (2000 scan per 7.3 s). They were then quantified as the background subtracted fluorescence intensity changes normalized to the background subtracted baseline fluorescence using Image J. The amplitude, maximal upstroke and decay velocity of calcium transient were analyzed by Clampfit version 9.2.0.09. (Axon Instruments, Inc, Foster City, CA).

Quantification of cardiac differentiation by flow cytometry

Beating clusters first appeared on day 2 after plating. The percentage of mESC-derived cardiomyocytes was quantified by FACS analysis on day 7 of mESC differentiation. Briefly, 10-cm dishes of EBs were dissociated to a single-cell suspension by collagenase B (1 mg/mL) with DNase (60 U/mL) (Roche Applied Sciences, Penzberg, Germany) treatment, and washed by DPBS twice. Cells were permeabilzed for 15 min using a Cytofix/Cytoperm permeabilization kit (BD Biosciences, San Diego, CA), treated with 1% fetal bovine serum to block non-specific antigens and incubated overnight at 4 °C. Cells were then stained with monoclonal anti-Troponin T [dilution 1:100; Cat no: MS-295-P0; Cardiac Isoform Ab-1 (Clone 13–11)], NeoMarker, Fremont, CA) for 1 h. After twice rinsing in washing buffer, anti-mouse IgG H+L-PE was used for secondary antibody staining (dilution 1:100; Beckman Coulter, Fullerton, CA, USA) for one more hour. Analysis was performed with a Beckman Coulter FC500 flow cytometer in which 10 000 events were counted. The background signal was determined using IgG_1 isotypic control as the primary antibody.

Measurement of ERK1/2, JNK, and p38 Western blot analysis

Cells were washed with PBS, and collected in RIPA buffer (Cell Signaling Technology, Danvers, MA) containing 0.2% Triton X-100, 5 mmol/L EDTA, 1 mmol/L PMSF, 10 μg/mL leupeptin, 10 μg/mL aprotinin, with additional 100 mmol/L NaF and 2 mmol/L Na_3VO_4 and lysed for 30 min on ice. Protein assay was performed using a Bio-Rad protein assay kit (Hercules, CA): 20 μg of protein was loaded per well on a 12.5% sodium dodecyl sulphate (SDS)-polyacrylamide gel, Proteins were subsequently transferred onto 0.45 m pore size nitrocellulose membranes and blocked with 5% non-fat dry milk in TBS (pH 7.4) with 0.5% Tween-20 at 4 °C. The blots were challenged with primary antibody (1:1000) overnight at 4 °C, followed by washing three times with TBST (0.1% Tween-20), then challenged with HRP-conjugated goat anti-rabbit (dilution 1:2000; Cell Signaling Technologies) respectively, followed by detection with enhanced chemiluminescent substrate (Millipore, Billerica, MA). As primary antibodies, the rabbit polyclonal anti-p38 MAPK, anti-ERK, anti-JNK, directed against the phosphorylated form of the proteins (dilution 1:1000; Cell Signaling Technology, Danvers, MA).

Statistical analysis

Continuous variables are expressed as mean±standard deviation. Statistical comparisons were performed using Student's *t* test. Calculations were performed with SPSS (version 14.0). A P value <0.05 was considered statistically significant.

Results

Ouabain enhanced cardiac differentiation of mESCs

The effect of ouabain on the viability of differentiating mESCs was determined by MTT assay at different concentrations of ouabain for 72 h. Ouabain was well tolerated even in relatively high concentrations in differentiating mESCs (Figure 1A). To assess whether ouabain treatment enhances cardiac differentiation of mESCs and to determine the optimal range ouabain dosage in enhancing cardiac differentiation, flow cytometry to determine the percentage of cardiomyocytes as identified by troponin-T positive cells was performed. As depicted in Figure 1B and 1C, the optimal dosage of ouabain to enhance cardiac differentiation of mESC was about 10 μmol/L (Figure 1A and 1B). Taken together with the viability test, ouabain at concentration of 20 μmol/L was selected for subsequent experiments. Cardiac differentiation of undifferentiated mESCs was assessed by the percentage of spontaneous beating EBs under the microscope and troponin-T positive cells using flow cytometry at d 7. In this study, spontaneous beating outgrowths from EBs were first observed on d 2 in both ouabain-treated EBs and controls (12.5%), and progressively increased until reaching a plateau at d 9. The administration of ouabain resulted in a higher percentage of spontaneous beating outgrowths of EBs compared with controls from d 6 to d 9 (Figure 1B). Standard, counting of beating outgrowths from EBs is nevertheless a very crude measurement of the efficiency of cardiac differentiation[4]. The percentage of cardiomyocytes was consistently significantly higher in the ouabain group (9.50%±1.82% *vs* 2.90%±0.20%; n=3, P<0.05).

Figure 2 shows the immunocytochemical pattern of cardiac-specific cytoskeletal proteins including troponin-T in mESC-derived cardiomyocytes. Cardiomyocytes derived from controls showed a homogeneous distribution of troponin-T protein resembling early stage cardiomyocytes (Figure 2)[23]; cardiomyocytes from the ouabain group demonstrated striations of the myofilament specific protein indicating sarcomere development, a marker for late-stage cardiomyocytes.

Ouabain-induced expression of cardiac specific genes

The effect of ouabain on the expression of cardiac marker genes in EBs was examined by quantitative RT-PCR. The expression of cardiac transcription factors, including Nkx2.5, significantly increased (almost double) in the ouabain group on d 7 (n=3, P<0.05), but not GATA-4 and GATA-6, the transcription factors common for mesoderm and endoderm (Figure 3A). In addition, gene expression of sarcomeric muscle proteins (α-MHC and β−MHC) was increased in the ouabain group compared with the control (n=3; P<0.05 and

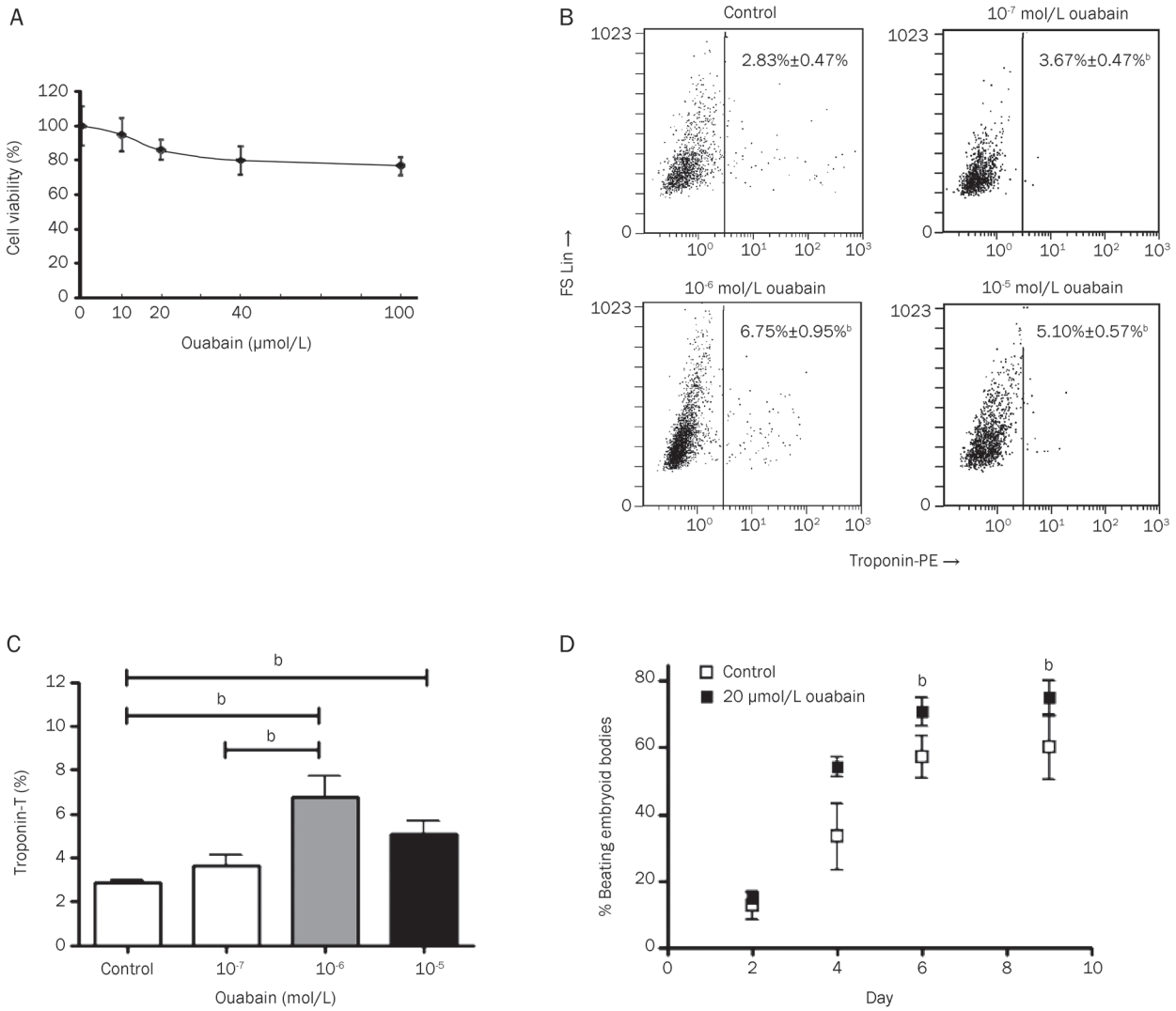

Figure 1. Enhanced *in vitro* cardiac differentiation with ouabain. (A) The effect of ouabain on the viability of differentiating D3 mESCs. The EBs were plated and exposed to various dosages of ouabain for 72 h and the viability of cells determined by MTT assay. Data are expressed as mean±SEM (n=6). (B) Dot plots of the percentage of mESC-derived cardiomyocytes (troponin-T positive cells) as determined by flow cytometry at various concentrations of Ouabain. (C) Bar chart of the Troponin-T positive cell counts. (D) Effect of ouabain on percentage of beating clusters of the differentiated ESCs. Number of day is defined as time beating cluster shown after plating of suspended EBs. Data are expressed as mean±SEM (n=3), whereas the significant difference was tested between ouabain-treated and control for each time point by unpaired t-test, $^bP<0.05$.

$P<0.01$ respectively). Of note, the expression of α-MHC, the adult isoform of myosin heavy chain, was markedly up-regulated with ouabain treatment by about 3.5-fold (Figure 3A). The authenticity of increase α-MHC gene expression was confirmed with Western blot experiment (Figure 3B). As a potential target of ouabain, the expression kinetics of α subunit isoforms of Na^+/K^+ ATPase in mESCs during differentiation was also investigated using RT-PCR. The mRNA of all three isoforms: α1, α2, and α3 subunits was detected in both undifferentiated mESCs and mESC-derived cardiomyocytes at 7-day differentiation; nonetheless α1 and 2 isoforms were the most responsive to ouabain treatment (Figure 3C). In addition, mRNA expression of a panel of calcium handling proteins, including RyR2 and SERCA2a, (Figure 3D) was up-regulated in the ouabain group.

Ouabain-enhanced calcium handling of cardiomyoyctes derived from mESCs

To investigate whether up-regulation of calcium handling proteins in cardiomyocytes from the ouabain group was associated with more mature calcium handling properties, spontaneous calcium oscillations in single cardiomyoyctes isolated from ouabain-treated EBs were characterized on d 7 using confocal laser microscopy and compared with that of the control. Consistent with the up-regulated calcium handling proteins, the ouabain group exhibited more mature calcium handling properties (Figure 4A). Specifically, cardiomyocytes from the ouabain group generated larger calcium transients

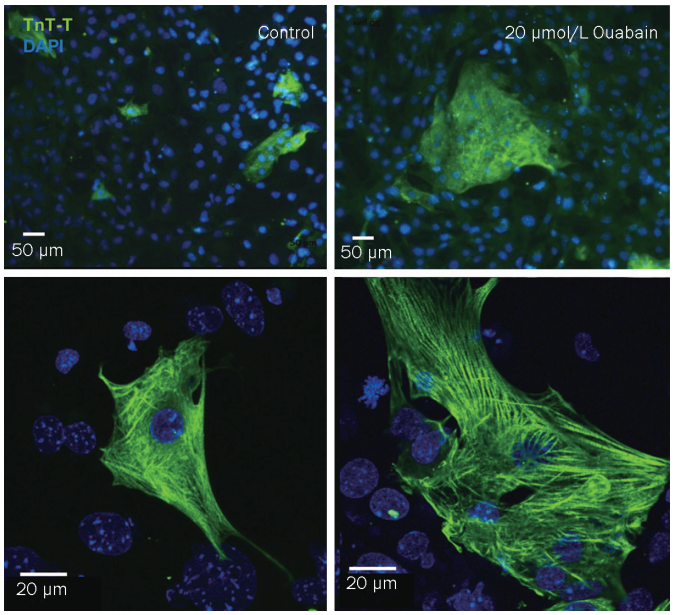

Figure 2. (A) Detection of typical cardiomyocyte proteins in mESC-CM of control (left) and ouabain-treated group (right). The cells were stained with anti-troponin T antibody (green). Nuclei are stained with DAPI (blue).

[14.52±4.45 (n=7) *vs* 6.86±0.87 (n=7)], as well as a significantly higher maximal and decay velocity (n=7; P<0.01 and P<0.05 respectively), suggestive of a more mature sarcoplasmic reticular (SR) function (Figure 4B–4D). Administration of caffeine (10 mmol/L) also elicited a significant larger surge in cytosolic Ca^{2+} in the ouabain group (1163±213.9 *vs* 612.4±99.7; P<0.05), indicating a substantial increase in SR calcium content conferred by ouabain treatment (Figure 5).

Ouabain increases cardiac differentiation of mESCs by Erk1/2 activation

Various MAPK-signaling cascades including ERK, c-JNK and p38 MAPK play important roles in cardiac hypertrophy[17, 24] and cardiac remodeling following myocardial infarction. In order to determine whether the enhanced cardiac differentiation on administration of ouabain is related to MAPK-signaling cascades involved in the hypertrophy pathway, phosphorylation of ERK, c-JNK, and p38 MAPK in ouabain-treated EBs was determined and compared with controls. On d 7, ouabain treatment resulted in a significant surge in phosphorylation of ERK1/2 (Figure 6A); no significant difference between the ouabain group and control was found in phosphorylation of either JNK1/2 or p38 MAPK (Figure 6B). The MEK1/2 inhibitor U0126 suppressed ouabain-activated tyrosine phosphorylation of ERK1/2 (Figure 7A), indicating that ERK1/2 was likely activated by ouabain stimulation of MEK1/2 activity. To further study the effect of Erk1/2 activation on cardiac differentiation of mESCs, FACS experiments were performed by blocking the Erk1/2 pathway. Addition of the MEK1 inhibitor, U0126, which subsequently blocks MEK1/2, upstream of ERK1/2, suppressed the percentage of troponin-T positive cells to 0.53%±0.28% (n=3, P<0.01 compared with control) (Figure 7) while ouabain rescued the effect to control levels (n=3, P<0.05 compared with U0126).

Discussion

We evaluated the effects of ouabain on cardiac differentiation of mESCs. Our results demonstrate that ouabain promotes cardiogenesis and myofibrillogenesis of ESCs, and matures the calcium handling properties of cardiomyocytes derived there-

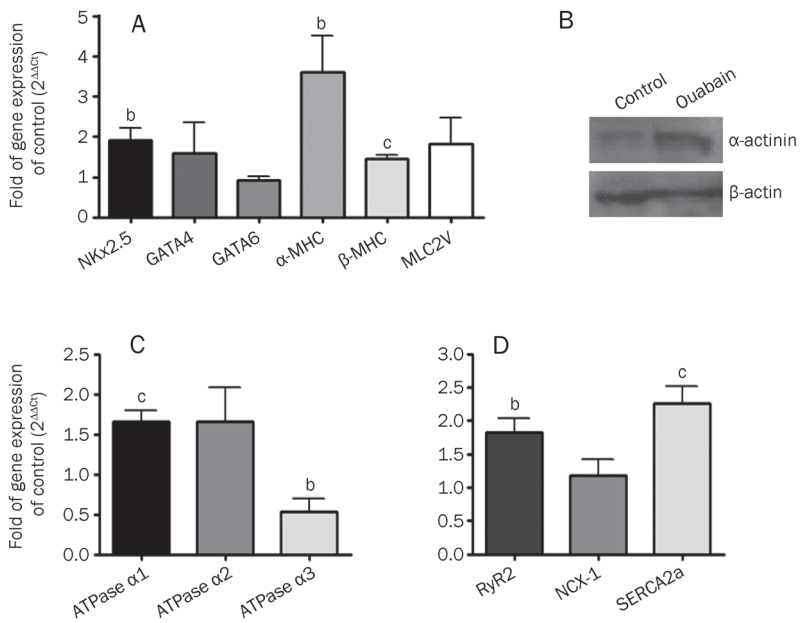

Figure 3. (A) Cardiac maker gene expression of mESC with ouabain-induced cardiac differentiation as revealed by quantitative RT-PCR. Nkx2.5, NK2 transcription factor related locus 5; GATA 4 and 6, GATA-binding protein 4 and 6; MLC2V, myosin light chain 2 ventricular transcripts; α- and β-MHC, α- and β-myosin heavy chain. GAPDH was used as internal control. (B) Western blot of cardiac cytoskeletal protein, alpha-MHC in differentiated mESCs. (C) Gene expression of three isoforms of sodium-potassium ATPase (Na^+/K^+ ATPase), α1, α2, and α3. (D) Gene expression of calcium handling proteins on sacroplasmic recticulum (SR). Three different experiments were repeated with similar results. RyR2, ryanodine receptor 2; SERCA2a, sarcoplasmic reticulum Ca^{2+} ATPase; NCX-1: Na/Ca exchanger. GAPDH was used as internal control. Data shown as mean±SEM from 3 independent experiments, significance difference was tested by unpaired t-test with ^bP<0.05 and ^cP<0.01.

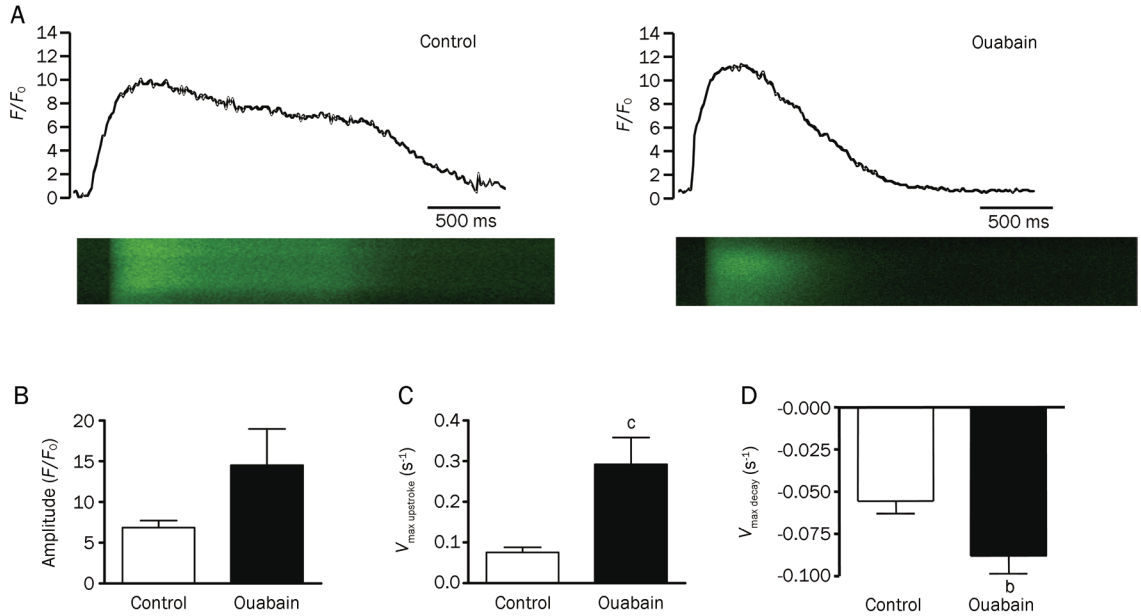

Figure 4. (A) Representative tracings of rythmic spontaneous Ca^{2+} transients showing in ouabain treated ESC-CM (right) and control (left). (B) Amplitude, (C) Maximal upstroke velocity ($V_{max\ upstroke}$), (D) Maximal decay velocity ($V_{max\ decay}$) of Ca^{2+} transients in the mESC-derived cardiomyocytes; Data shown as mean±SEM (n=7), seven cells of interest were selected from in three independent experiments. Unpaired t-test was performed between ouabain treated and control group; $^{b}P<0.05$, $^{c}P<0.01$.

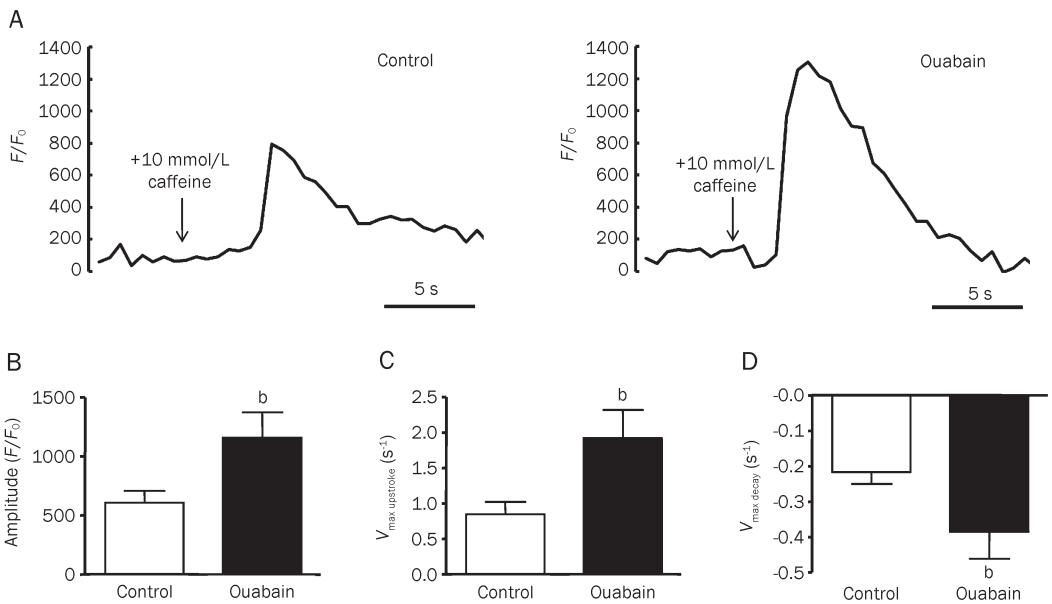

Figure 5. (A) Representative tracings of caffeine-induced SR Ca^{2+} release in control (left) and ouabain-treated (right) mESC-CM, demonstrating caffeine-sensitive Ca^{2+} stores and fractional release of total SR Ca^{2+} load during spontaneous activation. (B) Amplitude, (C) Maximal upstroke velocity ($V_{max\ upstroke}$), (D) Maximal decay velocity ($V_{max\ decay}$) of Ca^{2+} transients in the mESC-derived cardiomyocytes; Data shown as mean±SEM (n=5), five cells were analyzed in three independent experiments. Unpaired t-test was performed between ouabain treated and control group; $^{b}P<0.05$.

from. The main findings are as follows: 1) Ouabain-treated EBs showed an increased differentiation into cardiomyocytes (in terms of the percentages of beating outgrowths and troponin-positive cardiomyocytes), probably via Erk1/2 activation; 2) Ouabain increased gene expression of cardiogenesis (Nkx2.5) and myofibrillogenesis (α-MHC and β-MHC); 3) Ouabain increased the mRNA level of calcium handling protein (RyR2 and SERCA2a) with corresponding maturation of calcium handling properties as determined by confocal microscopy; 4) Ouabain significantly enhanced expression of the α1 isoform

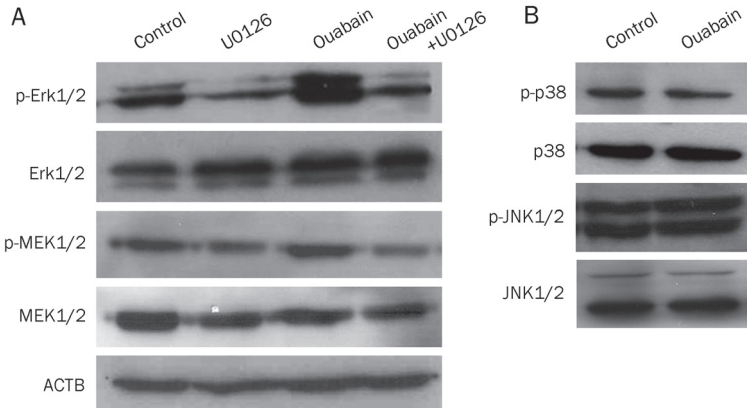

Figure 6. Expression of major MAPK, ERK1/2, p38 and JNK, involved in hypertrophy pathway of mESCs. (A) Ouabain increased Erk1/2 and MEK1/2 phosphorylation and rescued the suppression by U0126; (B) Unchanged phosphorylation of p38 and JNK upon ouabain treatment; at least three independent experiments were repeated with a similar result for each of the MAPK examined.

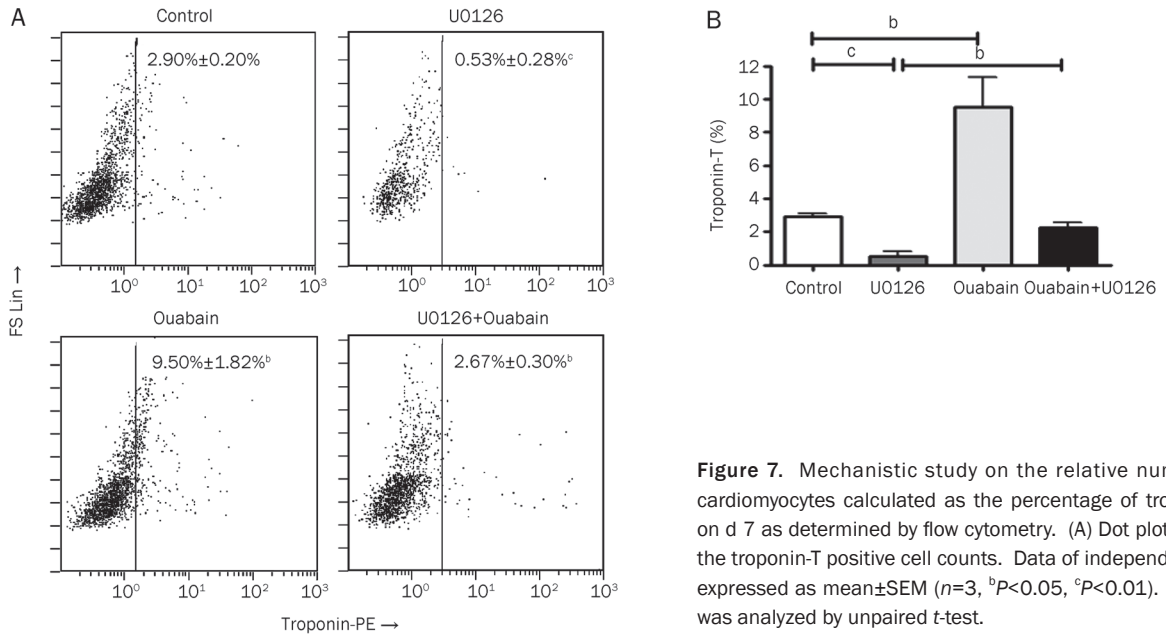

Figure 7. Mechanistic study on the relative number of ESC-derived cardiomyocytes calculated as the percentage of troponin-T positive cells on d 7 as determined by flow cytometry. (A) Dot plots and (B) bar chart of the troponin-T positive cell counts. Data of independent experiments were expressed as mean±SEM (n=3, ^bP<0.05, ^cP<0.01). Significant difference was analyzed by unpaired t-test.

of Na^+/K^+-ATPase, the predominant form in cardiac tissue.

ESC-derived cardiomyocytes hold great promise for cardiac regeneration. Nonetheless current protocols for cardiac differentiation of ESCs are in general inefficient, making it very difficult to obtain adequate numbers of cardiomyocytes for clinical therapy. Despite the well-known hypertrophic effects of ouabain on cardiomyocytes[17, 24] and the documented functional expression of Na^+/K^+-ATPase in undifferentiated mESCs[5], the potential procardiogenic effects of ouabain have not been explored. Binding of ouabain to Na^+/K^+-ATPase, in addition to the positive inotropic effect, also activates multiple MAPK pathways in a cell-type specific manner. Previous studies have suggested that MAPK activation may play a crucial role in mesoderm induction, which leads subsequently to cardiogenesis during embryonic development[25, 26]. Coordinated activation of the three major MAPKs involved in cardiac hypertrophy namely ERK1/2, JNK, and p38 MAPK, are essential to induce cardiac differentiation of P19 embryonic carcinomal cell line[27, 28]. In the present study, application of ouabain to undifferentiated mESCs resulted in a modest increase in the number of troponin-positive cells differentiated from mESCs. This was associated with increased expression of early cardiac specific transcription factors (Nkx2.5) and cardiac specific markers (α-MHC and β-MHC). Consistent with a previous study[29], ERK1/2, JNK and p38 MAPK were endogenously activated in mESCs during differentiation. Only ERK1/2 though was significantly activated upon ouabain treatment. Since specific blocker for ERK1/2 is not available, U0126, an upstream MEK1/2 blocker, were used to study the pathway, of which ouabain induced cardiogenesis. Due to the non-specificity of MEK1/2 blocker, it is possible that other mechanisms independent of ERK1/2 activation may be involved in ouabain induced cardiac differentiation in mECSs. Nonetheless, the specific role of ouabain in Erk1/2 activation was well defined by the inhibitor experiment. Interestingly, various cytokines or growth factors, including cardiotrophin-1[30], VEGF[31], and heregulin-β1[8], which promote cardiac differentiation of mESCs, also mediate via the

activation of ERK1/2 pathway. It has recently been shown that icariin, the active ingredient of the plant herb Epimedium, significant enhances cardiac differentiation of mESCs via activation of p38 MAPK[29]. Taken together, this evidence suggests that adult cardiac hypertrophic signals, particularly the MAPK pathway, may play a role in the cardiac differentiation in ESCs, and may be exploited to improve the efficiency of cardiac differentiation.

Another important hurdle for ESC-based cardiac therapies is the relative immature calcium handling properties of ESC-derived cardiomyocytes[2, 32–34]. In adult cardiomyocytes, calcium enters the cell through *L*-type calcium channels during phase 2 of action potentials. This relative small calcium influx in turn triggers a large calcium release from the internal calcium store, SR through ryanodine receptors[35]. This process is known as calcium-induced calcium release (CICR), the primary mechanism that links electrical excitation and mechanical contraction in cardiomyocytes. During diastole, calcium is actively removed from cytosol, mainly through sarco/endoplasmic reticulum Ca^{2+}-ATPase pump (SERCA), back into the SR and via Na^+-Ca^{2+} exchanger (NCX) out of cell[36]. mESC-derived cardiomyocytes are known to exhibit immature calcium dynamics: small cytosolic calcium transient amplitudes, slow rise and decay kinetics, and reduced calcium content of SR. This adversely affects excitation-contraction coupling[37] and is partly related to the relatively underdeveloped SR and partly to the developmental expression profiles of calcium handling proteins in mESC-derived cardiomyocytes. In the present study, ouabain treatment favorably altered the calcium handling properties of mESC-derived cardiomyocytes including larger calcium transients, a faster rate of rise and decay of calcium transients, and thus resulted in a stronger contractile force. In addition, cardiomyoctyes isolated from ouabain-treated EBs also appeared to have a larger internal store of calcium as evidenced by larger amplitude of caffeine-mediated calcium release. These changes could be related to the corresponding upregulation of key calcium handling proteins in cardiomyocytes isolated from ouabain-treated EBs. Specifically, the upregulated ryanodine receptor could result in the faster rate of calcium release, while the rate of calcium transient decay corresponds to the higher expression of SERCA in ouabain-treated cardiomyocytes. The enhanced intracellular calcium concentration due to Na^+/K^+-ATP inhibition nonetheless remains another plausible mechanism for such improvement.

Our results shed new light on the potential use of a hypertrophic stimulus on adult cardiomyocytes to enhance cardiac differentiation and maturation of ESC-CMs *in vitro*. Ouabain-driven cardiac differentiation of mESC-CMs is mediated by activation of Erk1/2 in the hypertrophy pathway. The relationship of the pathway with calcium handling in the cells was not identified. Nonetheless, our findings broaden knowledge of the differentiation processes of cultured ESCs, and may also contribute to the future development of step-cell based therapy for heart disease.

Acknowledgements

The project was supported by th grant HK RGC 777910 to Dr Chung-wah SIU and Prof Hung-fat TSE. We appreciated the help of Nil.

Author contribution

This research was designed by Chung-wah SIU, Hung-fat TSE, Chu-pak LAU, Deborah K LIEU, Cornilia MAN. The experiments were performed by Yee-ki LEE, Kwong-man NG, Wing-hon LAI. The new analytical tools and reagents were provided by Chung-wah SIU and Hung-fat TSE. Yee-ki LEE and Kwong-man NG were responsible for analyzing data. The manuscript was written by Yee-ki LEE, Kwong-man NG, and Chung-wah SIU.

References

1 Mummery CL, Ward D, Passier R. Differentiation of human embryonic stem cells to cardiomyocytes by coculture with endoderm in serum-free medium. Curr Protoc Stem Cell Biol 2007; Chapter 1: Unit 1F 2.
2 Siu CW, Moore JC, Li RA. Human embryonic stem cell-derived cardiomyocytes for heart therapies. Cardiovasc Hematol Disord Drug Targets 2007; 7: 145–52.
3 Thomson JA, Itskovitz-Eldor J, Shapiro SS, Waknitz MA, Swiergiel JJ, Marshall VS, *et al*. Embryonic stem cell lines derived from human blastocysts. Science 1998; 282: 1145–7.
4 Moore JC, van Laake LW, Braam SR, Xue T, Tsang SY, Ward D, *et al*. Human embryonic stem cells: genetic manipulation on the way to cardiac cell therapies. Reprod Toxicol 2005; 20: 377–91.
5 Otsu K, Kuruma A, Yanagida E, Shoji S, Inoue T, Hirayama Y, *et al*. Na^+/K^+ ATPase and its functional coupling with Na^+/Ca^{2+} exchanger in mouse embryonic stem cells during differentiation into cardiomyocytes. Cell Calcium 2005; 37: 137–51.
6 Passier R, Oostwaard DW, Snapper J, Kloots J, Hassink RJ, Kuijk E, *et al*. Increased cardiomyocyte differentiation from human embryonic stem cells in serum-free cultures. Stem Cells 2005; 23: 772–80.
7 Mummery C, Ward-van Oostwaard D, Doevendans P, Spijker R, van den Brink S, Hassink R, *et al*. Differentiation of human embryonic stem cells to cardiomyocytes: role of coculture with visceral endoderm-like cells. Circulation 2003; 107: 2733–40.
8 Kim HS, Cho JW, Hidaka K, Morisaki T. Activation of MEK-ERK by heregulin-beta1 promotes the development of cardiomyocytes derived from ES cells. Biochem Biophys Res Commun 2007; 361: 732–8.
9 Braunwald E. Effects of digitalis on the normal and the failing heart. J Am Coll Cardiol 1985; 5: 51A–59A.
10 Schwartz A, Grupp G, Wallick E, Grupp IL, Ball WJ Jr. Role of the Na^+K^+-ATPase in the cardiotonic action of cardiac glycosides. Prog Clin Biol Res 1988; 268B: 321–38.
11 Akera T, Ng YC. Digitalis sensitivity of Na^+, K^+-ATPase, myocytes and the heart. Life Sci 1991; 48: 97–106.
12 Manunta P, Stella P, Rivera R, Ciurlino D, Cusi D, Ferrandi M, *et al*. Left ventricular mass, stroke volume, and ouabain-like factor in essential hypertension. Hypertension 1999; 34: 450–6.
13 Balzan S, Neglia D, Ghione S, D'Urso G, Baldacchino MC, Montali U, *et al*. Increased circulating levels of ouabain-like factor in patients with asymptomatic left ventricular dysfunction. Eur J Heart Fail 2001; 3: 165–71.
14 Gottlieb SS, Rogowski AC, Weinberg M, Krichten CM, Hamilton BP, Hamlyn JM. Elevated concentrations of endogenous ouabain in patients with congestive heart failure. Circulation 1992; 86: 420–5.

15 D'Urso G, Frascarelli S, Balzan S, Zucchi R, Montali U. Production of ouabain-like factor in normal and ischemic rat heart. J Cardiovasc Pharmacol 2004; 43: 657–62.
16 D'Urso G, Frascarelli S, Zucchi R, Biver T, Montali U. Cardioprotection by ouabain and digoxin in perfused rat hearts. J Cardiovasc Pharmacol 2008; 52: 333–7.
17 Huang L, Li H, Xie Z. Ouabain-induced hypertrophy in cultured cardiac myocytes is accompanied by changes in expression of several late response genes. J Mol Cell Cardiol 1997; 29: 429–37.
18 Haas M, Askari A, Xie Z. Involvement of Src and epidermal growth factor receptor in the signal-transducing function of Na^+/K^+-ATPase. J Biol Chem 2000; 275: 27832–7.
19 Liu L, Zhao X, Pierre SV, Askari A. Association of PI3K-Akt signaling pathway with digitalis-induced hypertrophy of cardiac myocytes. Am J Physiol Cell Physiol 2007; 293: C1489–97.
20 Tian J, Liu J, Garlid KD, Shapiro JI, Xie Z. Involvement of mitogen-activated protein kinases and reactive oxygen species in the inotropic action of ouabain on cardiac myocytes. A potential role for mitochondrial K_{ATP} channels. Mol Cell Biochem 2003; 242: 181–7.
21 Au KW, Liao SY, Lee YK, Lai WH, Ng KM, Chan YC, *et al*. Effects of iron oxide nanoparticles on cardiac differentiation of embryonic stem cells. Biochem Biophys Res Commun 2009; 379: 898–903.
22 Mosmann T. Rapid colorimetric assay for cellular growth and survival: Application to proliferation and cytotoxicity assays. J Immunol Methods 1983; 65: 55–63.
23 Hescheler J, Fleischmann BK, Lentini S, Maltsev VA, Rohwedel J, Wobus AM, *et al*. Embryonic stem cells: a model to study structural and functional properties in cardiomyogenesis. Cardiovasc Res 1997; 36: 149–62.
24 Peng M, Huang L, Xie Z, Huang WH, Askari A. Partial inhibition of Na^+/K^+-ATPase by ouabain induces the Ca^{2+}-dependent expressions of early-response genes in cardiac myocytes. J Biol Chem 1996; 271: 10372–8.
25 Umbhauer M, Marshall CJ, Mason CS, Old RW, Smith JC. Mesoderm induction in Xenopus caused by activation of MAP kinase. Nature 1995; 376: 58–62.
26 Yao Y, Li W, Wu J, Germann UA, Su MS, Kuida K, *et al*. Extracellular signal-regulated kinase 2 is necessary for mesoderm differentiation. Proc Natl Acad Sci USA 2003; 100: 12759–64.
27 Eriksson M, Leppa S. Mitogen-activated protein kinases and activator protein 1 are required for proliferation and cardiomyocyte differentiation of P19 embryonal carcinoma cells. J Biol Chem 2002; 277: 15992–6001.
28 Davidson SM, Morange M. Hsp25 and the p38 MAPK pathway are involved in differentiation of cardiomyocytes. Dev Biol 2000; 218: 146–60.
29 Ding L, Liang XG, Hu Y, Zhu DY, Lou YJ. Involvement of p38MAPK and reactive oxygen species in icariin-induced cardiomyocyte differentiation of murine embryonic stem cells *in vitro*. Stem Cells Dev 2008; 17: 751–60.
30 Sauer H, Neukirchen W, Rahimi G, Grunheck F, Hescheler J, Wartenberg M. Involvement of reactive oxygen species in cardiotrophin-1-induced proliferation of cardiomyocytes differentiated from murine embryonic stem cells. Exp Cell Res 2004; 294: 313–24.
31 Chen Y, Amende I, Hampton TG, Yang Y, Ke Q, Min JY, *et al*. Vascular endothelial growth factor promotes cardiomyocyte differentiation of embryonic stem cells. Am J Physiol Heart Circ Physiol 2006; 291: H1653–8.
32 Lieu DK, Liu J, Siu CW, McNerney GP, Tse HF, Abu-Khalil A, *et al*. Absence of transverse tubules contributes to non-uniform Ca^{2+} wavefronts in mouse and human embryonic stem cell-derived cardiomyocytes. Stem Cells Dev 2009; 18: 1493-500.
33 Liu J, Fu JD, Siu CW, Li RA. Functional sarcoplasmic reticulum for calcium handling of human embryonic stem cell-derived cardiomyocytes: insights for driven maturation. Stem Cells 2007; 25: 3038–44.
34 Liu J, Lieu DK, Siu CW, Fu JD, Li R. Facilitated maturation of Ca^{2+} handling properties of human embryonic stem cell-derived cardiomyocytes by calsequestrin expression. Am J Physiol Cell Physiol 2009; 297: C152-9.
35 Bers DM. Cardiac excitation-contraction coupling. Nature 2002; 415: 198–205.
36 Satin J, Itzhaki I, Rapoport S, Schroder EA, Izu L, Arbel G, *et al*. Calcium handling in human embryonic stem cell-derived cardiomyocytes. Stem Cells 2008; 26: 1961–72.
37 Fu JD, Yu HM, Wang R, Liang J, Yang HT. Developmental regulation of intracellular calcium transients during cardiomyocyte differentiation of mouse embryonic stem cells. Acta Pharmacol Sin 2006; 27: 901–10.
38 Mauritz C, Schwanke K, Reppel M, Neef S, Katsirntaki K, Maier LS, *et al*. Generation of functional murine cardiac myocytes from induced pluripotent stem cells. Circulation 2008; 118: 507–17.
39 Wobu A, Guan K, Yang H, Boheler K. Embryonic stem cells as a model to study cardiac, skeletal muscle, and vascular smooth muscle cell differentiation. Methods Mol Biol 2002; 185: 127–56.

Acta Pharmacologica Sinica (2011) 32: 62–69
 1671-4083/11 $32.00
www.nature.com/aps

Original Article

Upregulation of NF-E2-related factor-2-dependent glutathione by carnosol provokes a cytoprotective response and enhances cell survival

Chien-chung CHEN[1, #], Hui-ling CHEN[2, #], Chia-wen HSIEH[3], Yi-ling YANG[2], Being-sun WUNG[3, *]

[1]Department of Neurology, Saint Martin De Porres Hospital, Chiayi, Taiwan, China; [2]Department of Biochemical Science and Technology, National Chiayi University, Chiayi, Taiwan, China; [3]Department of Microbiology and Immunology, National Chiayi University, Chiayi, Taiwan, China

Aim: To explore whether glutathione (GSH) increased through Nrf-2 activation is involved in the cytoprotective effects of carnosol in HepG2 cells.
Methods: Human hepatoma cell line HepG2 were exposed to rosemarry essential oil or carnosol. Cell viability was measured using an Alamar blue assay. The production of intracellular GSH was determined using monochlorobimane. The level of protein or mRNA was examined by Western blotting or RT-PCR, respectively.
Results: Rosemarry essential oil (0.005%-0.02%) and carnosol (5 and 10 mol/L) increased the intracellular GSH levels and GSH synthesis enzyme subunit GCLC/GCLM expression. Rosemary essential oil and carnosol increased nuclear accumulation of Nrf2 and enhanced Nrf2-antioxidant responsive element (ARE)-reporter activity. Transfection of the treated cells with an Nrf2 siRNA construct blocks GCLC/GCLM induction. Furthermore, pretreatment of the HepG2 cells with essential oil and carnosol exerted significant cytoprotective effects against H_2O_2 or alcohol. In TNFα-treated cells, the nuclear translocation and transcriptional activity of NF-κB was abolished for 12 h following carnosol pretreatment. Cotreatment with GSH also suppressed NF-κB nuclear translocation, whereas cotreatment with BSO, a GSH synthesis blocker, blocked the inhibitory effects of carnosol.
Conclusion: This study demonstrated that Nrf2 is involved in the cytoprotective effects by carnasol, which were at least partially mediated through increased GSH biosynthesis.

Keywords: carnosol; glutathione; Nrf2; NF-κB; human hepatoma cell line HepG2; cytoprotection

Acta Pharmacologica Sinica (2011) 32: 62–69; doi: 10.1038/aps.2010.181; published online13 Dec 2010

Introduction

Non-nutritional constituents in many foods may have beneficial health effects such as anti-inflammatory and anti-carcinogenic properties. *Rosmarinus officinalis* (rosemary) originates from southern Europe and is a commonly used herbal flavoring agent[1]. Rosemary extracts exhibit potent antioxidant activities that reduce lipid peroxidation, the production of reactive oxygen species (ROS), and inflammation[2, 3]. Carnosol is a diterpene derived from rosemary where it is found in considerable quantities; approximately 0.2%–1%, in dried rosemary[4], and 10.3% in commercially available rosemary extracts[5]. Although carnosic acid is the major polyphenolic compound present in rosemary plants, carnosol, an oxidation product of carnosic acid, has stronger anti-inflammatory effects[6]. Several studies including ours had been reported previously that the cytoprotective effects of carnosol have a number of beneficial properties from a medicinal standpoint, including antioxidation, anti-inflammation and anti-cancer effects in various cell types[7–9]. However, details of the mechanisms underlying the hepatitic cytoprotection of carnosol and its regulation remain to be elucidated.

To protect and survive against a variety of environmental or intracellular stresses, mammalian cells have developed robust cellular defensive systems, including mechanisms that alleviate oxidative stress. Among the factors involved in these defense responses are components of detoxifying systems, including phase II drug metabolizing enzymes such as glutathione S-transferase, NAD(P)H: quinone oxidoreductase, and UDP-glucuronosyltransferase[10], and anti-oxidant enzymes such as glutamine-cysteine ligase (GCL)[11, 12]. Previous studies have shown that these enzymes are coordinately regulated through transcription factor NF-E2-related factor-2 (Nrf2) activation in response to electrophiles[10]. Carnosol possesses

# These authors contributed equally to this work.
* To whom correspondence should be addressed.
E-mail bswung@mail.ncyu.edu.tw
Received 2010-06-13 Accepted 2010-09-15

high electrophilic activity and has been reported to activate Nrf2-related phase II detoxifying enzyme genes and antioxidant enzymes[13, 14]. GCL is one of the most readily induced anti-oxidant genes and is rate-limiting for glutathione (GSH) synthesis[15]. GSH is a tripeptide that functions in the detoxification of chemical substances and is therefore a major cellular antioxidative defense molecule. Increased intracellular GSH may thus provide cytoprotective effects under conditions of oxidative stress or inflammation. To more fully understand the mechanisms underlying this effect, in our current study we examined the cytoprotective characteristics of rosemary essential oil and carnosol in a human hepatoma cell line, HepG2. Our findings demonstrate that both substances induce GCL expression and also an elevation of the intracellular GSH levels. In addition, the increased GSH levels were found to be associated with the inhibition of TNFα-induced NF-κB nuclear accumulation.

Materials and methods

Materials

Bacterially derived TNFα was purchased from Calbiochem (San Diego, CA). The p3xARE/Luc vector was constructed as described previously[16]. Antibodies raised against Nrf2 were purchased from Santa Cruz Biotechnology (Santa Cruz, CA). p65 antibodies was obtained from Stressgen Biotechnologies (SB, San Diego, CA, USA). ECL reagents were purchased from Pierce (Rockford, IL, USA). Luciferase assay kits were purchased from Promega (Madison, WI, USA). Peroxidase-conjugated anti-rabbit and anti-mouse antibodies were obtained from Amersham (Arlington Heights, IL, USA) and nitrocellulose was obtained from Schleicher & Schuell (Dassel, Germany). All other reagents, including carnosol and rosemary essential oil were purchased from Sigma (St Louis, MO, USA).

Cell culture

HepG2 cells (ATCC HB-8065) were grown in high glucose Dulbecco's modified Eagle's medium (DMEM, Invitrogen) supplemented with 10% fetal bovine serum (FBS, Invitrogen), 100 U/mL penicillin and 100 μg/mL streptomycin. The cells were seeded at a density of 1.5 million cells per mL in T-25 culture flasks with 5 mL of complete medium and cultured at 37 °C with 5% carbon dioxide. The culture medium was then replaced with serum free DMEM and the cells were incubated for 12 h prior to experimental treatment.

GSH Assay

GSH levels were determined as described previously[17]. Briefly, cells were cultured at 37 °C in the presence or absence of the treatment reagents indicated in the corresponding figures, washed with PBS and incubated with monochlorobimane (MCB, 40 μmol/L) in the dark for 20 min at room temperature. After two further washes with PBS, the cells were solubilized with 1% SDS and 5 mmol/L Tris HCl (pH 7.4). Fluorescence was measured by spectrofluorophotometry (Shimadzu, Rf-5301PC), with excitation and emission wavelengths of 405 and 510 nm, respectively and samples were assayed in triplicate. The assay for detecting *in vitro* GSH levels was performed identically but without cell lysates. The levels of intracellular GSH were quantified using a GSH solution as a standard.

Cell viability assay

Cell viability was performed using an Alamar blue assay kit (Serotec, Oxford, UK) in accordance with the manufacturer's instructions. This assay is based on the detection of metabolic activity in living cells using a redox indicator that changes from an oxidized (blue) to a reduced (red) form. The intensity of the red color is proportional to the viability of the cells, and is calculated by the difference in the absorbance values at 570 and at 600 nm and expressed as a percentage of the control.

RNA isolation and RT-PCR

Total cellular RNA was extracted using the phenol-guanidinium isothiocyanate method[18]. Equal amounts (5 μg) of RNA from the different treatments were then reverse-transcribed for 50 min at 42 °C using 50 units of Superscript II (Invitrogen, Carlsbad, CA). Amplifications of the cDNA were performed in 25 μL of PCR buffer (10 mmol/L Tris-HCl, 50 mmol/L KCl, 5 mmol/L $MgCl_2$, and 0.1% Triton X-100, pH 9.0) containing 0.6 units of Taq DNA polymerase (Promega, Madison, WI) and 30 pmol of the specific primers GCLM forward, 5′-CAGCGAGGAGCTTCATGATTG-3′; reverse, 5′-TGATCACAGAATCCAGCTGTGC-3′; GCLC forward, 5′-GTTCTTGAAACTCTGCAAGAGAAG-3′; reverse, 5′-ATGGAGATGGTGTATTCTTGTCC-3′[19] and GAPDH forward 5′-TATCGTGGAAGGACTCATGACC-3′; reverse 5′-TACATGGCAACTGTGAGGGG-3′. Reaction products were separated electrophoretically in a 2.5% agarose gel and stained with ethidium bromide.

Quantitative PCR

For transcript quantification purposes, real-time PCR was performed. Then 1 μL of the reverse-transcriptase product was used in a 25 μL volume reaction containing 200 μmol/L of each dNTP, 5 pmol of each primer, 1×PCR buffer II, 1.5 mmol/L $MgCl_2$, 0.2×SYBR Green I (Molecular Probes), and 1.25 U of Amplitaq Gold (Applied Biosystems). Amplification was performed using ABI 7500 Real-Time PCR System (Applied Biosystems) programmed as 94 °C for 12 min followed by 40 cycles of (94 °C for 30 s, 57 °C for 20 s, 72 °C for 50 s). Variability in the initial quantities of cDNA was normalized to the internal control, GAPDH. A negative control was included in each set of experiments. Melting curve analysis was performed to enhance specificity of the amplification reaction, and the 7500 software was used to compare the amplification in the experimental samples during the log-linear phase.

Plasmids, transfections and luciferase assays

A NF-κB/Luc fragment containing tandem repeats of double-stranded oligonucleotides spanning the NF-κB binding site of ICAM-1: 5′-TGGAAATTCC-3′[20], sense: 5′-CCCG-GGTGGAAATTCCTGGAAATTCCTGGAAATTCCG-GAGTCTAGA-3′, anti-sense: 5′-TCTAGACTCCGGAATTTC-CAGGAATTTCCAGGAATTTCCACCCGGG-3′ was introduced into the pGL3 promoter plasmid (Promega, Madison,

WI, USA). The HepG2 cells were then grown to 60%–80% confluence and transfected with a total of 1 μg of NF-κB/Luc or Nrf2/Luc[16] using lipofectamine reagent (Invitrogen, Carlsbad, CA, USA) in accordance with the manufacturer's instructions. For luciferase assays, the cell lysate was first mixed with luciferase substrate solution (Promega), and the resulting luciferase activity was measured in a luminometer. For each experiment, luciferase activity was determined in triplicate and normalized with respect to β-galactosidase activity levels.

Transient transfection with siRNA targeting Nrf2

An siRNA targeting human Nrf2 5′-UCCCGUUUGUAGAUGACAA-3′[21] and a control siRNA 5′-GCAAGCUGACCCUGAAGUUCAU-3′ (non-sense) were purchased from Ambion (Austin, TX, USA). HepG2 cells were seeded onto 60-mm dishes, incubated for 24 h, and then transiently transfected with 100 nmol/L siRNA per dish at 90% confluence with Lipofectamine 2000. After 24 h of recovery in 10% serum medium, the cells were cultured in serum-free medium without serum for another 12 h prior to treatment.

Preparation of cytosolic and nuclear lysates

To separate the cytosolic and nuclear fractions from HepG2 cells, the cells were collected by scraping in cold PBS. The cell pellet was then lysed in 10 mmol/L HEPES, 1.5 mmol/L $MgCl_2$, 10 mmol/L KCl, 0.5 mmol/L DTT, 0.5 mmol/L PMSF and 0.3% nonidet P-40. After 5 min of centrifugation (3000 rounds per minute at 4 °C) the supernatant was collected and designated as the cytosolic fraction. Nuclear proteins were then extracted from this preparation using a buffer containing 25% glycerol, 20 mmol/L HEPES, 0.6 mol/L KCl, 1.5 mmol/L $MgCl_2$ and 0.2 mmol/L EDTA. Protein concentrations were determined using a protein assay DC system (Bio-Rad, Richmond, CA, USA).

Western blotting

Whole lysates of HepG2 were prepared as previously described[22]. A total of 1×10^6 cells were lysed on ice in lysis buffer (1% NP-40, 0.5% sodium deoxycholate, 0.1% SDS and a protease inhibitor mixture) and whole-cell extracts were boiled for 5 min prior to separation on 10% SDS-PAGE, in which the protein samples were evenly loaded. The proteins were then transferred to a nitrocellulose filter in Tris-glycine buffer at 100 V for 1.5 h. The membranes were then blocked with PBS containing 5% nonfat milk and incubated with antibodies for two hours at 4 °C, with gentle shaking. The results were visualized by chemiluminescence using ECL (Pierce, Rockford, IL, USA), according to the manufacturer's instructions.

Statistical analysis

Overall treatment effects were examined by ANOVA. *Post hoc* analysis was also performed to detect differences between specific groups using the Dunnett's test (SPSS 12.0 software package, Chicago, IL, USA). A confidence limit of $P<0.05$ was considered to be significant.

Results

Carnosol and essential oil of rosemary increase the intracellular GSH levels at non-cytotoxic concentrations

GSH is a well-studied tri-peptide and has numerous roles in protecting cells from oxidants and maintaining the cellular thiol redox status. We therefore tested the GSH levels in our current study in HepG2 cells exposed to essential oil or carnosol over a specific treatment period. As shown in Figure 1A and 2A, the GSH levels increased after 6 h of essential oil and carnosol treatment and persisted for over 12 h. Carnosol at 5 μmol/L increased GSH to near 160% of the starting levels after 12 h of treatment (Figure 2A). On the other hand, we subsequently detected a dose dependent increase in GSH levels following essential oil treatments for 12 h (Figure 1B and 2B). Significantly, an examination of the cytotoxic effects of these substances upon HepG2 cells using an Alamar blue assay indicated no adverse effects on cell viability upon exposure to 0.01% essential oil or 10 μmol/L carnosol (Figure 1C and 2C). Furthermore, there is no any detectable ROS production under 5 and 10 μmol/L carnosol treatment by using peroxide sensitive fluorescent probe 5-(and-6)-carboxy-2,7,dichlorodihydro fluorescein diacetate fluorescence assay (data not shown).

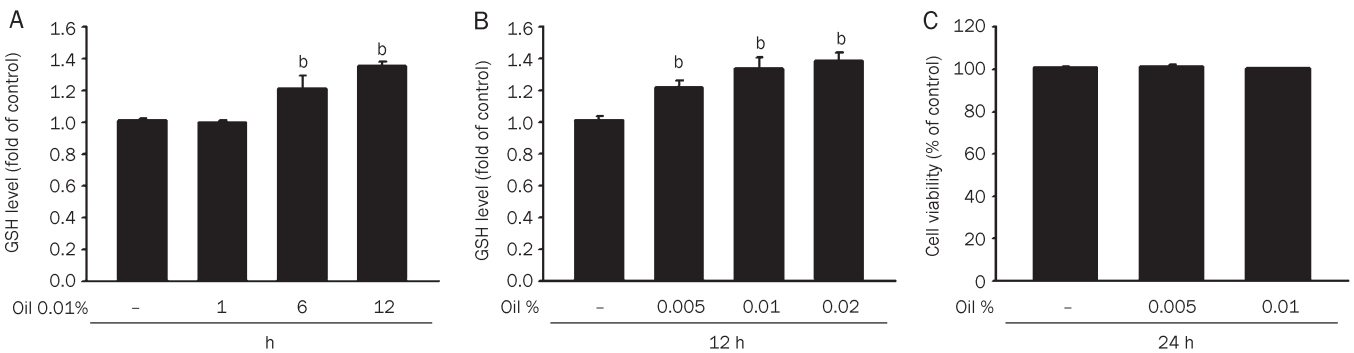

Figure 1. The GSH levels are increased in HepG2 cells treated with rosemary essential oil. (A) The intracellular GSH levels of HepG2 cells incubated with 0.01% rosemary essential oil for 1, 6 and 12 h. Data values are expressed as a percentage of the untreated control, which was set at 100%. Results are the mean±SEM (n=3). $^bP<0.05$ *vs* untreated cells. (B) The intracellular GSH levels of HepG2 cells incubated with the indicated doses of rosemary essential oil for 12 h. (C) Cell viability of HepG2 cells incubated with 0.005% and 0.01% rosemary essential oil for 24 h. Data are expressed as the mean±SEM of three independent experiments. No significant differences were found by ANOVA.

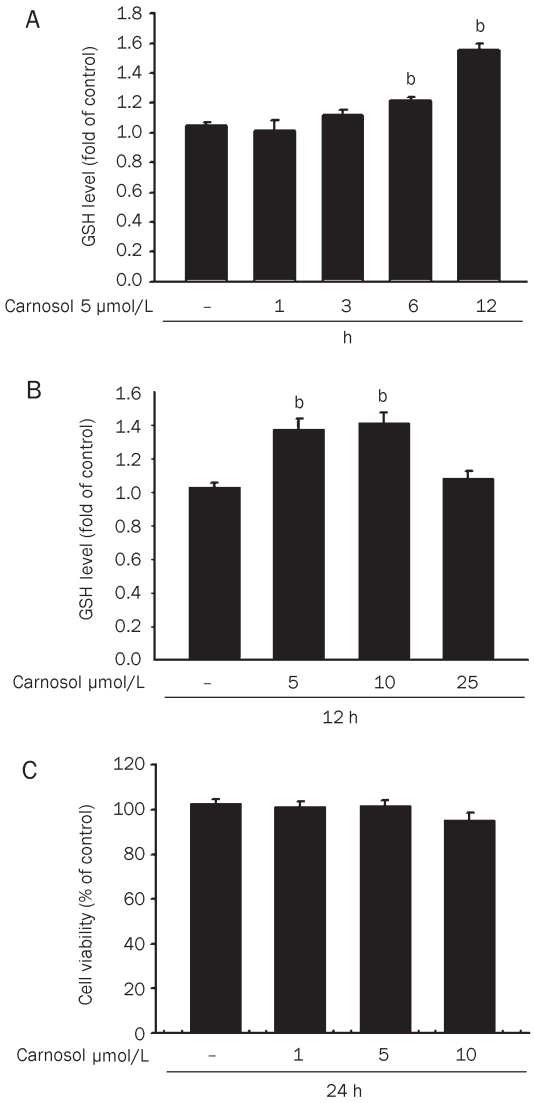

Figure 2. Increased GSH levels in HepG2 cells treated with carnosol. (A) The intracellular GSH levels of HepG2 cells incubated with 5 μmol/L carnosol for 1, 3, 6, and 12 h. Data values are expressed as a percentage of the untreated control, which was set at 100%. Results are presented as the mean±SEM (n=3). $^bP<0.05$ *vs* untreated cells. (B) The intracellular GSH levels of HepG2 cells incubated with the indicated doses of carnosol for 12 h. (C) Cells were incubated with the indicated doses of carnosol for 24 h and cell viability was measured. Data are expressed as the mean±SEM of three independent experiments. No significant differences were found by ANOVA.

Upregulation of both GSH and GSH synthesis enzyme levels in HepG2 cells by carnosol and essential oil of rosemary

The rate-limiting enzyme in the *de novo* synthesis of GSH is glutamate-cysteine ligase (GCL), also known as γ-glutamylcysteine synthetase. GCL consists of a catalytic heavy subunit (GCLC) and a modulatory light subunit (GCLM). We assayed both GCLC and GCLM expression in essential oil and carnosol-treated HepG2 cells. Treatment with 0.01% essential oil increased both the GCLC and GCLM expression levels over the course of the incubation time (Figure 3A). As shown in Figure 3B, an increase in both the GCLC and GCLM mRNA levels was detected following essential oil treatments at 0.01% and 0.02% for 12 h. In a similar experiment, carnosol exposure increased both the GCLC and GCLM gene expression levels after three hours treatment (Figure 3C). In addition, carnosol at 5 μmol/L and 10 μmol/L concentrations was found to increase GCLC and GCLM gene expression over 12 h treatments (Figure 3D). To further determine the effect of 0.01% essential oil and carnosol, cells were incubated for different times. Quantitative PCR reactions were performed to amplify GCLC and GCLM, the production of GCLC and GCLM were increased significantly by 0.01% essential oil or carnosol as early as 3 h and reached a maximum by 6 h (Figure 3E and 3F).

Effects of carnosol upon Nrf2 activation

In our present study, we have found that 0.01% rosemary essential oil and carnosol (5 μmol/L) increase the level of Nrf2 in the nucleus of HepG2 cells. We thus evaluated the specificity of carnosol for Nrf2 binding site, antioxidant response element (ARE) sequences, in our current study by transfecting HepG2 cells with luciferase reporter constructs harboring this element. Cells treated with 0.01% essential oil, and 5 μmol/L or 10 μmol/L carnosol, indeed displayed increased ARE-luciferase activity (Figure 4B). To further assess the mediating role of Nrf2 in the inhibitory effects of carnosol, a more targeted inhibition of Nrf2 using siRNA was undertaken. Cells were transfected with Nrf2 siRNA to reduce the Nrf2 protein level (Figure 4C) and this abolished the induction of both GCLC and GCLM expression following 12 h of carnosol pretreatment (Figure 4D). These findings suggested that carnosol promotes GCLC and GCLM expression via the activation of the Nrf2 pathway.

The protective effects of carnosol and rosemary essential oil against oxidative stress and ethanol

We investigated the effects of rosemary essential oil and carnosol on H_2O_2-induced cytotoxicity and as shown in Figure 5A, it was found that HepG2 cells treated with 3 mmol/L H_2O_2 showed significantly reduced cell viability. In contrast, this cytotoxicity was significantly reduced in cells pretreated with 0.01% essential oil or 5 μmol/L carnosol.

It is well-known that excess alcohol in the liver induces hepatotoxicity. To evaluate whether essential oil and carnosol had protective effects in this regard, we examined their effects upon cell viability in the presence of excess alcohol. The addition of 50 mmol/L ethanol to the culture medium tended to reduce cell viability (Figure 5B). In the presence of essential oil or carnosol however, no loss of cell viability was evident upon exposure to excess alcohol (Figure 5B). These results suggest that the protection against damage from oxidative stress or excess alcohol is dependent on an increased GSH level.

Carnosol inhibits TNFα-induced NF-κB activation via upregulated GSH

To evaluate its effects on NF-κB activation in HepG2 cells,

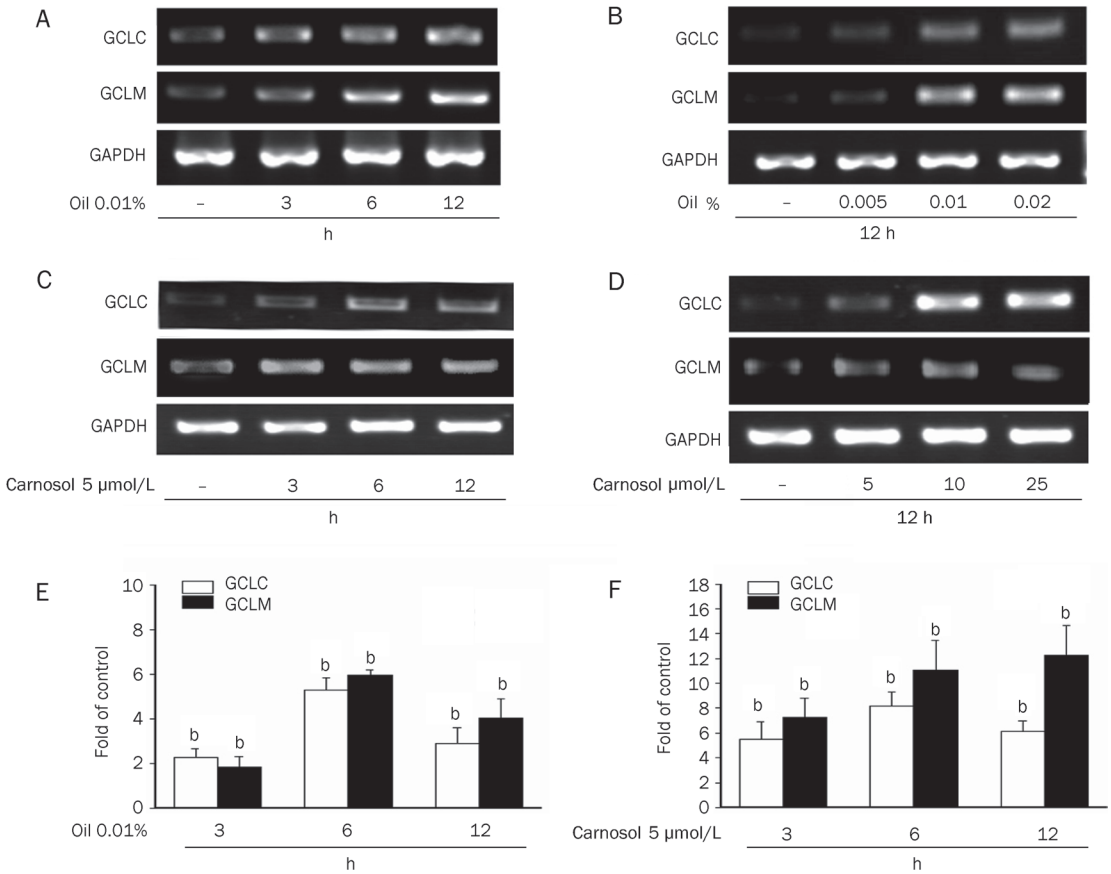

Figure 3. Upregulation of GSH synthesis enzyme levels in HepG2 cells by rosemary essential oil of and carnosol. The mRNA levels of GCLM and GCLC genes were assayed by RT-PCR in HepG2 cells. (A and C) Cells were treated with 0.01% rosemary essential oil or 5 μmol/L carnosol for the indicated time. (B and D) Cells were treated with the indicated doses of rosemary essential oil or carnosol for 12 h. (E and F) Cells were treated with 0.01% rosemary essential oil or 5 μmol/L carnosol for the indicated time. GCLM and GCLC were assayed by quantitative PCR. All samples were run in triplicate, the relative expression values were normalized to the expression value of GAPDH.

cells were treated with GSH for 30 min before TNFα stimulation. As shown in Figure 6A, GSH indeed inhibits TNFα-induced NF-κB nuclear accumulation. We next investigated the possible role of GSH in mediating the inhibitory effects of carnosol in HepG2 cells. Pretreatment of cells with buthionine sulfoximine (BSO), a specific inhibitor of γ-glutamyl cysteine synthetase at concentrations of 100 μmol/L abolished the suppressive effects of carnosol upon NF-κB activation (Figure 6B). Furthermore, we tested whether carnosol inhibits TNFα-induced P65 activation at the transcriptional level. Following pretreatment for 12 h and a luciferase assay (Figure 6C), we found that TNFα-induced NF-κB activation was indeed inhibited. The results of these experiments indicate that the inhibitory effects of carnosol are the result of increased cellular GSH levels.

Discussion

GSH is a well-studied tri-peptide and has numerous roles in protecting cells from oxidants and maintaining the cellular thiol redox status[23, 24]. It was found in our previous study that cinnamaldehyde increases the cellular GSH levels in HepG2 cells after 9 h of exposure[25]. Carnosol is an electrophilic phytochemical present in the rosemary herb and our present study provides new evidence that both rosemary essential oil and carnasol enhance the GSH levels in HepG2 cells by upregulating the expression of GCLC and GCLM at non-cytotoxic concentrations. Our present experiments also show that the translocation of Nrf2 into the nucleus following treatment with rosemary essential oil and carnosol is associated with increases in its ARE transcriptional activity. We further demonstrate that Nrf-2 siRNA abolishes the induction of GCLC and GCLM by carnosol. Hence, the presence of activated Nrf-2 is required for the protective effects of carnosol. These protective effects of both rosemary essential oil and carnosol were manifested by the maintenance of cell viability under conditions of oxidative stress and following ethanol treatment. In addition, the inhibitory effects of carnosol upon TNFα-induced NF-κB activation are mediated through an increase in the intracellular GSH level.

Oxidative stress occurs when the redox equilibrium, which is the ability of cells to protect against damage caused by production of free radicals, is disrupted. Oxidative stress has been implicated as a major cause of cellular injuries in a variety of human diseases. Previous studies have found that poly-

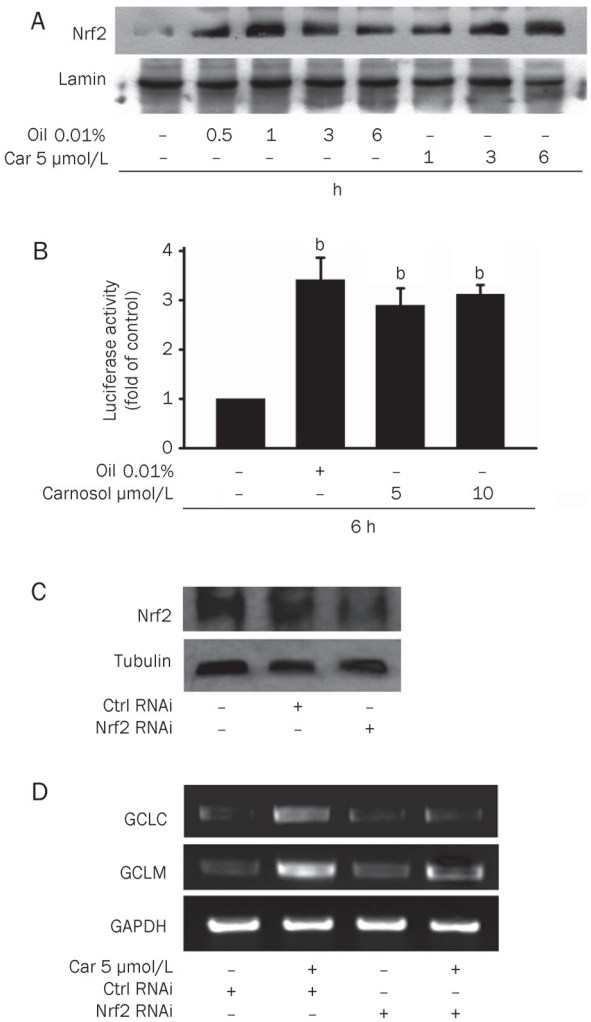

Figure 4. Effects of carnosol upon Nrf2 activation. (A) Nuclear extracts from HepG2 cells were prepared after treatment with 0.01% rosemary essential oil and 5 μmol/L carnosol for the indicated time periods. Immunoblots of nuclear lysates were then probed with Nrf2 specific antibodies. The nuclear lamin band intensities indicate equal loading of each well. (B) Cells were transfected with the ARE-luciferase construct (ARE) and then stimulated with 0.01% rosemary essential oil, 5 or 10 μmol/L carnosol. The cells were then lysed and analyzed for luciferase activity. Induction is indicated by an increase in the normalized luciferase activity in the treated HepG2 cells, relative to the control. Results are the means±SEM from at least three separate experiments. $^{b}P<0.05$ *vs* untreated HepG2 cells. (C) HepG2 cells were transfected with control or Nrf2 siRNA for 36 h and the intracellular protein levels of Nrf2 were determined by Western blotting. (D) HepG2 cells were transfected with control or Nrf2 siRNA for 36 h and then exposed to 5 μmol/L carnosol for 12 h. The mRNA levels of GCLM and GCLC genes were the determined by RT-PCR.

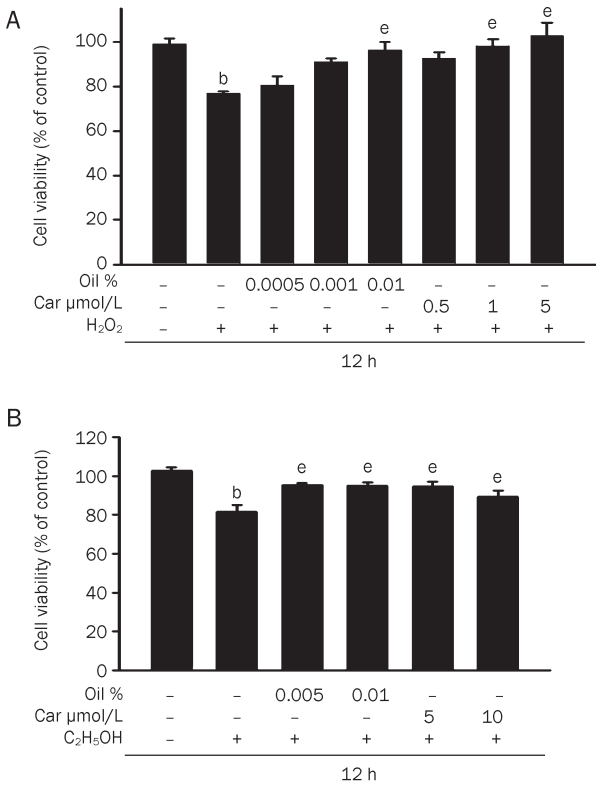

Figure 5. The protective effects of rosemary essential oil and carnosol against oxidative stress and alcohol. Cells were initially preincubated for 12 h in the presence of the indicated doses of rosemary essential oil or carnosol. The medium was then removed and the cells were exposed to 3 mmol/L H_2O_2 for 12 h. Cell viability was measured spectrophotometrically using an Alamar blue assay. Data are expressed as the mean±SEM of at least three independent experiments. $^{b}P<0.05$ *vs* control; $^{e}P<0.05$ *vs* H_2O_2 alone. (B) Cells were initially preincubated for 12 h in the presence of the indicated doses of essential oil or carnosol. The medium was then removed and the cells were exposed to 50 mmol/L ethanol for 12 h. Data are expressed as the mean±SEM of at least three independent experiments. $^{b}P<0.05$ *vs* control; $^{e}P<0.05$ *vs* ethanol alone.

phenolic compounds have intrinsic antioxidant characteristics and protect cells against oxidative cell damage via a Michael acceptor function. These compounds include curcumin, phenylethyl isothiocyanate, epigallocatechin gallate, and other green tea polyphenols[7]. Recently, much attention has focused on the upregulation of phase II detoxifying and antioxidant enzymes via the activation of the Nrf2 transcription factor[15, 26]. Carnosol, a diterpene derived from the rosemary herb, is a representative member of a family of plant-derived phenols[13]. Our present experiments show that carnosol induces Nrf2-mediated GCLC and GCLM expression, which in turn controls GSH synthesis[27]. Furthermore, our present data demonstrate that carnosol induces Nrf2 translocation and activates ARE-luciferase promoter activity, indicating that it directly induces Nrf2 via its ARE.

Recent studies have demonstrated that phytochemicals including resveratrol[28], sulforaphane[29], and epigallocatechin 3-O-gallate[30], induce a GSH increase in HepG2 cells and thus play an important role in cytoprotection. Tumor necrosis factor-α (TNFα) is an inflammatory cytokine that causes liver cell injury by generating oxidative stress[31]. Since glutathione (GSH) is a key cellular antioxidant that detoxifies reactive oxygen species, we next examined the effects of carnosol-

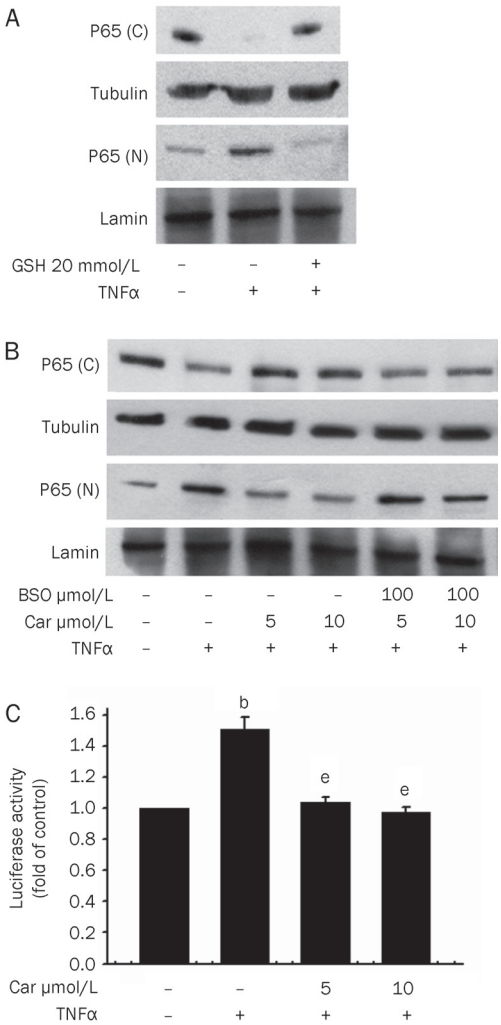

Figure 6. Carnosol inhibits TNFα-induced NF-κB activation via increased GSH. (A) Cells were pretreated with 20 mmol/L GSH for 30 min and then stimulated with 100 U/mL TNFα. Nuclear (N) and cytosolic (C) extracts were then prepared and subjected to Western blot analysis with p65 antibodies. The nuclear lamin band intensities indicate equal loading of each well. (B) Cells were pretreated with 5 or 10 μmol/L carnosol for 12 h and then stimulated with 100 U/mL TNFα. Nuclear (N) and cytosolic (C) extracts were again prepared and subjected to Western blot analysis with p65 antibodies. (C) HepG2 cells were co-transfected with the NF-κB luciferase reporter construct and β-galactosidase for 16 h. Cells were then exposed to 5 μmol/L carnosol for 12 h and to 100 U/mL TNFα for a further 6 h. Luciferase activity was normalized against β-galactosidase activity; the untreated value was taken as 1. $^{b}P<0.05$ *vs* untreated HepG2 cells; $^{e}P<0.05$ *vs* TNFα alone (mean±SEM).

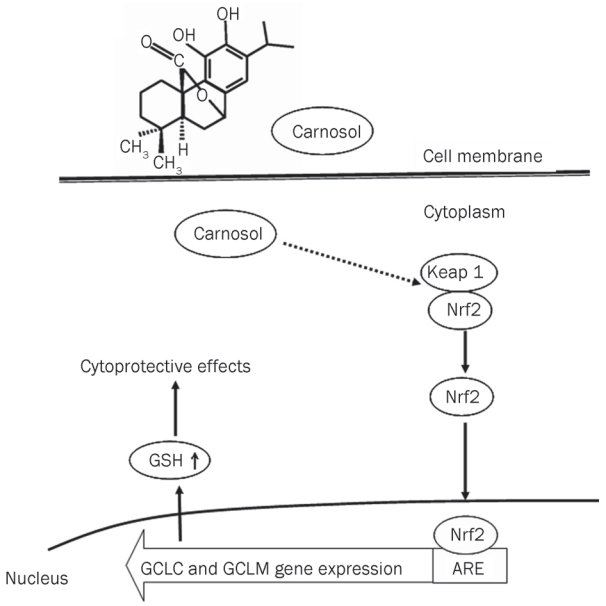

Figure 7. Proposed model of the protective effects of carnosol via Nrf2 activation.

increased GSH in TNFα-treated cells. TNFα stimulation has been shown to activate NF-κB signaling pathways[32]. We found in our current analyses that carnosol increases the GSH levels after six hours of treatment, and that BSO abolishes p65 translocation after a 12-h incubation with carnosol. In addition, treatment with GSH alone also inhibits p65 translocation. Thus, an increased GSH level is essential for carnosol-induced anti-inflammatory effects. Previous studies have demonstrated that changes in the thiol redox state of the cell might affect the posttranslational modification of p65, including the phosphorylation of critical residues shown to contribute to the nuclear import of this molecule[33, 34]. Moreover, a recent study has revealed that a number of redox-sensitive transcription factors are modified by GSH and thereby inhibit their function[35]. The p65 modification by GSH is thus implicated as an inhibitory mechanism by which carnosol regulates NF-κB activation through the increase in GSH levels.

Our present data thus reveal that carnosol induces cytoprotective mechanisms that may contribute to its putative beneficial effects in suppressing the liver cell response to oxidative stress, alcohol or cytokines during inflammation. Our present results thus expand our understanding of the role of phytochemicals in cytoprotection and potentially assist in the identification of new therapeutic strategies for diseases caused by oxidative damage and other environmental stresses.

Acknowledgements

This work was supported in part by grants from Saint Martin De Porres Hospital and (97-2321-B-415-002) from the National Science Council, Taiwan, China. We thank Yuan-Jun LIN, for assistance in selected experiments.

Author contribution

Chien-chung CHEN analyzed data and contributed analytic tools. Hui-ling CHEN performed research. Chia-wen HSIEH designed research. Yi-ling YANG contributed analytic tools. Being-sun WUNG designed research, analyzed data and wrote the paper.

References

1 Zeng HH, Tu PF, Zhou K, Wang H, Wang BH, Lu JF. Antioxidant properties of phenolic diterpenes from *Rosmarinus officinalis*. Acta Pharma-

col Sin 2001; 22: 1094–8.
2 Aruoma OI, Spencer JP, Rossi R, Aeschbach R, Khan A, Mahmood N, *et al*. An evaluation of the antioxidant and antiviral action of extracts of rosemary and Provencal herbs. Food Chem Toxicol 1996; 34: 449–56.
3 Peng CH, Su JD, Chyau CC, Sung TY, Ho SS, Peng CC, *et al*. Supercritical fluid extracts of rosemary leaves exhibit potent anti-inflammation and anti-tumor effects. Biosci Biotechnol Biochem 2007; 71: 2223–32.
4 del Baño MJ, Lorente J, Castillo J, Benavente-Garcia O, del Rio JA, Ortuño A, *et al*. Phenolic diterpenes, flavones, and rosmarinic acid distribution during the development of leaves, flowers, stems, and roots of Rosmarinus officinalis antioxidant activity. J Agric Food Chem 2003; 51: 4247–53.
5 Frankel EN, Huang SW, Aeschbach R, Prior E. Antioxidant activity of a rosemary extract and its constituents, carnosic acid carnosol and rosmarinic acid in bulk oil and oil-in-water emulsion. J Agric Food Chem 1996; 44: 131–5.
6 Poeckel D, Greiner C, Verhoff M, Rau O, Tausch L, Hörnig C, *et al*. Carnosic acid and carnosol potently inhibit human 5-lipoxygenase and suppress pro-inflammatory responses of stimulated human polymorphonuclear leukocytes. Biochem Pharmacol 2008; 76: 91–7.
7 Lo AH, Liang YC, Lin-Shiau SY, Ho CT, Lin JK. Carnosol, an antioxidant in rosemary, suppresses inducible nitric oxide synthase through down-regulating nuclear factor-kappaB in mouse macrophages. Carcinogenesis 2002; 23: 983–91.
8 Sotelo-Félix JI, Martinez-Fong D, Muriel De la Torre P. Protective effect of carnosol on CCl(4)-induced acute liver damage in rats. Eur J Gastroenterol Hepatol 2002; 14: 1001–6.
9 Lian KC, Chuang JJ, Hsieh CW, Wung BS, Huang GD, Jian TY, *et al*. Dual mechanisms of NF-κB inhibition in carnosol-treated endothelial cells. Toxicol Appl Pharmacol 2010; 245: 21–35.
10 Itoh K, Chiba T, Takahashi S, Ishii T, Igarashi K, Katoh Y, *et al*. An Nrf2/small Maf heterodimer mediates the induction of phase II detoxifying enzyme genes through antioxidant response elements. Biochem Biophys Res Commun 1997; 236: 313–22.
11 Ishii T, Itoh K, Takahashi S, Sato H, Yanagawa T, Katoh Y. Transcription factor Nrf2 coordinately regulates a group of oxidative stress-inducible genes in macrophages. J Biol Chem 2000; 275: 16023–9.
12 McMahon M, Itoh K, Yamamoto M, Chanas SA, Henderson CJ, McLellan LI, *et al*. The Cap'n'Collar basic leucine zipper transcription factor Nrf2 (NF-E2 p45-related factor 2) controls both constitutive and inducible expression of intestinal detoxification and glutathione biosynthetic enzymes. Cancer Res 2001; 61: 3299–307.
13 Martin D, Rojo AI, Salinas M, Diaz R, Gallardo G, Alam J, *et al*. Regulation of heme oxygenase-1 expression through the phosphatidylinositol 3-kinase/Akt pathway and the Nrf2 transcription factor in response to the antioxidant phytochemical Carnosol. J Biol Chem 2004; 279: 8919–29.
14 Satoh T, Izumi M, Inukai Y, Tsutsumi Y, Nakayama N, Kosaka K, *et al*. Carnosic acid protects neuronal HT22 cells through activation of the antioxidant-responsive element in free carboxylic acid- and catechol hydroxyl moieties-dependent manners. Neurosci Lett 2008; 434: 260–5.
15 Nguyen T, Yang CS, Pickett CB. The pathways and molecular mechanisms regulating Nrf2 activation in response to chemical stress. Free Radical Biol Med 2004; 37: 433–41.
16 Wu CC, Hsu MC, Hsieh CW, Lin JB, Lai PH, Wung BS. Upregulation of heme oxygenase-1 by epigallocatechin-3-gallate via the phosphatidylinositol 3-kinase/Akt and ERK pathways. Life Sci 2006; 78: 2889–97.
17 Kamencic H, Lyon A, Paterson PG, Juurlink BH. Monochlorobimane fluorometric method to measure tissue glutathione. Anal Biochem 2000; 286: 35–7.
18 Wung BS, Cheng JJ, Hsieh HJ, Shyy YJ, Wang DL. Cyclic strain-induced monocyte chemotactic protein-1 gene expression in endothelial cells involves reactive oxygen species activation of activator protein-1. Circ Res 1997; 81: 1–7.
19 Neurohr C, Lenz AG, Ding I, Leuchte H, Kolbe T, Behr J. Glutamate-cysteine ligase modulatory subunit in BAL alveolar macrophages of healthy smokers. Eur Respir J 2003; 22: 82–7.
20 van de Stolpe A, Caldenhoven E, Stade BG, Koenderman L, Raaijmakers JA, Johnson JP, *et al*. 12-O-tetradecanoylphorbol-13-acetate- and tumor necrosis factor alpha-mediated induction of intercellular adhesion molecule-1 is inhibited by dexamethasone. Functional analysis of the human intercellular adhesion molecular-1 promoter. J Biol Chem 1994; 269: 6185–92.
21 Singh A, Boldin-Adamsky S, Thimmulappa RK, Rath SK, Ashush H, Coulter J, *et al*. RNAi-mediated silencing of nuclear factor erythroid-2-related factor 2 gene expression in non-small cell lung cancer inhibits tumor growth and increases efficacy of chemotherapy. Cancer Res 2008; 68: 7975–84.
22 Wung BS, Cheng JJ, Chao YJ, Hsieh HJ, Wang DL. The modulation of Ras-Raf-ERK pathway by reactive oxygen species is involved in cyclic strain-induced early growth response-1 gene expression in endothelial cells. Circ Res 1999; 84: 804–12.
23 Dickinson DA, Forman HJ. Cellular glutathione and thiols metabolism. Biochem Pharmacol 2002; 64: 1019–26.
24 Sen CK. Cellular thiols and redox-regulated signal transduction. Curr Top Cell Regul 2000; 36: 1–30.
25 Liao BC, Hsieh CW, Liu YC, Tzeng TT, Sun YW, Wung BS. Cinnamaldehyde inhibits the tumor necrosis factor-alpha-induced expression of cell adhesion molecules in endothelial cells by suppressing NF-kappaB activation: effects upon IkappaB and Nrf2. Toxicol Appl Pharmacol 2008; 229: 161–71.
26 Balogun E, Hoque M, Gong P, Killeen E, Green CJ, Foresti R, *et al*. Curcumin activates the haem oxygenase-1 gene via regulation of Nrf2 and the antioxidant-responsive element. Biochem J 2003; 371: 887–95.
27 Mulcahy RT, Wartman MA, Bailey HH, Gipp JJ. Constitutive and beta-naphthoflavone-induced expression of the human gamma-glutamylcysteine synthetase heavy subunit gene is regulated by a distal antioxidant response element/TRE sequence. J Biol Chem 1997; 272: 7445–54.
28 Shin SM, Cho IJ, Kim SG. Resveratrol protects mitochondria against oxidative stress through AMPK-mediated GSK3{beta} inhibition downstream of poly(ADP-ribose)polymerase-LKB1 pathway. Mol Pharmacol 2009; 76: 884–95.
29 Kim BR, Hu R, Keum YS, Hebbar V, Shen G, Nair SS, *et al*. Effects of glutathione on antioxidant response element-mediated gene expression and apoptosis elicited by sulforaphane. Cancer Res 2003; 63: 7520–5.
30 Murakami C, Hirakawa Y, Inui H, Nakano Y, Yoshida H. Effects of epigallocatechin 3-O-gallate on cellular antioxidative system in HepG2 cells. J Nutr Sci Vitaminol (Tokyo) 2002; 48: 89–94.
31 Hoek JB, Pastorino JG. Ethanol, oxidative stress, and cytokine-induced liver cell injury. Alcohol 2002; 27: 63–8.
32 Baldwin AS Jr. The NF-κB and IκB proteins: new discoveries and insights. Annu Rev Immunol 1996; 14: 649.
33 Heiss E, Herhaus C, Klimo K, Bartsch H, Gerhauser C. Nuclear factor-kappa B is a molecular target for sulforaphane-mediated anti-inflammatory mechanisms. J Biol Chem 2001; 276: 32008–15.
34 Mattioli I, Sebald A, Bucher C, Charles RP, Nakano H, Doi T, *et al*. Transient and selective NF-kappaB p65 serine 536 phosphorylation induced by T cell costimulation is mediated by IkappaB kinase beta and controls the kinetics of p65 Nuclear Import. J Immunol 2004; 172: 6336–44.
35 Mieyal JJ, Gallogly MM, Qanungo S, Sabens EA, Shelton MD. Molecular mechanisms and clinical implications of reversible protein glutathionylation. Antioxid Redox Signal 2008; 10: 1941–88.

Acta Pharmacologica Sinica (2011) 32: 70–78
 1671-4083/11 $32.00
www.nature.com/aps

Original Article

Amelioration of glomerulosclerosis with all-*trans* retinoic acid is linked to decreased plasminogen activator inhibitor-1 and α-smooth muscle actin

Xia LIU[1, 2, #], Lei LÜ[1, #], Bei-bei TAO[1], Ai-ling ZHOU[2], Yi-chun ZHU[1, *]

[1]*Department of Physiology and Pathophysiology, Fudan University Shanghai Medical College, Shanghai 200032, China;* [2]*Department of Pathophysiology, Nantong University Nantong Medical College, Nantong 226001, China*

Aim: To examine the effects of all-*trans* retinoic acid (atRA) on renal morphology and function as well as on renal plasminogen activator inhibitor-1 (PAI-1) expression and plasmin activity in rats with 5/6 nephrectomy.
Methods: Adult male Sprague Dawley rats were given 5/6 nephrectomy or sham operation. Renal function was measured 2 weeks later. The nephrectomized rats were assigned to groups matched for proteinuria and treated with vehicle or atRA (5 or 10 mg/kg by gastric gavage once daily) for the next 12 weeks. Rats with sham operation were treated with vehicle. At the end of the treatments, kidneys were collected for histological examination, Western blot analysis, and enzymatic activity measurements.
Results: The 5/6 nephrectomy promoted hypertension, renal dysfunction, and glomerulosclerosis. These changes were significantly reduced in the atRA-treated group. The expressions of PAI-1 and α-smooth muscle actin (α-SMA) were significantly increased in the vehicle-treated nephrectomized rats. Treatment with atRA significantly reduced the expressions of PAI-1 and α-SMA. However, plasmin activity remained unchanged following atRA treatment.
Conclusion: Treatment with atRA ameliorates glomerulosclerosis and improves renal function in rats with 5/6 nephrectomy. This is associated with a decrease in PAI-1 and α-SMA, but not with a change in plasmin activity.

Keywords: nephrectomy; plasminogen activator inhibitor 1; plasmin; retinoids; α-smooth muscle actin

Acta Pharmacologica Sinica (2011) 32: 70–78; doi: 10.1038/aps.2010.200

Introduction

Glomerulosclerosis is a common phenomenon associated with renal failure that occurs regardless of the primary cause of damage[1]. It is characterized by the excessive accumulation of extracellular matrix (ECM) in the glomeruli. When ECM synthesis exceeds its degradation, ECM accumulation occurs[2]. In various types of glomerular injuries, mesangial cells are activated into ECM-producing myofibroblasts that undergo proliferation. These cells are phenotypically defined by their expression of α-smooth muscle actin (α-SMA)[3–6]. Recently, plasminogen activator inhibitor-1 (PAI-1) has been widely recognized as a key contributor in fibrosis. Under physiological conditions, PAI-1 expression is low in the kidney but is upregulated in response to renal injury[7]. Transgenic mice overexpressing PAI-1 develop severe fibrosis in several experimental fibrosis models[8–10]. In contrast, PAI-1 deficiency or inhibition results in decreased fibrosis[8, 10–16]. These studies demonstrate a role for PAI-1 in fibrogenesis. PAI-1 is a major physiological inhibitor of tissue-type plasminogen activator (t-PA) and urokinase-type plasminogen activator (u-PA), both of which convert plasminogen to plasmin. Plasmin can activate latent matrix metalloproteinases (MMPs). Plasmin and MMPs play key roles in the regulation of ECM degradation[17–19]. PAI-1's profibrotic effect is presumed to be exerted by inhibiting plasmin generation. This explanation, however, has been disputed in some reports[11, 12, 14, 16].

The retinoids are derivatives of vitamin A (retinol) and include all-*trans* retinoic acid (atRA), 9-*cis* RA, and 13-*cis* RA. RAs exert strong anti-proliferative and anti-inflammatory effects. They act via the retinoic acid receptor (RAR) and retinoid X receptor (RXR), which serve as transcription factors to regulate target gene expression. Retinoids have been reported to be renoprotective in some models of renal fibrosis[20–28]. We have previously shown that exogenous atRA decreases cardiac fibrosis in spontaneously hypertensive rats (SHR)[29] and inhibits the increases in PAI-1 and the ECM protein fibronectin, which are induced by the key fibrogenic cytokines trans-

# These authors contributed equally to this study.
* To whom correspondence should be addressed.
E-mail yczhu@shmu.edu.cn
Received 2010-07-15 Accepted 2010-09-01

forming growth factor-β1 (TGF-β1) and angiotensin II (Ang II) in cultured rat mesangial cells[30]. However, the mechanisms mediating the antifibrotic actions of retinoids remain to be further clarified. In the current study, we examined the effects of chronic atRA treatment on renal function and morphology in a rat model of 5/6 nephrectomy. The renal expressions of PAI-1 and α-SMA were examined. The activities of plasmin and MMP-2 were also measured.

Materials and methods

Experimental design and animals

Adult male Sprague Dawley rats that weighed 250−330 g and were obtained from the Department of Experimental Animals, Chinese Academy of Sciences (Shanghai, China) were used in this study. The rats were housed in plastic cages in a room with a controlled humidity of 40% and a temperature of 22 °C. Their exposure to light was controlled on a 12:12-h light-dark cycle. These rats had free access to water and a regular standard diet (0.6% salt). All experiments were performed in accordance with the national animal protection law. After the measurement of baseline blood pressure and renal function, all rats underwent 5/6 nephrectomy (5/6Nx) or sham operation. 5/6Nx was performed after ventral laparotomy under anesthesia with chloral hydrate (300 mg/kg, ip), by removal of the right kidney and ligation of 2 branches of the left renal artery, producing a total of 5/6 renal ablation. Rats that received sham operation underwent anesthesia, ventral laparotomy, and manipulation of the renal pedicles without removal of renal mass. Renal function was measured 2 weeks later, and nephrectomized rats were divided into three groups matched for proteinuria: 5/6Nx+vehicle (5/6Nx treated with soybean oil as placebo, 1 mL/kg, *n*=12), 5/6Nx+atRA1 (5/6Nx treated with 5 mg atRA/kg suspended in soybean oil at a concentration of 5 g/L, *n*=10), and 5/6Nx+atRA2 (5/6Nx treated with 10 mg atRA/kg suspended in soybean oil at a concentration of 10 g/L, *n*=12). Sham+vehicle (sham-operated rats treated with soybean oil, 1 mL/kg, *n*=7) served as a normal control. The dosages of atRA were chosen according to previous experiments from our laboratory that demonstrated an effective reduction of cardiac fibrosis in SHR with little toxic effects[29]. Fresh suspensions of atRA were prepared under reduced lighting conditions each day to limit its spontaneous isomerization to 9-*cis* RA and 13-*cis* RA. Oral treatment was performed by gavage once a day for the next 12 weeks. The rats were weighed once a week to adjust the amount of orally administered atRA.

Blood pressure recordings

Prior to operation, blood pressure (BP) was measured by the tail-cuff method in rats. At the end of the study period, the rats were anesthetized with chloral hydrate. A polypropylene tube (Portex, London, UK) was inserted into the left carotid artery and exteriorized behind the neck. The catheters were filled with a heparinized (10 U/mL) saline solution and plugged with a stainless steel pin. After catheterization, the rats were housed individually and had free access to water and rat chow. On the following day, the arterial catheters were attached to a pressure transducer. BP was measured 2-3 h after gavage. After an equilibrium period of 30 min, systolic BP (SBP), diastolic BP (DBP), mean arterial pressure (MAP), and heart rate (HR) were recorded in the conscious, freely moving animals for 30 min. After the hemodynamic parameters were recorded, terminal blood samples were collected for blood chemical analysis.

Assessment of renal function

Renal function was determined every 2 weeks. Rats were housed individually in metabolic cages to collect urine over 24 h. During this time, they were supplied with food and water *ad libitum*. Urine was stored at -20 °C until measurement. Tail vein blood samples were collected. Urine albumin and urine and serum creatinine concentrations were measured on an autoanalyzer, and the creatinine clearance was calculated accordingly.

Tissue preparation

After hemodynamic measurements at the end of the study period, rats were anesthetized and kidneys were removed immediately. After being washed in cold 0.9% saline, each kidney was blotted dry and cut into two parts. One part was fixed in 10% neutral buffered formalin, and the other part of the renal cortex was rapidly frozen in liquid nitrogen and stored at -80 °C until required for Western blotting and enzymatic activity analysis.

Light microscopy studies

Fixed kidney tissues were embedded in paraffin and cut into 4 μm-thick sections. Sections were stained with periodic acid-Schiff (PAS) reagent and counterstained with hematoxylin. PAS staining is used as a marker for the glomerular basement membrane. Sections were examined by two investigators without previous knowledge of the experimental group of the animal from which the tissue was taken. The semiquantitative glomerulosclerosis index was used to evaluate the degree of glomerular deposition of PAS-positive ECM according to the method of Raij L *et al*[31]. The severity of the lesions for each kidney was examined in the 100 glomeruli selected at random, graded from 0-4 points according to the percentage of morphological changes in each glomerulus (0=0%, 1+=1%−25%, 2+=26%−50%, 3+=51%−75%, 4+=76%−100%). The number of glomeruli with lesions of grades 0, 1+, 2+, 3+, and 4+ was n_0, n_1, n_2, n_3, and n_4, respectively. The glomerular sclerosis index was obtained from the following formula: $(0\times n_0+1\times n_1+2\times n_2+3\times n_3+4\times n_4)/100$.

Western blot analysis

Renal cortical tissue samples were homogenized in lysis buffer containing 20 mmol/L Tris (pH 7.5), 150 mmol/L NaCl, 1% Triton X-100, and a 1:50 dilution of a protease inhibitor cocktail (Roche Applied Science, Penzberg, Germany) on ice followed by centrifugation (12 000× *g*, 10 min, 4 °C). The supernatant was collected and the protein concentration was measured.

Thirty μg of total protein from samples were loaded and separated under reducing conditions with 10% SDS-PAGE and transferred onto PVDF membranes. Membranes were blocked in 5% milk in Tris-buffered saline with 0.1% Tween 20 (TBST) and incubated with the primary antibody against PAI-1 (BD Biosciences/Pharmingen, San Diego, CA, USA), α-SMA (Sigma-Aldrich, Saint Louis, MO, USA) or β-actin (Santa Cruz Biotechnology, CA, USA) followed by incubation with the corresponding peroxidase-conjugated secondary antibody. Peroxidase activity was detected using an enhanced chemiluminescence detection system.

Assay of plasmin activity

The plasmin activity in total renal cortical tissue homogenates was measured using the plasmin-specific chromogenic substrate Chromozym PL (Roche Diagnostics, Indianapolis, IN, USA), as described by Krag S *et al*[14]. This substance is specifically cleaved by plasmin into a residual peptide and 4-nitraniline, which can be detected spectrophotometrically at 405 nm. A standard linear curve was generated with serial dilutions of human plasmin (Roche Applied Science, Penzberg, Germany). Plasmin activity was determined from the standard curve. Results were expressed as μU/mg total protein.

Assay of MMP-2 activity

The renal cortex was homogenized, quantitated, and analyzed for MMP-2 activity by a commercial assay kit (Amersham Biosciences, Buckinghamshire, UK). As described in the protocol supplied, any active MMP-2 present in the sample is captured by the anti-MMP-2 antibody, and bound MMP-2 is detected using a specific chromogenic peptide substrate. Standard MMP-2 (0-16 ng/mL) and experimental samples were placed in 96-well plates for the detection of endogenous and active MMP-2. Plates were read at 405 nm at time zero and after 6 h. Active MMP-2 activity was determined from the standard curve. Results were expressed as pg/mg total protein.

Blood chemical analysis

To test for potential side effects of atRA, such as liver and kidney damage, serum parameters were measured using an autoanalyzer methodology.

Statistical analysis

Data were expressed as the mean±SEM. Statistical analysis was performed using SigmaStat 2.0 software. The differences in mean values between groups were analyzed with a one-way ANOVA followed by a Student-Newman-Keuls test or by a Kruskal-Wallis nonparametric ANOVA followed by a Dunn multiple comparison test, as appropriate. Correlation coefficient was tested for statistical significance using the Spearman's rank test and Pearson's rank coefficients. A P value of <0.05 was considered statistically significant.

Results

Effects of atRA treatment on blood pressure and renal function

Before the operation, BP measured by the tail-cuff method was similar in all of the groups used in the current study (Table 1). At week 14 after the operation, the systolic, diastolic, and mean BPs directly detected in cannulated, conscious rats were markedly elevated in the 5/6Nx+vehicle group compared with Sham+vehicle rats (P<0.05). Treatment with either dose of atRA decreased systolic BP in 5/6 nephrectomized rats (P<0.05 *vs* 5/6Nx+vehicle). At the end of the experiment, the average heart rates were similar for each group. Twenty four-hour urinary protein excretion was progressively increased in the 5/6Nx+vehicle group (P<0.05 *vs* Sham+vehicle) (Figure 1A). Proteinuria was markedly decreased as early as week 2 after atRA administration, and this antiproteinuric effect of atRA was so effective that urinary albumin was almost normalized to control levels (P<0.05 *vs* 5/6Nx+vehicle). In the 5/6Nx+vehicle group, the serum creatinine concentration remained elevated throughout the entire experimental period (P<0.05 *vs* Sham+vehicle) (Figure 1B). Treatment with either dose of atRA decreased the elevated serum creatinine levels in 5/6 nephrectomized rats (P<0.05 *vs* 5/6Nx+vehicle). Following 5/6Nx, rats developed renal failure with a marked decrease in glomerular filtration rate, as estimated by creatinine clearance (P<0.05 *vs* Sham+vehicle) (Figure 1C). The creatinine clearance in 5/6 nephrectomized rats was slightly increased by atRA. However, this increase only reached statistical significance at the time point of week 6 after atRA administration.

Table 1. Effects of atRA on hemodynamic parameters.

Group	Initial	Final (14 week)			
	Tail-cuff pressure (mmHg)	SBP (mmHg)	DBP (mmHg)	MAP (mmHg)	HR (beats/min)
Sham+vehicle (n=7)	125±5	144±3	101±4	120±4	348±6
5/6Nx+vehicle (n=8)	121±4	189±4[b]	132±7[b]	160±5[b]	339±18
5/6Nx+atRA1 (n=9)	124±3	166±7[be]	113±7	138±7	363±13
5/6Nx+atRA2 (n=10)	125±3	167±8[be]	116±8	144±8[b]	340±10

Values are mean±SEM. n, number of rats. SBP, systolic blood pressure; DBP, diastolic blood pressure; MAP, mean arterial pressure; HR, heart rate. [b]P<0.05 *vs* Sham+vehicle; [e]P<0.05 *vs* 5/6Nx+vehicle.

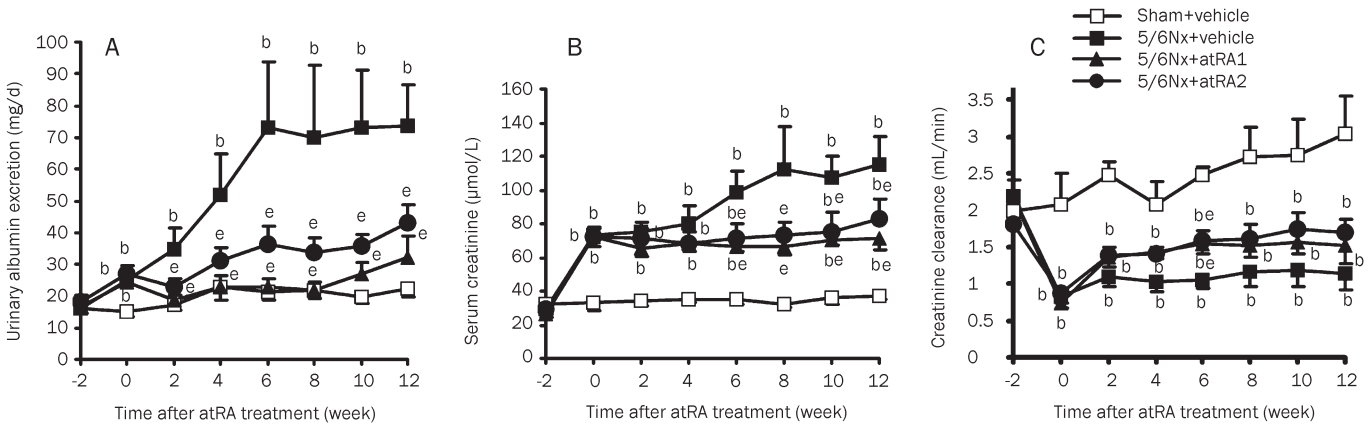

Figure 1. Effects of atRA on urinary albumin excretion (A), serum creatinine level (B), and creatinine clearance (C). The 5/6 nephrectomy provoked the increases in proteinuria and serum creatinine as well as the reduction in the glomerular filtration rate, as estimated by creatinine clearance. Treatment with atRA (5 or 10 mg/kg) at week 2 after the 5/6 nephrectomy for 12 weeks reduced the increases in proteinuria and serum creatinine. This treatment had no effect on the fall in creatinine clearance except at week 6 after atRA treatment. Values are mean±SEM. n=7–10 rats/group. ^{b}P<0.05 *vs* Sham+vehicle, ^{e}P<0.05 *vs* 5/6Nx+vehicle.

Effect of atRA treatment on glomerulosclerosis

Figure 2A shows representative PAS stains of glomeruli from sham-operated (Figure 2Aa) and 5/6 nephrectomized rats that were treated with vehicle alone (Figure 2Ab), or with low- (Figure 2Ac) or high-dose atRA (Figure 2Ad). The glomerular sclerosis index was markedly higher in the 5/6Nx+vehicle group compared to the Sham+vehicle group (P<0.05) (Figure 2B). Treatment with the two doses of atRA lowered the glomerulosclerosis index in 5/6 nephrectomized rats (P<0.05 *vs* 5/6Nx+vehicle).

Effect of atRA treatment on protein expressions of PAI-1 and α-SMA

Figure 3A shows the protein expression levels of PAI-1 and α-SMA in renal cortex extract from Western blot analyses. PAI-1 expression was increased approximately 16-fold in the 5/6Nx+vehicle group compared with the Sham+vehicle group (P<0.05) (Figure 3B). PAI-1 expression induced by 5/6Nx was markedly downregulated by atRA treatment in a concentration-dependent fashion (P<0.05 *vs* 5/6Nx+vehicle). α-SMA expression was increased more than 4-fold in 5/6Nx+vehicle rats compared with Sham+vehicle rats (P<0.05) (Figure 3C). Treatment with atRA markedly suppressed the elevation of α-SMA expression in 5/6 nephrectomized rats in a dose-dependent manner (P<0.05 *vs* 5/6Nx+vehicle). The expression of α-SMA correlated well with that of PAI-1 (r= 0.759, P<0.0001) (Figure 3D).

Effect of atRA on the activities of plasmin and MMP-2

Figure 4 shows the activities of plasmin and MMP-2 in kidney cortical homogenates. Somewhat surprisingly, plasmin activity remained unchanged in 5/6 nephrectomized rats (Figure 4A). Moreover, plasmin activity was not altered by either dose of atRA, although PAI-1 expression was downregulated. Also unexpectedly, MMP-2 activity was increased in the

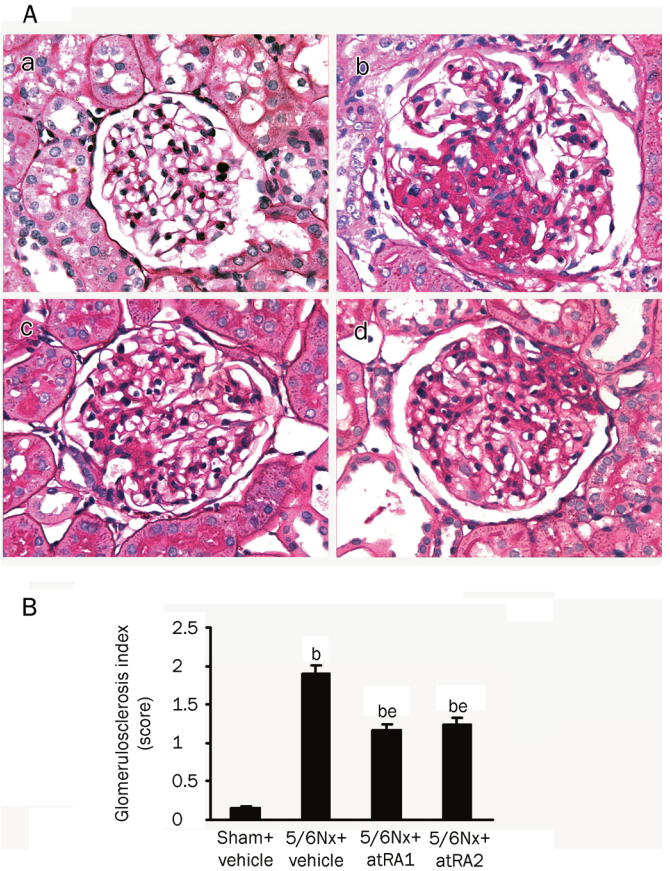

Figure 2. Degree of glomerulosclerosis. (A) Representative images of PAS stains of glomeruli from sham-operated rats treated with vehicle (a) and 5/6 nephrectomized rats that were treated with vehicle (b) or 5 mg/kg atRA (c) or 10 mg/kg atRA (d) once daily. Magnification, ×400. (B) Glomerulosclerosis index (GSI) (0 to 4 score). The GSI was increased in vehicle-treated rats with 5/6 nephrectomy. This increase in GSI was decreased with atRA treatment. Values are mean±SEM. n=7–10 rats/group. ^{b}P<0.05 *vs* Sham+vehicle. ^{e}P<0.05 *vs* 5/6Nx+vehicle.

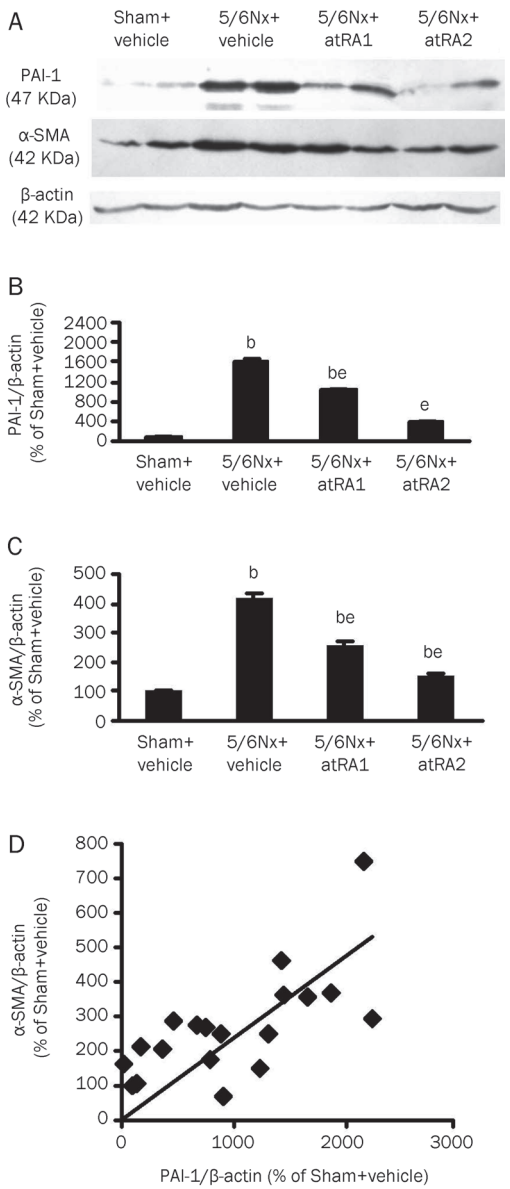

Figure 3. Western blot analysis of protein expressions for plasminogen activator inhibitor-1 (PAI-1) and α-smooth muscle actin (α-SMA) in the renal cortex. (A) Representative protein bands of PAI-1, α-SMA, and β-actin. (B) PAI-1/β-actin protein ratio according to band density. (C) α-SMA/β-actin protein ratio. The protein ratios of PAI-1/β-actin and α-SMA/β-actin were markedly increased in vehicle-treated rats with 5/6 nephrectomy. These increases were attenuated by atRA treatment in a dose-dependent manner. Values are mean±SEM. n=6. ^{b}P<0.05 *vs* Sham+vehicle; ^{e}P<0.05 *vs* 5/6Nx+vehicle. (D) Correlation between α-SMA and PAI-1 expression (r=0.759, P<0.0001).

5/6Nx+vehicle group (P<0.05 *vs* Sham+vehicle) (Figure 4B). The low dose of atRA moderately decreased the elevation of MMP-2 activity in 5/6 nephrectomized rats, but did not reach statistical significance. The high dose of atRA had no effect on MMP-2 activity.

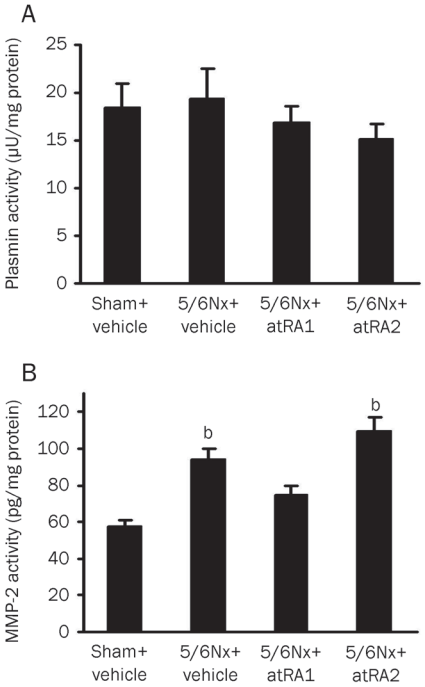

Figure 4. Chromogenic assay for activities of plasmin (A) and MMP-2 (B) in the renal cortex. Plasmin activity was unchanged and MMP-2 activity was increased in vehicle-treated rats with 5/6 nephrectomy. Treatment with atRA had no effect on the activity of either plasmin or MMP-2. Values are mean±SEM. n=7−10 rats/group. ^{b}P<0.05 *vs* Sham+vehicle.

Effect of atRA on body weight and serum parameters

Table 2 shows that there was no statistical difference in the initial or final body weights of the four groups. There was also no statistical difference in serum parameters such as alanine aminotransferase (ALT), glucose (GLU), triglyceride (TG), and cholesterol (CHO) levels, although at the higher dose of atRA, a slight increase in serum TG level was observed. It is therefore unlikely that either of the two doses of atRA caused any obvious side effects.

Discussion

The major finding of this study is that the amelioration of glomerulosclerosis with atRA is associated with a decrease in PAI-1 and α-SMA, but is not associated with changes in the activities of plasmin and MMP-2. This study expands our understanding of the mechanisms of atRA-mediated renoprotection and provides further evidence that both a pathogenic role for PAI-1 induction and a protective role for PAI-1 inhibition in renal fibrosis might be independent of the effects on the regulation of plasmin and MMP-2 activity.

It has been reported that renin-dependent and renin-independent mechanisms are responsible for hypertension in rats with 5/6Nx[32, 33]. In the present study, hypertension in 5/6 nephrectomized rats was decreased by treatment with two doses of atRA. This decrease is, at the very least, attributed to the known inhibitory effects of retinoids on the activity of the

Table 2. Effects of atRA on body weight and blood chemistry.

Group	Initial	Final (14 week)				
	Body weight (g)	Body weight (g)	ALT (U/L)	GLU (mmol/L)	TG (mmol/L)	CHO (mmol/L)
Sham+vehicle (*n*=7)	283±12	546±14	80.7±10.6	8.53±0.63	0.83±0.15	1.91±0.14
5/6Nx+vehicle (*n*=8)	289±16	538±23	75.0±13.9	7.46±0.94	1.29±0.41	1.87±0.09
5/6Nx+atRA1 (*n*=9)	284±11	529±20	74.8±6.9	8.08±0.51	1.13±0.11	1.84±0.10
5/6Nx+atRA2 (*n*=10)	269±8	539±13	68.4±9.0	7.82±0.56	1.75±0.29	1.88±0.08

Values are mean±SEM. *n*, number of rats. ALT, alanine aminotransferase; GLU, glucose; TG, triglyceride; CHO, cholesterol. There was no statistical difference in body weight or the blood chemical profile in any group.

renin-angiotensin system, particularly on the expression of the Ang II type 1 receptor[26, 27]. However, previous work from our laboratory has shown that identical doses of atRA tended to lower blood pressure in SHR but failed to reach statistical significance[29]. Some possible explanations for this may be the different model and the different starting time of atRA administration. Because hypertension is a risk factor for the progression of renal diseases[34], a decrease in hypertension underlies the renoprotective effects of atRA.

Twenty four-hour urinary protein excretion was measured every 2 weeks to serve as a surrogate marker for glomerular damage. The time course of proteinuria showed that proteinuria in 5/6 nephrectomized rats was so effectively decreased with atRA treatment that it was almost normalized. This antiproteinuric effect occurred as early as week 2 after treatment. Treatment with atRA has also been reported to decrease proteinuria in other models of kidney disease[23–25]. It is well known that defects in the glomerular filtration barrier lead to proteinuria[35], and that podocytes play a pivotal role in glomerular barrier function[36, 37]. The upregulation of nephrin and podocin in podocytes by atRA, *in vivo* and *in vitro*, was proposed as a possible mechanism for its antiproteinuric effect[23, 24]. Because proteinuria is also a risk factor for the progression of renal diseases[38], a decrease in proteinuria at least partly mediates the renoprotective effects of atRA.

The glomerular filtration rate, as reflected by creatinine clearance, was markedly decreased by 5/6Nx. This decrease is mainly due to a reduction in functional nephron number. Additionally, with the development of glomerular injury, mesangial cell proliferation and mesangial matrix deposition lead to narrowness or obliteration of glomerular capillary loops[39], which eventually results in the loss of originally functional nephrons and a further decrease in glomerular filtration rate. A slightly increased creatinine clearance was observed in atRA-treated 5/6 nephrectomized rats over the period observed. Although this increase appeared to be insignificant, it occurred despite severe nephron loss. Obviously, the increased creatinine clearance in atRA-treated nephrectomized rats is due to less glomerulosclerosis and less destruction of renal structure. Accordingly, the increase in creatinine clearance leads to a decrease in serum creatinine level in the atRA-treated nephrectomized group.

Treatment with atRA decreased glomerulosclerosis in 5/6 nephrectomized rats, as evidenced by the decreased glomerular deposition of PAS positive ECM. It is well known that the cell type responsible for most ECM synthesis is the myofibroblast, distinguished by the acquisition of a α-SMA phenotype. In normal kidney, α-SMA is expressed exclusively in the intrarenal arteries; however, in a number of glomerulonephritis models, mesangial cells are activated into α-SMA positive myofibroblasts and proliferate, producing excessive ECM in glomeruli[3–6]. In the present study, Western blot analysis showed that α-SMA expression was increased in the renal cortex of nephrectomized rats and that it was decreased with atRA treatment. Since atRA is a well-known powerful anti-proliferative drug that can inhibit the proliferation of many cell types, including mesangial cells[40–44], we speculate that atRA can inhibit the proliferation of glomerular α-SMA positive myofibroblasts, thus limiting ECM production. Additionally, atRA may inhibit α-SMA expression per cell. Wen X *et al*[45] showed that 9-*cis* RA, an isomer of atRA, inhibited the TGF-β1-induced α-SMA expression in cultured mesangial cells without influencing cell number.

Recently, attention has focused on the role of PAI-1 in the pathogenesis of fibrosis based on its increased expression in a variety of fibrotic diseases and on the beneficial effects of its inhibition or depletion in some fibrosis models[9–15]; however, the mechanism of its action remains controversial. *In vitro* studies document that ECM degradation by cultured mesangial cells is inhibited by plasmin inhibitors and increased by the addition of a PAI-1 monoclonal antibody[19]. In experimental anti-thy-1 nephritis, glomerulosclerosis is developed and accompanied by a decrease in plasmin activity in isolated glomeruli; these changes can be reversed by a mutant noninhibitory PAI-1 that competes with endogenous PAI-1 or by recombinant t-PA[15, 46]. It seems likely that PAI-1 exerts profibrotic effect through inhibiting plasmin generation. However, this explanation is not supported by our study. In the present study, Western blot analysis of renal cortex homogenates showed a greater than 16-fold increase in PAI-1 expression in disease controls compared with sham-operated rats. We expected the activities of plasmin and MMP-2 to decrease. However, plasmin activity was unchanged and MMP-2 activity was increased. Moreover, PAI-1 expression was sup-

pressed by atRA administration. We expected the activities of plasmin and MMP-2 to increase. However, we observed that they were unchanged. This is conceivable based on the fact that PAI-1 is just one of regulators of plasmin activity. For example, α_2-antiplasmin is also an inhibitor of plasmin. Indeed, α_2-antiplasmin, the most abundant form in normal kidneys, was suppressed following ureteral obstruction[11]. Consistent with our results, some reports have shown that the increase in PAI-1 and fibrosis is not always accompanied by a decrease in plasmin and MMP-2 activities[11, 12, 14, 16]. Further, PAI-1 deficiency and decreased fibrosis are not always accompanied by an augmentation of plasmin and MMP-2 activities. These data and our results suggest that PAI-1, at least, has a plasmin/MMP-2-independent fibrogenic function. However, the mechanism by which it controls fibrosis remains largely unknown[7]. Oda T *et al* reported that PAI-1 promoted macrophage chemotaxis *in vitro*[11]. Our results showed an excellent correlation between α-SMA and PAI-1 expression, but the causal relation between them is not known.

It must be emphasized that PA, plasmin, and MMP are not always protective and have both beneficial and injurious effects on fibrogenesis, depending on the model of fibrosis. Injections with t-PA restored declined glomerular plasmin activity and ameliorated fibrosis in experimental glomerulonephritis[46]. The deficiency of either plasminogen or t-PA in mice increased the severity of crescentic glomerulonephritis[47], but decreased the degree of renal interstitial fibrosis after unilateral ureteral obstruction[48, 49]. Active MMP-2 has been reported to directly lead to a transition of cultured mesangial cells from the quiescent phenotype to the activated phenotype, characterized by an augmentation in the proliferation and synthesis of ECM proteins[50]. Active MMP-2 or plasmin can promote the transdifferentiation of murine tubular epithelial cells to myofibroblasts[51, 52]. Plasmin has also been shown to play a role in leukocyte recruitment[53]. These data suggest that PA, plasmin, and MMP-2 have other actions in addition to degrading the ECM. Together, all these actions determine whether the net effect is profibrotic or antifibrogenic.

Ang II and TGF-β1 have been established as crucial contributors to ECM expansion and fibrosis in a number of renal diseases[54–56]. PAI-1 is strongly induced by these two cytokines. PAI-1 reduction by atRA treatment in the present study is likely to be associated with the retinoids' inhibitory effects on the activities of Ang II/Ang II type 1 receptor and TGF-β1/TGF-β receptor[26–28]. We have recently shown that atRA directly inhibits PAI-1 production induced by TGF-β1 and Ang II in cultured mesangial cells *in vitro*[30].

The reduction in PAI-1 and α-SMA by atRA was dose dependent, suggesting that atRA may have direct inhibitory effects on PAI-1 and α-SMA expressions. In contrast, the beneficial effects of atRA on renal function, including decreasing proteinuria and serum creatinine concentration, were inversely dose dependent. This finding may reflect a toxic effect of the higher dose of atRA, as indicated by a slight increase in serum triglyceride levels in rats that received the high dose of atRA (10 mg/kg). Morath C *et al* showed that higher doses of retinoids may evoke some side effects[27]. The reduction in the glomerular deposition of ECM by atRA showed no dose-dependent difference. This phenomenon can be explained because high doses of atRA had a tendency to reduce the specific beneficial effects of atRA administration due to its concomitant unspecific toxicity.

Taken altogether, our findings suggest that the beneficial effects of atRA on glomerular damage in a rat model of 5/6 nephrectomy are, in part, due to the reduction of PAI-1 and α-SMA expressions, independent of plasmin activity. Treatment with atRA could be a promising intervention for kidney disease. Further studies are required to determine the atRA dose that is the most effective without causing harm.

Acknowledgements

This work was supported by grants from the Ministry of Science and Technology of China (No 2010CB912601, 2006CB503804, 2009ZX09303-006, 2009ZX09301-011), the National Natural Science Foundation of China (No 30825016, 30971064), the Science and Technology Commission of Shanghai Municipality (No 09XD1400400, 08JC1401400) and College Natural Science Research Foundation of Jiangsu Province (No 07KJD310171).

We would like to thank Dr Peter ROSE for critical comments regarding this manuscript.

Author contribution

Xia LIU, Lei LÜ, and Yi-chun ZHU designed research; Xia LIU and Lei LÜ performed research; Xia LIU, Lei LÜ, Bei-bei TAO, and Ai-ling ZHOU analyzed data; Xia LIU and Yi-chun ZHU wrote the paper.

References

1 Remuzzi G, Bertani T. Pathophysiology of progressive nephropathies. N Engl J Med 1998; 339: 1448–56.
2 Birkedal-Hansen H. Proteolytic remodeling of extracellular matrix. Curr Opin Cell Biol 1995; 7: 728–35.
3 Johnson RJ, Floege J, Yoshimura A, Iida H, Couser WG, Alpers CE. The activated mesangial cell: a glomerular "myofibroblast"? J Am Soc Nephrol 1992; 2: S190–7.
4 Zhang G, Moorhead PJ, el Nahas AM. Myofibroblasts and the progression of experimental glomerulonephritis. Exp Nephrol 1995; 3: 308–18.
5 Johnson RJ, Iida H, Alpers CE, Majesky MW, Schwartz SM, Pritzi P, *et al*. Expression of smooth muscle cell phenotype by rat mesangial cells in immune complex nephritis. Alpha-smooth muscle actin is a marker of mesangial cell proliferation. J Clin Invest 1991; 87: 847–58.
6 Muchaneta-Kubara EC, el Nahas AM. Myofibroblast phenotypes expression in experimental renal scarring. Nephrol Dial Transplant 1997; 12: 904–15.
7 Eddy AA. Plasminogen activator inhibitor-1 and the kidney. Am J Physiol Renal Physiol 2002; 283: F209–20.
8 Eitzman DT, McCoy RD, Zheng X, Fay WP, Shen T, Ginsburg D, *et al*. Bleomycin-induced pulmonary fibrosis in transgenic mice that either lack or overexpress the murine plasminogen activator inhibitor-1 gene. J Clin Invest 1996; 97: 232–7.
9 Matsuo S, López-Guisa JM, Cai X, Okamura DM, Alpers CE, Bumgarner RE, *et al*. Multifunctionality of PAI-1 in fibrogenesis: evidence from

obstructive nephropathy in PAI-1-overexpressing mice. Kidney Int 2005; 67: 2221–38.
10 Kitching AR, Kong YZ, Huang XR, Davenport P, Edgtton KL, Carmeliet P, *et al*. Plasminogen activator inhibitor-1 is a significant determinant of renal injury in experimental crescentic glomerulonephritis. J Am Soc Nephrol 2003; 14: 1487–95.
11 Oda T, Jung YO, Kim HS, Cai X, López-Guisa JM, Ikeda Y, *et al*. PAI-1 deficiency attenuates the fibrogenic response to ureteral obstruction. Kidney Int 2001; 60: 587–96.
12 Nicholas SB, Aguiniga E, Ren Y, Kim J, Wong J, Govindarajan N, *et al*. Plasminogen activator inhibitor-1 deficiency retards diabetic nephropathy. Kidney Int 2005; 67: 1297–307.
13 Ma J, Weisberg A, Griffin JP, Vaughan DE, Fogo AB, Brown NJ. Plasminogen activator inhibitor-1 deficiency protects against aldosterone-induced glomerular injury. Kidney Int 2006; 69: 1064–72.
14 Krag S, Danielsen CC, Carmeliet P, Nyengaard J, Wogensen L. Plasminogen activator inhibitor-1 gene deficiency attenuates TGF-beta1-induced kidney disease. Kidney Int 2005; 68: 2651–66.
15 Huang Y, Haraguchi M, Lawrence DA, Border WA, Yu L, Noble NA. A mutant, noninhibitory plasminogen activator inhibitor type 1 decreases matrix accumulation in experimental glomerulonephritis. J Clin Invest 2003; 112: 379–88.
16 Omasu F, Oda T, Yamada M, Yoshizawa N, Yamakami K, Sakurai Y, *et al*. Effects of pioglitazone and candesartan on renal fibrosis and the intrarenal plasmin cascade in spontaneously hypercholesterolemic rats. Am J Physiol Renal Physiol 2007; 293: F1292–8.
17 Heidland A, Sebekova K, Paczek L, Teschner M, Dämmrich J, Gaciong Z. Renal fibrosis: role of impaired proteolysis and potential therapeutic strategies. Kidney Int Suppl 1997; 62: S32–5.
18 Visse R, Nagase H. Matrix metalloproteinases and tissue inhibitors of metalloproteinases: structure, function, and biochemistry. Circ Res 2003; 92: 827–39.
19 Baricos WH, Cortez SL, el-Dahr SS, Schnaper HW. ECM degradation by cultured human mesangial cells is mediated by a PA/plasmin/MMP-2 cascade. Kidney Int 1995; 47: 1039–47.
20 Adams J, Kiss E, Arroyo AB, Bonrouhi M, Sun Q, Li Z, *et al*. 13-*cis* retinoic acid inhibits development and progression of chronic allograft nephropathy. Am J Pathol 2005; 167: 285–98.
21 Han SY, So GA, Jee YH, Han KH, Kang YS, Kim HK, *et al*. Effect of retinoic acid in experimental diabetic nephropathy. Immunol Cell Biol 2004; 82: 568–76.
22 Schaier M, Jocks T, Grone HJ, Ritz E, Wagner J. Retinoid agonist isotretinoin ameliorates obstructive renal injury. J Urol 2003; 170: 1398–402.
23 Suzuki A, Ito T, Imai E, Yamato M, Iwatani H, Kawachi H, *et al*. Retinoids regulate the repairing process of the podocytes in puromycin aminonucleoside-induced nephrotic rats. J Am Soc Nephrol 2003; 14: 981–91.
24 Vaughan MR, Pippin JW, Griffin SV, Krofft R, Fleet M, Haseley L, *et al*. ATRA induces podocyte differentiation and alters nephrin and podocin expression *in vitro* and *in vivo*. Kidney Int 2005; 68: 133–44.
25 Wagner J, Dechow C, Morath C, Lehrke I, Amann K, Waldherr R, *et al*. Retinoic acid reduces glomerular injury in a rat model of glomerular damage. J Am Soc Nephrol 2000; 11: 1479–87.
26 Dechow C, Morath C, Peters J, Lehrke I, Waldherr R, Haxsen V, *et al*. Effects of all-*trans* retinoic acid on renin-angiotensin system in rats with experimental nephritis. Am J Physiol Renal Physiol 2001; 281: F909–19.
27 Morath C, Ratzlaff K, Dechow C, Schwenger V, Schaier M, Zeier B, *et al*. Chronic low-dose isotretinoin treatment limits renal damage in subtotally nephrectomized rats. J Mol Med 2009; 87: 53–64.
28 Morath C, Dechow C, Lehrke I, Haxsen V, Waldherr R, Floege J, *et al*. Effects of retinoids on the TGF-beta system and extracellular matrix in experimental glomerulonephritis. J Am Soc Nephrol 2001; 12: 2300–9.
29 Lü L, Yao T, Zhu YZ, Huang GY, Cao YX, Zhu YC. Chronic all-*trans* retinoic acid treatment prevents medial thickening of intramyocardial and intrarenal arteries in spontaneously hypertensive rats. Am J Physiol Heart Circ Physiol 2003; 285: H1370–7.
30 Liu X, Lü L, Tao BB, Zhu YC. All-*trans* retinoic acid inhibits the increases in fibronectin and PAI-1 induced by TGF-beta1 and Ang II in rat mesangial cells. Acta Pharmacol Sin 2008; 29: 1035–41.
31 Raij L, Azar S, Keane W. Mesangial immune injury, hypertension, and progressive glomerular damage in Dahl rats. Kidney Int 1984; 26: 137–43.
32 Griffin KA, Picken MM, Churchill M, Churchill P, Bidani AK. Functional and structural correlates of glomerulosclerosis after renal mass reduction in the rat. J Am Soc Nephrol 2000; 11: 497–506.
33 Gonçalves AR, Fujihara CK, Mattar AL, Malheiros DM, Noronha Ide L, de Nucci G, *et al*. Renal expression of COX-2, ANG II, and AT1 receptor in remnant kidney: strong renoprotection by therapy with losartan and a nonsteroidal anti-inflammatory. Am J Physiol Renal Physiol 2004; 286: F945–54.
34 Ljutić D, Kes P. The role of arterial hypertension in the progression of non-diabetic glomerular diseases. Nephrol Dial Transplant 2003; 18: v28–30.
35 Mayer G, Lafayette RA, Oliver J, Deen WM, Myers BD, Meyer TW. Effects of angiotensin II receptor blockade on remnant glomerular permselectivity. Kidney Int 1993; 43: 346–53.
36 Pavenstädt H, Kriz W, Kretzler M. Cell biology of the glomerular podocyte. Physiol Rev 2003; 83: 253–307.
37 Shankland SJ. The podocyte's response to injury: role in proteinuria and glomerulosclerosis. Kidney Int 2006; 69: 2131–47.
38 Zoja C, Benigni A, Remuzzi G. Cellular responses to protein overload: key event in renal disease progression. Curr Opin Nephrol Hypertens 2004; 13: 31–7.
39 Lee LK, Meyer TW, Pollock AS, Lovett DH. Endothelial cell injury initiates glomerular sclerosis in the rat remnant kidney. J Clin Invest 1995; 96: 953–64.
40 Raffo P, Emionite L, Colucci L, Belmondo F, Moro MG, Bollag W, *et al*. Retinoid receptors: pathways of proliferation inhibition and apoptosis induction in breast cancer cell lines. Anticancer Res 2000; 20: 1535–43.
41 Hansen LA, Sigman CC, Andreola F, Ross SA, Kelloff GJ, De Luca LM. Retinoids in chemoprevention and differentiation therapy. Carcinogenesis 2000; 21: 1271–9.
42 Simonson MS. Anti-AP-1 activity of all-*trans* retinoic acid in glomerular mesangial cells. Am J Physiol 1994; 267: F805–15.
43 Haxsen V, Adam-Stitah S, Ritz E, Wagner J. Retinoids inhibit the actions of angiotensin II on vascular smooth muscle cells. Circ Res 2001; 88: 637–44.
44 Miano JM, Kelly LA, Artacho CA, Nuckolls TA, Piantedosi R, Blaner WS. All-*trans*-retinoic acid reduces neointimal formation and promotes favorable geometric remodeling of the rat carotid artery after balloon withdrawal injury. Circulation 1998; 98: 1219–27.
45 Wen X, Li Y, Hu K, Dai C, Liu Y. Hepatocyte growth factor receptor signaling mediates the anti-fibrotic action of 9-*cis*-retinoic acid in glomerular mesangial cells. Am J Pathol 2005; 167: 947–57.
46 Haraguchi M, Border WA, Huang Y, Noble NA. t-PA promotes glomerular plasmin generation and matrix degradation in experimental glomerulonephritis. Kidney Int 2001; 59: 2146–55.

47 Kitching AR, Holdsworth SR, Ploplis VA, Plow EF, Collen D, Carmeliet P, *et al*. Plasminogen and plasminogen activators protect against renal injury in crescentic glomerulonephritis. J Exp Med 1997; 185: 963–8.
48 Yang J, Shultz RW, Mars WM, Wegner RE, Li Y, Dai C, *et al*. Disruption of tissue-type plasminogen activator gene in mice reduces renal interstitial fibrosis in obstructive nephropathy. J Clin Invest 2002; 110: 1525–38.
49 Edgtton KL, Gow RM, Kelly DJ, Carmeliet P, Kitching AR. Plasmin is not protective in experimental renal interstitial fibrosis. Kidney Int 2004; 66: 68–76.
50 Turck J, Pollock AS, Lee LK, Marti HP, Lovett DH. Matrix metalloproteinase 2 (gelatinase A) regulates glomerular mesangial cell proliferation and differentiation. J Biol Chem 1996; 271: 15074–83.
51 Cheng S, Lovett DH. Gelatinase A (MMP-2) is necessary and sufficient for renal tubular cell epithelial-mesenchymal transformation. Am J Pathol 2003; 162: 1937–49.
52 Zhang G, Kernan KA, Collins SJ, Cai X, López-Guisa JM, Degen JL, *et al*. Plasmin(ogen) promotes renal interstitial fibrosis by promoting epithelial-to-mesenchymal transition: role of plasmin-activated signals. J Am Soc Nephrol 2007; 18: 846–59.
53 Ploplis VA, French EL, Carmeliet P, Collen D, Plow EF. Plasminogen deficiency differentially affects recruitment of inflammatory cell populations in mice. Blood 1998; 91: 2005–9.
54 Border WA, Noble N. Maximizing hemodynamic-independent effects of angiotensin II antagonists in fibrotic diseases. Semin Nephrol 2001; 21: 563–72.
55 Gagliardini E, Benigni A. Therapeutic potential of TGF-beta inhibition in chronic renal failure. Expert Opin Biol Ther 2007; 7: 293–304.
56 Wolf G. Link between angiotensin II and TGF-beta in the kidney. Miner Electrolyte Metab 1998; 24: 174–80.

Acta Pharmacologica Sinica (2011) 32: 79–88
 1671-4083/11 $32.00
www.nature.com/aps

Original Article

Enhancement of cytotoxicity of antimicrobial peptide magainin II in tumor cells by bombesin-targeted delivery

Shan LIU, Hao YANG, Lin WAN, Hua-wei CAI, Sheng-fu LI, You-ping LI, Jing-qiu CHENG, Xiao-feng LU*

Key Lab of Transplant Engineering and Immunology, Ministry of Health, West China Hospital, Sichuan University, Chengdu 610041, China

Aim: To investigate whether the conjugation of magainin II (MG2), an antimicrobial peptides (AMPs), to the tumor-homing peptide bombesin could enhance its cytotoxicity in tumor cells.
Methods: A magainin II-bombesin conjugate (MG2B) was constructed by attaching magainin II (MG2) to bombesin at its N-terminus. The peptides were synthesized using Fmoc-chemistry. The *in vitro* cytotoxicity of the peptide in cancer cells was quantitatively determined using the CCK-8 cell counting kit. Moreover, the *in vivo* antitumor effect of the peptide was determined in tumor xenograft models.
Results: The IC_{50} of MG2B for cancer cells (10-15 μmol/L) was at least 10 times lower than the IC_{50} of unconjugated MG2 (125 μmol/L). Moreover, the binding affinity of MG2B for cancer cells was higher than that of unconjugated MG2. In contrast, conjugation to a bombesin analog lacking the receptor-binding domain failed to increase the cytotoxicity of MG2, suggesting that bombesin conjugation enhances the cytotoxicity of MG2 in cancer cells through improved binding. Indeed, MG2B selectively induced cell death in cancer cells *in vitro* with the IC_{50} ranging from 10 to 15 μmol/L, which was about 6–10 times lower than the IC_{50} for normal cells. MG2B (20 mg/kg per day, intratumorally injected for 5 d) also exhibited antitumor effects in mice bearing MCF-7 tumor grafts. The mean weights of tumor grafts in MG2B- and PBS-treated mice were 0.21±0.05 g and 0.59±0.12 g, respectively.
Conclusion: The results suggest that conjugation of AMPs to bombesin might be an alternative approach for targeted cancer therapy.

Keywords: targeted cancer therapy; antimicrobial peptide; tumor-homing peptide; bombesin; magainin

Acta Pharmacologica Sinica (2011) 32: 79–88; doi: 10.1038/aps.2010.162; published online 6 Dec 2010

Introduction

Conventional cancer chemotherapy is limited by the lack of specificity and multi-drug resistance. Thus, novel approaches to cancer therapy with a higher degree of selectivity for cancer cells and a lower risk for induction of resistance is desired[1, 2]. Recent attention has focused on membrane-active antimicrobial peptides (AMPs) with selective anticancer activity[1, 3, 4]. AMPs are positively charged molecules that exert their cytotoxicity by binding to the outer membrane of cancer cells, which contain 3%–9% anionic phosphatidylserine. In contrast, membranes of normal cells consist largely of zwitterionic phospholipids (neutral in net charge) and are therefore less attractive to cationic AMPs[5]. AMPs are selectively cytotoxic in cancer cells[4] and are usually membrane-active, suggesting a low risk for induction of resistance[4]. Overall, AMPs are selective cytotoxic agents for cancer cells with therapeutic implications.

A great number of AMPs have been isolated from the skin secretions of amphibians[4, 6, 7]. Of these peptides, the best studied AMP is magainin II (MG2), which was isolated from the skin of the African clawed frog *Xenopus laevis*[8]. MG2 has been reported to be selectively cytotoxic for hematopoietic and solid tumor cells[2, 9, 10]. However, MG2 only exhibits obvious cytotoxicity in cancer cells at high concentrations. The average IC_{50} of MG2 against many cancer cell lines is greater than 100 μmol/L[2, 9, 11]. Most likely, this poor potency arises from the limited cell membrane-binding ability of MG2. Because electrostatic interactions between the peptide's positive charges and the negative charges on the cell membrane play a crucial role in the binding process[4], one strategy for improving peptide binding is to increase the number of positive charges on the peptide by amino acid substitution. MG2 analogs with increased positive charges show enhanced membrane binding affinities[12] and cytotoxicity[9, 11]. In addition, conjugation of

* To whom correspondence should be addressed.
E-mail xiaofenglu@yahoo.com
Received 2010-05-05 Accepted 2010-08-16

the cationic KLA peptide $(KLAKLAK)_2$ to a carrier peptide significantly enhanced its cytotoxicity in cancer cells[13, 14]. Consequently, conjugation of MG2 to a carrier peptide recognizing a specific surface marker on cancer cells might also improve its cytotoxicity.

Tumor-homing peptides can bind to tumor cells or tumor blood/lymphatic vessels with high affinity and specificity[15, 16]. In addition, many tumor-homing peptides can be internalized by tumor cells and accumulate in tumors at high concentrations[17, 18]. Therefore, these tumor-homing peptides are attractive drug carriers. Among these peptides, somatostatin and its analogs have been extensively investigated. The radiolabeled somatostatin analog ^{111}In-DTPA-octreotide (^{111}In-OctreoScan, Novartis) has been approved by the US Food and Drug Administration for scintigraphy in patients with NETs[19]. In addition, bombesin and its analogs also show great promise for tumor targeting. Bombesin is a 14-amino acid tumor-homing peptide that was isolated from frog skin[20]. Its receptors are overexpressed in a variety of common human cancers, such as neuroblastoma and small cell lung cancer, as well as cancers of the prostate, kidney, uterus, ovary, breast, pancreas, gastrointestinal tract, head and neck, and esophagus [21, 22]. Bombesin can effectively deliver radioactive[23] and chemotherapeutic agents[24] to target cells due to its high affinity for these receptors. Because bombesin can specifically bind to its receptors with high affinity, the conjugation MG2 to bombesin might enhance the cytotoxicity of MG2 in cancer cells by improving its binding affinity.

In this paper, we first measured the binding of fluorescein isothiocyanate (FITC)-labeled bombesin to solid tumor cells, malignant hematopoietic cells, and normal cells. Subsequently, two conjugates were constructed by attaching MG2 to bombesin and a mutant form of bombesin lacking the receptor-binding domain. The cytotoxicity and binding ability of these peptides were further analyzed. Finally, the *in vivo* antitumor effect of the MG2-bombesin conjugate was evaluated. It was found that the conjugation to bombesin significantly enhanced the cytotoxicity of MG2 in cancer cells.

Materials and methods

Peptide synthesis

To probe bombesin-targeted delivery of MG2 to tumor cells, the MG2-bombesin conjugate (MG2B) was constructed by attaching MG2 to bombesin at its N-terminus. Another conjugate, MG2Ba, which contained MG2 and a bombesin analog lacking the C-terminal 8-14 amino acids, was also constructed. Because the C-terminal domain of bombesin is crucial for its receptor-binding activity[25], the attachment of MG2 to the bombesin analog lacking the receptor-binding domain should not significantly improve its membrane-binding affinity. Unconjugated bombesin, unconjugated MG2, and an unrelated peptide (URP) were synthesized. All peptides (Table 1) were synthesized using Fmoc-chemistry (Genescript Inc, Nanjing, China). The purity of these peptides (>95%) was analyzed by reversed-phase high performance liquid chromatography, and the mass of the peptide was determined using matrix-assisted laser desorption ionization time-of-flight mass spectrometry. FITC labels were linked to the N-terminus of peptides by introducing 5-carboxyfluorescein during the final synthesis cycle. All peptides were dissolved in isotonic phosphate-buffered saline (PBS: 137 mmol/L NaCl, 2.68 mmol/L KCl, 8.09 mmol/L Na_2HPO_4, 1.76 mmol/L KH_2PO_4, pH 7.4) and stored at -70 °C until further use.

Cell culture

Unless otherwise mentioned, all cells were purchased from the American Type Culture Collection, USA. The following cells were used in this experiment: human breast cancer cells (MCF-7 and ZR-75-30); human melanoma cells (A375, M14, and A875); human prostate cancer cells (DU145); human cervical cancer cells (HeLa); human lung adenocarcinoma cells (A549); human Burkitt's lymphoma cells (Raji); human promyelocytic leukemia cells (NB4); African green monkey kidney cells (Vero E6) and Ad5 transformed human embryonic kidney cells (Hek-293A); human fibroblast cells (HSF); and human vein endothelial cells (HUVECs). Human peripheral blood mononuclear cells (hPBMCs) were isolated from healthy volunteers by Percoll density gradient centrifugation. All of the cells were cultured in either Dulbecco's modified Eagle's medium (DMEM) or RPMI 1640 supplemented with 10% fetal bovine serum (GIBCO-BRL, USA), 2 mmol/L *L*-glutamine, 100 U/mL penicillin, and 100 μg/mL streptomycin at 37 °C in a 5% CO_2 humidified atmosphere.

Cellular peptide uptake

To observe cellular uptake of FITC-labeled peptide under a fluorescence microscope, 1×10^4 cells/well were seeded into

Table 1. Peptides and sequences.

Peptide	Sequence	Length (aa*)	Molecular Weight (Da)
MG2	GIGKFLHSAKKFGKAFVGEIMNS	23	2466
Bombesin	QRLGNQWAVGHLM	13	1509
MG2B	GIGKFLHSAKKFGKAFVGEIMNSGGQRLGNQWAVGHLM	38	4072
MG2Ba	GIGKFLHSAKKFGKAFVGEIMNSGGQRLGNQ	31	3277
URP	DSHAKRHHGYKRKFHEKHHSHRGY	24	3036

*: amino acid

96-well plates and the cells were allowed to attach overnight. After being washed in PBS, the cells were further incubated with FITC-labeled peptides in 100 μL of medium supplemented with 2% bovine serum albumin (BSA) for 1 h at 37 °C. The cells were then washed and observed under a fluorescence microscope. To analyze cellular uptake of peptide by fluorescence-activated cell sorting (FACS), the adherent cells were first digested by the addition of 0.25% (*w/v*) trypsin in serum-free medium containing 0.02% of EDTA at 37 °C. After being washed with PBS, the cells (2×10^5) were incubated with 300 μL of FITC-labeled peptides at 37 °C for 1 h. The cells were then washed three times with 1 mL of PBS and analyzed by FACS.

Cytotoxicity assays

Assays were performed according to the methods of Laakkonen *et al*[26] with some modifications. Adherent cells were plated in a 96-well plate at a density of 1×10^4 cells/well and allowed to attach overnight. The cells in suspension were collected and seeded in a 96-well plate (1×10^4 cells/well) immediately before use. After being washed once with PBS, 100 μL peptide diluted in serum-free medium supplemented with 2% BSA was added to the cells and further incubated at 37 °C for 2 h. Subsequently, 10 μL of CCK-8 solution was added to the wells and the absorbance was measured 4 h later at 450 nm. Cytotoxicity was expressed as the percentage of viable cells after treatment with peptide, which was calculated by assuming 100% survival with the PBS control. Each sample was processed in triplicate and the IC_{50} value was obtained from the respective cell viability curves.

The Live/Dead BacLight bacterial viability kit (Molecular Probe) was used as an additional method to evaluate the cytotoxicity of peptides. The DNA-binding SYTO 9 and propidium iodide (PI) are green and red dyes, respectively. The former, but not the latter, is membrane permeable. Based on their differences in membrane-permeability, the Syto 9 and PI mixture stained living cells green and dead cells red. After treatment with peptide for 2 h, the cells were then double stained with SYTO 9 and PI for 5 min in the dark followed by observation under a fluorescence microscope.

Detection of apoptosis using Annexin V and PI staining

Annexin V binds to phosphatidylserine exposed on the outer cell membrane during the early stages of apoptosis. Thus, double staining with FITC-Annexin V (appearing green) and propidium iodide (appearing red) is often used to detect cells undergoing apoptosis[27]. After treatment with peptide, the cells were then double stained with FITC-Annexin V and PI according to the manufacturer's instructions. Exposure of phosphatidylserine on the outer membrane of cells was first observed under a fluorescence microscope. Simultaneously, 3×10^4 events were analyzed by FACS. Cells stained with FITC-Annexin V alone (Annexin V^+/PI^-) were considered in early apoptosis, whereas those stained with both FITC-Annexin V and PI (Annexin V^+/PI^+) were considered in the advanced stages of apoptosis or necrosis. The FITC-Annexin V and PI double-negative (Annexin V^-/PI^-) cells were considered alive.

Detection of apoptosis by monitoring mitochondrial depolarization

The cells were treated with the peptides and stained with JC-1 dye (2 μmol/L) for 30 min at 37 °C in the dark, according to the manufacturer's instructions. The cells were subsequently washed twice with PBS and analyzed using FACS. To observe the mitochondria using a fluorescence microscope, the cells were double stained with JC-1 (showing mitochondria) and DAPI (showing nuclei). The JC-1 dye forms fluorescent red J-aggregates upon localization to healthy mitochondria, whereas the monomeric form of the dye fluoresces green in the cytoplasm. Consequently, a decrease in the ratio of red to green fluorescence reflects the loss of mitochondrial membrane potential[27].

Detection of the caspase-mediated pathway in apoptosis

The assay was performed according to the method of Rege *et al*[27]. The cells were preincubated with the pan-caspase inhibitor z-VAD-Fmk (100 μmol/L) for 2 h and then treated with peptide for an additional 2 h. Cell viability was determined using the CCK-8 kit. The cytotoxicity of the peptides to cells that were preincubated with inhibitor and those that were not was compared.

Tumor xenograft model

All protocols for the animal models were approved by the University Animal Care and Use Committee. Six to eight-week-old female nude mice were obtained from the University Animal Center. About 1×10^7 MCF-7 cells suspended in 100 μL of saline were injected subcutaneously into the right flank of mice. At the onset of a palpable tumor (about 50–100 mm^3), 18 mice were divided into three groups that were intratumorally injected with 20 mg/kg MG2B, MG2 or an equivalent volume of PBS every day for a total of five days. The tumor volume (mm^3) was calculated as length×$width^2$×0.5. At the end of the experiment, all animals were killed and the tumor masses were measured.

To probe the death of tumor cells *in vivo*, a single dose of peptide (200 μg, 100 μL) was injected into the tumor graft (<1000 mm^3). The same volume of PBS was intratumorally injected into the mice of the control group. Sixteen hours post-injection, the mice were killed and the tumor grafts were excised, paraffin-embedded, sectioned, and stained with hematoxylin/eosin (H&E) to examine the histological architecture. Simultaneously, terminal nucleotidyl transferase–mediated nick end labeling (TUNEL) staining (Invitrogen) was used to examine the apoptosis of tumor cells.

Statistical analysis

Results are presented as the mean±SD of at least three experiments. Statistical comparisons were made using Student's *t* test.

Results

Bombesin specifically binds to tumor cells

As shown in Figure 1, bombesin bound 28-32 times more to MCF-7, DU145, and A375 cells than did the negative control

peptide URP. The amount of bombesin bound to HeLa, A875, M14, A549, ZR-75-30, Raji, NB4, and K562 is about 12-18 times greater than the amount of the negative control peptide URP. In contrast, both bombesin and URP bound to normal cells, including HUVECs, HSF, hPBMCs, Vero E6, and 293A at similarly low levels. These data indicate that bombesin can bind to tumor cells with high affinity.

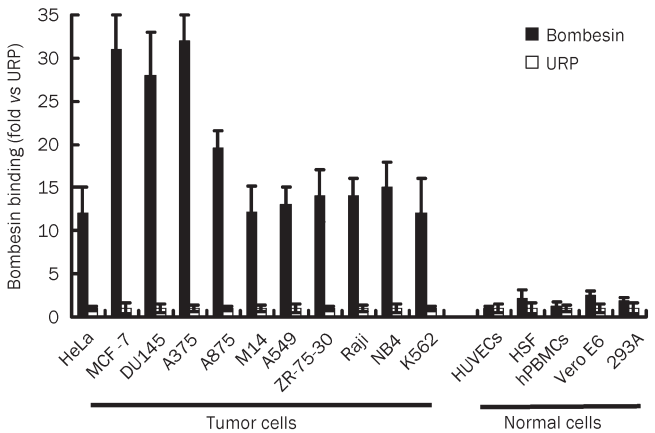

Figure 1. Binding of bombesin to tumor cells and normal cells. In preparation, about 2×10^5 cells were collected and incubated with the FITC-labeled bombesin peptide (10 μmol/L, 300 μL) at 37 °C for 1 h. After being washed with PBS, 3×10^4 cells were analyzed using FACS in each assay. The FITC-labeled URP peptide was used as a control. The binding of bombesin is shown relative to the binding of the negative control peptide URP, for which the value of mean fluorescence was set to 1. The data are expressed as means±SD.

Bombesin enhances cytotoxicity of MG2 in tumor cells

The unconjugated MG2 peptide only showed mild cytotoxicity in cancer cells at high concentrations. As shown in Figure 2A, the mixture containing unconjugated MG2 and unconjugated bombesin induced about 20% cell death in MCF-7 and A375 cells at 125 μmol/L. The IC_{50} of the unconjugated MG2 for these cells was over 200 μmol/L. However, the MG2-bombesin conjugate MG2B induced approximately 30%–40% cell death in MCF-7 and A375 cells at a low concentration of 10 μmol/L. Moreover, MG2B induced over 80% cell death in these cells when the concentration was increased to 20 μmol/L. The IC_{50} of the MG2B peptide for MCF-7 and A375 cells was within the range of 10-15 μmol/L, which is about 13–16 times lower than that for unconjugated MG2 in these cells. However, another conjugate MG2Ba, in which the MG2 peptide was conjugated to a bombesin analog lacking 8-14 amino acids at the C-terminus of bombesin, was similar to unconjugated MG2 in terms of cytotoxicity in MCF-7 and A375 cells (Figure 2A). These results suggest that the attachment to bombesin, but not the bombesin analog lacking the receptor-binding domain, at its N-terminus significantly increases the cytotoxicity of MG2 in tumor cells.

Further analysis demonstrated that MG2B is different than unconjugated MG2 in its binding ability. Figure 2B shows that 20 μmol/L of unconjugated MG2 bound to 2% MCF-7 and 8.1% A375 cells, respectively. In contrast, MG2B bound over 80% of both cells at the same concentration, as determined by FACS (Figure 2B). MG2B and unconjugated MG2 are different in efficacy of cellular translocation. Compared to unconjugated MG2 peptide, MG2B was internalized to a higher extent by MCF-7 cells (Figure 2C). In addition, the internalized MG2B peptide was uniformly distributed in the cytoplasm and rich in the nucleolus of MCF-7 cells (Figure 2D). The cytotoxicity of MG2B and MG2 was closely related to their binding and cellular translocation efficacy. These data suggest that conjugated bombesin contributes to the enhancement of cytotoxicity through improved binding and cellular translocation of MG2.

The MG2-bombesin conjugate MG2B selectively induces cell death in tumor cells

Cell viability assays using CCK-8 demonstrated that MCF-7, DU145, and A375 cells were most sensitive to MG2B. As shown in Figure 3A, the survival rates of these three cells were lower than 20% after treatment with MG2B at 20 μmol/L for 2 h. Other tumor cells including HeLa, A875, M14, A549, ZR-75-30, Raji, NB4, and K562 were also sensitive to MG2B. Twenty μmol/L MG2B induced approximately 60%–70% cell death in these tumor cells. When the concentration of MG2B was increased to 30 μmol/L, the survival rates of these tumor cells were reduced by 80%–90%. The IC_{50} of MG2B for these tumor cells was within the range of 10–15 μmol/L. However, normal cells including HUVECs, HSF, hPBMCs, Vero E6, and 293A were relatively resistant to MG2B. The IC_{50} of MG2B for these normal cells was within the range of 80 to 100 μmol/L, which is about 6-10 times higher than the IC_{50} of MG2B for tumor cells.

The selective cytotoxicity of MG2B in tumor cells was also proven by live/dead assays. As shown in Figure 3B, over 80% MCF-7 cells were indicated as dead (appearing red) after treatment with 20 μmol/L MG2B. However, over 90% of normal HSF cells were indicated as live (appearing green) after treatment with MG2B at the same concentration. These results demonstrate that tumor cells, but not normal cells, are sensitive to MG2B. The selectivity of MG2B in other tumor cells and normal cells was also detected using the live/dead assay (data not shown). FACS analysis demonstrated that MG2B bound to tumor cells with greater affinity than to normal cells. Figure 3C shows that 20 μmol/L MG2B binds to 81.9% of MCF-7 tumor cells compared to 6.1% of normal HSF cells. These results suggest that the selectivity of MG2B in tumor cells and normal cells is closely related to its binding preference in these cells.

Involvement of the caspase-dependent pathway in MG2B-induced cell death

Under phase contrast microscopy, we observed that MG2B-dependent cell death in adherent tumor cells was accompanied

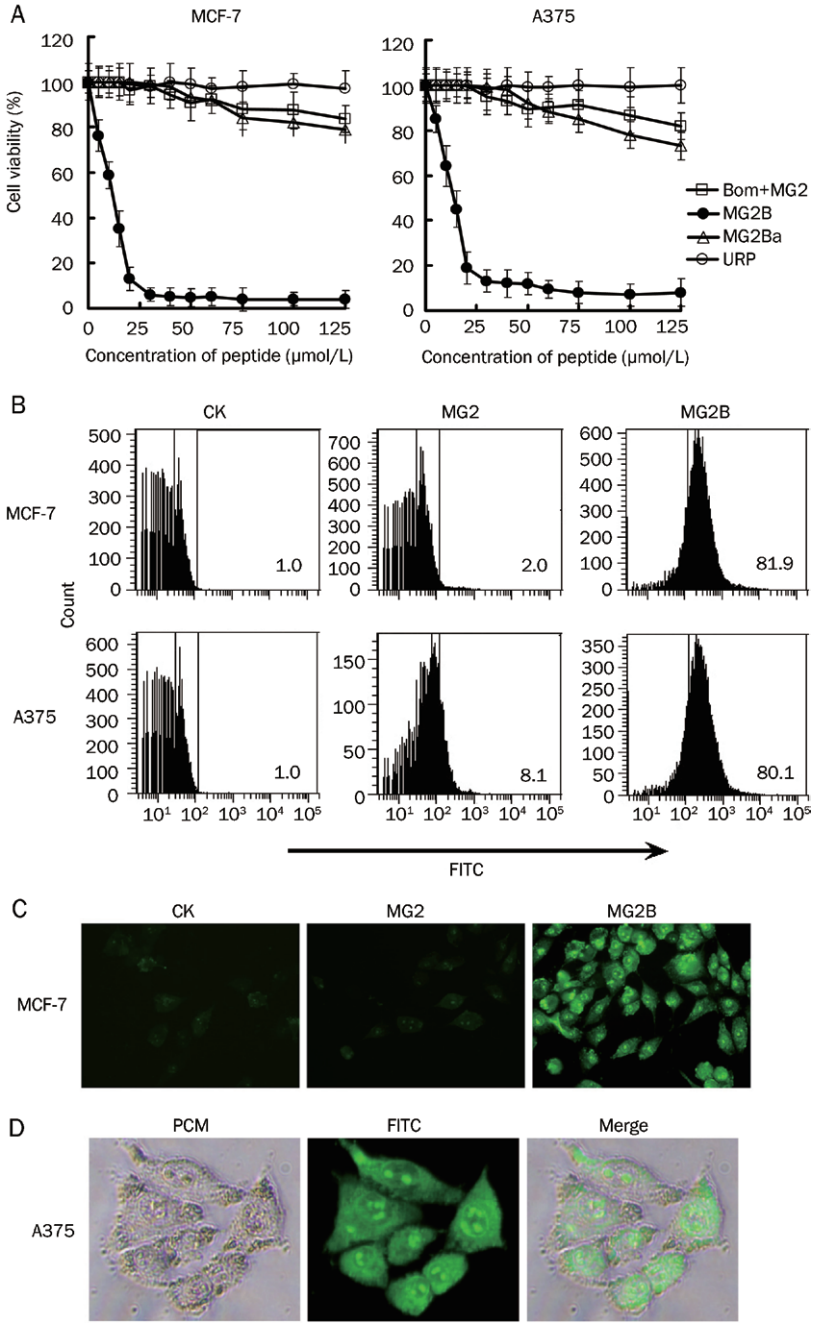

Figure 2. Enhancement of MG2-induced cytotoxicity in tumor cells by attachment to bombesin at its N-terminus. (A) Comparison of cytotoxicity of the MG2-bombesin conjugate, MG2B, and unconjugated MG2 in MCF-7 and A375 cells. Solution (100 μL) containing increasing concentrations (0–125 μmol/L) of peptide was added to cells (1×10^4 cells/well) and further incubated at 37 °C for 2 h. Subsequently, cell viability was determined using the cell counting reagent CCK-8. Results were expressed as the percentage of viable cells after treatment with peptide, which was calculated assuming 100% survival with the PBS control. Bom+MG2: unconjugated bombesin plus unconjugated MG2; MG2B: MG2-bombesin conjugate; MG2Ba: MG2-bombesin analog conjugate; URP: a negative control peptide. (B) Different binding affinities of MG2B and unconjugated MG2 to MCF-7 and A375 cells. About 1×10^5 cells were collected and incubated with FITC-labeled peptide (40 μmol/L, 300 μL) at 37 °C for 1 h. After being washed with PBS, the cells were analyzed by FACS. The URP peptide was used as a negative control. The percentage of positive cells is indicated. (C) Cellular translocation of MG2B in MCF-7 cells. The cells were seeded into 96-well plates (1×10^4 cells/well) and allowed to attach overnight. After incubation with FITC-labeled peptide (20 μmol/L, 100 μL) and being washed once with PBS, the cells were observed under a fluorescence microscope (original magnification, ×160). (D) Distribution of FITC-labeled MG2B in MCF-7 cells. After incubation with FITC-labeled peptide, the cells were observed under a phase-contrast microscope (PCM) and a fluorescence microscope (original magnification, ×320).

by condensed nuclei, rounding, cell detachment, and clumping (data not shown). After treatment with peptide and double staining with Annexin V and PI, we observed many Annexin V^+/PI^+ and Annexin V^+/PI^- MCF-7 cells under fluorescence microscopy (Figure 4A). Annexin V^+/PI^+ cells were considered necrotic cells or apoptotic cells at an advanced stage of apoptosis. Annexin V^+/PI^- cells were considered apoptotic cells at an early stage of apoptosis. Consequently, the observation of Annexin V^+/PI^- cells demonstrates that MG2B induced apoptosis in MCF-7 cells. Further FACS analysis also revealed numerous Annexin V^+/PI^- cells in MG2B-treated MCF-7 cells. The percentage ratio of apoptotic/necrotic cells resulting from 0, 30, and 50 μmol/L MG2B was 2.2/4.0, 21.2/18.1, and 22.1/21.8, respectively (Figure 4B). JC-1 staining showed rich granule-like mitochondria (indicating healthy mitochondria) in cells treated with PBS. However, the MG2B-induced cell death was accompanied by the disappearance of the granule-like mitochondria in most peptide-treated cells (Figure 4C). Simultaneously, significant loss in mitochondrial membrane potentials in MG2B-treated cells was reflected by changes in the ratio of red/green fluorescence cells from 89.2/10.8 to 43.4/56.6 (Figure 4C). Moreover, preincubation of cells with the pan-caspase inhibitor z-VAD-Fmk before the addition of peptide reduced MG2B-induced cell death by 15%–30%

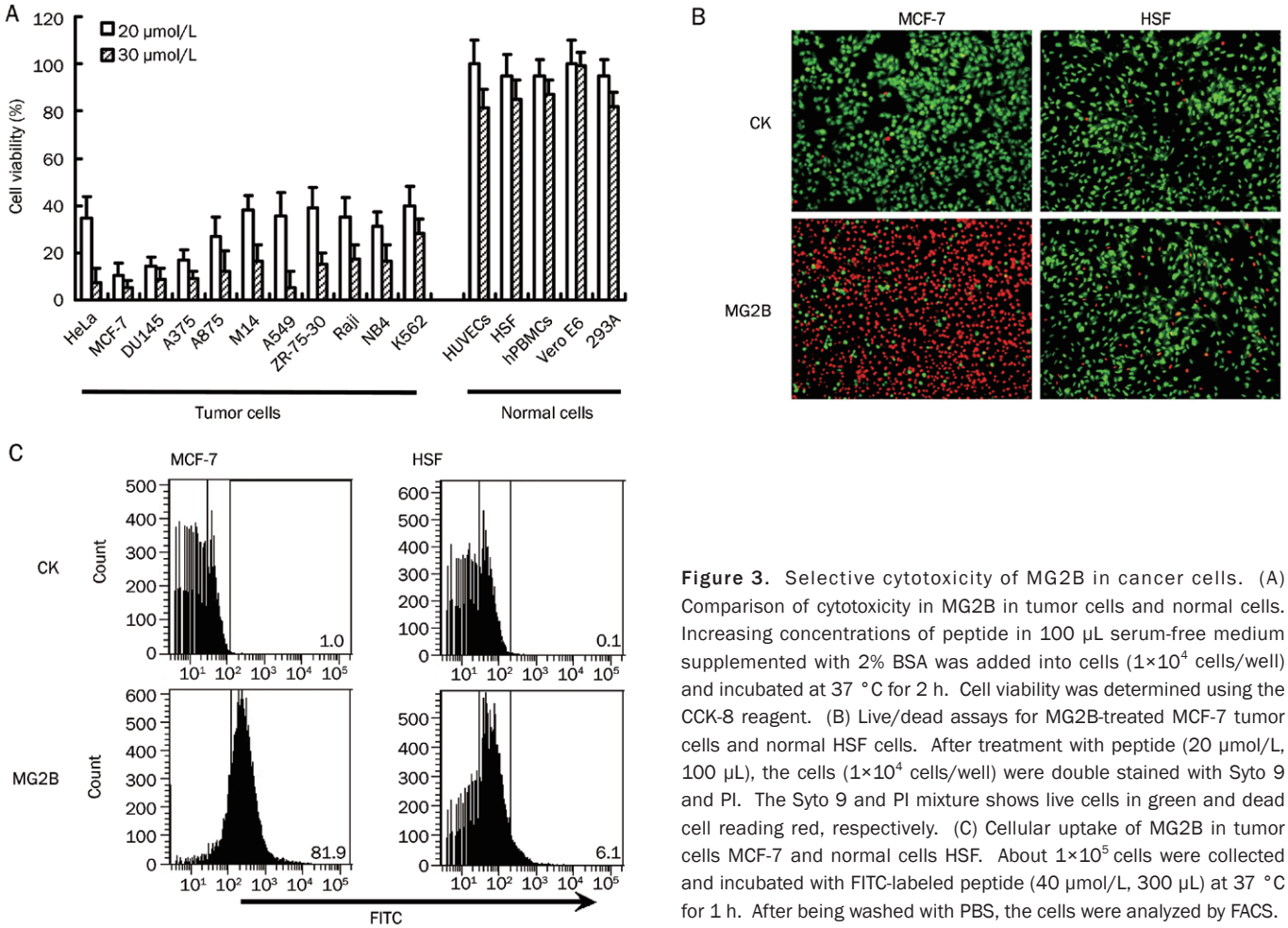

Figure 3. Selective cytotoxicity of MG2B in cancer cells. (A) Comparison of cytotoxicity in MG2B in tumor cells and normal cells. Increasing concentrations of peptide in 100 μL serum-free medium supplemented with 2% BSA was added into cells (1×10^4 cells/well) and incubated at 37 °C for 2 h. Cell viability was determined using the CCK-8 reagent. (B) Live/dead assays for MG2B-treated MCF-7 tumor cells and normal HSF cells. After treatment with peptide (20 μmol/L, 100 μL), the cells (1×10^4 cells/well) were double stained with Syto 9 and PI. The Syto 9 and PI mixture shows live cells in green and dead cell reading red, respectively. (C) Cellular uptake of MG2B in tumor cells MCF-7 and normal cells HSF. About 1×10^5 cells were collected and incubated with FITC-labeled peptide (40 μmol/L, 300 μL) at 37 °C for 1 h. After being washed with PBS, the cells were analyzed by FACS.

(Figure 4D). These results demonstrate that MG2B induces caspase-dependent apoptosis in tumor cells.

MG2B suppresses tumor growth *in vivo*

Figure 5A shows that MG2B exerts an obvious antitumor effect *in vivo*. When the average volume of tumor masses reached approximately 50-100 mm^3, MG2B or MG2 was intratumorally injected into mice bearing a MCF-7 tumor graft at 20 mg/kg every day for a total of five days. The mice in the control group were injected with an equal volume of PBS. Rapid growth of tumor grafts in PBS-injected mice was observed as early as 10 days post-injection. However, tumor grafts in MG2B-injected mice grew slowly over the course of the experiment. Beginning on day 14 post-injection, the mean volume of tumor grafts in MG2B-treated mice was significantly different ($P<0.01$) from the tumor volume of MG2- and PBS-treated mice. At the end of this experiment, the average volume of tumor grafts in MG2B-injected mice was about 172±136 mm^3, compared to 944±295 mm^3 and 1081±264 mm^3 in MG2- and PBS-treated mice, respectively (Figure 5A). The tumor masses excised from MG2B-treated mice were smaller than the tumor masses of PBS-treated mice. The mean weights of tumor masses in MG2B-treated mice, MG2-treated mice and PBS-treated mice were 0.21±0.05 g, 0.51±0.16 g and 0.59±0.12 g, respectively (Figure 5B).

Further histological examination demonstrated that MG2B caused extensive necrosis in tumor cells. As shown in Figure 5C, H&E staining shows a large number of cells with a condensed and fragmented nucleus in tumor tissues at the injection sites. Rich TUNEL-positive stained cells were also observed in these tumor tissues (Figure 5C). These results demonstrate that MG2B induces apoptosis of tumor cells *in vivo*. However, no obvious histological damage was observed in the liver, kidney, and heart of mice injected with the peptides (data not shown).

Discussion

Here, we report the enhanced cytotoxicity of the MG2-bombesin conjugate MG2B compared to the unconjugated MG2 peptide. The IC_{50} of the MG2B for cancer cells was at least 10 times lower than the IC_{50} of unconjugated MG2 for these cells. The enhancement of cytotoxicity of MG2 is closely related to its improved binding affinity. In contrast, conjugation of MG2 to a bombesin analog lacking the receptor-binding domain failed to increase its cytotoxicity. These results demonstrate that conjugated bombesin enhances binding and thus enhances

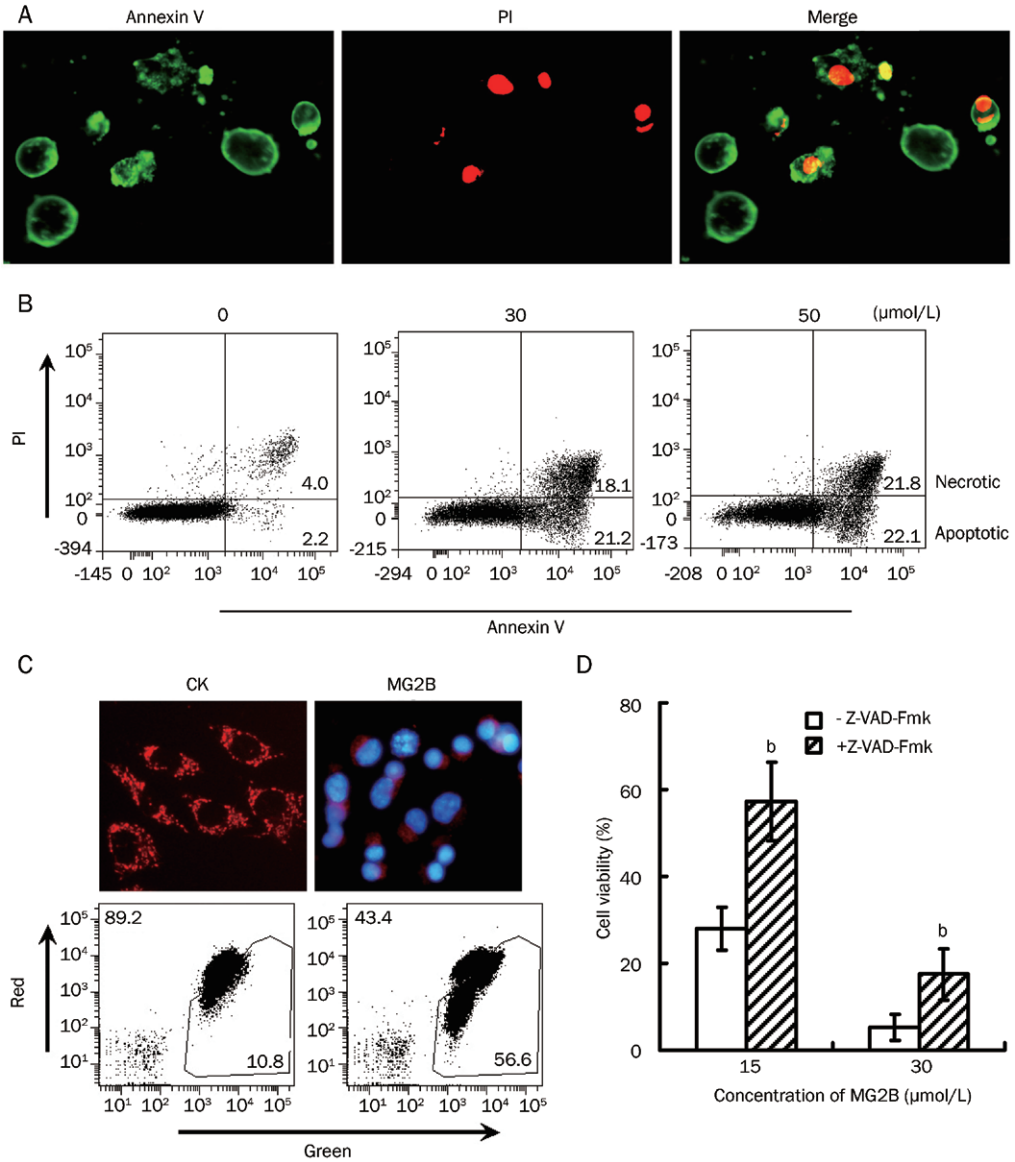

Figure 4. MG2B induced caspase-dependent apoptosis in tumor cells. (A) Microscope view of MG2B-induced apoptotic cells. After treatment with MG2B, the cells were double stained with FITC-Annexin V (Green) and PI (Red) and then observed under a fluorescence microscope. Annexin V^+/PI^- cells were considered apoptotic cells at early stages of apoptosis. Annexin V^+/PI^+ cells were considered apoptotic cells at an advanced stage of apoptosis or necrotic cells. (B) FACS analysis for MG2B-induced apoptotic cells. About 1×10^5 cells were pooled and incubated with 0, 30, and 50 μmol/L MG2B at 37 °C for 1 h. Peptide-treated cells were then double stained with FITC-Annexin V and PI and assayed by FACS. The percentage of apoptotic (Annexin V^+/PI^-) and necrotic (Annexin V^+/PI^+) cells is indicated. (C) MG2B-induced loss of mitochondrial membrane potential in MCF-7 cells. To observe the mitochondria in cells, the adherent MCF-7 cells (1×10^4 cells/well) were incubated with 100 μL MG2B (20 μmol/L) at 37 °C for 2 h followed by staining with JC-1 and observed under a fluorescence microscope. To analyze the mitochondrial membrane potential by FACS, 1×10^5 cells were collected and incubated with 100 μL MG2B (0, 75 μmol/L) at 37 °C for 1 h followed by staining with JC-1 and washing with PBS. The percentage of red and green cells is indicated. (D) Inhibition of the MG2B-induced cell death by pan-caspase inhibitor. Cells (1×10^4 cells/well) were preincubated with 100 μmol/L of pan-caspase inhibitor z-VAD-Fmk for 2 h at 37 °C before addition of peptide. The cytotoxicity of MG2B (15-30 μmol/L) in MCF-7 cells was then determined using the CCK-8 reagent. The cytotoxicity of MG2B in MCF7 cells in the presence of z-VAD-Fmk is significantly ($^bP<0.05$) different from the cytotoxicity of MG2B in the absence of z-VAD-Fmk.

cytotoxicity of MG2 in cancer cells. Due to the specificity of conjugated bombesin, MG2B showed selective cytotoxicity in cancer cells by inducing caspase-dependent apoptosis *in vitro*. Furthermore, MG2B exerted obvious antitumor effects in an animal model. Our data suggest that conjugation of cationic AMPs to bombesin increases their cytotoxicity in cancer cells and thus present a potential novel approach to targeted cancer therapy.

Membrane-active AMPs are potential cancer therapies due to their low risk for induction of resistance[4]. Electrostatic

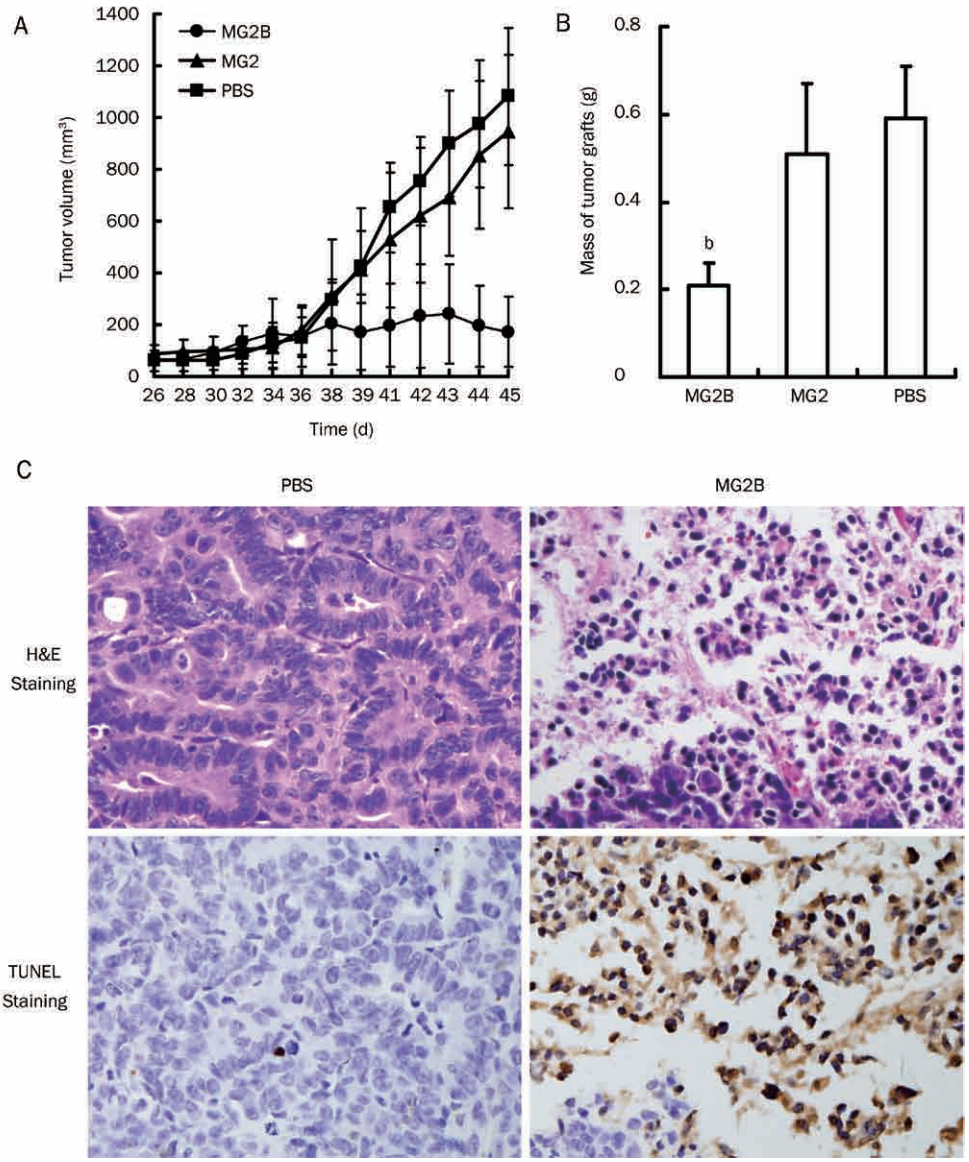

Figure 5. Suppression of tumor growth by MG2B. (A) Growth curve of MCF-7 tumor grafts in mice administered with MG2B. (B) Tumor masses excised from mice in treatment group and control group. The average mass of tumor grafts from MG2B-treated mice is significantly ($^bP<0.05$) different than the average mass in PBS-treated mice and in MG2-treated mice. Tumors were established in BALB/c nude mice by subcutaneous injection of 100 μL of saline containing 1×10^7 MCF-7 cells. MG2B peptide (20 mg/kg) was intratumorally injected into mice bearing tumor grafts every other day for a total of 5 days. The mice in the control group were injected with equivalent volumes of PBS. The tumor volume (mm^3) was calculated as length×width^2×0.5. (C) Histological examination of MG2B-induced necrosis *in vivo*. Peptide (200 μg, in 100 μL PBS) was intratumorally injected into mice bearing MCF-7 xenografts (<1000 mm^3). Approximately 16 h later, the tumor masses were excised. We then performed H&E and TUNEL staining on paraffin-embedded tumor tissues. Original magnification: ×400.

interactions between the peptide's positive charges and the membrane's negative charges contribute to the binding of AMPs to the cell membrane, which is crucial for the cytotoxicity of these peptides in cancer cells[4]. Increasing the number of positive charges by amino acid substitution is an effective way to enhance the membrane-binding ability and cytotoxicity of AMPs[9, 11, 12]. In this work, we tried an alternative method to improve the anticancer activity of AMPs by conjugating the peptide to a tumor-homing peptide that can bind to its receptors.

We first constructed an MG2-bombesin conjugate MG2B by attaching MG2 to bombesin at its N-terminus. As expected, MG2B showed greater cytotoxicity in cancer cells compared to unconjugated MG2 peptide. We found that the IC_{50} of MG2B for cancer cells was within the range of 10–15 μmol/L, which is over 10 times lower than the IC_{50} of unconjugated MG2 (Figure 2A). Further investigation demonstrated that conjugated bombesin contributes to the binding affinity of MG2B to cancer cells. MG2B, but not unconjugated MG2, can bind and enter about 80% of cancer cells at a concentration of 20 μmol/L (Figure 2B). These results suggest that conjugation to bombesin at its N-terminus enhances the cytotoxicity of MG2 by increasing its membrane binding/translocation ability. However, conjugation of MG2 to a bombesin analog lacking the C-terminal 8-14 amino acids (WAVGHLM) failed to increase the cytotoxicity of MG2 in cancer cells. The C-terminal domain of bombesin is critical for its receptor binding affinity[25]. Therefore, conjugation of MG2 to a bombesin analog lacking this receptor-binding domain does not enhance cytotoxicity in cancer cells.

Bombesin receptors are overexpressed in numerous human cancer cells. Spectrum analysis demonstrates that the cytotoxicity of the MG2-bombesin conjugate MG2B in cancer cells and normal cells is positively related to the binding affinity of

bombesin to these cells. Bombesin binds to cancer cells with 10-30 times greater affinity than to normal cells (Figure 1). The IC_{50} of MG2B for cancer cells was about 6–10 times lower than the IC_{50} for normal cells (Figure 3A). Because the conjugation to a bombesin analog lacking receptor-binding domain failed to enhance the cytotoxicity of MG2 (Figure 2A), we conclude that bombesin conjugation enhances the cytotoxicity and selectivity of MG2B. Bombesin shows high affinity to its receptors including the neuromedin B preferring receptor (BB1), gastrin-releasing peptide preferring receptor (BB2), orphan bombesin receptor subtype-3 (BB3), and BB4 receptor[21]. Therefore, it is possible for bombesin to enhance the cytotoxicity of MG2 by improving its ability to bind to the membrane of cancer cells. During the preparation of this paper, we also constructed many other AMPs-bombesin conjugates including attachment of the cationic KLA peptide[27], BMAP27(1–18)[28], and BMAP28(1-18)[29] to bombesin. We found that all AMPs-bombesin conjugates enhanced the binding affinity and cytotoxicity in cancer cells. Moreover, bombesin receptors are overexpressed in a variety of primary cancer cells[21, 22]. Therefore, a bombesin-directed peptide such as MG2B might be potential target in spontaneous tumors.

Because the MG2 has been suggested to form pores on cell membranes[30], the MG2-bombesin conjugate MG2B might induce necrosis in cancer cells by cell membrane-disruption. After treatment with the MG2B peptide, numerous necrotic cells (Annexin V^+/PI^+) with compromised membranes were observed under a microscope (Figure 4A) or detected by FACS analysis (Figure 4B). Although Annexin V^+/PI^+ cells might be apoptotic cells at advanced stages of apoptosis, the possibility of MG2B to induce necrosis in cancer cells cannot be excluded. Some cationic AMPs also induce apoptosis by binding to the mitochondrial membrane[4]. Imura *et al* observed that internalized MG2 peptide mainly accumulates in the mitochondria[30]. Westerhoff *et al* showed that MG2 can dissipate the membrane potential of isolated rat mitochondria[31]. These observations suggest that MG2 might also trigger the apoptosis in cancer cells through mitochondrial disruption. In our experiment, we observed numerous cells at an early stage of apoptosis (Annexin V^+/PI^-) in MG2B-treated cells (Figure 4A and 4B). MG2B-induced cell death was accompanied by the disappearance of healthy granule-like mitochondria and the loss of mitochondrial membrane potential (Figure 4C). Moreover, the involvement of caspase-dependent pathways in MG2B-induced cell death was revealed using a pan-caspase inhibitor (Figure 4D). These results demonstrate that MG2B induces caspase-dependent apoptosis by triggering mitochondrial disruption in cancer cells. Due to the rapid disruption of mitochondria by MG2B, it is difficult for us to capture a picture with high quality to show the peptide accumulation in mitochondria with a mitochondrial trace marker. However, it is understandable that the uniform distribution of MG2B in the cytoplasm (Figure 2D) allows it to bind and disrupt mitochondria.

To date, 65 AMPs have been identified as anticancer peptides[32]. In addition to MG2, many other cationic AMPs such as Cecropin A and Cecropin B also exhibit weak cytotoxicity in cancer cells[33]. Conjugation of these peptides to tumor-homing peptides might also enhance their cytotoxicity. Compared to antibody-directed immunotoxins with high molecular weights[34], a tumor-homing peptide may offer advantages in the penetration of tumors. In addition, the peptide can be synthesized economically by chemical synthesis, thus avoiding the use of potentially hazardous biomolecules. Moreover, *D*-amino acids might be used to enhance the resistance of peptides to proteolytic degradation and increase its *in vivo* efficiency.

Conclusions

Magainin II shows weak cytotoxic efficacy in tumor cells due to its limited membrane binding affinity. The tumor-homing peptide bombesin can bind specifically to tumor cells with high affinity. Thus, conjugation to bombesin at its N-terminus significantly enhanced the cytotoxicity of magainin II in tumor cells through improved cell binding. Moreover, the magainin II-bombesin conjugate MG2B selectively induces cell death in cultured tumor cells. MG2B exerts promising antitumor effects *in vivo*. These results suggest that more novel approaches to targeted cancer therapy might be developed by the conjugation of antimicrobial peptides to the tumor-homing peptide bombesin.

Acknowledgements

This work was supported by the National Basic Research Program of China (2009CB522401), and the National Natural Science Foundation of China (81072566).

Author contribution

Shan LIU performed most experiments. Hao YANG analyzed the peptide-induced apoptosis. Lin WAN and Hua-wei CAI contributed to the *in vivo* experiments. Sheng-fu LI cultured many cells. You-ping LI and Jing-qiu CHENG analyzed the data. Xiao-feng LU designed the experiments and wrote the paper.

References

1 Mader JS, Hoskin DW. Cationic antimicrobial peptides as novel cytotoxic agents for cancer treatment. Expert Opin Investig Drugs 2006; 15: 933–46.
2 Lehmann J, Retz M, Sidhu SS, Suttmann H, Sell M, Paulsen F, *et al*. Antitumor activity of the antimicrobial peptide magainin II against bladder cancer cell lines. Eur Urol 2006; 50: 141–7.
3 Bhutia SK, Maiti TK. Targeting tumors with peptides from natural sources. Trends Biotechnol 2008; 26: 210–7.
4 Hoskin DW, Ramamoorthy A. Studies on anticancer activities of antimicrobial peptides. Biochim Biophys Acta 2008; 1778: 357–75.
5 Papo N, Seger D, Makovitzki A, Kalchenko V, Eshhar Z, Degani H, *et al.* Inhibition of tumor growth and elimination of multiple metastases in human prostate and breast xenografts by systemic inoculation of a host defense-like lytic peptide. Cancer Res 2006; 66: 5371–8.
6 Conlon JM, Kolodziejek J, Nowotny N. Antimicrobial peptides from the skins of North American frogs. Biochim Biophys Acta 2009; 1788: 1556–63.

7 Fernandez DI, Gehman JD, Separovic F. Membrane interactions of antimicrobial peptides from Australian frogs. Biochim Biophys Acta 2009; 1788: 1630–8.
8 Zasloff M. Magainins, a class of antimicrobial peptides from *Xenopus* skin: isolation, characterization of two active forms, and partial cDNA sequence of a precursor. Proc Natl Acad Sci USA 1987; 84: 5449–53.
9 Cruciani RA, Barker JL, Zasloff M, Chen HC, Colamonici O. Antibiotic magainins exert cytolytic activity against transformed cell lines through channel formation. Proc Natl Acad Sci USA 1991; 88: 3792–6.
10 Jacob L, Zasloff M. Potential therapeutic applications of magainins and other antimicrobial agents of animal origin. Ciba Found Symp 1994; 186: 197-216; discussion 216–23.
11 Baker MA, Maloy WL, Zasloff M, Jacob LS. Anticancer efficacy of Magainin2 and analogue peptides. Cancer Res 1993; 53: 3052–7.
12 Matsuzaki K, Nakamura A, Murase O, Sugishita K, Fujii N, Miyajima K. Modulation of magainin 2-lipid bilayer interactions by peptide charge. Biochemistry 1997; 36: 2104–11.
13 Liu Y, Steiniger SC, Kim Y, Kaufmann GF, Felding-Habermann B, Janda KD. Mechanistic studies of a peptidic GRP78 ligand for cancer cell-specific drug delivery. Mol Pharm 2007; 4: 435–47.
14 Nishimura S, Takahashi S, Kamikatahira H, Kuroki Y, Jaalouk DE, O'Brien S, *et al*. Combinatorial targeting of the macropinocytotic pathway in leukemia and lymphoma cells. J Biol Chem 2008; 283: 11752–62.
15 Laakkonen P, Zhang L, Ruoslahti E. Peptide targeting of tumor lymph vessels. Ann N Y Acad Sci 2008; 1131: 37–43.
16 Corti A, Curnis F, Arap W, Pasqualini R. The neovasculature homing motif NGR: more than meets the eye. Blood 2008; 112: 2628–35.
17 Zwanziger D, Beck-Sickinger AG. Radiometal targeted tumor diagnosis and therapy with peptide hormones. Curr Pharm Des 2008; 14: 2385–400.
18 Khan IU, Beck-Sickinger AG. Targeted tumor diagnosis and therapy with peptide hormones as radiopharmaceuticals. Anticancer Agents Med Chem 2008; 8: 186–99.
19 Okarvi SM. Peptide-based radiopharmaceuticals and cytotoxic conjugates: potential tools against cancer. Cancer Treat Rev 2008; 34: 13–26.
20 Anastasi A, Erspamer V, Bucci M. Isolation and structure of bombesin and alytesin, two analogous active peptides from the skin of the European amphibians Bombesina and Alytes. Experientia 1971; 27: 166–9.
21 Reubi JC, Wenger S, Schmuckli-Maurer J, Schaer JC, Gugger M. Bombesin receptor subtypes in human cancers: detection with the universal radioligand (125)I-[D-TYR(6), beta-ALA(11), PHE(13), NLE(14)] bombesin(6-14). Clin Cancer Res 2002; 8: 1139–46.
22 Cornelio DB, Roesler R, Schwartsmann G. Gastrin-releasing peptide receptor as a molecular target in experimental anticancer therapy. Ann Oncol 2007; 18: 1457–66.
23 de Visser M, Verwijnen SM, de Jong M. Update: improvement strategies for peptide receptor scintigraphy and radionuclide therapy. Cancer Biother Radiopharm 2008; 23: 137–57.
24 Engel JB, Keller G, Schally AV, Halmos G, Hammann B, Nagy A. Effective inhibition of experimental human ovarian cancers with a targeted cytotoxic bombesin analogue AN-215. Clin Cancer Res 2005; 11: 2408–15.
25 Smith CJ, Volkert WA, Hoffman TJ. Radiolabeled peptide conjugates for targeting of the bombesin receptor superfamily subtypes. Nucl Med Biol 2005; 32: 733–40.
26 Laakkonen P, Akerman ME, Biliran H, Yang M, Ferrer F, Karpanen T, *et al*. Antitumor activity of a homing peptide that targets tumor lymphatics and tumor cells. Proc Natl Acad Sci USA 2004; 101: 9381–6.
27 Rege K, Patel SJ, Megeed Z, Yarmush ML. Amphipathic peptide-based fusion peptides and immunoconjugates for the targeted ablation of prostate cancer cells. Cancer Res 2007; 67: 6368–75.
28 Skerlavaj B, Gennaro R, Bagella L, Merluzzi L, Risso A, Zanetti M. Biological characterization of two novel cathelicidin-derived peptides and identification of structural requirements for their antimicrobial and cell lytic activities. J Biol Chem 1996; 271: 28375–81.
29 Risso A, Braidot E, Sordano MC, Vianello A, Macrì F, Skerlavaj B, *et al*. BMAP-28, an antibiotic peptide of innate immunity, induces cell death through opening of the mitochondrial permeability transition pore. Mol Cell Biol 2002; 22: 1926–35.
30 Imura Y, Choda N, Matsuzaki K. Magainin 2 in action: distinct modes of membrane permeabilization in living bacterial and mammalian cells. Biophys J 2008; 95: 5757–65.
31 Westerhoff HV, Hendler RW, Zasloff M, Juretić D. Interactions between a new class of eukaryotic antimicrobial agents and isolated rat liver mitochondria. Biochim Biophys Acta 1989; 975: 361–9.
32 Wang G, Li X, Wang Z. APD2: the updated antimicrobial peptide database and its application in peptide design. Nucleic Acids Res 2009; 37: D933–7.
33 Suttmann H, Retz M, Paulsen F, Harder J, Zwergel U, Kamradt J, *et al*. Antimicrobial peptides of the Cecropin-family show potent antitumor activity against bladder cancer cells. BMC Urol 2008; 8: 5.
34 Pastan I, Hassan R, FitzGerald DJ, Kreitman RJ. Immunotoxin treatment of cancer. Annu Rev Med 2007; 58: 221–37.

Acta Pharmacologica Sinica (2011) 32: 89–98
 1671-4083/11 $32.00
www.nature.com/aps

Original Article

WJ9708012 exerts anticancer activity through PKC-α related crosstalk of mitochondrial and endoplasmic reticulum stresses in human hormone-refractory prostate cancer cells

Ting-chun KUO[1], Wei-jan HUANG[2], Jih-hwa GUH[1, *]

[1]*School of Pharmacy, National Taiwan University, Taipei, Taiwan, China;* [2]*Graduate Institute of Pharmacognosy, College of Pharmacy, Taipei Medical University, Taipei, Taiwan, China*

Aim: To investigate the anticancer mechanism of a methoxyflavanone derivative, WJ9708012, highlighting its role on a crosstalk between endoplasmic reticulum (ER) and mitochondrial stress.
Methods: Cell proliferation was examined using sulforhodamine B assay. Cell-cycle progression, Ca^{2+} mobilization and mitochondrial membrane potential ($\Delta\Psi_m$) were detected using flow cytometric analysis. Protein expression was detected using Western blot.
Results: WJ9708012 displayed an antiproliferative and apoptotic activity in human hormone-refractory prostate cancer cells with IC_{50} values of 6.4 and 5.3 μmol/L in PC-3 and DU-145 cells. WJ9708012 induced a prompt increase of cytosolic Ca^{2+} level and activation of protein kinase C (PKC)-α. The cleavage of μ-calpain was also induced by WJ9708012. Furthermore, WJ9708012 induced cell-cycle arrest at G_1-phase associated with down-regulation of cyclin D1, cyclin E and cyclin-dependent kinase-4 expressions. It also caused a rapid and time-dependent decrease of phosphorylation level of mTOR (Ser^{2448}), 4E-BP1 (Thr^{37}/Thr^{46}/Thr^{70}) and p70S6K (Thr^{389}), indicating the inhibition of mTOR-mediated translational pathways. The ER stress was activated by the identification of up-regulated GADD153 and glucose-regulated protein-78 protein levels. The subsequent mitochondrial stress was also identified by the observation of a decreased Bcl-2 and Bcl-xL expressions, an increased truncated Bid and Bad and a loss of $\Delta\Psi_m$.
Conclusion: WJ9708012 induces an increase of cytosolic Ca^{2+} concentration and activation of PKC-α. Subsequently, a crosstalk between ER stress and mitochondrial insult is induced, leading to the inhibition of mTOR pathways and arrest of the cell-cycle at G_1 phase. The apoptosis is ultimately induced by a severe damage of mitochondrial function.

Keywords: methoxyflavanone; Ca^{2+} mobilization; protein kinase C-α; endoplasmic reticulum stress; mitochondrial stress

Acta Pharmacologica Sinica (2011) 32: 89–98; doi: 10.1038/aps.2010.173; published online 6 Dec 2010

Introduction

Endoplasmic reticulum (ER) is the major organelle responsible for folding and maturation of transmembrane, secretory and ER-resident proteins. ER stress is originally an adaptive response that can be induced by various perturbations in normal ER function, including the accumulation of unfolded/misfolded proteins, lipid or glycolipid imbalances, or changes of ER Ca^{2+} homeostasis. ER stress triggers several signaling pathways to cope with the abnormal load in ER lumen. The unfolded protein response pathway causes an up-regulation of ER chaperones, such as GRP78 through C/EBP homologous transcription factor GADD153 and the ER overload response pathway induces the activation of nuclear factor κB (NF-κB), leading to production of cytokines[1, 2]. However, ER stress may also contribute to cell suicide when abnormalities become extensive. GADD153, NF-κB and caspase-12 have been implicated in the apoptotic regulation[1, 3]. Besides, ER stress can crossly react with mitochondrial stress, resulting in an increase of cytochrome *c* release and subsequent caspase-dependent apoptotic reaction[4, 5]. Recently, the ER stress caused by exogenously applied stimuli has been considered a potential strategy in anticancer approach[6, 7].

Intracellular Ca^{2+} is an essential element in the control of cellular function and a lot of physical events. However, an overload of intracellular Ca^{2+} may cause stresses on target organelles, leading to oxidative stress and massive activation of a lot of enzymes and an ultimate cell death. ER and mitochondria play crucial roles in the maintenance of intracellular Ca^{2+}

* To whom correspondence should be addressed.
E-mail jhguh@ntu.edu.tw
Received 2010-07-25 Accepted 2010-09-13

homeostasis and, therefore, regulate cell death[8–10]. The evidence suggests that sufficient extracellular Ca^{2+} influx causes Ca^{2+}-activated ER stress, which contributes predominantly to apoptosis in many types of cells including prostate cancer cells[11, 12]. Notably, an increase of cytosolic Ca^{2+} can also impair protein processing, promoting ER stress and inhibiting translation pathways[13, 14] that explain the down-regulation of cell-cycle regulators and arrest of the cell cycle by several anticancer agents[13, 15]. Ca^{2+} also serves as an effector communicating between ER- and mitochondria-mediated signaling cascades. Bcl-2 has been revealed to be associated with the ER and outer mitochondrial membrane[10, 16] and plays a central role on negative regulation of Ca^{2+} homeostasis since Bcl-2 overexpression is capable of reducing the Ca^{2+} level released from the ER and diminishes cell apoptosis[17]. Bax and Bak, are two pro-apoptotic members of Bcl-2 family that impair mitochondrial function, also localize to the ER. Scorrano and colleagues provided evidence that both ER-released Ca^{2+} and the presence of mitochondrial Bax or Bak were required to fully restore apoptosis by several apoptotic stimuli[18]. Altogether, these data support that Ca^{2+} mobilization is a key regulator in the crosstalk between ER and mitochondria in propagating apoptotic signals.

Flavonoids are a family of polyphenolic phytochemicals including flavones and isoflavones. A large body of evidence shows that diet high in flavonoids is associated with the reduced incidence of some cancers[19]. Flavonoids are extensively studied to display anticancer activity through numerous signaling pathways[5, 20, 21]. Of note, most of the flavonoids exhibit antioxidant activities[22]. This activity has been implicated to reduce anticancer capability of flavonoids since reactive oxygen species (ROS) acts as important apoptotic mediators. It appears that ROS generation is important for stimulation of apoptotic cell death that is crucial protective effects in the body for killing cancer cells. This oxidative stress is also critical for effective cancer chemotherapy and radiation treatment[23, 24]. Furthermore, Salganik and colleagues reported that antioxidant-depleted diets, but not antioxidant-enriched diets, were capable of increasing ROS levels and dramatically increased apoptosis occurs within tumors[25]. To avoid the interruption of antioxidant effect, we synthesized methoxyflavanone derivatives and found that WJ9708012 [6-(3-Hydroxy-3-methylbutyl)-2′-(7-hydroxy-3,7-dimethyloctyl)-3′,4′,5,7-tetramethoxyflavanone] displayed effective anticancer activity without antioxidant effect in human hormone-refractory prostate cancer cells. The anticancer mechanisms of WJ9708012 were identified to be related to Ca^{2+} and protein kinase C (PKC)-α involved interaction of ER and mitochondria stresses. This study provides evidence that flavonoids, in the absence of antioxidant effect, may have potential as a cancer therapy against human prostate cancers.

Materials and methods

Materials

RPMI 1640 medium, fetal bovine serum (FBS), penicillin, streptomycin, and all other cell culture reagents were obtained from GIBCO/BRL Life Technologies (Grand Island, NY, USA). Antibodies to cyclin D1, cyclin E, cyclin-dependent kinase 4 (Cdk4), Bcl-2, Bcl-xL, Bak, Bax, Bid, Bad, glucose-regulated protein-78 (GRP78), cytochrome *c*, protein kinase C (PKC)-α, and anti-mouse and anti-rabbit IgGs were obtained from Santa Cruz Biotechnology, Inc (Santa Cruz, CA, USA). Antibodies to AMP-activated protein kinase (AMPK)-α, phospho-AMPKα^{Thr172}, mammalian target of rapamycin (mTOR), phospho-mTOR^{Ser2448}, phospho-p70S6K^{Thr389}, phospho-4E-BP1^{Thr70}, phospho-4E-BP1$^{Thr37/Thr46}$, procaspase-3, procaspase-7, PARP, GADD153 (growth arrest and DNA damage-inducible gene 153), apoptosis-inducing factor (AIF), endonuclease G, and α-tubulin were from Cell Signaling Technologies (Boston, MA, USA). Fluo-3/AM and 2′,7′-dichlorofluorescin diacetate (DCF-DA) were from Molecular Probes Inc (Eugene, OR, USA). Sulforhodamine B (SRB), propidium iodide (PI), phenylmethylsulfonylfluoride (PMSF), leupeptin, dithiothreitol, rhodamine 123, EDTA, carbonylcyanide-m-chlorophenylhydrazone (CCCP), W7, *N*-acetylcysteine (NAC), trolox, Go 6983, Compound C (6-[4-(2-Piperidin-1-ylethoxy)phenyl]-3-pyridin-4-ylpyrazolo[1,5-a]pyrimidine) and all of the other chemical reagents were obtained from Sigma-Aldrich (St Louis, MO, USA). Ro-318220 was purchased from Calbiochem (La Jolla, CA, USA). WJ9708012 [6-(3-Hydroxy-3-methylbutyl)-2′-(7-hydroxy-3,7-dimethyloctyl)-3′,4′,5,7-tetramethoxyflavanone] (Figure 1A) was synthesized and provided by our colleagues (Dr Wei-jan HUANG). The purity is more than 95% by the examination using high-resolution MS and nuclear magnetic resonance.

Cell lines and cell culture

The cancer cell lines including PC-3 and DU-145 were from American Type Culture Collection (Rockville, MD, USA). The cells were cultured in RPMI-1640 medium with 10% FBS (*v/v*) and penicillin (100 units/mL)/streptomycin (100 μg/mL). Cultures were maintained in a humidified incubator at 37 °C in 5% CO_2/95% air.

SRB assays

Cells were seeded in 96-well plates in medium with 5% FBS. After 24 h, cells were fixed with 10% trichloroacetic acid (TCA) to represent cell population at the time of compound addition (T_0). After additional incubation of DMSO or WJ9708012 for 48 h, cells were fixed with 10% TCA and SRB at 0.4% (*w/v*) in 1% acetic acid was added to stain cells. Unbound SRB was washed out by 1% acetic acid and SRB bound cells were solubilized with 10 mmol/L Trizma base. The absorbance was read at a wavelength of 515 nm. Using the following absorbance measurements, such as time zero (T_0), control growth (C), and cell growth in the presence of the compound (Tx), the percentage growth was calculated at each of the compound concentrations levels. Percentage growth inhibition was calculated as: $100–[(Tx–T_0)/(C–T_0)]\times100$. Growth inhibition of 50% (IC_{50}) is determined at the compound concentration which results in 50% reduction of total protein increase in control cells during the compound incubation.

Annexin V-PI staining of apoptotic cell

Cells were cultured in 6-well plate for 24 h and then treated with vehicle or 30 μmol/L WJ9708012 for 12 or 24 h. After the treatment, cells were washed twice with phosphate-buffered saline (PBS) and stained with fluorescein isothiocyanate (FITC) annexin V and PI as per the manufacturer's directions (Annexin V-FITC Apoptosis Detection Kit, R&D Systems Inc, Minneapolis, MN, USA). The stained cells were evaluated by flow cytometry. The cells binding FITC-annexin V (excitation, 488 nm; emission, 520 nm) but not PI (excitation, 540 nm; emission, 630 nm) were termed annexin V-positive (early apoptosis) and the cells permeant to PI (regardless of FITC-annexin V binding) were deemed necrosis or late apoptosis[26].

In situ labeling of apoptotic cells

In situ detection of apoptotic cells was performed using TUNEL (terminal dUTP nick-end labeling) apoptosis detection methods. The TUNEL method identifies apoptotic cells using TdT to transfer biotin-dUTP to the free 3′-OH of cleaved DNA. The biotin-labeled cleavage sites were then visualized by reaction with fluorescein conjugated avidin (avidin-FITC). After the treatment of cells with or without WJ9708012 (30 μmol/L) or taxol (0.1 μmol/L) for 12 or 24 h, the cells were washed, fixed and stained for apoptotic detection according to the protocol provided by the suppliers (Promega, Madison, WI, USA). The photomicrographs were obtained by a fluorescence microscopic examination (Nikon).

FACScan flow cytometric assay

After the indicated treatment, the cells were harvested by trypsinization, fixed with 70% (*v/v*) alcohol at 4 °C for 30 min and washed with PBS. After centrifugation, cells were incubated in 0.1 mL of phosphate-citric acid buffer (0.2 mol/L Na_2HPO_4, 0.1 mol/L citric acid, pH 7.8) for 30 min at room temperature. Then, the cells were centrifuged and resuspended with 0.5 mL PI solution containing Triton X-100 (0.1% *v/v*), RNase (100 μg/mL) and PI (80 μg/mL). DNA content was analyzed with FACScan and CellQuest software (Becton Dickinson, Mountain View, CA, USA).

Western blotting

After the treatment, cells were harvested with trypsinization, centrifuged and lysed in 0.1 mL of lysis buffer containing 10 mmol/L Tris-HCl (pH 7.4), 150 mmol/L NaCl, 1 mmol/L EGTA, 1% Triton X-100, 1 mmol/L PMSF, 10 μg/mL leupeptin, 10 μg/mL aprotinin, 50 mmol/L NaF and 100 μmol/L sodium orthovanadate. In some experiments, the mitochondrial/cytosol fractionation kit (Biovision, Mountain View, CA, USA) was used to separate mitochondrial and cytosolic fraction. Total protein was quantified, mixed with sample buffer and boiled at 90 °C for 5 min. Equal amount of protein (30 μg) was separated by electrophoresis in 8% or 12% SDS-PAGE, transferred to PVDF membranes and detected with specific antibodies. The immunoreactive proteins after incubation with appropriately labeled secondary antibody were detected with an enhanced chemiluminescence detection kit (Amersham, Buckinghamshire, UK).

Measurement of intracellular Ca^{2+} level

Cells were pre-incubated with fluo 3-AM (5 μmol/L) for 30 min. Then, the cells were washed twice and incubated in fresh medium. Vehicle (0.1% DMSO) or WJ9708012 was added to the cells for the indicated times and the intracellular Ca^{2+} level was measured by flow cytometric analysis.

Measurement of mitochondrial membrane potential ($\Delta\Psi_m$) and ROS

Cells were treated without or with the agent for the indicated times. Thirty minutes before the termination of incubation, a rhodamine 123 solution (final concentration of 5 μmol/L, for $\Delta\Psi_m$ measurement) or DCF-DA (final concentration of 10 μmol/L, for ROS measurement) was added to the cells and incubated for the last 30 min at 37 °C. The cells were finally harvested and the accumulation of rhodamine 123 or ROS was determined using FACScan flow cytometric analysis.

Immunofluorescence microscopic examination

Cells were seeded in 8-well chamber slides. After the compound treatment, the cells were fixed with 100% methanol at -20 °C for 5 min and incubated in 1% bovine serum albumin (BSA) containing 0.1% Triton X-100 at 37 °C for 30 min. The cells were washed twice with PBS for 5 min and incubated with primary antibodies at 37 °C for 1 h. The cells were washed three times with PBS for 10 min and incubated with FITC-conjugated secondary antibody at 37 °C for 40 min. The nuclei were recognized by the staining with DAPI (1 μg/mL). The labeled targets in cells were detected by a confocal laser microscopic system (Leica TCS SP2).

Data analysis

The compound was dissolved in dimethyl sulfoxide (DMSO). The final concentration of DMSO was 0.1% in cell culture media. Data are presented as the mean±SEM for the indicated number of separate experiments. Statistical analysis of data was performed with one-way analysis of variance (ANOVA) followed by a *t*-test and *P*-values less than 0.05 were considered significant.

Results

Anti-proliferative and apoptosis-inducing activities in prostate cancer cells

The antiproliferative effect of WJ9708012 was examined in human hormone-refractory prostate cancer PC-3 and DU-145 cell lines by SRB assay. WJ9708012 inhibited cell proliferation in a concentration-dependent manner with IC_{50} values of 6.4 and 5.3 μmol/L in PC-3 and DU-145 cells, respectively (Figure 1B). WJ9708012 also induced a time-dependent apoptotic cell death by the detection of positive annexin V-staining and TUNEL-positive cells (Figures 1C and 1D). Besides, the flow cytofluorometric analysis of cell cycle by PI staining showed that WJ9708012 induced an increase of cell population at G_1 phase and a time-dependent apoptosis in PC-3 cells. The data

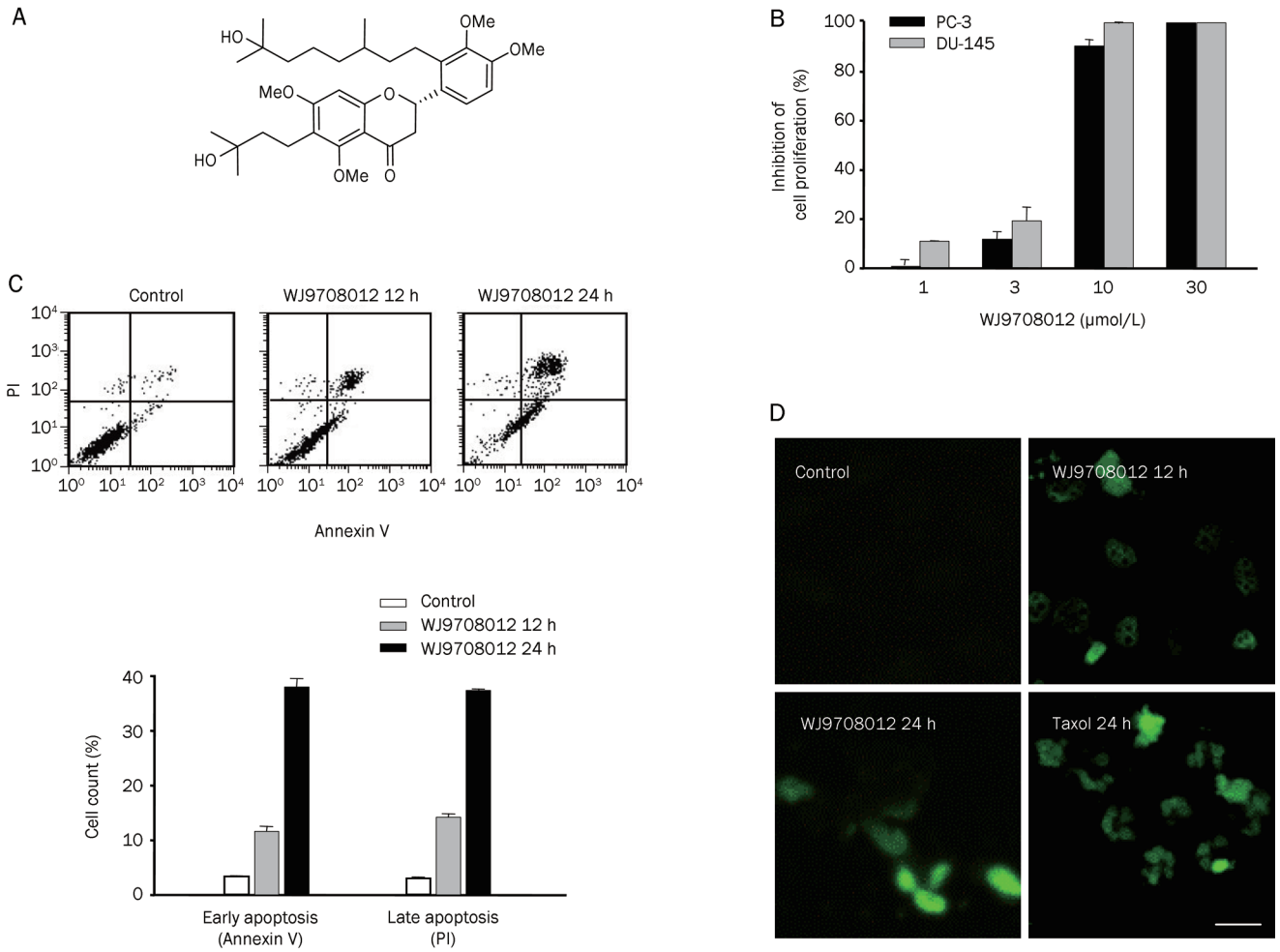

Figure 1. Identification of anti-proliferative and apoptotic effects. (A) Chemical structure of WJ9708012. (B) The graded concentrations of WJ9708012 were added to cells for 48 h. Then, the cells were fixed and stained with SRB and the data were analyzed as described in the Materials and methods section. Data are expressed as mean±SEM of four determinations (each in triplicate). (C and D) PC-3 cells were treated with the indicated agent. Then, the cells were harvested for annexin V-PI double staining of apoptosis or *in situ* detection of apoptotic cells by using TUNEL apoptosis detection methods. Data are expressed as mean±SEM of three determinations. Scale bar, 20 μm.

revealed that the cells were more susceptible to arrest at G_1 phase than the induction of apoptosis to WJ9708012 action (Figure 2).

Effect of WJ9708012 on Ca^{2+} mobilization and PKC-α activity

The Ca^{2+} mobilization was examined in the present work. The data in Figure 3A demonstrated that WJ9708012 triggered a significant increase of Ca^{2+} influx in extracellular Ca^{2+}-containing medium other than Ca^{2+}-free solution. In a parallel experiment, the Ca^{2+}-free solution supplemented with EGTA significantly inhibited WJ9708012-induced loss of $\Delta\Psi_m$, indicating that the influx of extracellular Ca^{2+} served as an upstream initiator to cause cellular stresses (Figure 3B). Furthermore, several pharmacological inhibitors were used to study the related target proteins. As a result, W7 (a membrane-permeable calmodulin inhibitor), Ro-318220 and Go-6983 (PKC inhibitors) significantly reduced WJ9708012-induced apoptotic effect (Figure 3C). Since PKC-α is the only conventional (Ca^{2+}-dependent) PKC isoform detected in PC-3 cells[27], the effect of WJ9708012 on PKC-α translocation was identified. The immunofluorescence microscopic examination showed that PKC-α translocated to plasma membrane after the exposure of cells to WJ9708012. The data were confirmed by Western blot that detected the plasma membrane fraction and demonstrated a time-dependent increase of PKC-α protein expression (Figure 3D). The data suggest that WJ9708012 induces the activation of PKC-α in PC-3 cells.

Effect of WJ9708012 on several cellular stresses

Numerous lines of evidence suggest that Ca^{2+} plays a central role not only on the induction of ER stress and mitochondrial insult but also on the communication of these two events[8, 10–12, 16]. Accordingly, several cellular stresses were determined in this study. The data demonstrated that WJ9708012 induced an early and sustained ER stress by the identification of up-regulated GADD153 and GRP78 protein

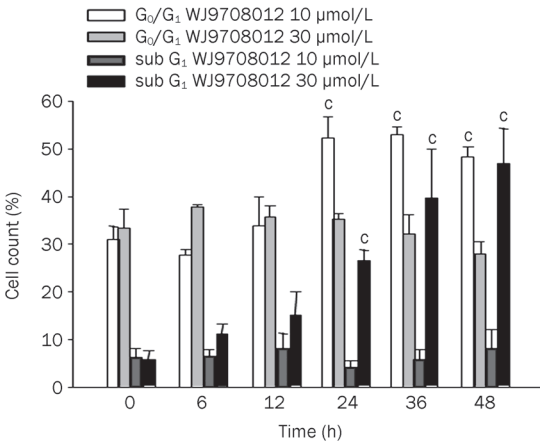

Figure 2. Effect of WJ9708012 on cell-cycle progression. PC-3 cells were treated without or with WJ9708012 for the indicated times. After the treatment, the cells were fixed and stained with propidium iodide to analyze DNA content by FACScan flow cytometer. Data are expressed as mean±SEM of three determinations. °P<0.01 compared with the respective control.

levels (Figure 4). The mitochondrial stress was also induced by the alteration of mitochondria-related signals, including the down-regulation of Bcl-2 and Bcl-xL expressions and the degradation of Bid and Bad associated with the formation of their truncated active fragments (tBid and tBad), two more potent inducers of apoptosis than the wild-type proteins[28, 29] (Figure 4). As expected, the activation of caspase-3 and caspase-7, and the cleavage of downstream effector PARP were induced by WJ9708012 (Figure 4).

Effect of WJ9708012 on mitochondrial stress

Excessive generation of ROS renders a cell oxidatively stressed and impairs membrane proteins, leading to mitochondrial dysfunction and apoptotic cell death. A lot of flavonoids have been reported to exhibit antioxidant activities[22], which reduce apoptotic capability of these compounds. WJ9708012 did not show antioxidant effect. Instead, it induced a moderate but significant increase of ROS production (Figure 5A), an effect prior to a loss of $\Delta\Psi_m$ (Figure 5B). Cytochrome *c*, AIF and endonuclease G are three pro-apoptotic proteins and are frequently found in the cytosol after apoptotic induction. In this study, WJ9708012 induced a dramatic increase of cytosolic level of cytochrome *c* and AIF (Figure 5C) in the time comparable to the impact on Bcl-2 family proteins (Figure 4). Additionally, we examined if WJ9708012 played a role on calpain activity. As a result, the cleavage of μ-calpain other than m-calpain was induced by WJ9708012 (Figure 5D).

Effect of WJ9708012 on the expression of cell-cycle regulators and mTOR pathway signals

The cell-cycle progression is regulated by periodic activation of various Cdk/cyclin complexes. Accordingly, several cyclins and Cdks that regulate G_1 phase of the cell cycle were examined. The data demonstrated that the protein expressions of cyclin D1, cyclin E and Cdk4 were down-regulated by WJ9708012 (Figure 6) that correlated with the cell-cycle arrest at G_1 phase. The data also showed a rapid down-regulation of cyclin D1 expression reflecting a short half-life of this protein (Figure 6). To examine if translational signaling pathways were affected by WJ9708012-induced stress, we detected several related protein expressions and the phosphorylation state, including mTOR, 4E-BP1 and p70S6K. mTOR, a serine/threonine kinase, is a key regulator of protein translation/synthesis. The phosphorylation of mTOR at Ser^{2448} is a marker of mTOR activation, which transmits positive signals to activate p70S6K (phosphorylation at Thr^{389}) and inactivate the translation repressor protein 4E-BP1 through sequential phosphorylation at Thr^{37}/Thr^{46} and Thr^{70}. The data showed that WJ9708012 induced a rapid and time-dependent decrease of phosphorylation level of mTOR (Ser^{2448}), 4E-BP1 (Thr^{70} and Thr^{37}/Thr^{46}) and p70S6K (Thr^{389}), suggesting the inhibition of mTOR-mediated translational pathways (Figure 6).

Discussion

The signaling pathways that control cell proliferation have been extensively studied in recent decades. Cell cycle progression is delicately controlled in cells responsive to diverse mitogenic signals, which stimulate sequential signaling cascades and regulate various cell cycle proteins through transcriptional control, posttranslational modifications and protein degradation. Cells are prone to arrest of the cell cycle in response to a variety of cellular stresses, including radiation, chemicals, oxidants and metabolite signals. This study showed that WJ9708012, a methoxyflavanone derivative, posed a cellular stress, leading to an arrest of the cell cycle at G_1 phase and a subsequent apoptosis in prostate cancer cells. The impact on several G_1-phase regulatory proteins was observed during the stress response, such as the down-regulation of cyclin D1, cyclin E and Cdk4. The data provided evidence that WJ9708012 reduced the protein levels of these regulators through an inhibition of mTOR-mediated translational pathways. Of note, cyclin D1 was the most susceptible protein to this inhibitory activity. It can be explained by the impairment of cyclin D1 stability since it has been suggested that a constitutive activation of phosphatidyl inositol 3-kinase/Akt that keeps glycogen synthase kinase (GSK)-3β inhibited increases cyclin D1 stability. Rapamycin, an mTOR inhibitor, blocks the inhibitory action on (GSK)-3β, leading to a nuclear export of cyclin D1 and a decrease of cyclin D1 stability[30].

Ca^{2+} is a double-edged sword in physiological control of cellular function as well as an inducer of cell death. Calcium has been implicated in propagating apoptotic signaling cascades in many types of cancer cells including prostate cancers[31]. However, a massive and acute influx of Ca^{2+} may cause cell necrosis without programmed death mechanism that is not an appropriate anticancer strategy. Classical PKC isoforms, including PKC-α, -β_I, -β_{II}, and -γ, are Ca^{2+}-dependent and are activated by diacylglycerol and phorbol esters through the cysteine-rich C1 domains[32]. Classical PKC isoforms are also well-known downstream effectors of Ca^{2+} in signaling cell

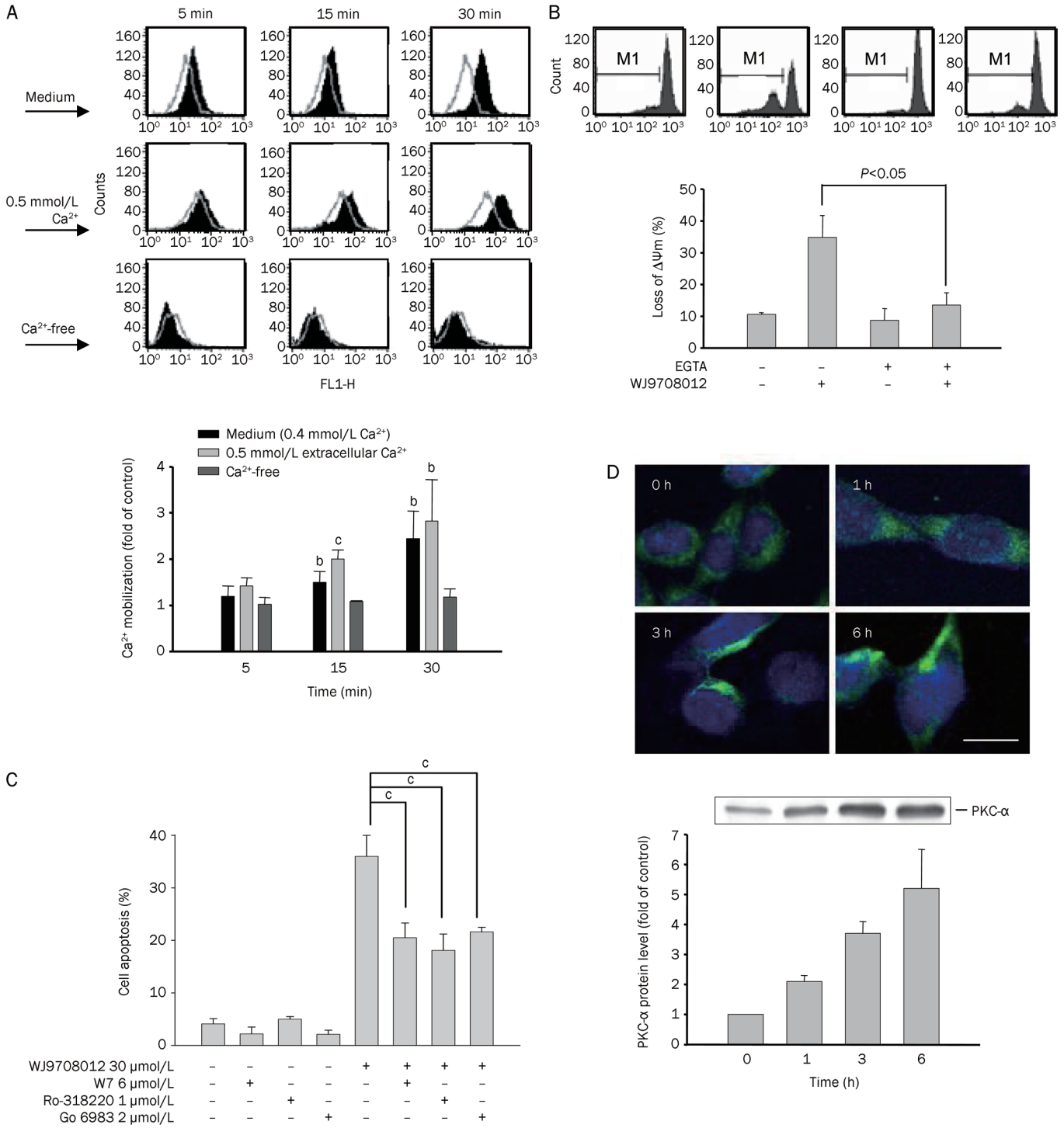

Figure 3. Effect of WJ9708012 on Ca^{2+}-related function and PKC-α membrane translocation. (A) PC-3 cells were treated with WJ9708012 (30 μmol/L) for 0 (control), 5, 15, or 30 min in various mediums containing different extracellular Ca^{2+} levels. After the treatment, the intracellular Ca^{2+} level was measured as described in the Materials and methods section. (B and C) PC-3 cells were pre-treated without or with EGTA (1 mmol/L, B) or the indicated agent for 30 min. WJ9708012 (30 μmol/L) was added for another 6 h (B) or 24 h (C). After the treatment, the flow cytometric analysis of rhodamine 123 or PI staining were used to detect the change of mitochondrial membrane potential ($\Delta\Psi_m$) or cell-cycle progression. Data are expressed as mean±SEM of three determinations. $^bP<0.05$, $^cP<0.01$ compared with the respective control. (D) PC-3 cells were treated without or with WJ9708012 (30 μmol/L) for the indicated time. After the treatment, the cells were fixed for the detection of PKC-α by confocal microscopic examination or the cells were harvested and the cell membrane was separated for the detection of PKC-α expression by Western blot. The data are representative of two independent experiments. The expressions were quantified using the computerized image analysis system ImageQuant (Amersham Biosciences). Scale bar, 20 μm.

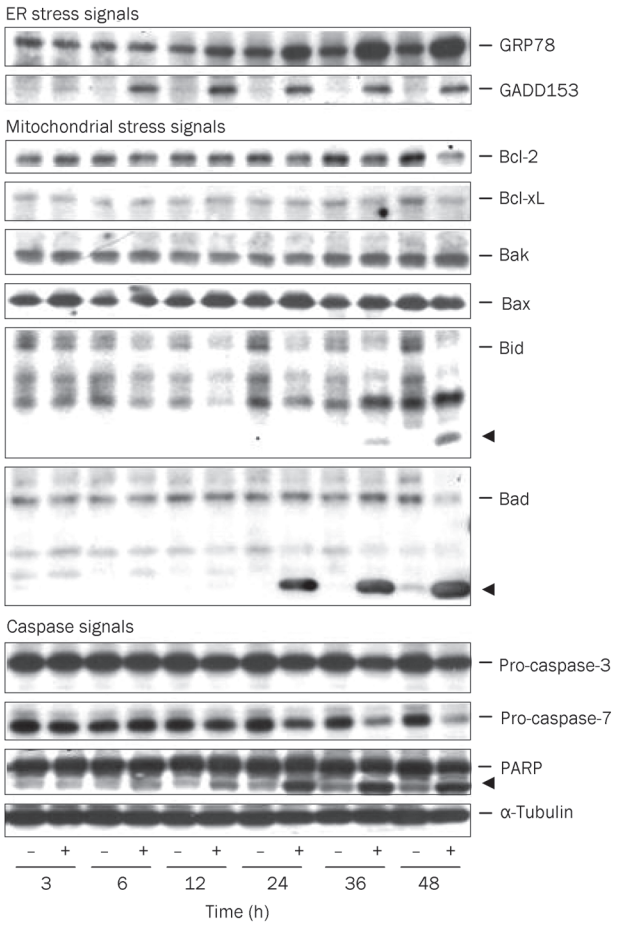

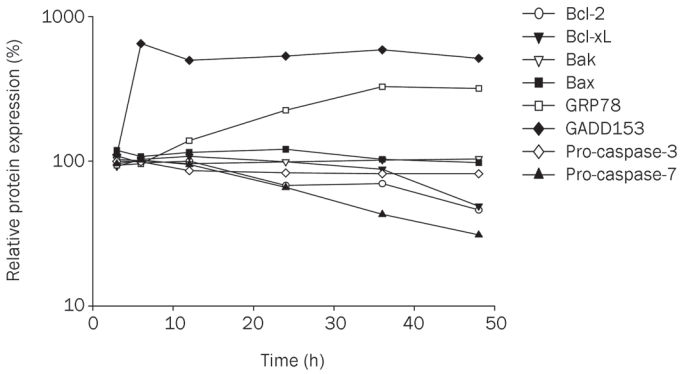

Figure 4. Effect of WJ9708012 on the expression of several ER and mitochondrial stress-related proteins. PC-3 cells were incubated in the absence or presence of WJ9708012 (30 μmol/L) for the indicated time. After the treatment, the cells were harvested and lysed for the detection of the indicated protein expressions by Western blot. The data are representative of three independent experiments. The expressions were quantified using the computerized image analysis system ImageQuant (Amersham Biosciences).

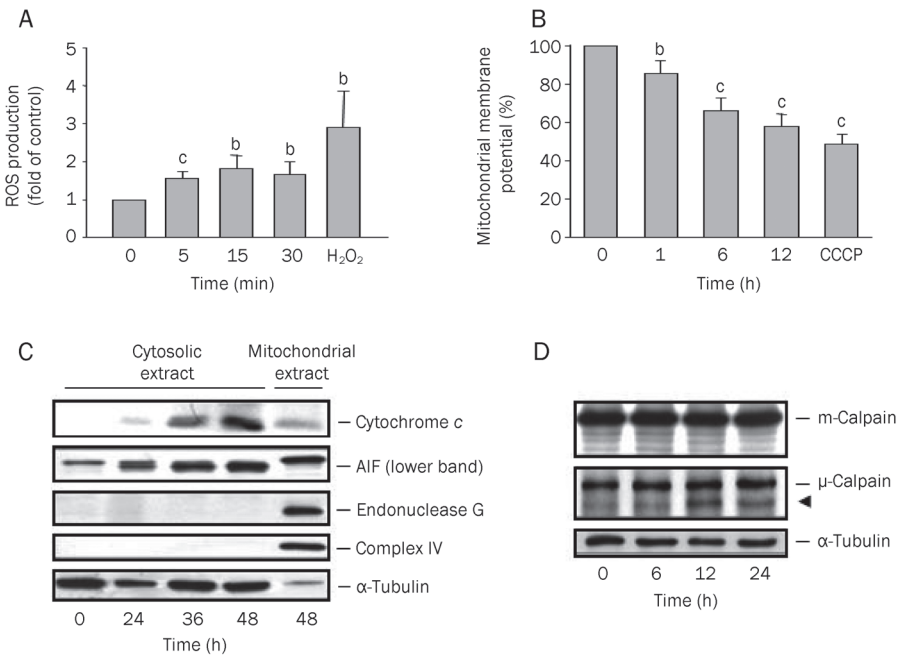

Figure 5. Effect of WJ9708012 on mitochondria-related function and calpain cleavage. PC-3 cells were treated without or with WJ9708012 (30 μmol/L) for the indicated time. After the treatment, the ROS production (A) or mitochondrial membrane potential (B) were measured as described in the Materials and methods section. Data are expressed as mean±SEM of three to five determinations. $^{b}P<0.05$, $^{c}P<0.01$ compared with the respective control. (C) The cells were harvested. The cytosolic and mitochondrial fractions were obtained for the detection of the indicated protein expressions by Western blot. (D) The detection of calpain cleavage by Western blot. The data are representative of two independent experiments.

proliferation, differentiation and apoptosis. PKC-α is the predominant isoform in many types of cancer cells[33]. Depending on the tumor type and different treatment, contradictory results have been described in PKC-α-mediated cell survival and apoptosis. For example, PKC-α knockout mice have been demonstrated to increase the tendency of developing

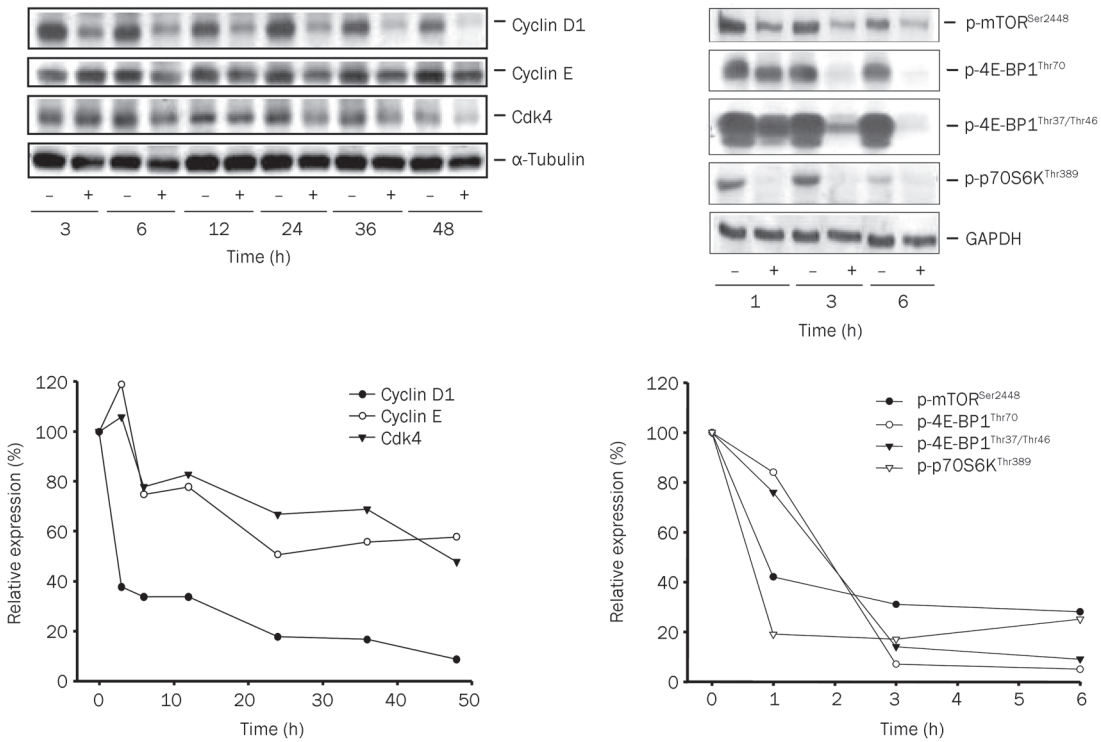

Figure 6. Effect of WJ9708012 on several protein expressions. PC-3 cells were treated without or with WJ9708012 (30 μmol/L) for the indicated time. After the treatment, the cells were harvested and lysed for the detection of the indicated protein expressions by Western blot. The expressions were quantified using the computerized image analysis system ImageQuant (Amersham Biosciences).

spontaneous intestinal tumors[34]. In contrast, Varga and the colleagues provided the data showing that the expression of PKC-α gradually increased with increasing tumor grades[35]. The data in this study showed that WJ9708012 induced an increase of intracellular Ca^{2+} level through extracellular origin. The increased Ca^{2+} subsequently induced cell apoptosis through a PKC-α-dependent pathway. Our data also showed the induction of ER stress to WJ9708012. Recent studies reveal that PKC is involved in the induction of GRP78[36], a major ER chaperone and a crucial regulator of ER homeostasis. Furthermore, PKC-α has been reported to mediate growth arrest in human embryonal rhabdomyosarcoma cells by inducing an activation of c-Jun N-terminal protein kinases (JNKs), p38 kinase and extracellular signal-regulated kinases (ERKs)[37], which are involved in the induction of ER stress[36, 38]. These reports support the present study that WJ9708012 activates PKC-α which in turn, directly or indirectly, induces ER stress in PC-3 cells.

Permeabilization of the outer mitochondrial membrane and release of pro-apoptotic proteins are the most extensively characterized pathways to cell apoptosis and make the mitochondria an attractive target for cancer chemotherapy[39]. Recently, a crosstalk between ER and mitochondria that reinforces the efficacy and efficiency of anticancer agents has been widely addressed[8]. Several pathways have been suggested to connect the interaction between ER and mitochondria. The electron tomographic examination shows that the ER network forms close or direct contacts with the mitochondria[8, 40, 41]. Several studies also reveal that ER may communicate with mitochondria via mitochondria-associated membranes[41]. In addition to direct network connection, a large body of evidence points to the Ca^{2+} as a central player that is released from the ER store and, in turn, causes a load in mitochondria, leading to necessary biochemical activities. However, an overload of mitochondrial Ca^{2+} induces the release of apoptotic proteins from the mitochondria, including cytochrome *c*, AIF and endonuclease G. Cytochrome *c* is a central co-factor in intrinsic apoptotic pathways. AIF and endonuclease G are also responsible for the nuclear DNA fragmentation upon numerous apoptotic stimuli[8, 29, 39]. In this study, WJ9708012 induced an increase of intracellular Ca^{2+} and ER stress, leading to the down-regulation of Bcl-2 and Bcl-xL expressions and a dramatic increase of cytosolic level of cytochrome *c* and AIF. The data reveal a crosstalk between ER and mitochondria in communicating WJ9708012-mediated apoptotic signaling pathways.

Calpains are consisted of a class of intracellular cysteine proteases that are activated by Ca^{2+} [42]. μ-Calpain (calpain-I) and m-calpain (calpain-II) are two major forms that are activated by micromolar and millimolar concentrations of Ca^{2+}, respectively. Several Bcl-2 family members, such as Bcl-2, Bid, and Bcl-xL, are reported to be processed by calpain[43]. Furthermore, calpain-mediated cleavage of Bid to an active fragment has been implicated in mitochondrial permeabilization

and cell death[44]. Recently, Polster and the colleagues used isolated mitochondria model and demonstrated that μ-calpain induced the cleavage and release of AIF[29]. In this study, WJ9708012 also induced the cleavage and release of AIF. The effect may be explained by the activation of μ-calpain.

Taken together, the data suggest that WJ9708012 induces an increase of cytosolic Ca^{2+} concentration and the activation of PKC-α in PC-3 cells. Subsequently, a crosstalk between ER stress and mitochondrial insult is induced, leading to the inhibition of mTOR translational pathways and arrest of the cell cycle at G_1 phase. Moreover, the summation of WJ9708012-mediated stress results in the down-regulation of Bcl-2 and Bcl-xL protein expressions and an increased release of cytochrome *c* and AIF, leading to apoptotic cell death. The data also demonstrate that WJ9708012 is an effective methoxyflavanone worth further investigation and development.

Acknowledgements

This work was supported by a research grant of the National Science Council of the Taiwan, China (NSC 98-2323-B-002-006). Facilities provided by grants from the National Science Council of the Republic of China (NSC 98-2323-B-002-001) are also acknowledged.

Author contribution

Ting-chun KUO performed the study; Wei-jan HUANG synthesized and provided the compound WJ9708012; Jih-hwa GUH designed the study and prepared the manuscript.

References

1 Herr I, Debatin KM. Cellular stress response and apoptosis in cancer therapy. Blood 2001; 98: 2603–14.
2 Wang XZ, Lawson B, Brewer JW, Zinszner H, Sanjay A, Mi LJ, *et al*. Signals from the stressed endoplasmic reticulum induce C/EBP-homologous protein (CHOP/GADD153). Mol Cell Biol 1996; 16: 4273–80.
3 Groenendyk J, Michalak M. Endoplasmic reticulum quality control and apoptosis. Acta Biochim Pol 2005; 52: 381–95.
4 Momoi T. Caspases involved in ER stress-mediated cell death. J Chem Neuroanat 2004; 28: 101–5.
5 Yeh TC, Chiang PC, Li TK, Hsu JL, Lin CJ, Wang SW, *et al*. Genistein induces apoptosis in human hepatocellular carcinomas via interaction of endoplasmic reticulum stress and mitochondrial insult. Biochem Pharmacol 2007; 73: 782–92.
6 Boelens J, Lust S, Offner F, Bracke ME, Vanhoecke BW. The endoplasmic reticulum: a target for new anticancer drugs. *In Vivo* 2007; 21: 215–26.
7 Linder S, Shoshan MC. Lysosomes and endoplasmic reticulum: targets for improved, selective anticancer therapy. Drug Resist Updat 2005; 8: 199–204.
8 Pinton P, Giorgi C, Siviero R, Zecchini E, Rizzuto R. Calcium and apoptosis: ER-mitochondria Ca^{2+} transfer in the control of apoptosis. Oncogene 2008; 27: 6407–18.
9 Zecchini E, Siviero R, Giorgi C, Rizzuto R, Pinton P. Mitochondrial calcium signaling: message of life and death. Ital J Biochem 2007; 56: 235–42.
10 Pinton P, Rizzuto R. Bcl-2 and Ca^{2+} homeostasis in the endoplasmic reticulum. Cell Death Differ 2006; 13: 1409–18.
11 Pyrko P, Kardosh A, Liu YT, Soriano N, Xiong W, Chow RH, *et al*. Calcium-activated endoplasmic reticulum stress as a major component of tumor cell death induced by 2,5-dimethyl-celecoxib, a non-coxib analogue of celecoxib. Mol Cancer Ther 2007; 6: 1262–75.
12 Akamatsu K, Shibata MA, Ito Y, Sohma Y, Azuma H, Otsuki Y. Riluzole induces apoptotic cell death in human prostate cancer cells via endoplasmic reticulum stress. Anticancer Res 2009; 29: 2195–204.
13 Pyrko P, Kardosh A, Schönthal AH. Celecoxib transiently inhibits cellular protein synthesis. Biochem Pharmacol 2008; 75: 395–404.
14 Brostrom MA, Brostrom CO. Calcium dynamics and endoplasmic reticular function in the regulation of protein synthesis: implications for cell growth and adaptability. Cell Calcium 2003; 34: 345–63.
15 Jakobsen CH, Størvold GL, Bremseth H, Follestad T, Sand K, Mack M, *et al*. DHA induces ER stress and growth arrest in human colon cancer cells: associations with cholesterol and calcium homeostasis. J Lipid Res 2008; 49: 2089–100.
16 Yano M, Terada K, Gotoh T, Mori M. *In vitro* analysis of Bcl-2 proteins in mitochondria and endoplasmic reticulum: similarities in anti-apoptotic functions and differences in regulation. Exp Cell Res 2007; 313: 3767–78.
17 Lam M, Dubyak G, Chen L, Nunez G, Miesfeld RL, Distelhorst CW. Evidence that BCL-2 represses apoptosis by regulating endoplasmic reticulum-associated Ca^{2+} fluxes. Proc Natl Acad Sci USA 1994; 91: 6569–73.
18 Scorrano L, Oakes SA, Opferman JT, Cheng EH, Sorcinelli MD, Pozzan T, *et al*. BAX and BAK regulation of endoplasmic reticulum Ca^{2+}: a control point for apoptosis. Science 2003; 300: 135–9.
19 Cornwell T, Cohick W, Raskin I. Dietary phytoestrogens and health. Phytochemistry 2004; 65: 995–1016.
20 Khan N, Mukhtar H. Multitargeted therapy of cancer by green tea polyphenols. Cancer Lett 2008; 269: 269–80.
21 Lee DH, Szczepanski M, Lee YJ. Role of Bax in quercetin-induced apoptosis in human prostate cancer cells. Biochem Pharmacol 2008; 75: 2345–55.
22 Miranda CL, Stevens JF, Ivanov V, McCall M, Frei B, Deinzer ML, *et al*. Antioxidant and prooxidant actions of prenylated and nonprenylated chalcones and flavanones *in vitro*. J Agric Food Chem 2000; 48: 3876–84.
23 Verhaegen S, McGowan AJ, Brophy AR, Fernandes RS, Cotter TG. Inhibition of apoptosis by antioxidants in the human HL-60 leukemia cell line. Biochem Pharmacol 1995; 50: 1021–9.
24 Zeisel SH. Antioxidants suppress apoptosis. J Nutr 2004; 134: 3179S–80S.
25 Salganik RI, Albright CD, Rodgers J, Kim J, Zeisel SH, Sivashinskiy MS, *et al*. Dietary antioxidant depletion: enhancement of tumor apoptosis and inhibition of brain tumor growth in transgenic mice. Carcinogenesis 2000; 21: 909–14.
26 Vermes I, Haanen C, Steffens-Nakken H, Reutelingsperger C. A novel assay for apoptosis. Flow cytometric detection of phosphatidylserine expression on early apoptotic cells using fluorescein labelled Annexin V. J Immunol Methods 1995; 184: 39–51.
27 Lamm ML, Long DD, Goodwin SM, Lee C. Transforming growth factor-beta1 inhibits membrane association of protein kinase C alpha in a human prostate cancer cell line, PC3. Endocrinology 1997; 138: 4657–64.
28 Condorelli F, Salomoni P, Cotteret S, Cesi V, Srinivasula SM, Alnemri ES, *et al*. Caspase cleavage enhances the apoptosis-inducing effects of BAD. Mol Cell Biol 2001; 21: 3025–36.
29 Polster BM, Basañez G, Etxebarria A, Hardwick JM, Nicholls DG. Calpain I induces cleavage and release of apoptosis-inducing factor from isolated mitochondria. J Biol Chem 2005; 280: 6447–54.

30 Dal Col J, Dolcetti R. GSK-3beta inhibition: at the crossroad between Akt and mTOR constitutive activation to enhance cyclin D1 protein stability in mantle cell lymphoma. Cell Cycle 2008; 7: 2813–6.
31 Flourakis M, Prevarskaya N. Insights into Ca^{2+} homeostasis of advanced prostate cancer cells. Biochim Biophys Acta 2009; 1793: 1105–9.
32 Geiger M, Wrulich OA, Jenny M, Schwaiger W, Grunicke HH, Uberall F. Defining the human targets of phorbol ester and diacylglycerol. Curr Opin Mol Ther 2003; 5: 631–41.
33 Martiny-Baron G, Fabbro D. Classical PKC isoforms in cancer. Pharmacol Res 2007; 55: 477–86.
34 Oster H, Leitges M. Protein kinase C-α but not PKC-ζ suppresses intestinal tumor formation in ApcMin/+ mice. Cancer Res 2006; 66: 6955–63.
35 Varga A, Czifra G, Tallai B, Nemeth T, Kovacs I, Kovacsand L, *et al*. Tumor grade-dependent alterations in the protein kinaseC isoform pattern in urinary bladder carcinomas. Eur Urol 2004; 46: 462–5.
36 Song MS, Park YK, Lee JH, Park K. Induction of glucose-regulated protein 78 by chronic hypoxia in human gastric tumor cells through a protein kinase C-epsilon/ERK/AP-1 signaling cascade. Cancer Res 2001; 61: 8322–30.
37 Mauro A, Ciccarelli C, De Cesaris P, Scoglio A, Bouché M, Molinaro M, *et al*. PKCα-mediated ERK, JNK and p38 activation regulates the myogenic program in human rhabdomyosarcoma cells. J Cell Sci 2002; 115: 3587–99.
38 Lien YC, Kung HN, Lu KS, Jeng CJ, Chau YP. Involvement of endoplasmic reticulum stress and activation of MAP kinases in beta-lapachone-induced human prostate cancer cell apoptosis. Histol Histopathol 2008; 23: 1299–308.
39 Gogvadze V, Orrenius S, Zhivotovsky B. Mitochondria as targets for cancer chemotherapy. Semin Cancer Biol 2009; 19: 57–66.
40 Marsh BJ, Mastronarde DN, Buttle KF, Howell KE, McIntosh JR. Organellar relationships in the Golgi region of the pancreatic beta cell line, HIT-T15, visualized by high resolution electron tomography. Proc Natl Acad Sci USA 2001; 98: 2399–406.
41 Vance JE. Phospholipid synthesis in a membrane fraction associated with mitochondria. J Biol Chem 1990; 265: 7248–56.
42 Goll DE, Thompson VF, Li H, Wei W, Cong J. The calpain system. Physiol Rev 2003; 83: 731–801.
43 Gil-Parrado S, Fernández-Montalván A, Assfalg-Machleidt I, Popp O, Bestvater F, Holloschi A, *et al*. Ionomycin-activated calpain triggers apoptosis. A probable role for Bcl-2 family members. J Biol Chem 2002; 277: 27217–26.
44 Chen M, He H, Zhan S, Krajewski S, Reed JC, Gottlieb RA. Bid is cleaved by calpain to an active fragment *in vitro* and during myocardial ischemia/reperfusion. J Biol Chem 2001; 276: 30724–8.

Acta Pharmacologica Sinica (2011) 32: 99–107

www.nature.com/aps

Original Article

The distinct role of guanine nucleotide exchange factor Vav1 in Bcl-2 transcription and apoptosis inhibition in Jurkat leukemia T cells

Jie YIN, Ya-juan WAN, Shi-yang LI, Ming-juan DU, Cui-zhu ZHANG, Xing-long ZHOU, You-jia CAO*

Tianjin Key Laboratory of Protein Sciences, Department of Biochemistry and Molecular Biology, College of Life Sciences, Nankai University, Tianjin 300071, China

Aim: To investigate a novel function of proto-oncogene Vav1 in the apoptosis of human leukemia Jurkat cells.
Methods: Jurkat cells, Jurkat-derived *vav1*-null cells (J.Vav1) and Vav1-reconstituted J.WT cells were treated with a Fas agonist antibody, IgM clone CH11. Apoptosis was determined using propidium iodide (PI) staining, Annexin-V staining, DNA fragmentation, cleavage of caspase 3/caspase 8, and *poly* (*ADP-ribose*) polymerase (PARP). Mitochondria transmembrane potential ($\Delta\Psi_m$) was measured using $DiOC_6(3)$ staining. Transcription and expression of the Bcl-2 family of proteins were evaluated using semi-quantitative RT-PCR and Western blot, respectively. Bcl-2 promoter activity was analyzed using luciferase reporter assays.
Results: Cells lacking Vav1 were more sensitive to Fas-mediated apoptosis than Jurkat and J.WT cells. J.Vav1 cells lost mitochondria transmembrane potential ($\Delta\Psi_m$) more rapidly upon Fas induction. These phenotypes could be rescued by re-expression of Vav1 in J.Vav1 cells. The expression of Vav1 increased the transcription of pro-survival Bcl-2. The guanine nucleotide exchange activity of Vav1 was required for enhancing Bcl-2 promoter activity, and the Vav1 downstream substrate, small GTPase Rac2, was likely involved in the control of Bcl-2 expression.
Conclusion: Vav1 protects Jurkat cells from Fas-mediated apoptosis by promoting Bcl-2 transcription through its GEF activity.

Keywords: Vav1; guanine nucleotide exchange factor; Jurkat T cells; apoptosis; Bcl-2

Acta Pharmacologica Sinica (2011) 32: 99–107; doi: 10.1038/aps.2010.185; published online 13 Dec 2010

Introduction

Vav1 is a member of the guanine nucleotide exchange factors (GEFs) for Rac/Rho small GTPases, and it is predominantly expressed in hematopoietic cells[1]. The other two members of the Vav family, Vav2 and Vav3, are ubiquitously expressed[2, 3]. The functional importance of Vav1 has been demonstrated in thymocyte development, T cell activation, and tumor malignancy. Mice deficient in Vav1 exhibit decreased numbers of double positive and single positive T cells[4, 5]. This phenotype is more profound when all three Vav genes are eliminated[6]. T cells isolated from Vav knock-out mice or genetically derived from human leukemia Jurkat T cells show obvious defects in T cell receptor (TCR)-mediated activation[5, 7]. In humans, reduced expression of Vav1 is associated with common variable immunodeficiency with defective T-cell function (T-CVID), which is characterized by hypogammaglobulinemia due to impaired T cell function[8]. By contrast, overexpression of Vav1 is associated with B cell chronic lymphocytic leukemia[9]. The aberrant expression of Vav1 has also been reported in non-hematopoietic cancer malignancies, such as neuroblastoma[10], pancreatic adenocarcinoma[11], and melanoma[12], indicating an indispensable role for Vav1 in cell growth and survival.

Vav proteins contain multiple structural motifs, including a Dbl homology domain for activation of Rho family GTPases, a calponin homology domain (CH), an acidic motif, a pleckstrin homology domain (PH), a cysteine-rich domain (CRD), and two SH3 domains flanking a single SH2 region[13]. Upon T cell activation, Vav1 is rapidly tyrosine phosphorylated and uses its GEF activity on several small GTPases, including Rac1, Rac2, and Cdc42, leading to the recruitment of signaling molecules and the formation of the immune synapse[14, 15]. Vav1 also plays GEF-independent roles, such as modulating TCR-stimulated calcium flux[16] and potentiating calcium release by association with calmodulin[17]. Vav1 is activated upon ligation of the co-stimulatory receptor, CD28, which leads to the

* To whom correspondence should be addressed.
E-mail caoyj@nankai.edu.cn
Received 2010-07-28 Accepted 2010-09-28

nuclear translocation of Vav1[18]; the nuclear function of Vav1 has yet to be addressed. The structural complexity of Vav1 suggests its involvement in diverse cellular processes.

Apoptosis is an essential process in both the development of lymphocytes and the contraction phase of immune responses[19]. Accumulating evidence suggests that Vav1 is involved in the regulation of cell apoptosis. For example, during negative selection, Vav1 promotes antigen-induced thymocyte apoptosis, and inhibitors of the actin cytoskeleton or protein kinase C (PKC) reverse the effect[20]. In activated $CD4^+$ T cells, the Vav1-Rac pathway is a critical component of TCR-induced cell death[21]. However, Vav1 has also been reported to be a pro-survival molecule in different signaling contexts. For instance, overexpression of Vav1 counteracts CD4-mediated apoptosis of T cells by reducing mitochondrial damage and inhibiting Bax expression[22]. Deletion of all three Vav members decreases the number of mature B cells[23]. The pro-survival function of Vav1 is also evident in studies that treated leukemia with Vav1 antisense oligonucleotides[24] or by blocking the Vav1-Rac signaling pathway[25]. In addition, Vav1 expression in non-hematopoietic cells is associated with cancer malignancy[26]. Overall, Vav1 participates in regulating cell survival, but the mechanisms of Vav1 association with the apoptotic pathway remain to be elucidated. Because Vav1 possesses promiscuous substrates and various functional motifs that overlap with Vav2 and Vav3, it is important to identify the unique role of Vav1.

Using leukemia Jurkat T cells and *vav1*-null cells (J.Vav1)[7], we investigated the function of Vav1 in T cell apoptosis without evoking signals from the TCR and CD28. We found that the expression of Vav1 promotes Bcl-2 transcription. We further showed that Rac2 is likely to be the downstream effector of Vav1 in this signaling context.

Materials and methods

Antibodies and reagents

The anti-Vav1 and anti-Bax antibodies were purchased from Santa Cruz Biotechnology (Santa Cruz, CA, USA). The anti-ZAP70 antiserum was raised against residues 326 to 341 of human ZAP70[7]. The anti-Fas (human, activating) IgM clone CH11 was purchased from Upstate (Lake Placid, NY, USA). The anti-α tubulin and anti-flag antibodies were purchased from Sigma (St Louis, MO, USA). The antibodies for caspase 3, caspase 8, *poly (ADP-ribose)* polymerase (PARP), Bcl-2, Bcl-xL, and Bim were purchased from Cell Signaling Technology (Danvers, MA, USA). PE-conjugated anti-Fas IgG was purchased from Jingmei Biotech (Beijing, China). PE-conjugated human Annexin-V recombinant protein was purchased from Bender MedSystems (Vienna, Austria). Proteinase K was obtained from Merck (Darmstadt, Germany). RNase A and the transfection reagent, polyethylenimine (PEI) were purchased from Sigma (St Louis, MO, USA). The TRIzol RNA extraction reagent was purchased from Invitrogen (Carlsbad, CA, USA). RNase-free DNase I was purchased from Promega (Madison, WI, USA). The RNA LA PCR kit (AMV) was purchased from Takara (Otsu, Shiga, Japan). *Taq* polymerase was purchased from Tiangen (Beijing, China).

Cell lines and cell culture

Jurkat T leukemia cell line E6 was obtained from ATCC (Manassas, VA, USA). J.Vav1 cells were derived from Jurkat cells by knocking out vav1 alleles with somatic gene targeting as described previously[7]. The J.WT cell line was generated from a single clone of J.Vav1 cells transfected with a plasmid encoding wild-type Vav1 and selected using a drug resistance marker. HeLa and MCF7 cell lines were also from ATCC.

Jurkat, J.Vav1, and J.WT cells were grown in RPMI 1640 medium containing 10% (*v/v*) fetal bovine serum and 1% (*v/v*) penicillin/streptomycin. Cervical cancer HeLa cells were cultured in DMEM medium containing 10% (*v/v*) newborn calf serum and 1% (*v/v*) penicillin/streptomycin. Breast cancer MCF7 cells were kept in RPMI 1640 medium containing 10% (*v/v*) fetal bovine serum and 1% (*v/v*) penicillin/streptomycin. All cells were incubated at 37 °C with 5% CO_2.

Plasmid constructs

The coding region of full-length Vav1 (FL), deletion of the calponin homology domain (Del-CH), and deletion of the C-terminal SH3 domain (Del C-SH3) were subcloned into pcDNA4/HisMax vectors and designated Vav1 (FL), Vav1 (ΔCH), and Vav1 (ΔC-SH3), respectively, as described previously[17]. The plasmids, pEF-Vav1 (L213A) and pEF-c-myc-Vav1 (Y174F), were kindly provided by Dr Altman's lab (La Jolla Institute for Allergy & Immunology, USA) and used as described previously[7]. Flag-tagged human Vav2 and Vav3 expression plasmids were prepared by subcloning the coding region of human Vav2 and Vav3 cDNAs, respectively, into the pCMV-Tag2B vector at EcoRI-HindIII restriction sites. The Bcl-2 expression plasmid, pSG5-Bcl-2, was provided by Dr Quan CHEN (College of Life Science, Nankai University, China). The reporter plasmid, pBcl-2-Luc (Bcl-2 promoter region from ATG to -3934), was obtained from Addgene (http://www.addgene.org/) and originated from Dr Boxer's lab (Stanford School of Medicine, USA). The flag-tagged human Rac2 expression construct was prepared by subcloning the human Rac2 cDNA into the pCMV-Tag2B vector as a BamHI-EcoRI restriction fragment. Rac2 mutations, Rac2 (Q61L) and Rac2 (D57N), were generated by overlap PCR with the pCMV-Tag2B plasmid.

DNA transfection and luciferase reporter assay

Transfections were performed with 2×10^7 Jurkat cells or J.Vav1 cells by electroporation with a BTX Electro Square Porator, model ECM 830 (BTX Inc, San Diego, CA, USA) at 310 mv, 10 ms with 40 μg of total plasmid DNA. For HeLa and MCF7 cells, PEI transfection was performed with 3 μg of total plasmid DNA per 1×10^5 cells. Transfected cells were harvested 24 h later and prepared for luciferase assay. Firefly and pRL-TK-derived Renilla luciferase (RL) activities were measured according to the manufacturer's protocol with a Dual Luciferase Assay kit (Promega, Madison, WI, USA). The promoter activity was recorded as the ratio of firefly luciferase

to the RL activity and expressed as normalized relative light units (RLU). Results are presented as the mean±standard deviation (SD) of triplicate samples. All reporter gene assays were repeated independently a minimum of three times. The expression of transfected genes was analyzed by Western blot.

Western blot analysis

Unless otherwise specified, cells (1×10^6) were collected and lysed with RIPA buffer (20 mmol/L Tris-HCl, pH 7.5, 150 mmol/L NaCl, 0.5 mmol/L EDTA, 1% Triton X-100, 1 mmol/L PMSF, 1 mmol/L NaF, 1 μg/mL leupeptin) at 4 °C. Protein concentration was determined by Bradford assay. Equal amounts of protein from each cell lysate were subjected to 10% or 15% SDS-polyacrylamide gel electrophoresis (SDS-PAGE) as indicated. The resolved proteins were transferred to PVDF membranes and blotted with indicated antibodies.

Flow cytometry analysis

Cells were collected, and 1×10^6 cells per mL were resuspended in 1×PBS (pH 7.4) containing 1% FBS and incubated with PE-conjugated Annexin-V or propidium iodide (PI) in the dark for 20 min at room temperature. Cells were then washed once with 1 mL of PBS and resuspended in 500 μL of PBS containing 1% FBS. Flow cytometric analysis was performed on a flow cytometer (FACS Calibur, Becton Dickinson, Franklin Lakes, NJ, USA) using CellQuest software (Becton Dickinson).

For mitochondrial transmembrane potential ($\Delta\Psi_m$) measurement, cells were treated with 10 ng/mL CH11 or left untreated for 6 h. The $\Delta\Psi_m$ indicator, $DiOC_6(3)$ (2 μL of a 2 μmol/L stock solution in DMSO), was added to a 400 μL cell suspension in PRMI-1640 medium and incubated at 37 °C for 5 min. $\Delta\Psi_m$ was analyzed by flow cytometry with excitation at 488 nm. A decrease in $DiOC_6(3)$ fluorescence (530±30 nm) indicates a loss of $\Delta\Psi_m$.

DNA fragmentation

One million cells were collected by centrifugation (room temperature, 110×*g*, 5 min), washed briefly with 1×PBS (pH 7.4) and centrifuged again. Cell pellets were then treated with 50 μL lysis buffer (1% NP40 in 20 mmol/L EDTA, 50 mmol/L Tris-HCI, pH 7.5), and supernatants were collected by centrifugation (room temperature, 1600×*g*, 5 min). The supernatants were then sequentially incubated with RNase A (5 μg/μL, 37 °C, 2 h) and proteinase K (2.5 μg/μL, 58 °C, 2 h) to eliminate RNA and protein contamination. The extracted DNA was obtained by ethanol precipitation, dissolved in gel loading buffer, and separated by agarose gel eletrophoresis.

RNA isolation and semi-quantitative RT PCR

Total RNA was isolated from 1×10^7 cells as indicated with TRIzol reagent following the manufacturer's instructions (Invitrogen, Carlsbad, CA, USA). The RNA was then resuspended in DEPC-treated TE (pH 8.0) and treated with RNase-free DNase I (Promega) for 1 h. Two micrograms of total RNA was reverse-transcribed at 42 °C using the Takara RNA LA PCR kit (AMV) with oligo dT primers. Semi-quantitative PCR was performed by 30 cycles of denaturation at 94 °C for 30 s, annealing at 60 °C for 30 s, and extension at 72 °C for 20 s. Hypoxanthine guanine phosphoribosyl transferase (HPRT) was used as an internal control for gene expression. The primers used for semi-quantitative PCR were as follows: Bcl-2 5′-TTCTTTGAGTTCGGTGGGGTC-3′(forward) and 5′-AGCCAGGAGAAATCAAACAGAGG-3′ (reverse); HPRT 5′-TGACACTGGCAAAACAATGCA-3′ (forward) and 5′-GGTCCTTTTCACCAGCAAGCT-3′ (reverse). The PCR products were resolved by 1.5% agarose gel electrophoresis. The net intensity of each band was quantified using Quantity One software (BIO-RAD, Hercules, CA, USA).

Statistical analysis

Most of our results are representative of at least three independent experiments and are presented as the mean±standard deviation (SD) of triplicate samples.

Results

Loss of Vav1 leads to high sensitivity of cells to apoptosis

Fas-mediated apoptosis is the main mechanism of T cell homeostasis. Here, we used the Fas agonist antibody, CH11, to induce apoptosis in cells in the presence or absence of Vav1 (Figure 1A). After treatment with 10 ng/mL of CH11 for 8 h, 50% of J.Vav1 cells underwent apoptosis, whereas 70%−80% of Jurkat or J.WT cells were viable based on PI analysis (Figure 1B), indicating a protective role for Vav1 against Fas-mediated cell death. To exclude possible variations in expression of Fas due to the cloning process, we stained the three cell lines with a PE conjugated Fas-specific antibody (IgG) that does not induce apoptosis. Flow cytometry analysis showed the same shift in PE fluorescence intensity (Figure 1C), indicating the same level of surface Fas molecules on these cells. One of the characteristic early events of apoptosis is the reversed location of phosphatidylserine. When treated with CH11 for 12 h, nearly 50% of J.Vav1 cells were Annexin-V positive in comparison with 30% of Jurkat or J.WT cells that were Annexin-V positive (Figure 1D). The final event of apoptosis, DNA fragmentation, was also found to be higher in J.Vav1 (Figure 1E) *versus* Jurkat and J.WT cells. The above results indicate that cells lacking Vav1 are more sensitive to apoptosis by CH11. Similar trends of cell death were also seen with other apoptotic stimuli, such as serum starvation and oxidation (Supplementary Figure 1). These data indicate that the loss of Vav1 results in cells being more sensitive to apoptotic stimuli. We also examined the cleavage of the terminal molecule in the caspase pathway, caspase 3, and its substrate, PARP, and observed an earlier cleavage and activation pattern of caspase 3/PARP in J.Vav1 cells (Figure 1F).

Fas engagement leads to the formation of the DISC (death inducing signaling complex) and the activation of caspase 8, and Vav1 could negatively regulate DISC formation by competing for actin binding sites with Ezrin, a linker between Fas and the actin cytoskeleton[27]. Thus, we examined the kinetics of caspase 8 cleavage in the presence or absence of Vav1 upon anti-Fas CH11 treatment. We found detectable

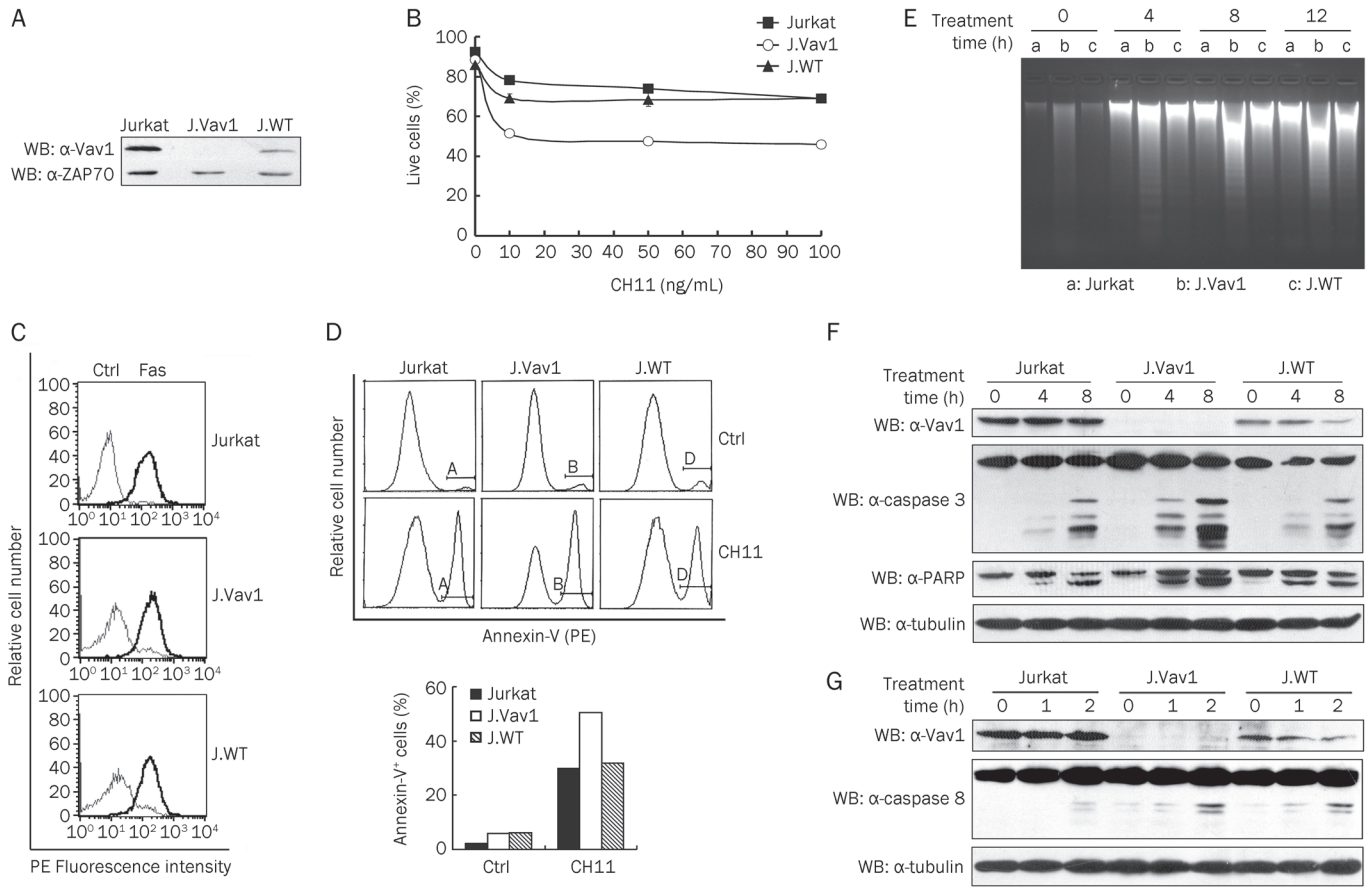

Figure 1. Effect of Vav1 on Fas-mediated cell death. (A) Vav1 protein expression in the indicated cells was determined by immunoblot using an antibody against Vav1, and ZAP70 was used as a loading control. (B) Cells with or without Vav1 were treated with increasing concentrations of CH11 for 8 h, and percentages of live cells were determined by flow cytometry using PI staining. Data represent the mean with standard deviation of 3 experiments. (C) Expression of surface Fas was analyzed by flow cytometry with PE-conjugated anti-Fas IgG (darker lines). The pre-immune IgG was used as control (lighter lines). (D) Comparison of Fas-mediated apoptosis with or without Vav1. Cells were treated with CH11 (10 ng/mL) for 12 h and stained with Annexin-V PE. The apoptotic cells (AV^+) were analyzed by flow cytometry, and percentages of AV^+ cells are quantitatively displayed in the graph. (E) Cells were treated with CH11 for the indicated time, and extracted DNA was subjected to agarose gel electrophoresis. Cleavage of caspase 3, PARP (F) and caspase 8 (G) in cell lysates was examined after treatment with CH11 (10 ng/mL) for the indicated times. Tubulin was used as a loading control. (A), (C), (D), (E), (F), and (G) are representative of at least three independent experiments.

cleavage of caspase 8 1 h after treatment in J.Vav1 and J.WT cells and 2 h after treatment in Jurkat cells (Figure 1G). The decreased expression of Vav1 in J.WT compared to Jurkat cells may not provide enough Vav1 to compete with Ezrin and thus cannot block the formation of the DISC. On the other hand, the rescue of caspase 3 and PARP in J.WT (Figure 1F) also indicates that caspase 8 is not the upstream mediator of caspase 3 cleavage.

As Jurkat cells are type II cells in which the FasL-induced apoptosis is mitochondria-dependent[28], the above data suggest that Vav1 plays an anti-apoptotic role in mitochondria-dependent apoptosis.

Vav1 maintains mitochondrial membrane integrity

The disintegration of the mitochondrial membrane marks the earliest event of apoptosis upon CH11 treatment. We determined the change in mitochondrial transmembrane potential ($\Delta\Psi_m$) in Jurkat, J.Vav1, and J.WT cells by flow cytometry using the fluorescent dye, $DiOC_6(3)$, as a tracer. We found that in the absence of Vav1 (J.Vav1), more than 62% of cells had lower $\Delta\Psi_m$ compared with that of Jurkat (35%) and J.WT cells (39%) (Figure 2). Thus, the integrity of the mitochondrial membrane is severely impaired in the absence of Vav1 upon treatment with CH11.

Vav1 sustains Bcl-2 transcription in T cells

T cell fate is precisely controlled by the balanced expression of the Bcl-2 family of proteins. In activated T cells, Bcl-2 levels are reduced by nearly 50%, allowing them to undergo activation-induced apoptosis in the contraction phase of T cell response[29]. We therefore asked whether there were differences in the expression of Bcl-2-related proteins. A panel of pro-apoptotic proteins (Bax, Bim, Bmf, Puma, and Bok) and anti-apoptotic proteins (Bcl-2, Bcl-xL, and Mcl-

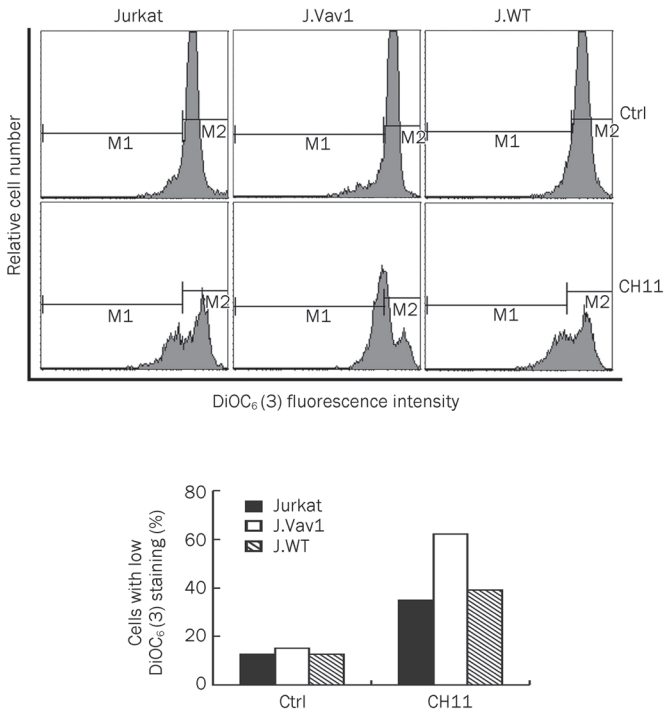

Figure 2. Effect of Vav1 on mitochondrial membrane integrity. Changes in mitochondrial membrane potential ($\Delta\Psi_m$) in the three cell lines were detected by $DiOC_6(3)$ staining after CH11 treatment. The percentages of cells shifting to lower fluorescence intensity are shown in the bar graph. These data are representative of three independent experiments.

1) were examined. Among these proteins, the expression of Bcl-2 was significantly reduced in J.Vav1 cells, but not in Jurkat or J.WT cells. No significant differences in expression of the other family members, such as pro-survival Bcl-xL, pro-apoptotic Bax, or BH3 only Bim, were observed (Figure 3A). This experiment demonstrated that loss of Vav1 decreased the expression of Bcl-2, and reconstitution of cells with Vav1 restored the levels of Bcl-2. Therefore, Vav1 is required for maintaining the expression of Bcl-2 in Jurkat T cells. Because the level of Bcl-2 proteins in cells is strictly regulated, the transcription of Bcl-2 was examined. Semi-quantitative RT-PCR showed that the level of Bcl-2 mRNA in J.Vav1 cells was only half of that in Jurkat or J.WT cells (Figure 3B), in agreement with the observed reduction in Bcl-2 protein expression (Figure 3A). The Bcl-2 synthesis and degradation rates were unchanged in the presence or absence of Vav1 (data not shown). Therefore, Vav1 affects the transcription of Bcl-2.

To confirm the effect of Vav1 on Bcl-2 transcription, we performed a reporter assay in which the luciferase gene was under the control of the full promoter region (from ATG to -3934) of Bcl-2[30]. Transient expression of Vav1 increased Bcl-2 promoter activity to the level as that in Jurkat cells (Figure 3C), whereas J.Vav1 cells transfected with control empty vectors displayed only 50% of the promoter activity observed in Jurkat cells (Figure 3C), consistent with the mRNA analysis (Figure 3B). This suggests that Vav1 promotes Bcl-2 transcription in Jurkat cells. In addition, Bcl-2 transcription was further enhanced in Jurkat cells overexpressing Vav1 (Figure 3C), implying a dose-dependent transcription of Bcl-2 by Vav1. In agreement with this, the ectopic expression of Vav1 or Bcl-2 could rescue J.Vav1 from CH11-induced cell death (Figure 3D), suggesting that the amount of Vav1 influences the transcription of Bcl-2.

The GEF activity of Vav1 is specifically required for maintaining Bcl-2 transcription

Vav1 contains multiple structural domains that permit its function as a GEF and a scaffold protein[31, 32]. To explore the possible mechanisms by which Vav1 enhances the transcription of Bcl-2, we constructed a series of Vav1 mutations (Figure 4A). As previously reported, disruption of the Dbl homology domain by the L213 mutation, referred to as Vav1 (L213A), abolishes the GEF activity of Vav1. By contrast, Vav1 (Y174F) and Vav1 (ΔCH) possess constitutive GEF activity due to the unmasked DH domain[13, 33]. Deletion of the C-terminal SH3 domain, Vav1 (ΔC-SH3), eliminates the interaction of Vav1 with many nuclear proteins[32]. Expression of the Bcl-2 reporter gene was measured in the presence of the above Vav1 mutations. Whereas the expression of wild-type Vav1 in J.Vav1 cells increased luciferase expression by more than two-fold of that in the control sample (pcDNA4), Vav1 (Y174F) and Vav1 (ΔCH) further enhanced Bcl-2 transcription (Figure 4B). By contrast, GEF-deficient Vav1 (L213A) failed to induce Bcl-2 transcription (Figure 4B). Vav1 (ΔC-SH3) promoted Bcl-2 transcription to levels similar to wild-type Vav1 (Figure 4B), ruling out the effect of nuclear interactions of Vav1. Taken together, the mutation analyses demonstrate that the GEF activity of Vav1 is required for maintaining Bcl-2 transcription.

Vav family members (Vav1, 2, and 3) possess highly homologous DH domains and redundant GEF functions. Because of the presence of Vav2 and Vav3 in Jurkat cells, we examined their effect on Bcl-2 transcription and found that overexpressed Vav2 or Vav3 had no significant influence on Bcl-2 promoter activation (Figure 4C). Thus, among Vav family members, only Vav1 is responsible for promoting the transcription of Bcl-2 in Jurkat T cells. We further tested the effect of Vav1 expression on Bcl-2 transcription in the non-hematopoietic cancer cell lines, HeLa and MCF7, and found similar trends in Bcl-2 promoter activity (Figure 4D).

Vav1 enhances Bcl-2 transcription via the small GTPase, Rac2

Vav family proteins function as GEFs for many small GTPases with nonspecific and overlapping specificity[14]. Vav1 can activate the GDP/GTP exchange for Rac1, Rac2, and RhoG; Vav2 is a GEF for RhoA, RhoB, and RhoG; and Vav3 preferentially activates RhoA, RhoG, and to a lesser extent, Rac1[32]. Among these small GTPases, Rac2 is predominantly expressed in hematopoietic cells and is activated by Vav1[34]. To investigate whether Rac2 was downstream of Vav1 in the regulation of Bcl-2 transcription, we examined cells with mutations in Rac2. The results showed that full-length Vav1 enhanced reporter activity, whereas Rac2 alone had no detectable effect

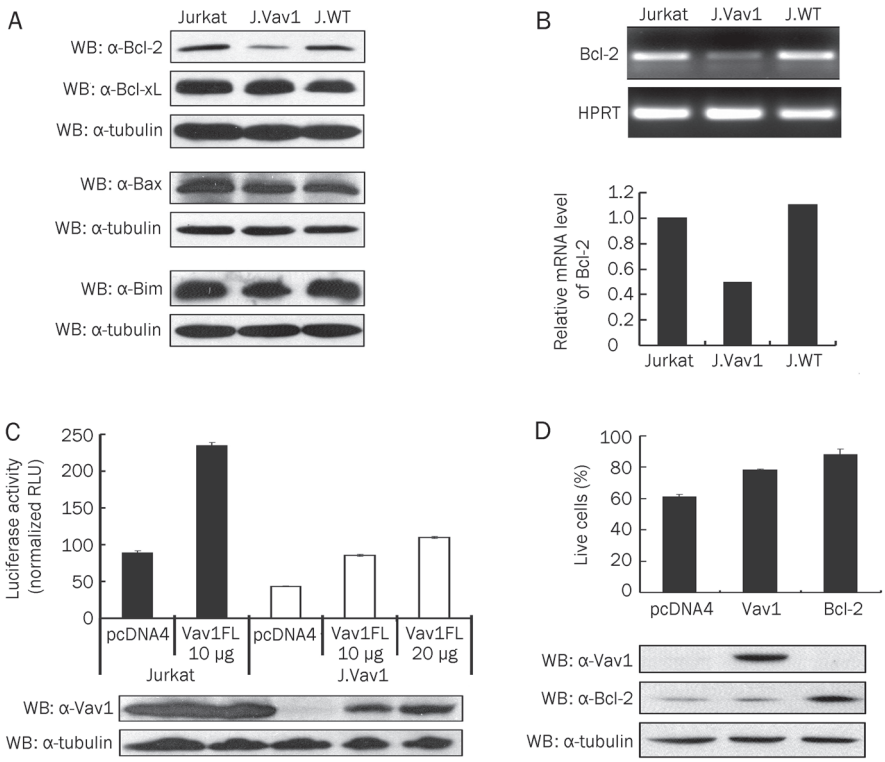

Figure 3. Expression of the Bcl-2 family of proteins in the presence or absence of Vav1. (A) Expression of indicated Bcl-2 family members was analyzed by Western blot with tubulin as the loading control. (B) Bcl-2 transcripts in Jurkat, J.Vav1, and J.WT cells were analyzed by semi-quantitative RT-PCR. The relative amount of Bcl-2 mRNA was calculated as a ratio of the control HPRT mRNA (bar graph). (C) Jurkat cells (solid bars) and J.Vav1 cells (open bars) were co-transfected with the pBcl-2-Luc reporter and pTK-RL plasmids, together with the empty vector (pcDNA4) or the indicated amount of the Vav1 plasmid. Twenty-four hours post-transfection, cells were collected, and Bcl-2 promoter activity was measured as firefly luciferase activity normalized to the Renilla luciferase activity and presented as relative light units (RLU). Bars indicate the mean±SD from triplicate samples. The lower panel shows the expression of Vav1 protein in each sample, with tubulin as the loading control. (D) J.Vav1 cells were co-transfected with pEGFP plus control vector (pcDNA4) and the Vav1 expression vector or Bcl-2 expression plasmid. Twenty-four hours later, each transfection group was divided into two groups with one group treated with 20 ng/mL CH11 and the other left untreated for 5 h, and cells were then analyzed by flow cytometry. The percentage of live cells was obtained by dividing the percentage of GFP positive cells in the CH11-treated group by that in the untreated group. Bars indicate the mean±SD from triplicate samples. Protein expression was determined by immunoblot with lysates from total transfected cells (lower panel). Data in (A) and (B) are representative of three independent experiments

on promoter activity and the constitutively active Rac2 (Q61L) increased Bcl-2 transcription to levels similar to Vav1 (FL) (Figure 5A). Expression of a dominant negative form of Rac2, Rac2 (D57N), further suppressed Bcl-2 promoter activity (Figure 5A) and suppressed 64% and 51% of the Bcl-2 promoter activity enhanced by Vav1 and Vav1 (Y174), respectively (Figure 5B). For comparison, we also tested the small GTPase Rac1, a major downstream effector of Vav1 during TCR activation, and the constitutively active form of Rac1 failed to increase Bcl-2 transcription (data not shown). These data indicate that Rac2 is a molecule downstream of Vav1 for Bcl-2 transcription.

Discussion

Apoptosis is important for maintenance of T cell homeostasis. Vav1 has been implicated in the regulation of T cell survival in both physiological and pathological processes[16] in addition to its essential role in T cell activation. Here, the use of a *vav1* genetically knocked-out cell line, J.Vav1, enabled us to address the distinct role of Vav1 in the regulation of apoptosis; this role is not compensated by the co-existing Vav2 and Vav3. In our model, Vav1 promotes Bcl-2 transcription through its GEF activity and the downstream small GTPase, Rac2. The increased Bcl-2 expression protects mitochondrial membrane integrity against apoptotic stimuli (Figure 6). Vav1 has also been reported to promote antigen-induced thymocyte apoptosis during negative selection[20], and the Vav1-Rac pathway is a critical component for TCR-induced CD4+ T cell death[21]. We speculate that Vav1 may play opposing roles in different contexts; Vav1 has a pro-survival role in quiescent T cells to maintain homeostasis and a pro-apoptotic role during T cell responses. In support of this, we found that Vav1 promoted Bcl-2 transcription in non-hematopoietic cells, which may contribute to cancer malignancy in conjunction with Vav1 overexpression.

As one of the GEFs for the Rho family of small GTPases,

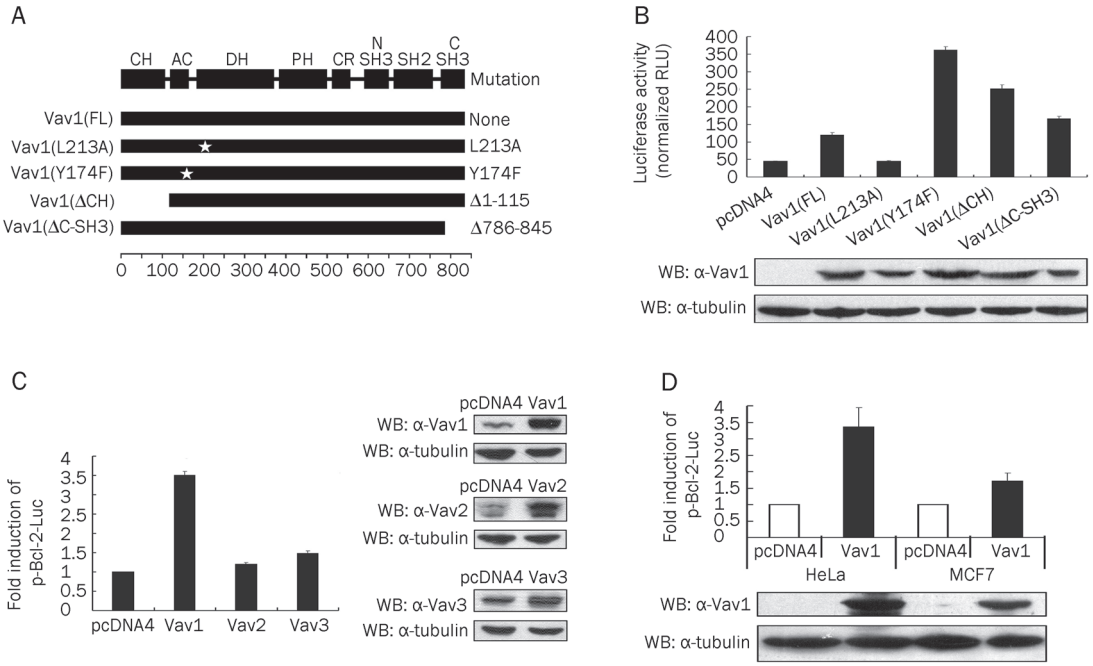

Figure 4. Effect of Vav1 mutations on Bcl-2 promoter activity. (A) A schematic depiction of Vav1 and its mutations. The structural domains of Vav1 are indicated on the top line. Solid bars indicate the mutated forms of Vav1, and point mutations were indicated with stars. The plasmids, pBcl-2-Luc and control reporter pTK-RL, were transfected into J.Vav1 cells (B), Jurkat cells (C), or non-hematopoietic HeLa or MCF7 cells (D) with control pcDNA4 or protein expression plasmids as indicated. Luciferase activity in each sample was measured and presented either as RLU (B) or as fold induction over the control group (C and D). The results show the mean±SD from triplicate samples. The expression of transfected proteins was analyzed by immunoblot with tubulin as the loading control.

the function of Vav1 is important in TCR-mediated signal transduction and actin polymerization[32]. There are GEF-dependent and GEF-independent activities modulating cellular signaling. As all three Vav proteins are present in T cells, the high structural similarity and overlapping functions of Vav proteins suggest that they may compensate for the loss of another. The significance of Vav1 GEF activity in T cell activation has been recently challenged because TCR-mediated actin polymerization and Rac1 activation were rescued by introduction of a GEF-inactive Vav1 in J.Vav1 or primary T cells lacking all Vav members[35]. Thus, the GEF function of Vav1 is not required for T cell activation. This raises the question of the genuine cellular function of the Vav1 GEF. Our data demonstrated the requirement of the GEF activity of Vav1, but not Vav2 or Vav3, in inducing Bcl-2 transcription. Vav1 dose-dependently promoted the increase in Bcl-2 transcription (Figure 3C), and neither endogenous nor transiently expressed Vav2 or Vav3 affected Bcl-2 transcription in Jurkat cells (Figure 4C). These results suggest that one of the functions of the Vav1 GEF lies in the activation of its downstream GTPase(s) to induce Bcl-2 transcription.

Small GTPases are critical for regulating cell survival, and one of their functional mechanisms is to induce the transcription of the Bcl-2 family of proteins. We identified Rac2 as the likely downstream effector of Vav1 in the context of Bcl-2 transcription rather than the commonly recognized Rac1 in T cell activation. Rac2 has been reported to participate in apoptosis. Mast cells from Rac2 knock-out mice are deficient in growth factor-induced survival and have increased expression of Bad and decreased expression of Bcl-xL at basal levels[36]. Because Vav1 and Rac2 are both predominantly expressed in hematopoietic cells, it is very likely that the transcriptional control of Bcl-2 by Vav1-Rac2 is also specific for hematopoietic cells. However, we cannot rule out the participation of other Vav1 substrates in this context.

The involvement of Vav1 in transcription has been suggested in previous studies by its nuclear localization and binding to nuclear proteins using its C-SH3 domain[37–40]. The nuclear function of Vav1 has been further emphasized by its association with DNA as a transcriptional complex[41]. We tested Bcl-2 transcription in the presence of different mutations of Vav1 using a reporter assay and found that the C-SH3 domain had no obvious effect on the promoter activity of Bcl-2 (Figure 4B). Evidence from *vav* triple knock-out mice has indicated that reduced NFκB activity may be responsible for the decrease in Bcl-2 expression. Indeed, we previously showed decreased NFκB activity in the absence of Vav1 (J.Vav1), and reconstituted expression of Vav1 could counteract this deficiency[7]. Furthermore, caspase 3 has been found to cleave Vav1 at the DLYD^{161}C site during apoptosis, and the cleaved Vav1 displayed a severely impaired ability to activate NFκB and AP-1[42]. Therefore, the transcriptional control of Bcl-2 by Vav1 does not occur directly via its predicted transcriptional activity, rather it involves signaling pathways that control the

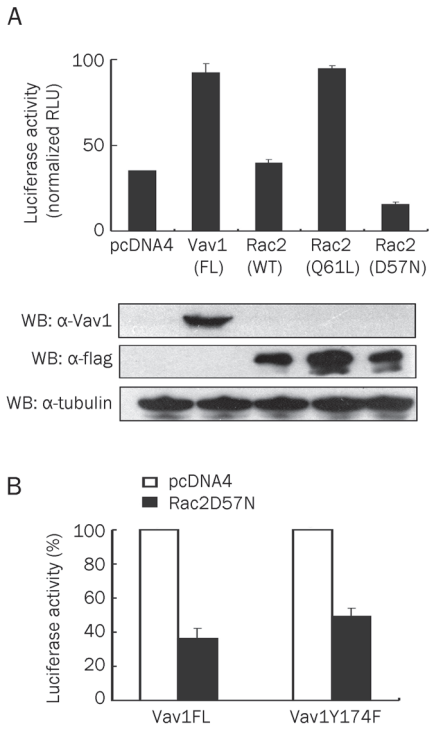

Figure 5. Effect of small GTPase, Rac2, on Bcl-2 promoter activity. (A) J.Vav1 cells were co-transfected with pBcl-2-Luc reporter constructs plus an empty vector (pcDNA4), a plasmid encoding full-length Vav1 (FL), or flag-tagged Rac2 variants (WT: wild-type; constitutively active Q61L; or dominant negative D57N). Luciferase activity of each transfection was measured and presented as RLU. The results are shown as the mean±SD from triplicate samples. (B) J.Vav1 cells were transiently transfected with reporter constructs (as above) together with wild-type Vav1 (FL) or constitutively active Vav1 (Y174F), in combination with vehicle plasmid (pcDNA4) or dominant negative Rac2 (D57N). The inhibition of Rac2 (D57N) (solid bars) on Bcl-2 promoter activity is presented as the percentage of vehicle control (open bars). Bar graph shows the mean±SD from triplicate experiments. The expression of transfected Vav1 and Rac2 were analyzed by immunoblot using α-Vav1 and α-flag antibodies with tubulin as the loading control (lower panel).

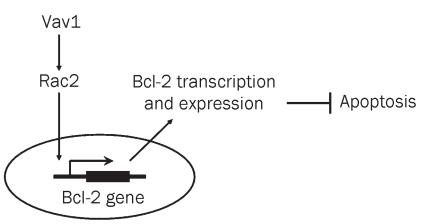

Figure 6. A model for Vav1 function in apoptosis.

balance between cell survival and cell death.

In conclusion, our results showed that the loss of Vav1 led to a higher sensitivity of Jurkat cells to the induction of apoptosis, including via Fas activation. We further found that mRNA levels of Bcl-2 were significantly reduced in J.Vav1 cells. The GEF activity of Vav1 was essential to the transcription of Bcl-2, probably via the Vav1 substrate, Rac2. The transcriptional control of Bcl-2 was exclusive to Vav1 despite the presence of the other Vav family proteins, Vav2 and Vav3. This finding suggests that Vav1, in addition to its importance in TCR-mediated T cell activation, plays a distinct role in controlling the transcription of Bcl-2 and thus protects T cells from apoptosis. Unveiling these mechanisms helps to better understand the homeostatic control of lymphocytes. As Vav1 is specifically expressed in hematopoietic cells, control of Vav1 expression and its GEF activity may be a potential therapeutic strategy for the treatment of T-CVID and lymphoma.

Acknowledgements

This work was supported by grants from the National Natural Science Foundation of China (No 30870128), the Ministry of Science and Technology of China (No 2006CB910103 and 2007CB914800), and the 111 Project (No B08011). The authors would like to thank Drs Keith BURRIDGE and Quan CHEN for providing reagents and helpful discussions.

Author contribution

Jie YIN and Dr You-jia CAO initiated the project, Jie YIN conducted most of the experiments, Ya-juan WAN and Ming-juan DU helped on the plasmid constructions and some biochemistry assays, Shi-yang Li and Xing-long ZHOU performed the flow cytometry for apoptotic analysis, Dr Cui-zhu ZHANG provided technical support, and Dr You-jia CAO and Jie YIN wrote the manuscript.

Supplementary information

Supplementary figure is available at Acta Pharmacologica Sinica website of NPG.

References

1 Katzav S, Martin-Zanca D, Barbacid M. vav, a novel human oncogene derived from a locus ubiquitously expressed in hematopoietic cells. EMBO J 1989; 8: 2283–90.
2 Movilla N, Bustelo XR. Biological and regulatory properties of Vav-3, a new member of the Vav family of oncoproteins. Mol Cell Biol 1999; 19: 7870–85.
3 Schuebel KE, Bustelo XR, Nielsen DA, Song BJ, Barbacid M, Goldman D, *et al*. Isolation and characterization of murine vav2, a member of the vav family of proto-oncogenes. Oncogene 1996; 13: 363–71.
4 Fischer KD, Zmuldzinas A, Gardner S, Barbacid M, Bernstein A, Guidos C. Defective T-cell receptor signalling and positive selection of Vav-deficient CD^{4+} CD^{8+} thymocytes. Nature 1995; 374: 474–7.
5 Turner M, Mee PJ, Walters AE, Quinn ME, Mellor AL, Zamoyska R, *et al*. A requirement for the Rho-family GTP exchange factor Vav in positive and negative selection of thymocytes. Immunity 1997; 7: 451–60.
6 Fujikawa K, Miletic AV, Alt FW, Faccio R, Brown T, Hoog J, *et al*. Vav1/2/3-null mice define an essential role for Vav family proteins in lymphocyte development and activation but a differential requirement in MAPK signaling in T and B cells. J Exp Med 2003; 198: 1595–608.
7 Cao Y, Janssen EM, Duncan AW, Altman A, Billadeau DD, Abraham RT. Pleiotropic defects in TCR signaling in a Vav-1-null Jurkat T-cell line. EMBO J 2002; 21: 4809–19.
8 Paccani SR, Boncristiano M, Patrussi L, Ulivieri C, Wack A, Valensin S, *et al*. Defective Vav expression and impaired F-actin reorganization

in a subset of patients with common variable immunodeficiency characterized by T-cell defects. Blood 2005; 106: 626–34.
9 Prieto-Sanchez RM, Hernandez JA, Garcia JL, Gutierrez NC, San MJ, Bustelo XR, *et al*. Overexpression of the VAV proto-oncogene product is associated with B-cell chronic lymphocytic leukaemia displaying loss on 13q. Br J Haematol 2006; 133: 642–5.
10 Hornstein I, Pikarsky E, Groysman M, Amir G, Peylan-Ramu N, Katzav S. The haematopoietic specific signal transducer Vav1 is expressed in a subset of human neuroblastomas. J Pathol 2003; 199: 526–33.
11 Fernandez-Zapico ME, Gonzalez-Paz NC, Weiss E, Savoy DN, Molina JR, Fonseca R, et al. Ectopic expression of VAV1 reveals an unexpected role in pancreatic cancer tumorigenesis. Cancer Cell 2005; 7: 39–49.
12 Bartolome RA, Molina-Ortiz I, Samaniego R, Sanchez-Mateos P, Bustelo XR, Teixido J. Activation of Vav/Rho GTPase signaling by CXCL12 controls membrane-type matrix metalloproteinase-dependent melanoma cell invasion. Cancer Res 2006; 66: 248–58.
13 Zugaza JL, Lopez-Lago MA, Caloca MJ, Dosil M, Movilla N, Bustelo XR. Structural determinants for the biological activity of Vav proteins. J Biol Chem 2002; 277: 45377–92.
14 Tybulewicz VL, Henderson RB. Rho family GTPases and their regulators in lymphocytes. Nat Rev Immunol 2009; 9: 630–44.
15 Fischer KD, Kong YY, Nishina H, Tedford K, Marengere LE, Kozieradzki I, *et al*. Vav is a regulator of cytoskeletal reorganization mediated by the T-cell receptor. Curr Biol 1998; 8: 554–62.
16 Katzav S. Vav1: an oncogene that regulates specific transcriptional activation of T cells. Blood 2004; 103: 2443–51.
17 Zhou Z, Yin J, Dou Z, Tang J, Zhang C, Cao Y. The calponin homology domain of Vav1 associates with calmodulin and is prerequisite to T cell antigen receptor-induced calcium release in Jurkat T lymphocytes. J Biol Chem 2007; 282: 23737–44.
18 Blanchet F, Cardona A, Letimier FA, Hershfield MS, Acuto O. CD28 costimulatory signal induces protein arginine methylation in T cells. J Exp Med 2005; 202: 371–7.
19 Rathmell JC, Thompson CB. Pathways of apoptosis in lymphocyte development, homeostasis, and disease. Cell 2002; 109: S97–107.
20 Kong YY, Fischer KD, Bachmann MF, Mariathasan S, Kozieradzki I, Nghiem MP, *et al*. Vav regulates peptide-specific apoptosis in thymocytes. J Exp Med 1998; 188: 2099–111.
21 Ramaswamy M, Dumont C, Cruz AC, Muppidi JR, Gomez TS, Billadeau DD, *et al*. Cutting edge: Rac GTPases sensitize activated T cells to die via Fas. J Immunol 2007; 179: 6384–8.
22 Tuosto L, Marinari B, Piccolella E. CD4-Lck through TCR and in the absence of Vav exchange factor induces Bax increase and mitochondrial damage. J Immunol 2002; 168: 6106–12.
23 Vigorito E, Gambardella L, Colucci F, McAdam S, Turner M. Vav proteins regulate peripheral B-cell survival. Blood 2005; 106: 2391–8.
24 Opalinska JB, Machalinski B, Ratajczak J, Ratajczak MZ, Gewirtz AM. Multigene targeting with antisense oligodeoxynucleotides: an exploratory study using primary human leukemia cells. Clin Cancer Res 2005; 11: 4948–54.
25 Poppe D, Tiede I, Fritz G, Becker C, Bartsch B, Wirtz S, *et al*. Azathioprine suppresses ezrin-radixin-moesin-dependent T cell-APC conjugation through inhibition of Vav guanosine exchange activity on Rac proteins. J Immunol 2006; 176: 640–51.
26 Katzav S. Flesh and blood: the story of Vav1, a gene that signals in hematopoietic cells but can be transforming in human malignancies. Cancer Lett 2007; 255: 241–54.
27 Koncz G, Kerekes K, Chakrabandhu K, Hueber AO. Regulating Vav1 phosphorylation by the SHP-1 tyrosine phosphatase is a fine-tuning mechanism for the negative regulation of DISC formation and Fas-mediated cell death signaling. Cell Death Differ 2008; 15: 494–503.
28 Scaffidi C, Fulda S, Srinivasan A, Friesen C, Li F, Tomaselli KJ, *et al*. Two CD95 (APO-1/Fas) signaling pathways. EMBO J 1998; 17: 1675–87.
29 Hildeman DA, Zhu Y, Mitchell TC, Bouillet P, Strasser A, Kappler J, *et al*. Activated T cell death *in vivo* mediated by proapoptotic bcl-2 family member bim. Immunity 2002; 16: 759–67.
30 Heckman CA, Mehew JW, Boxer LM. NF-kappaB activates Bcl-2 expression in t(14;18) lymphoma cells. Oncogene 2002; 21: 3898–908.
31 Bustelo XR. Vav proteins, adaptors and cell signaling. Oncogene 2001; 20: 6372–81.
32 Tybulewicz VL. Vav-family proteins in T-cell signalling. Curr Opin Immunol 2005; 17: 267–74.
33 Aghazadeh B, Lowry WE, Huang XY, Rosen MK. Structural basis for relief of autoinhibition of the Dbl homology domain of proto-oncogene Vav by tyrosine phosphorylation. Cell 2000; 102: 625–33.
34 Yu H, Leitenberg D, Li B, Flavell RA. Deficiency of small GTPase Rac2 affects T cell activation. J Exp Med 2001; 194: 915–26.
35 Miletic AV, Graham DB, Sakata-Sogawa K, Hiroshima M, Hamann MJ, Cemerski S, *et al*. Vav links the T cell antigen receptor to the actin cytoskeleton and T cell activation independently of intrinsic Guanine nucleotide exchange activity. PLoS One 2009; 4: e6599.
36 Yang FC, Kapur R, King AJ, Tao W, Kim C, Borneo J, *et al*. Rac2 stimulates Akt activation affecting BAD/Bcl-XL expression while mediating survival and actin function in primary mast cells. Immunity 2000; 12: 557–68.
37 Romero F, Dargemont C, Pozo F, Reeves WH, Camonis J, Gisselbrecht S, *et al*. p95vav associates with the nuclear protein Ku-70. Mol Cell Biol 1996; 16: 37–44.
38 Hobert O, Jallal B, Schlessinger J, Ullrich A. Novel signaling pathway suggested by SH3 domain-mediated p95vav/heterogeneous ribonucleoprotein K interaction. J Biol Chem 1994; 269: 20225–8.
39 Romero F, Germani A, Puvion E, Camonis J, Varin-Blank N, Gisselbrecht S, *et al*. Vav binding to heterogeneous nuclear ribonucleoprotein (hnRNP) C. Evidence for Vav-hnRNP interactions in an RNA-dependent manner. J Biol Chem 1998; 273: 5923–31.
40 Houlard M, Romero-Portillo F, Germani A, Depaux A, Regnier-Ricard F, Gisselbrecht S, *et al*. Characterization of VIK-1: a new Vav-interacting Kruppel-like protein. Oncogene 2005; 24: 28–38.
41 Houlard M, Arudchandran R, Regnier-Ricard F, Germani A, Gisselbrecht S, Blank U, *et al*. Vav1 is a component of transcriptionally active complexes. J Exp Med 2002; 195: 1115–27.
42 Hofmann TG, Hehner SP, Droge W, Schmitz ML. Caspase-dependent cleavage and inactivation of the Vav1 proto-oncogene product during apoptosis prevents IL-2 transcription. Oncogene 2000; 19: 1153–63.

Acta Pharmacologica Sinica (2011) 32: 108–115
 1671-4083/11 $32.00
www.nature.com/aps

Original Article

Mixed micelles loaded with silybin-polyene phosphatidylcholine complex improve drug solubility

Rui-ling DUAN, Xun SUN, Jie LIU, Tao GONG*, Zhi-rong ZHANG*

Key Laboratory of Drug Targeting and Drug Delivery Systems, Ministry of Education, West China School of Pharmacy, Sichuan University, Chengdu 610041, China

Aim: To prepare a novel formulation of phosphatidylcholine (PC)-bile salts (BS)-mixed micelles (MMs) loaded with silybin (SLB)-PC complex for parenteral applications.
Methods: SLB-PC-BS-MMs were prepared using the co-precipitation method. Differential scanning calorimetry (DSC) analysis was used to confirm the formation of the complex and several parameters were optimized to obtain a high quality formulation. The water-solubility, drug loading, particle size, zeta potential, morphology and *in vivo* properties of the SLB-PC-BS-MMs were determined.
Results: The solubility of SLB in water was increased from 40.83±1.18 μg/mL to 10.14±0.36 mg/mL with a high drug loading (DL) of 14.43%±0.44% under optimized conditions. The SLB-PC-BS-MMs were observed by transmission electron microscopy (TEM) and scanning electron microscopy (SEM) and showed spherical shapes. The particle size and zeta potential, as measured by photon correlation spectroscopy (PCS), were about 30±4.8 nm and −39±5.0 mV, respectively. *In vivo* studies showed that incorporation of the SLB-PC complex into PC-BS-MMs led to a prolonged circulation time of the drug.
Conclusion: This novel formulation appears to be a good candidate for drug substances that exhibit poor solubility for parenteral administration.

Keywords: silybin; bile salts; phospholipid complex; mixed micelles; solubility

Acta Pharmacologica Sinica (2011) 32: 108–115; doi: 10.1038/aps.2010.192; published online 20 Dec 2010

Introduction

The solubility of active pharmaceutical ingredients (APIs) has always been a concern for formulations because inadequate aqueous solubility may hamper the development of parenteral products and limit their bioavailability[1]. To solve this problem, several approaches have emerged to improve API solubility, such as salt formation[2], crystal engineering[3], nanosizing[4], lipid formulation[5], cyclodextrin complexation[6] and prodrug strategies[7]. Among these, we focused on the mixed micelle systems due to their synergistic properties, such as increased micelle stability and drug loading efficiency, which are superior to those of the individual components[8].

In the current study, we selected silybin (SLB) as the model drug to validate the feasibility of mixed micelle systems. Silybin, a flavolignane that represents approximately 60%–70% of silymarin, is an antioxidant isolated from the fruits of milk thistle, *Silybum marianum* Gaertn. Interest in this agent has grown in recent years due to its wide array of beneficial pharmacological effects, including antioxidative, anti-lipid-peroxidative, antifibrotic, anti-inflammatory, immunomodulating and even liver regenerating effects[9–11].

Despite the promising biological effects of SLB, its poor water solubility (about 40 μg/mL) and oral bioavailability (about 0.73%) in both rodents and humans, as reported by several researchers[12–15], has restricted its clinical application. To improve this situation, there have been many contributions to the development of SLB formulations[15–17]. However, few have produced a marked effect, and a majority of them are based on oral drug delivery systems. Because no proper formulation of silybin has been approved for intravenous administration, our goal was to develop a novel mixed micelle system for its parenteral application that could dramatically improve its solubility.

Upon consideration of its physiological compatibility and solubilizing capacity, the phosphatidylcholine-bile salts-mixed micelle system (PC-BS-MM) seems to be a good candidate for intravenous drug administration[18, 19]. Bile salts (BS), detergent-like chemicals produced by the liver and stored in the gall bladder, are able to solubilize phosphatidylcholine

* To whom correspondence should be addressed.
E-mail gongtaoy@126.com (Tao GONG);
zrzzl@vip.sina.com (Zhi-rong ZHANG)
Received 2010-06-20 Accepted 2010-10-12

(PC) to a large extent, forming a clear mixed micellar solution that is able to solubilize substances with poor water solubility[20]. Previous studies have shown that the hemolytic effect of bile salts can be neutralized by solubilized phospholipids[21]. In addition, PC-BS-MMs can be locally and systemically tolerated with no embryotoxic, teratogenic or mutagenic effects[22]. Therefore, these PC-BS-MMs might be the ideal drug carrier of SLB for parenteral administration.

Despite the encouraging potential applications of PC-BS-MMs mentioned above, preparing formulations of SLB with poor solubility enveloped in these carriers remains a challenge. Thus, it is expected that the SLB-PC complex, with changed solubility, would be better incorporated into PC-BS-MMs.

To examine the potential of our model (PC-BS-MMs) as a novel delivery vehicle for water-insoluble drugs, the specific objectives of this work were (i) to formulate an SLB-PC complex in PC-BS-MMs for parenteral application by screening different formulation factors, (ii) to investigate the characteristics of the optimized SLB-PC-BS-MM formulation and (iii) to compare the pharmacokinetic parameters *in vivo* between the SLB-PC-BS-MMs and silybin-*N*-methylglucamine.

Materials and methods

Silybin (SLB) was purchased from Xi'an Sino-herb Bio-technology Co Ltd (Xi'an, china), purity 98.32%. Polyene Phosphatidylcholine (PPC) was obtained from Lipoid GmbH (Germany), purity 94%. Sodium deoxycholate (SDC) was supplied by Beijing Aoboxing Biotechnologies Co Ltd (Beijing, China). The other chemical reagents were of analytical grade or better.

Male Wistar rats were provided by the West China Experimental Animal Center of Sichuan University (China). The protocol was approved by the Institutional Animal Care and Use Committee of Sichuan University.

Preparation of SLB-PPC complex

The preparation of SLB-PPC complex was carried out as previously described[15] with slight modifications. The complex was prepared with SLB and PPC at a molar ratio of 1:1. Weighed amounts of SLB and PPC were placed in a round bottom flask and dissolved in acetone. The mixture was then refluxed at 50 °C for 2 h. After the acetone was evaporated off under vacuum (Büchi, R-144 rotary evaporator, Switzerland), the dried residues were collected and placed in desiccators.

Structure validation of SLB-PPC complex by differential scanning calorimetry (DSC)

DSC was performed on an EXSTAR 6000 thermogravimetric analyzer (EIKO, Japan), and a scan speed of 5 °C from 0 to 250 °C was employed. DSC thermograms of SLB, PPC, a physical mixture of SLB and PPC, and the SLB-PPC complex were compared to identify formation of the complex.

Preparation of PPC-BS-MMs loaded with the SLB-PPC complex (SLB-PPC-BS-MMs)

Because the SLB-PPC complex exhibited good solubility in anhydrous ethanol, the complex was easily loaded into PPC-BS-MMs using the co-precipitation method[23]. In brief, the complex, PPC and sodium deoxycholate (SDC) at certain molar ratios were dissolved in anhydrous ethanol. A film was formed after evaporation of the organic solvent at 50 °C. The resulting films were dispersed in double distilled water. To remove unsolubilized drug, the solutions were centrifuged at 16 000×*g* (Allegra X-22R Centrifuge, F2402H rotor, Beckman Coulter Inc, CA, USA) for 10 min. The supernatant contained the freshly formed mixed micelles. To increase the stability of the MMs, they were pre-frozen at -40 °C for at least 4 h and then lyophilized under a vacuum for 24 h.

Determination of drug solubility and drug loading (DL%) in different micelle systems

The content of the SLB solubilized by MMs was determined by reverse-phase HPLC. SLB-PPC-SDC-MMs were diluted with methanol to a certain concentration and injected into an HPLC system. The stationary phase, a Kromasil C18 column (150 mm×4.6 mm, 5 μm), was kept at 35 °C. The mobile phase consisted of a mixture of acetonitrile and double distilled water (35:65) [pH adjusted to 3-4 using 10% phosphoric acid (*v/v*)]. The injection volume of the samples and standards was 20 μL. The flow rate was 1.0 mL/min and the detection wavelength was 288 nm.

The drug loading (DL%) was calculated as follows:

$$DL\% = \frac{\text{Amount of drug in prescription}}{\text{Amount of drug added} + \text{Amount of excipent added}} \times 100\% \quad (1)$$

Determination of particle size and Zeta potential of SLB-PPC-SDC-MMs

After suspending the freeze-dried SLB-PPC-SDC-MMs in double distilled water, photon correlation spectroscopy (PCS) (Malvern Zetasizer Nano ZS90, Malvern instruments Ltd, UK) was used to measure the particle size and zeta potential of the MMs. Each sample was then analyzed in triplicate.

Morphology of SLB-PPC-SDC-MMs determined by scanning electron microscopy (SEM) and transmission electron microscopy (TEM)

One drop of the diluted SLB-PPC-SDC-MMs was placed on a graphite surface. After being oven-dried, the sample was coated with gold using an ion sputter and examined with a conventional scanning electron microscope (JSM-5900LV, JEOL, Japan).

Before analysis by transmission electron microscopy, diluted samples were placed on copper grids with films and then stained with 2% (*w/v*) phosphotungstic acid; the excess staining solution was removed with filter paper. After being air dried, the films were observed with a transmission electron microscope (H-600, Hitachi, Japan).

In vivo studies in rats

Ten rats (200±20 g) were divided into 2 groups at random.

Silybin-*N*-methylglucamine solution or SLB-PPC-SDC-MMs (corresponding to a dose of 80 mg/kg) was injected into the tail vein of the rats of each group, respectively. After administration, blood was collected from the end of the tail at specific time points. Blood was immediately processed for plasma by centrifugation at 1500×*g* for 10 min. The obtained plasma was stored at -20 °C until analysis.

The plasma samples were prepared as follows to determine the SLB. One hundred microliters of internal standard (andrographolide: 200 μg/mL) and 100 μL of 0.1 mol/L phosphate buffer (pH 8.0) were added to 100 μL of plasma, followed by agitation for 30 s. Then, 2.5 mL of absolute ether was added, and this mixture was shaken for 15 min and then centrifuged at 1500×*g* for 5 min. Two milliliters of the organic phase was quantitatively transferred into clear centrifuging tubes and evaporated under nitrogen at 40 °C. The residues were resuspended in 100 μL of methanol and centrifuged at 9200×*g* for 10 min. Next, 20 μL of the supernatant was injected for HPLC analysis. The HPLC conditions were the same as the determination of drug solubility.

Statistical analysis

The results were analyzed by Drug and Statistics (DAS) software. Significance was tested by a two-tailed *t*-test and a value of $P<0.05$ was considered statistically significant.

Results

Structure identification of SLB-PPC complex by DSC

Differential scanning calorimetry (DSC) is a fast and reliable method to identify the formation of phospholipid complexes[15, 24]. Figure 1 shows the DSC thermograms of pure silybin (SLB), polyene phosphatidylcholine (PPC), the SLB-PPC complex and a physical mixture of SLB and PPC.

The melting point of SLB was 136.5 °C. The DSC profile of PPC showed two different types of endothermal peaks. The first mild endothermal peak at approximately 109.4 °C was probably due to movement of the polar regions of the PPC molecule. The second endothermal peak at 232.1 °C was very sharp, and its appearance was likely due to a phase transition from a gel to a liquid crystalline state. The non-polar hydrocarbon tail of PPC may melt during this phase, yielding a sharp peak.

The thermogram of a physical mixture of SLB and PPC was almost the overlap of each individual component, except for some slight differences. Specifically, the peak at 135.9 °C, which should be the melting point of SLB, was a little lower than that of pure SLB. The second peak of PPC disappeared, indicating that the PPC melted and the drug dissolved in the PPC at higher temperature. It is likely that a SLB-PPC complex was partially formed.

The thermogram of the SLB-PPC complex showed that the endothermal peaks of SLB and PPC had almost disappeared with the exception of a small peak at 236.9 °C, which was probably due to a very small amount of unreacted PPC. Two more new peaks at 92.0 and 194.6 °C were present, indicating the formation of a SLB-PPC complex. The peak at 92.0 °C was attributed to interactions of the polar groups of SLB and PPC in the form of hydrogen bonds, which occur through the –OH groups of the phenol rings of SLB[15, 24]. Such interactions are supposed to be the dominant factor in the complexation process, as the peak at 92.0 °C in the DSC curve absorbed more energy than the others. The peak at 194.6 °C, which absorbed less energy, might be associated with the changed spatial structure of the hydrocarbon chains.

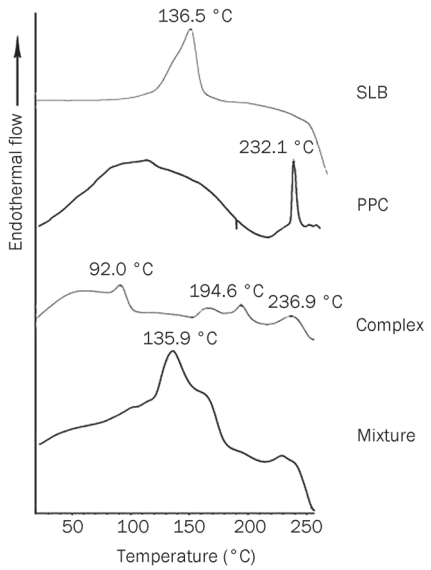

Figure 1. DSC thermograms of SLB, PPC, the SLB-PPC complex and a physical mixture of SLB and PPC.

Determination of drug solubility and drug loading (DL%) in different micelle systems

The influence of the SDC concentration on SLB solubility in the mixed micelles and the drug loading efficiency is shown in Figure 2. Upon increasing the SDC concentration from 8 to 40 mg/mL, a significant increase in SLB solubility was observed, but a further increase in SDC concentration led to saturation. As for the drug loading efficiency, an enhanced SDC concentration (from 8 to 20 mg/mL) led to an increased drug loading of up to 14.43%. However, a continuous increase in SDC

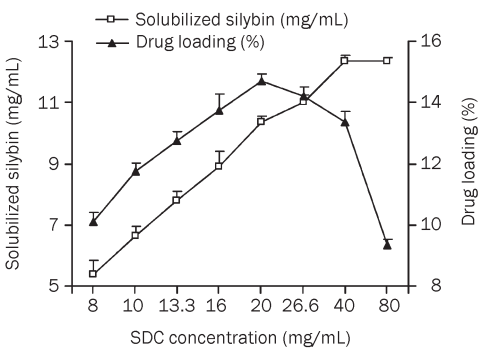

Figure 2. Influence of the SDC concentration on SLB solubility and drug loading at 10 °C (PPC conc, 40 mg/mL) (*n*=3).

concentration did not improve the solubilization efficiency. Therefore, an SDC concentration of 20 mg/mL, at which concentration the PPC-SDC molar ratio was 1 and solubilized silybin could be up to 10.14±0.36 mg/mL, was adopted for further investigations.

The influence of the PPC concentration on SLB solubility and drug loading efficiency was also investigated. As shown in Figure 3, SLB solubility was enhanced by incorporating increasing amounts of PPC in the MM system. After reaching a concentration of 60 mg/mL, continuously increasing the PPC concentration resulted in a relatively stable solubilization of SLB and eventually decreased solubility. However, a further increase in the PPC amount (after 40 mg/mL) led to a dramatic decrease in drug loading efficiency. Hence, to ensure higher solubilization efficiency and lower viscosity, a PPC concentration of 40 mg/mL was chosen for further investigations. At this concentration, the PPC-SDC molar ratio was 1, which agrees with the results regarding the influence of the SDC concentration.

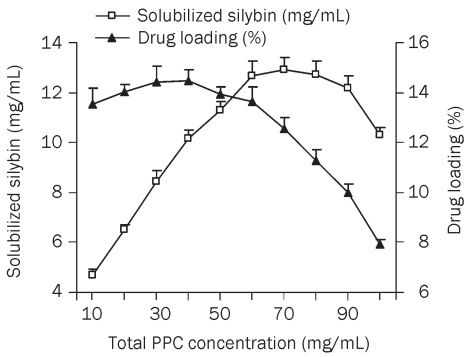

Figure 3. Influence of total PPC concentration on SLB solubility and drug loading at 10 °C (SDC conc, 20 mg/mL) (*n*=3).

The effect of the pH value on the solubility of SLB in PPC-SDC-MMs is shown in Figure 4. The results showed that enhancing the pH value of the mixed micellar solvent can dramatically increase the solubility of SLB when the pH is between 2 and 8. However, SLB was not stable at pH values above 9 or even 8. Hence, the optimum condition was between pH 7 and 8, which was exactly the pH value of the mixed micelles. Therefore, it was not necessary to use an additional pH regulator in this delivery system.

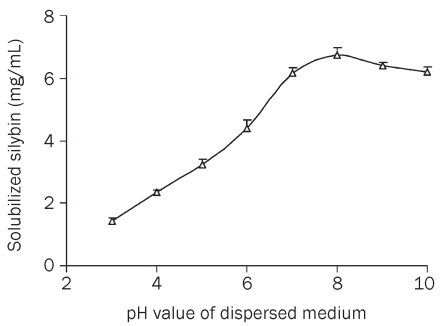

Figure 4. Effect of pH on SLB solubility in PPC-SDC-MMs at 10 °C (PPC/SDC molar ratio=1; PPC conc 40 mg/mL; dispersion medium: 0.05 mol/L phosphate buffer) (*n*=3).

Other factors that affect the solubility of mixed micelles, such as ionic strength and temperature, were investigated, and the results are shown in Table 1. A rapid decrease in the solubility of silybin occurred with increasing ionic strength and temperature. Therefore, a low ionic strength and temperature are recommended for the preparation of SLB-PPC-SDC-MMs.

Table 1. Effect of ionic strength and temperature on silybin solubility in PPC-SDC-MMs (PPC/SDC molar ratio=1; PPC conc 40mg/mL) (*n*=3).

Temperature (°C)	Dispersion medium	SLB solubility (mg/mL)
10	Water	10.34±0.29
10	Phosphate buffer, pH 7.4, 25 mmol/L	8.73±0.37
10	Phosphate buffer, pH 7.4, 50 mmol/L	6.46±0.31
25	Water	9.57±0.24
40	Water	8.22±0.25

Particle size and morphology of SLB-PPC-SDC-MMs

SLB-PPC-SDC-MMs were characterized by PCS and exhibited an average diameter of (30.7±4.8) nm. SEM and TEM images of SLB-PPC-SDC-MMs are presented in Figures 5 and 6, respectively. Both techniques confirmed that the mixed micelles were spherical in shape with a diameter of about 30 nm.

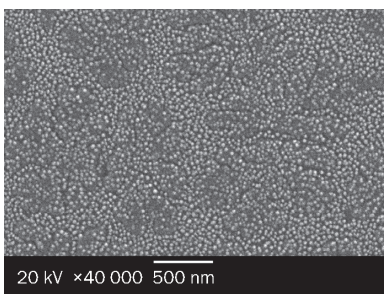

Figure 5. Scanning electron micrographs of SLB-PPC-SDC-MMs at ×40 000 magnification; scale bar: 500 nm.

Zeta potential

Zeta potential is an important factor in evaluating the stability of a colloidal dispersion[25]. Generally speaking, the particles were stable when the absolute value of the zeta potential was above 30 mV due to the electric repulsion between particles[26–28]. The average zeta potential of the SLB-PPC-SDC-MMs was (–39±5.0) mV, which suggests that the MMs obtained in this study could be a dynamic stable system.

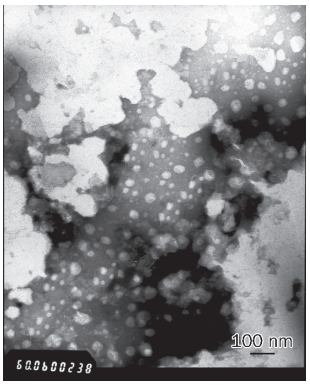

Figure 6. Transmission electron micrographs of SLB-PPC-SDC-MMs at ×60 000 magnification; scale bar: 100 nm.

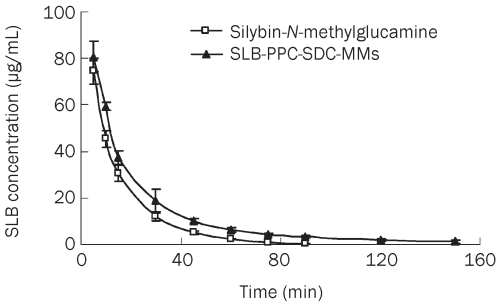

Figure 8. Mean plasma concentration-time curve of silybin in rats after intravenous administration of silybin-*N*-methylglucamine and SLB-PPC-SDC-MMs (n=5).

In vivo studies in rats

As seen in Figure 7, the internal standard (andrographolide) and silybin in plasma were completely separated under our analytical conditions, with retention time of 5 and 7 min, respectively. Figure 8 and Table 2 show the main pharmacokinetic parameters in rats after intravenous injection of silybin-*N*-methylglucamine or SLB-PPC-SDC-MMs (equivalent to 80 mg/kg of silybin), respectively (n=5). From the profile, we could see the mean retention time (MRT) and $AUC_{(0-\infty)}$ of the SLB-PPC-SDC-MMs group were 29.8 min and 2190 mg/L·min, respectively. In comparison, the MRT and $AUC_{(0-\infty)}$ of the silybin-*N*-methylglucamine group were 14.8 min and 1517 mg/L·min, respectively, which were significantly lower (P<0.05) than that of the SLB-PPC-SDC-MMs group. However, these two groups achieved approximately the same C_{max} value (P>0.05). These results suggested the SLB-PPC-SDC-MMs could remain in circulation *in vivo* longer than silybin-*N*-methylglucamine, which results in a higher $AUC_{(0-\infty)}$ (1.44-fold).

Table 2. The main pharmacokinetic parameters of silybin-*N*-methylglucamine and SLB-PPC-SDC-MMs in rats (n=5).

Parameters	Silybin-*N*-methylglucamine	SLB-PPC-SDC-MMs	*t*-test
$AUC_{(0-t)}$ (mg/L·min)	1508±131	2128±234	P<0.05
$AUC_{(0-\infty)}$ (mg/L·min)	1517±130	2191±266	P<0.05
$t_{1/2}$ (min)	13.0±0.83	36.1±6.61	P<0.05
$MRT_{(0-t)}$ (min)	14.2±0.18	25.0±1.57	P<0.05
$MRT_{(0-\infty)}$ (min)	14.8±0.11	29.8±3.79	P<0.05
C_{max} (mg/L)	74.6±5.66	80.7±6.47	P>0.05
Relative bioavailability (%)		144	

Discussion

The phosphatidylcholine-bile salts-mixed micelle system has demonstrated great potential as a novel delivery vehicle for parenteral administration to overcome the obstacles of inadequate aqueous solubility and oral bioavailability. However, researchers are facing challenges associated with encapsulating drug substances that are neither lipophilic nor hydrophilic into such carriers. The development of a drug-phospholipid complex is expected to overcome this problem. In the current study, the complex greatly enhanced the lipophilicity of the drug substances, which proved to be well incorporated in the mixed micelles. Additionally, polyene phosphatidylcholine, the phospholipid we employed in the complexation process, has the same biological effect as SLB in maintaining liver health and treating liver disorders[29]. This suggests that the use of a SLB-PPC complex is a promising strategy for the systemic delivery of SLB.

In order to optimize the SLB-PPC-SDC-MM preparation, different process variables were evaluated, and the water-solubility and drug loading efficiency were employed as evaluation parameters. First, the influence of SDC concentration was investigated, and the results are shown in Figure 2. An increase of SDC concentration of up to 20 mg/mL resulted in a significant enhancement of drug solubility and drug loading efficiency. However, a further increase of SDC concentration led to dramatic reduction in drug loading efficiency, although SDC could still solubilize the drug to some extent. This underlying process accounts for achievement of the highest combination rate of SDC and PPC when the SDC concentration was

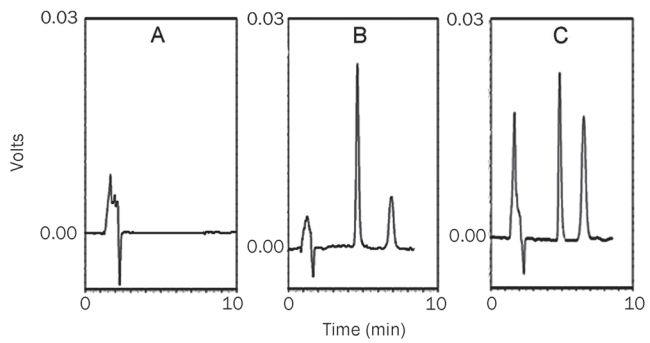

Figure 7. Typical chromatograms of silybin. (A) Blank rat plasma; (B) Blank rat plasma spiked with internal standard (andrographolide) and silybin; (C) A sample after intravenous administration of the SLB-PPC-SDC-MMs.

increased to 20 mg/mL. Although excess free SDC micelles could also solubilize SLB, the solubilizing capacity was weaker than that of the mixed micelles.

Another important factor in the SLB-PPC-SDC-MM formulation was PPC concentration. When the molar ratio of PPC/SDC was below 1.0 (PPC concentration at 40 mg/mL), the increase in solubility and drug loading efficiency of SLB was dramatic, which was due to the dual increase of both the size and the lipophilicity of PPC-SDC-MM upon the incorporation of PPC[19]. Continuously increasing the PPC concentration resulted in a relatively stable solubilization of SLB and a rapid decrease in drug loading efficiency. This was also because the strongest binding force between PPC and SDC was achieved, similar to the influence of the SDC concentration. In addition, an increase in the PPC concentration resulted in a higher viscosity and, consequently, less partition of the drug into the mixed micellar space.

As for the effect of pH on the solubility of SLB, the results showed that the optimum condition for the SLB-PPC-SDC-MMs was between pH 7 and 8. This could be attributed to the different surface charges of the mixed micelles under different conditions. The lipid carrier displayed a less negative zeta potential at pH 2 than pH 8 and led to aggregation and further precipitation of the mixed micelles at lower pH values, which resulted in less solubilization of SLB under these conditions. However, some interactions between silybin and phospholipids, such as the combination of hydrogen bonds or van der Waals forces[13, 30, 31], may not be very stable in highly charged environments (above pH 8). Therefore, a moderate pH value of medium is recommended for the preparation of the SLB-PPC-SDC-MMs.

Other factors such as increased ionic strength and temperature resulted in a rapid decrease in the solubility of silybin. This may be due to an increased critical micelle concentration under those conditions. Consequently, fewer micelles were available for the solubilization process. These findings are in good agreement with previous reports[32, 33].

After different parameters were screened to obtain the optimized formulation, some characteristics of the SLB-PPC-SDC-MMs were investigated, such as particle size, zeta potential and morphology. The results showed the particles were 30 nm, –39 mV and spherical in shape, indicating it was a dynamic, stable and uniform system. Hence, it was necessary to develop a schematic representation of the structure of this formulation.

As mentioned in the identification of the SLB-PPC complex by DSC, hydrogen bonding played a major role in SLB-PPC complexation[13–15, 31]; the –OH groups of the phenol rings of SLB were engaged in hydrogen bonding with the phospholipids. This indicated that it was the polar part of PPC that interacted with the silybin. The structure of the PC-BS-MMs, studied systematically by many researchers[19, 34], is widely accepted to be a 'mixed disk model' [35]. In this model, the mixed micelle consists of a disk-like portion of a phospholipid bilayer surrounded at its perimeter by bile salt molecules, exposing their hydrophilic surfaces to the aqueous solvent and their lipophilic surfaces to the hydrocarbon tails of the phospholipid molecules. However, our observations by SEM and TEM indicated that the SLB-PPC-SDC-MMs were spherical in shape, which may be due to the presence of the SLB-PPC complex. Therefore, based on our experimental results, a schematic representation of the structure of the SLB-PPC-SDC-MMs is presented in Figure 9. Silybin first combines with the polar head group of PPC, forming a SLB-PPC complex. Then, using the co-precipitation method, the hydrocarbon tails of the PPC bind to the hydrophobic surface of SDC, forming spheres and exposing the hydrophilic surfaces of SDC to contact with the aqueous solvent.

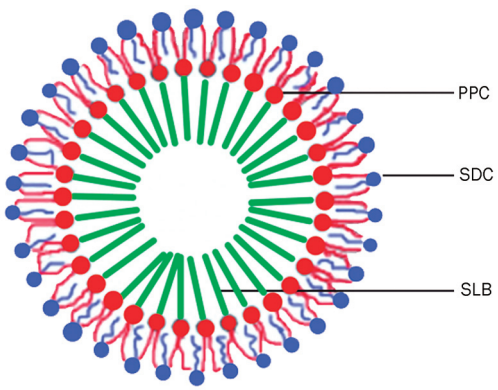

Figure 9. Schematic representation of the structure of the SLB-PPC-SDC-MMs.

To further understand the characteristics of the SLB-PPC-SDC-MMs *in vivo*, pharmacokinetic studies were also performed. The results showed that the SLB-PPC-SDC-MMs remained in circulation *in vivo* longer than silybin-*N*-methylglucamine, which resulted in a higher AUC. Theoretically, the increased MRT and AUC were attributed to interactions between the drug and PPC-SDC-MMs when the mixed micelles were above the CMC[36, 37] at the beginning of administration. These combined forces would prolong the release of SLB into the blood. However, once the mixed micelles were diluted below the critical micelle concentration, the entrapped drug would be released into circulation. At this time, the released SLB-PPC complex, with different lipophilicity and solubility behavior, would play a major role in enhancing the MRT and AUC of SLB *in vivo*. This assumption is also verified by other literature[15], which found that oral administration of a SLB-phospholipid complex could greatly enhance the MRT and AUC of SLB. In conclusion, it was the PPC-SDC-MMs and SLB-PPC complex combined that influenced the behavior of SLB *in vivo*.

Therefore, the SLB-PPC complex could not only improve the lipophilicity of SLB to be better enveloped in the PPC-SDC-MMs, but also increase its circulation time *in vivo*. The mixed micelle system, which remarkably improved the solubility of the SLB-PPC complex in water, could be used as a formulation for intravenous administration. PPC-SDC-MMs have been

investigated for the oral administration of silybin[38]. Nevertheless, we encapsulated the SLB-PPC complex in this carrier for intravenous administration because the oral bioavailability of SLB in rats was estimated to only be 0.73%[12]. To maximize the drug efficacy, it was necessary to develop a delivery system that can directly distribute into each organ, thereby avoiding the absorption process. Therefore, the obtained SLB-PPC-SDC-MMs in the current study should provide a dramatic increase in bioavailability compared to oral administration.

Conclusions

In this paper, we have shown that silybin, a poorly soluble behavior drug, can be successfully enveloped into PPC-SDC-MMs after the formation of an SLB-PPC complex. The novel formulation with optimized formulation parameters dramatically improved both the water-solubility and the mean retention time of the drug *in vivo*. As a result, a new pattern of mixed micelles loaded with a phospholipid complex was proposed. This novel strategy was believed to be attractive for the development of drug substances that exhibit poor solubility.

Acknowledgements

Financial support of this research was provided by the National Science & Technology Major Project of China (grant No 2009ZX09310-002) and the National Natural Science Foundation of China (No 30873165).

The authors thank Zhi-xiang YUAN, San-jun SHI and Chang-tao LUAN for their help with these experiments.

Author contribution

Zhi-rong ZHANG and Tao GONG designed the research; Ruiling DUAN performed the research and wrote the paper; Xun SUN and Jie LIU revised the paper.

References

1 Dressman J, Reppas C. Drug solubility: how to measure it, how to improve it. Adv Drug Deliver Rev 2007; 59: 531–2.
2 Serajuddin, Abu TM. Salt formation to improve drug solubility. Adv Drug Deliver Rev 2007; 59: 603–16.
3 Blagden N, Matas M de, Gavan PT, York P. Crystal engineering of active pharmaceutical ingredients to improve solubility and dissolution rates. Adv Drug Deliver Rev 2007; 59: 617–30.
4 Kesisoglou F, Panmai S, Wu Y. Nanosizing — Oral formulation development and biopharmaceutical evaluation. Adv Drug Deliver Rev 2007; 59: 631–44.
5 Hauss DJ. Oral lipid-based formulations. Adv Drug Deliver Rev 2007; 59: 667–76.
6 Brewster ME, Loftsson T. Cyclodextrins as pharmaceutical solubilizers. Adv Drug Deliver Rev 2007; 59: 645–66.
7 Stella VJ, Nti-Addae KW. Prodrug strategies to overcome poor water solubility. Adv Drug Deliver Rev 2007; 59: 677–94.
8 Gao Y, Li LB, Zhai G. Preparation and characterization of Pluronic/TPGS mixed micelles for solubilization of camptothecin. Colloid Surface B 2008; 64: 194–9.
9 Kvasnicka F, Biba B, Sevcik R, Voldrich M, Kratka J. Analysis of the active components of silymarin. J Chromatogr A 2003; 990: 239–45.
10 Tedesco D, Tava A, Galletti S, Tameni M, Varisco G, Costa A, *et al*. Effects of silymarin, a natural hepatoprotector, in periparturient dairy cows. J Dairy Sci 2004; 87: 2239–47.
11 Trappoliere M, Caligiuri A, Schmid M, Bertolani C, Failli P, Di Manzano C, *et al*. Silybin is a direct antifibrogenic and antiinflammatory agent: Cellular and molecular mechanisms. Digest Liver Dis 2008; 40: A127.
12 Wu JW, Lin LC, Hung SC, Chi CW, Tsai TH. Analysis of silibinin in rat plasma and bile for hepatobiliary excretion and oral bioavailability application. J Pharmaceut Biomed 2007; 45: 635–41.
13 Lasonder E, Weringa WD. An NMR and DSC study of the interaction of phospholipids vesicles with some anti-inflammatory agents. J Colloid Interf Sci 1990; 139: 469–78.
14 Morazzoni P, Magistretti MJ, Giachetti C, Zanolo G. Comparative bioavailability of silipide, a new flavanolignan complex, in rats. Euro J Drug Metab Pharmacokinet 1992; 17: 39–44.
15 Xiao YY, Song YM, Chen ZP, Ping QN. The preparation of silybin - phospholipid complex and the study on its pharmacokinetics in rats. Int J Pharm 2006; 307: 77–82.
16 Chen W, Xia H, Wu W. Optimized preparation of silymarin dripping pills by a central composite design-response surface method. Chin Trad Herb Drug 2005; 36: 679–83.
17 Wu W, Wang Y, Que L. Enhanced bioavailability of silymarin by self-microemulsifying drug delivery system. Eur J Pharm Biopharm 2006; 63: 288–94.
18 Alkan-Onyuksel H, Ramakrishnan S, Chai HB, Pezzuto JM. A mixed micellar formulation suitable for the parenteral administration of taxol. Pharm Res 1994; 11: 206-12.
19 Hammad MA, Müller BW. Increasing drug solubility by of bile salt-phosphatidylcholine-based mixed micelles. Eur J Pharm Biopharm 1998; 46: 361–7.
20 Hammad MA, Müller BW. Solubility and stability of tetrazepam in mixed micelles. Eur J Pharm Sci 1998; 7: 49–55.
21 Steffen H. Prinzip Mischmizelle. Die Gallensäure-Lecithin-Mischmizllen als Trägersystem schwer wasserlösliche Wirkstoffe. Roche Magazine 1984; 20: 2–9.
22 Teelmann K, Schläppi B, Schüpbach M, Kistler A. Preclinical safety evaluation of intravenously administered mixed micelles. Arzneimittelforschung 1984; 34: 1517–23.
23 Schurtenberger P, Mazer N, Känzig W. Miceller vesicle transition in aqueous solution of bile salt and lecithin. J Phys Chem 1985; 89: 1042–9.
24 Maiti K, Mukherjee K, Gantait A, Saha BP, Mukherjee PK. Curcumin–phospholipid complex: Preparation, therapeutic evaluation and pharmacokinetic study in rats. Int J Pharm 2007; 330: 155–63.
25 Komatsu H, Kitajima A, Okada S. Pharmaceutical characterzation of commercially available intravenous fat emulsions: estimation of average particle size, size distribution and surface potential using photon correlation spectroscopy. Chem Pharm Bull 1995; 43: 1412–5.
26 Müller RH, Mäder K, Gohla S. Solid lipid nanoparticles (SLN) for controlled drug delivery — a review of the state of the art. Eur J Pharm Biopharm 2000; 50: 161–77.
27 Müller RH, Rühl D, Runge SA. Biodegradation of solid lipid nanoparticles as a function of lipase incubation time. Int J Pharm 1996; 144: 115–21.
28 Liu J, Gong T, Wang CG, Zhong ZR, Zhang ZR. Solid lipid nanoparticles loaded with insulin by sodium cholate–phosphatidylcholine-based mixed micelles: Preparation and characterization. Int J Pharm 2007; 340: 153–62.
29 Horejsová M, Urban J. The effect of polyene phosphatidylcholine (Essentiale forte) in the treatment of liver steatosis and ultrasound findings–preliminary study. Cas Lek Cesk 1994; 133: 366–9.

30 Hwang SB, Shen TY. Membrane effects of anti-inflammatory agents. 2. Interaction of nonsteroidal anti-inflammatory drugs with liposome and purple membranes. J Med Chem 1981; 24: 1202–12.
31 Venema FR, Weringa WD. The interactions of phospholipid vesicles with some anti-inflammatory agents. J Colloid Interf Sci 1988; 125: 484–500.
32 Flockhart BD. The effect of temperature on the critical micelle concentration of some paraffin-chain salt. J Colloid Sci 1961; 16: 484–92.
33 Alkan-Onyuksel H, Son K. Mixed micelles as proliposomes for the solubilization of tenposide. Pharm Res 1992; 9: 1556–62.
34 Carey MC, Small DM. The characteristics of mixed micellar solutions with particular reference to bile. Amer J Med 1970; 49: 590–608.
35 Mazer NA, Benedek GB, Carey MC. Quasielastic light-scattering studies of aqueous biliary lipid systems. Mixed micelle formation in bile salt-lecithin solutions. Biochem 1980; 19: 601–15.
36 Dongowski G, Fritzscb B, Giessler J, Härtl A, Kuhlmann O, Neuber RHH. The influence of bile salts and mixed micelles on the pharmacokinetics of quinine in rabbits. Eur J Pharm Biopharm 2005; 60: 147–51.
37 Ploema FGJ, Tucker JJ, Crommelin DJA. The role of bile salts in the intestinal absorption of drugs. Acta Pharm Technol 1990; 36: 43–52.
38 Yu JN, Zhu Y, Wang L, Peng M, Tong SS, Cao X, *et al*. Enhancement of oral bioavailability of the poorly water-soluble drug silybin by sodium cholate/phospholipid-mixed micelles. Acta Pharmacol Sin 2010; 31: 759–64.

Acta Pharmacologica Sinica (2011) 32: 116–125
 1671-4083/11 $32.00
www.nature.com/aps

Original Article

Race differences: modeling the pharmacodynamics of rosuvastatin in Western and Asian hypercholesterolemia patients

Juan YANG[1], Lu-jin LI[1], Kun WANG[1], Ying-chun HE[1], Yu-cheng SHENG[1], Ling XU[1], Xiao-hui HUANG[2], Feng GUO[3], Qing-shan ZHENG[1, *]

[1]Laboratory of Pharmacometrics, Center for Drug Clinical Research, Shanghai University of Chinese Medicine, Shanghai 201203, China; [2]School of Pharmacy, Anhui Medical University, Hefei 230032, China; [3]Pfizer (China) Research and Development Co, Ltd, Shanghai 201203, China

Aim: To evaluate race differences in the pharmacodynamics of rosuvastatin in Western and Asian hypercholesterolemia patients using a population pharmacodynamic (PPD) model generated and validated using published clinical efficacy trials.
Methods: Published studies randomized trials with rosuvastatin treatment for at least 4 weeks in hypercholesterolemia patients were used for model building and validation. Population pharmacodynamic analyses were performed to describe the dose-response relationship with the mean values of LDL-C reduction (%) from dose-ranging trials using NONMEM software. Baseline LDL-C and race were analyzed as the potential covariates. Model robustness was evaluated using the bootstrap method and the data-splitting method, and Monte Carlo simulation was performed to assess the predictive performance of the PPD model with the mean effects from the one-dose trials.
Results: Of the 36 eligible trials, 14 dose-ranging trials were used in model development and 22 one-dose trials were used for model prediction. The dose-response of rosuvastatin was successfully described by a simple E_{max} model with a fixed E_0, which provided a common E_{max} and an approximate twofold difference in ED_{50} for Westerners and Asians. The PPD model was demonstrated to be stable and predictive.
Conclusion: The race differences in the pharmacodynamics of rosuvastatin are consistent with those observed in the pharmacokinetics of the drug, confirming that there is no significant difference in the exposure-response relationship for LDL-C reduction between Westerners and Asians. The study suggests that for a new compound with a mechanism of action similar to that of rosuvastatin, its efficacy in Western populations plus its pharmacokinetics in bridging studies in Asian populations may be used to support a registration of the new compound in Asian countries.

Keywords: rosuvastatin; LDL; dose-response relationship; race difference; clinical trial; hypercholesterolemia

Acta Pharmacologica Sinica (2011) 32: 116–125; doi: 10.1038/aps.2010.169; published online 13 Dec 2010

Introduction

Rosuvastatin, the seventh drug in the statin class, is a synthetic and orally active inhibitor of HMG-CoA reductase used for the treatment of hypercholesterolemia. Early research indicated that rosuvastatin may achieve better outcomes than the other drugs in its class[1–6]. The pharmacokinetics of rosuvastatin were evaluated and reported previously. Both the maximum plasma concentration (C_{max}) and the area under the plasma concentration curve (AUC) are proportional to the dose[7–9]. Age, gender, smoking status, weight, body surface area, and lean body mass had no significant effect on rosuvastatin pharmacokinetics[10, 11]. A population pharmacokinetic analysis revealed no clinically relevant differences in pharmacokinetics among Caucasian, Hispanic, and Black or Afro-Caribbean groups[11]. Nevertheless, pharmacokinetic studies of rosuvastatin, including one conducted in North America, have demonstrated an approximate twofold elevation in median exposure (AUC and C_{max}) in Asian subjects compared with Caucasians[12, 13]. In dose-ranging studies, rosuvastatin produced dose-dependent mean reductions in LDL-C in both Western and Japanese hypercholesterolemia patients[1, 14]. Nevertheless, whether there are similar race differences in rosuvastatin pharmacodynamics is unknown because of a lack of clinical research directly comparing Western and Asian

* To whom correspondence should be addressed.
E-mail Zheng.zqs@gmail.com
Received 2010-06-04 Accepted 2010-08-23

patients. At present, considering the potential for increases in systemic exposure, it is recommended in the rosuvastatin product monograph that the dose range of rosuvastatin be 5 to 40 mg orally once a day, that the starting dose be 10 mg in Western patients and 5 mg in Asian patients, and that the maximum dose be 40 mg in Western patients and 20 mg in Asian patients[12]. Therefore, studies of the pharmacodynamics of rosuvastatin in Western and Asian patients are of clinical interest, and the results would improve clinical outcomes and optimize drug development.

This study attempted to pool the mean values of LDL-C reduction (%) from the eligible trials to develop a population pharmacodynamic (PPD) model for evaluating race differences in the pharmacodynamics of rosuvastatin in Western and Asian hypercholesterolemia patients.

Materials and methods

Clinical studies included

A comprehensive literature search in the Medline database was performed from January 1990 to June 2009, with the MeSH terms "rosuvastatin", "hypercholesterolemia" and "clinical trials". There were no language restrictions. Studies were eligible for inclusion if the following conditions were met: (1) the study was a randomized trial to investigate treatment with daily dosing of rosuvastatin in patients with hypercholesterolemia; (2) the percentage change in LDL-C from baseline was reported and the number of patients in each group was greater than 10; (3) the intervention duration was at least 4 weeks. Trials including statin-naive and switched-to-rosuvastatin patients were not eligible when they reported the pooled efficacy from only the two groups of patients. In addition, two Chinese clinical trials were available from our department. Of the eligible studies, the dose-ranging trials were used for model development and the one-dose trials were used for model prediction.

Data extraction and data sets

The mean percentage change in LDL-C from baseline, *ie*, the primary efficacy endpoint, was extracted from each eligible study. In the case of a force-titrated trial, only the efficacy of the starting dose with intervention duration greater than 4 weeks was used in this investigation. Variables for which data were collected included intervention duration, baseline LDL-C, race (Western or Asian), and year of publication. The Western patients consisted predominantly of Whites/Caucasians and the Asian patients comprised Chinese, Japanese, and South Asian subjects.

Population model construction

Population pharmacodynamic analysis of rosuvastatin dose-response data was performed using the nonlinear mixed-effect modeling program NONMEM (Version V, Level 1.1; Globo-Max LLC, Hanover, MD, USA) and DAS version 3.0 (Bontz Inc, Beijing, China). A previously reported sigmoidal E_{max} model was used to characterize the dose-response relationship for rosuvastatin[15]:

$$E=\frac{E_{max}\times Dose^{\gamma}}{ED_{50}^{\gamma}+Dose^{\gamma}}+E_0$$

where E_{max} is the maximal drug effect, reflecting the maximal difference in response between placebo and rosuvastatin; Dose is the dose of rosuvastatin; ED_{50} is the drug dose associated with an effect equal to 50% of E_{max}; and γ is the Hill coefficient reflecting the steepness of the dose-response curve. The term E_0 represents the placebo effect.

The following model structure was used for the PPD analysis:

$$Y_{obs}=E+\eta+\varepsilon$$

where Y_{obs} is the observed effect (the percentage change in LDL-C), η is a trial-specific random effect assumed to be normally distributed with a mean of 0 and an unknown variance of ω^2, and ε is the residual error assumed to be normally distributed parameter with a mean of 0 and a variance of σ^2.

The model was established using the forward inclusion-backward elimination method[16, 17]. In the first step, the PPD analysis was conducted without any covariates in the basic model. In the second step, each candidate covariate (baseline LDL-C and race) was screened in turn by incorporating it into the basic model parameters to develop the intermediate and full models and by observing the decrease in the objective function value (OFV). Covariates were cumulatively added to the PPD model in a forward, stepwise manner in order of their contribution to the reduction in the OFV and until there was no further reduction in OFV. The difference in the OFV was maintained as a χ^2 distribution, and an OFV greater than 3.84, associated with a P value of 0.05 (1 degree of freedom), was used for statistical significance. There were also many indicators of improved fit due to the addition of the following parameters to the model: decrease in standard error of the parameter estimates, reduction in intertrial variability, agreement between the observed and predicted effects, reduction in weighted residuals, and uniformity of the scatter plot of weighted residuals (WRES) versus predicted effects. Finally, a backward elimination step was performed by removing covariates one by one that already exited in the model. In the refinement of the PPD analysis, more stringent cutoff values were applied when determining whether to include a certain covariate or not. Covariates were retained in the model if their removal increased the OFV by 6.63, corresponding to a P value of 0.01 (1 degree of freedom).

Baseline LDL-C was included in the model as a continuous covariate. For the categorical covariate race (RACE), the covariate modeling was described by the following example:

$$P=TVP\times\theta^{RACE}$$

where P is one of the pharmacodynamic parameters and TVP is the typical population parameter value of P. The covariate RACE equals 0 for Westerners and 1 for Asians. If θ^{RACE} is significantly different from 1, it indicates that a race difference exists in the two populations.

Validation and prediction method

Model validation and prediction were used to test the robustness of the parameter estimates and the predictive capacity of the model. Validation of the PPD model was performed by the bootstrap method[18] and the data-splitting method[19]. The means of parameter estimates calculated from the 1000 bootstrap replications with successful runs (*ie*, both the estimation and covariance steps successfully converged) were compared with the final parameter estimates obtained from the original data set. For the data-splitting method, data (subsets) were obtained by deleting one trial at a time in the full data set. Each subset was analyzed by NONMEM with the final model to obtain the parameter estimates, which were compared with those resulting from the full data set.

Monte Carlo simulations were performed 1000 times to predict the 50th percentile LDL-C reduction (as an estimator of the population predicted effect) and the 2.5th and 97.5th percentile LDL-C reductions. The predictive performance of the PPD model was evaluated by observing the mean effects with 95% intervals for Westerners and Asians.

Results

Data

The literature search yielded 93 trials (Figure 1). Of the 54 trials retrieved for detailed assessment, 20 were excluded: one because it focused on a special population (postmenopausal women receiving hormone replacement therapy), one because it included a small number of subjects, two because they reported without number of subjects, four because they included patients whose medications had been switched, five for duplicate reporting, and seven for lack of reduction in LDL-C outcomes. Therefore, 34 eligible studies were identified, 12 of which were dose-ranging trials (9 examined Westerners and 3 examined Asians)[1–3, 5, 14, 20–26] and 22 were one-dose trials (18 comprising Westerners and 4 comprising Asians)[27–48]. In addition to the eligible published studies, two eligible dose-ranging trials in Asians were available from our department. All 14 of the dose-ranging trials were randomized, parallel-group studies; among them, 12 were double-blind, three were placebo-controlled, and the majority were multicenter studies. Tables 1 and 2 summarize the Western and Asian dose-ranging trials. A total of 46 effect samples from the 14 dose-ranging trials were available for the development of the PPD model. A summary of the one-dose trials used for model prediction is presented in Table 3.

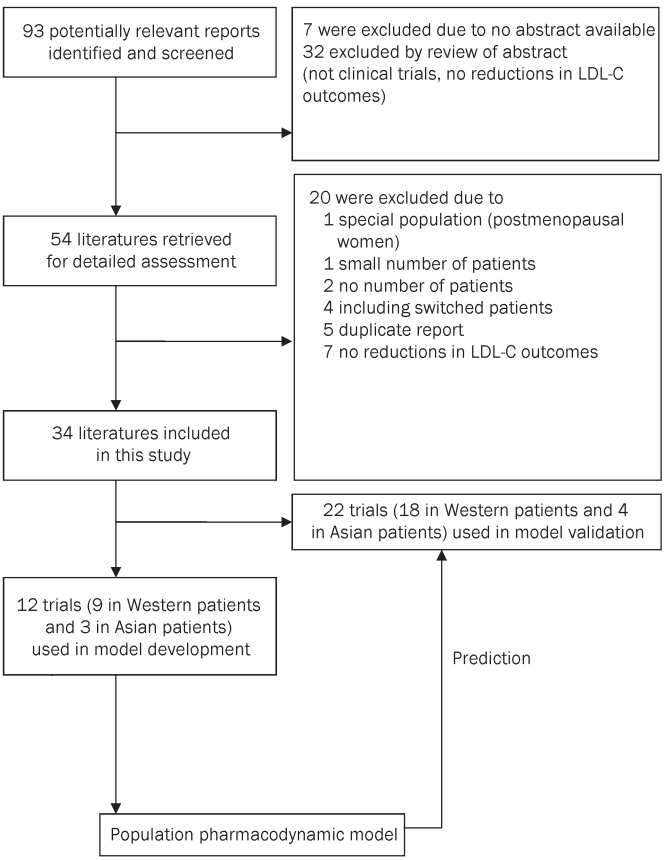

Figure 1. Flow of literatures through the dose-response relationship analysis.

Population pharmacodynamics

In this study, the previously reported sigmoidal E_{max} model described the dose-response relationship for rosuvastatin with incorrect pharmacodynamic parameters. Then, γ was fixed at 1; that is, a simple E_{max} model was used and the estimated parameters were acceptable except for a large relative standard error (RSE) in E_0. Therefore, E_0 was presumed to be -0.802% based on the literature value[15], and the simple E_{max} model was used successfully as the basic model for subsequent covariate analysis. Only the covariate race on ED_{50} produced a small but significant decrease in the OFV (7.095). The resulting population model with the covariate ED_{50} was as follows:

$$ED_{50}=1.74\times0.564^{RACE}$$

The PPD parameters in the final model are listed in Table 4. The RSE values for the parameters were acceptable, with a range from 3.86% to 28.55%. Figure 2 shows the fits of the observed effects with the parameters obtained from the final model. Figure 3 shows the final model-predicted dose-response curves for Westerners and Asians.

The goodness-of-fit plots for the final PPD model are presented in Figure 4. Generally, there was good agreement between observed (OBS) and population model-predicted (PRED) effects, as well as between OBS and individual model-predicted (IPRED) effects, with the magnitude of the WRES being small and randomly distributed over the entire range of PRED. Moreover, the goodness of fit to the model did not vary significantly among the trials.

Validation and prediction

Analysis of each of the 1000 bootstrap samples resulted in 928 samples that successfully converged. The mean values of the parameters after 928 repetitions of the bootstrap estimation were consistent with the parameter estimates of the original data set (Table 5), and the 95% CI was within reasonable

Table 1. Overview of Western dose-ranging trials for model building.

Reference	Year	Duration (week)	Dose (mg)	No of patients	LDL-C baseline (mg/dL)	Reductions in LDL-C (%) Mean	SE
1	2001	6					
			0	29	197.2	3.6	1.7
			1	13	189.4	34.3	2.6
			2.5	13	189.4	40.7	2.6
			5	17	193.4	42.5	2.4
			10	16	189.4	50.5	2.4
			20	13	181.7	57	2.7
			40	34	185.6	62.6	1.5
			80	31	189.4	64.8	2
2	2001	12					
			5	119	190	42	1.3
			10	111	186	49	1.3
3	2002	12					
			5	135	188.0	46	1.3
			10	132	185.9	50	1.3
20	2002	12					
			0	132	187	0	1.2
			5	128	188	40	1.3
			10	129	185	43	1.3
21	2002	12					
			5	121	187.3	39.1	1.3
			10	115	187.0	47.4	1.3
22	2003	6					
			5	38	193	41.5	1.4
			10	45	190	46.6	1.1
			20	38	188	51.7	0.9
			40	44	188	56.8	1.1
			80	42	198	61.9	1.4
5	2003	6					
			10	156	188	45.8	1.0
			20	160	187	52.4	1.1
			40	157	194	55	1.1
23	2004	12					
			5	127	188	39.8	1.1
			10	128	186	47.1	1.1
24	2006	6					
			10	475	172	45.8	0.5
			20	478	173	52.3	0.5
			40	475	173	56.7	0.5

SE, standard error. Dose=0, placebo.

limits.

The values of E_{max}, ED_{50}, and θ (race on ED_{50}) in the full data set and in the subsets are shown in Figure 5. The results indicated that the parameter values for subsets were within the range of the SE of the full data set estimates except for θ (race on ED_{50}) in subset 11.

The visual predictive check using Monte Carlo simulations showed the mean values of LDL-C reduction (%) from the one-dose trials were distributed, in most cases, within the 5th- to 95th-percentile boundaries of the dose-response profiles for both Westerners and Asians (Figure 6).

Discussion

Rosuvastatin is widely used for the treatment of hypercholesterolemia and the recommended doses for Western and Asian patients are different because of a reported race difference in rosuvastatin pharmacokinetics. However, whether there are race differences in rosuvastatin pharmacodynamics remains unclear. In the absence of randomized, controlled studies directly comparing race differences in rosuvastatin pharmacodynamics, an indirect comparison through a model-based meta-analysis was used, characterizing the dose-response relationship for rosuvastatin in Western and Asian patients.

Table 2. Summary of Asian dose-ranging trials for model building.

Reference	Year	Duration (week)	Dose (mg)	No of patients	LDL-C baseline (mg/dL)	Reductions in LDL-C (%) Mean	SE
25	2002	8					
			1	19	219.4	30.0	3.3
			2	16	217.8	36.5	2.2
			4	18	203.8	41.5	3.5
14	2003	6					
			0	12	190.0	3.2	3.2
			1	15	184.0	35.8	2.7
			2.5	17	184.9	45.0	2.6
			5	12	181.3	52.7	3.1
			10	14	182.2	49.7	2.8
			20	18	185.8	58.2	2.5
			40	13	181.0	66.0	2.9
26	2007	6					
			10	183	157	44.7	1.3
			20	171	153	49.5	1.3
NP	2007	8					
			5	82	168.7	42.3	1.8
			10	82	180.3	48.2	1.7
NP	2008	8					
			5	85	157.7	44	1.7
			10	91	163.8	47.4	1.7

SE, standard error. Dose=0, placebo. NP, not published.

Table 3. Summary of one dose trials for model validation.

Reference	Race	Year	Duration (week)	No of patients	Dose (mg)	LDL-C baseline (mg/dL)	Reductions in LDL-C (%)
27	Western	2004	4	12	10	167.6	45.4
28	Western	2004	12	627	10	173.7	46.92
29	Western	2004	6	153	40	257	52.2
30	Western	2005	16	521	10	164.9	47.5
31	Western	2005	12	358	10	171	40.9
32	Western	2005	12	482	10	178.4	45.6
33	Western	2007	8	428	40	189.3	55.9
34	Western	2007	6	230	40	191	57
35	Western	2007	6	152	40	194	54
36	Western	2008	24	17	10	254	47
37	Western	2008	4	25	40	137.8	60
38	Western	2007	8	240	10	131	51
39	Western	2007	12	1230	40	216	54
40	Western	2008	12	252	10	188	42.9
41	Western	2008	48	13	5	153.6	38.2
42	Western	2008	6	498	10	189.2	46.5
43	Western	2008	48	52	10	>200	44.32
44	Western	2009	4	32	10	206.7	37
45	Asian	2004	6	23	10	177.5	43.4
46	Asian	2006	8	40	40	181.73	48.22
47	Asian	2007	12	515	10	166.8	47.5
48	Asian	2009	12	35	10	157.25	47.5

Table 4. Final population pharmacodynamic parameter estimates of rosuvastatin.

Parameters	TVP	SE	RSE (%)	95%CI
E_{max} (%)	57.0	2.2	3.86	52.7, 61.3
ED_{50} (mg)	1.74	0.38	21.8	1.00, 2.48
γ	1			
E_0 (%)	-0.802			
θ (race on ED_{50})	0.564	0.161	28.55	0.248, 0.880
Inter-trial variability	3.0			
Residual error (SD)	3.1			

TVP, typical population parameter value. SE, standard error. RSE, relative standard error, calculated as SE/TVP and expressed as a percentage. 95% CI, lower and upper limits of the 95% confidence interval, calculated as parameter estimates ±1.96 SE. Inter-trials variability was calculated by taking the square root of η. Residual error was expressed as standard deviation. γ was fixed at 1 and E_0 was presumed to be -0.802% based on the literature value.

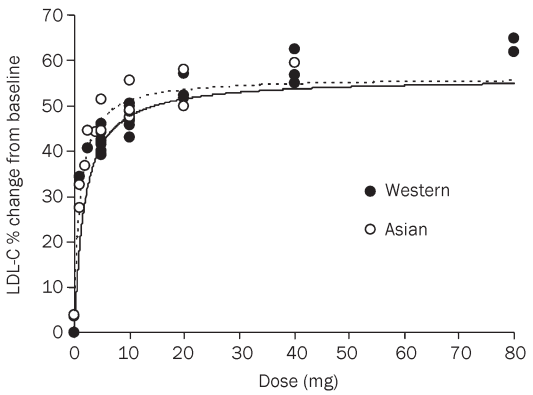

Figure 2. The fits through the observed effects with the parameters obtained from the final model. ●, the observed effects in Western patients; ○, the observed effects in Asian patients. The solid curve is the model-predicted dose-response curve in Western patients and the dashed curve is the model-predicted dose-response curve in Asian patients.

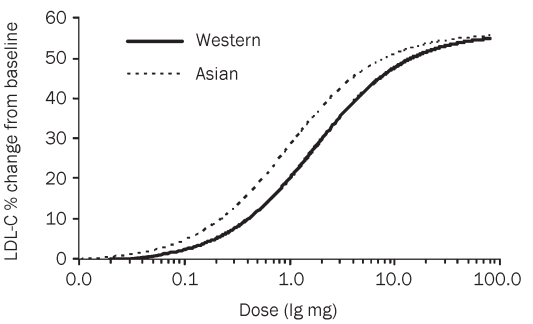

Figure 3. The dose-response logarithmic curve of rosuvastatin in Western and Asian hypercholesterolemic patients. The solid line, LDL-C% change in Western patients; the dashed line, LDL-C% change in Asian patients.

Table 5. Summary of bootstrap validation on the present population pharmacodynamic model.

Parameters	Final estimates	Results of bootstrap simulations		Bootstrap mean/final estimate ratio (%)
		Mean	95% CI	
E_{max} (%)	57.0	57.2	54.8, 59.6	100.4
ED_{50} (mg)	1.74	1.79	1.22, 2.37	102.9
θ (Race on ED_{50})	0.564	0.600	0.334, 0.866	106.4

TVP, typical population parameter value. SE, standard error. RSE, relative standard error, calculated as SE/TVP and expressed as a percentage. 95% CI, lower and upper limits of the 95% confidence interval, calculated as parameter estimates ±1.96 SE. Inter-trials variability was calculated by taking the square root of η. Residual error was expressed as standard deviation. γ was fixed at 1 and E_0 was presumed to be -0.802% based on the literature value.

Because the mean percentage change in LDL-C from baseline is generally accepted as the primary efficacy endpoint for lipid-lowering drugs, the PPD analysis in this study focused on the relationship between dose and LDL-C reduction (%).

The final model in this study successfully provided the pharmacodynamic profile of rosuvastatin in Western and Asian patients. The rosuvastatin-induced reductions in LDL-C were best described by the simple E_{max} model fixing E_0 at -0.802. Race was found to affect the parameter ED_{50} and has a value of 1 for Westerners and 0.564 for Asians. No other significant covariate was found. This finding showed that the ED_{50} was approximately twofold higher in Western patients compared with Asian patients. The result was consistent with the reported race difference in rosuvastatin pharmacokinetics: the AUC_{0-t} values were 2.31-, 1.91-, and 1.63-fold higher and the C_{max} values were 2.36-, 2.00-, and 1.68-fold higher in Chinese, Malay, and Asian Indian subjects, respectively, compared with white subjects[13]. The pharmacodynamics of rosuvastatin with a common E_{max} and a different ED_{50} for Westerners and Asians confirmed that there is no significant difference between these two populations in the exposure-response relationship for LDL-C reduction. It supports the current dosing recommendation for Westerners (10 to 40 mg) and Asians (5 to 20 mg) that was based on pharmacokinetic exposure[12]. Although the dose in Asians is half that in Westerners, the LDL-C reductions (%) are similar in the two populations. In other words, the two populations exhibit no difference in the LDL-C-lowing effect of rosuvastatin. The findings of this study imply that for a new compound with a similar mechanism of action as rosuvastatin, its efficacy (LDL-C-lowering effect) in Western populations plus its pharmacokinetics in bridging studies[49, 50] in Asian populations may be used to support a registration of the new compound in Asian countries, or vice versa. This will avoid unnecessary duplication of efficacy trials in different races, reduce the cost of drug development, and minimize the exposure of patients to doses with uncertain safety and

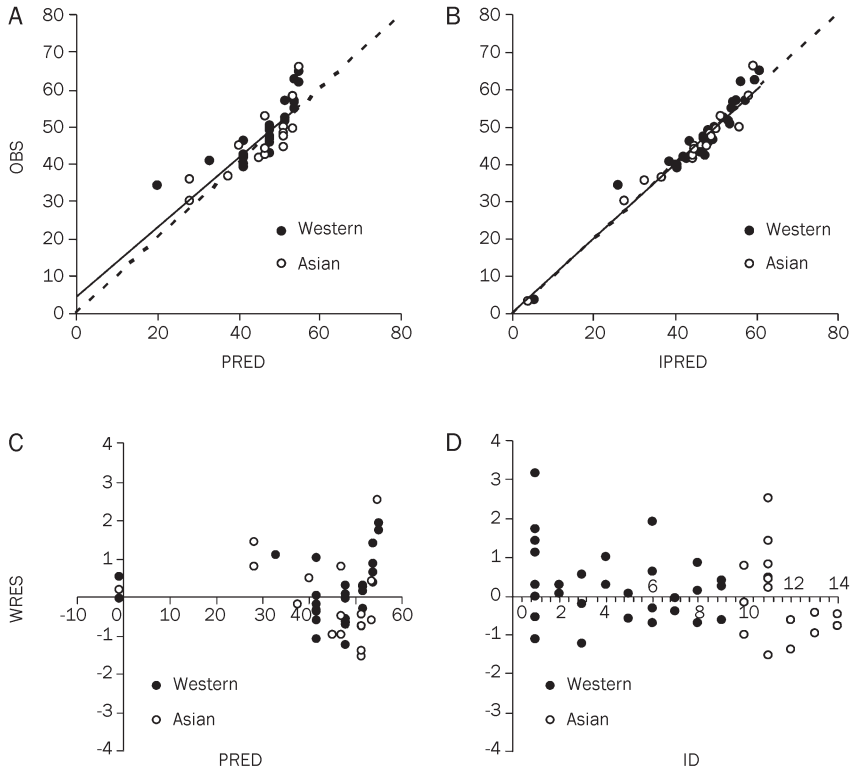

Figure 4. The goodness-of-fit plots for the final PPD model. (A) Scatter plot of population model-predicted effects (PRED) *versus* observed effects (OBS). (B) Scatter plot individual model-predicted effects (IPRED) *versus* OBS. The solid line is a linear regression line and the dashed line is unity. (C) Plot of weighted residuals (WRES) *versus* PRED. (D) Plot of WRES *versus* the trials' identification number (ID).

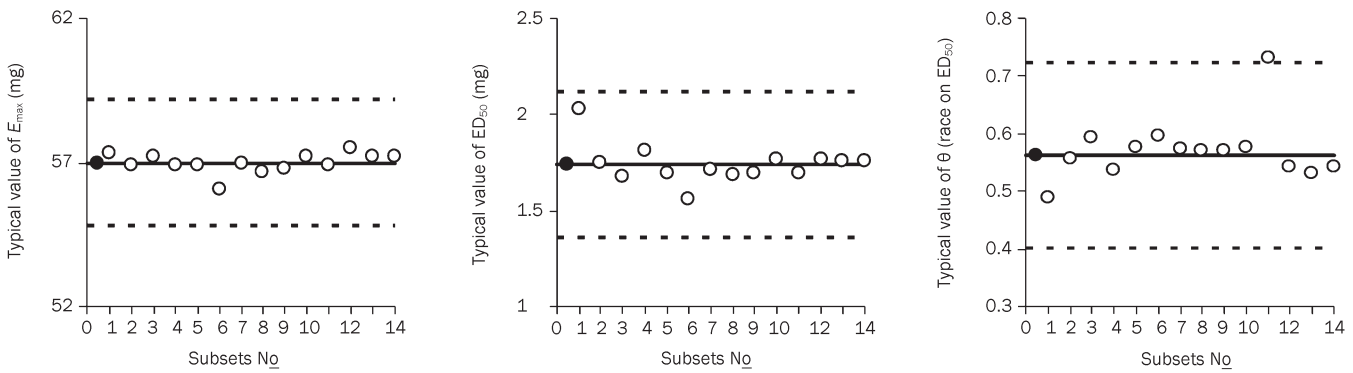

Figure 5. The values of E_{max}, ED_{50}, and θ (race on ED_{50}) in the full data set (●) and for 14 different subsets (○). The solid and dashed lines are the parameter value and ±SE values from the full data set, respectivly.

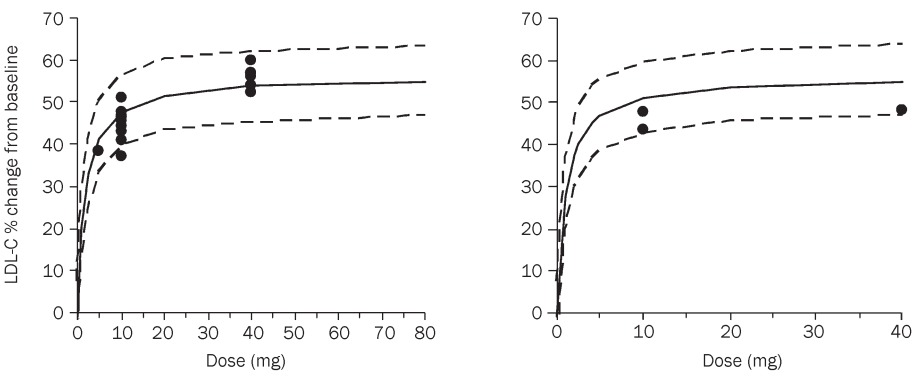

Figure 6. The visual predictive check for the final PPD model in Westerns (left) and Asians (right). The dots are the mean values of LDL-C reduction (%) from the one dose trials. The population-predicted profile (50th percentile) estimated from 1000 Monte Carlo simulations is shown by the solid line, and the 95% prediction intervals are encompassed by the dashed lines in each plot.

efficacy.

Because of the limited amount of data (46 effect samples) available for this study, a previously reported sigmoidal E_{max} model was not suitable for estimating the four required parameters. Therefore, a simple E_{max} model was used and the values of E_{max}, ED_{50}, E_0, and θ were 55.5%, 1.84 mg, 1.21%, and 0.571. In that case, however, the RSE for the estimated E_0 was greater than 900%. To reduce the RSE, E_0 was fixed based on literature values. In fact, the estimated values of E_{max}, ED_{50}, and θ (race on ED_{50}) were not affected by fixing E_0. Consequently, the final model, a simple E_{max} model with a fixed E_0 (-0.812%), was successfully used to describe rosuvastatin pharmacodynamics. Moreover, the robustness of the final model was evaluated by the nonparametric bootstrap and the data-splitting methods[51, 52], which indicated that selected combinations of data yielded results very similar to those obtained using the original full data set. The predictive performance of the final model was confirmed by the visual predictive check using Monte Carlo simulations, which showed that the mean values of LDL-C reduction (%) from the one-dose trials were mostly distributed within the 5th- to 95th-percentile boundaries of the predictive dose-response profiles for both Westerners and Asians.

It has been reported that the maximum response is usually obtained within 2–4 weeks and is maintained during chronic therapy for a fixed dose of rosuvastatin. For this reason, only the mean values of LDL-C reduction (%) that were observed at least 4 weeks after administration were used in the model development. Therefore, it should be noted that the final model in this study was developed to describe the steady state for the LDL-C-lowering effect of rosuvastatin.

In conclusion, the race difference in the pharmacodynamics of rosuvastatin is consistent with that in the pharmacokinetics of the drug, which confirms that there is no significant difference in the exposure-response relationship for LDL-C reduction between Asians and Westerners. This study suggests that for a new compound with a mechanism of action similar to that of rosuvastatin, its efficacy in Western populations plus its pharmacokinetics in bridging studies in Asian populations may be used to support a registration of the new compound in Asian countries.

Acknowledgements

We thank Dr Ya-ning WANG (US FDA) for valuable discussions and advice. This study was supported by the National Science and Technology Supporting Projects of China (2008BAI51B03, 2009ZX09502-021), E-Institute of Shanghai High Education (E03008), the Leading Academic Discipline Project of the Shanghai Municipal Education Commission (J50303, 2008GSP19-5), and the Special Fund of Scientific Research for Selecting and Training Outstanding Young Teachers of Shanghai Municipal Education (SZY07027).

Author contribution

Juan YANG and Qing-shan ZHENG conceived and designed the study. Juan YANG, Ying-chun HE, and Yu-cheng SHENG performed the electronic literature retrieval and data extraction. Juan YANG, Lu-jin LI, Kun WANG, and Ling XU analyzed the data. Xiao-hui HUANG and Feng GUO discussed the results. Juan YANG and Qing-shan ZHENG wrote the paper. All authors checked the final manuscript before submission.

References

1 Olsson AG, Pears J, McKellar J, Mizan J, Raza A. Effect of rosuvastatin on low-density lipoprotein cholesterol in patients with hypercholesterolemia. Am J Cardiol 2001; 88: 504–8.
2 Paoletti R, Fahmy M, Mahla G, Mizan J, Southworth H. Rosuvastatin demonstrates greater reduction of low-density lipoprotein cholesterol compared with pravastatin and simvastatin in hypercholesterolaemic patients: a randomized, double-blind study. J Cardiovasc Risk 2001; 8: 383–90.
3 Olsson AG, Istad H, Luurila O, Ose L, Stender S, Tuomilehto J, *et al*. Effects of rosuvastatin compared over 52 weeks for treatment in patients with hypercholesterolemia. Am Heart J 2002; 144: 1044–51.
4 Carswell CI, Plosker GL, Jarvis B. Rosuvastatin. Drugs 2002; 62: 2075–85.
5 Jones PH, Davidson MH, Stein EA, Bays HE, McKenney JM, Miller E, *et al*. Comparison of the efficacy and safety of rosuvastatin versus atorvastatin, simvastatin, and pravastatin across doses (STELLAR* Trial). Am J Cardiol 2003; 92: 152–60.
6 Rader DJ, Davidson MH, Caplan RJ, Pears JS. Lipid and apolipoprotein ratios: association with coronary artery disease and effects of rosuvastatin compared with atorvastatin, pravastatin, and simvastatin. Am J Cardiol 2003; 91: 20C–23C.
7 McTaggart F, Buckett L, Davidson R, Holdgate G, McCormick A, Schneck D, *et al*. Preclinical and clinical pharmacology of Rosuvastatin, a new 3-hydroxy-3-methylglutaryl coenzyme A reductase inhibitor. Am J Cardiol 2001; 87: 28B–32B.
8 Leonard KA. Treatment and prevention of dyslipidemia with rosuvastatin (Crestor). Nurse Pract 2004; 29: 11–5.
9 Martin PD, Warwick MJ, Dane AL, Cantarini MV. A double-blind, randomized, incomplete crossover trial to assess the dose proportionality of rosuvastatin in healthy volunteers. Clin Ther 2003; 25: 2215–24.
10 Martin PD, Dane AL, Nwose OM, Schneck DW, Warwick MJ. No effect of age or gender on the pharmacokinetics of rosuvastatin: a new HMG-CoA reductase inhibitor. J Clin Pharmacol 2002; 42: 1116–21.
11 Tzeng TB, Schneck DW, Birmingham BK, Mitchell PD, Zhang H, Martin PD, *et al*. Population pharmacokinetics of rosuvastatin: implications of renal impairment, race, and dyslipidaemia. Curr Med Res Opin 2008; 24: 2575–85.
12 AstraZeneca Canada Inc. PRODUCT MONOGRAPH. Pr CRESTOR ® rosuvastatin. Tablets, 5, 10, 20, and 40 mg. LIPID METABOLISM REGULATOR [monograph on the Internet]. 2008 [cited 2009 May 7]. Available from: http://www.astrazeneca.ca/documents/ProductPortfolio/CRESTOR_PM_en.pdf.
13 Lee E, Ryan S, Birmingham B, Zalikowski J, March R, Ambrose H, *et al*. Rosuvastatin pharmacokinetics and pharmacogenetics in white and Asian subjects residing in the same environment. Clin Pharmacol Ther 2005; 78: 330–41.
14 Saito Y, Goto Y, Dane A, Strutt K, Raza A. Randomized dose-response study of rosuvastatin in Japanese patients with hypercholesterolemia. J Atheroscler Thromb 2003; 10: 329–36.
15 Mandema JW, Hermann D, Wang W, Sheiner T, Milad M, Bakker-

Arkema R, *et al*. Model-based development of gemcabene, a new lipid-altering agent. AAPS J 2005; 7: E513–22.
16 Mandema JW, Verotta D, Sheiner LB. Building population pharmacokinetic — pharmacodynamic models. I. Models for covariate effects. J Pharmacokinet Biopharm 1992; 20: 511–28.
17 Beal SL, Sheiner LB. NONMEM Users Guides. San Francisco: NONMEM Project Group, University of California, San Francisco, CA. 1989.
18 Ette EI. Stability and performance of a population pharmacokinetic model. J Clin Pharmacol 1997; 37: 486–95
19 Ishibashi T, Yano Y, Oguma T. Population pharmacokinetics of platinum after nedaplatin administration and model validation in adult patients. Br J Clin Pharmacol 2003; 56: 205–13.
20 Davidson M, Ma P, Stein EA, Gotto AM Jr, Raza A, Chitra R, *et al*. Comparison of effects on low-density lipoprotein cholesterol and high-density lipoprotein cholesterol with rosuvastatin versus atorvastatin in patients with type IIa or IIb hypercholesterolemia. Am J Cardiol 2002; 89: 268–75.
21 Brown WV, Bays HE, Hassman DR, McKenney J, Chitra R, Hutchinson H, *et al*. Efficacy and safety of Rosuvastatin compared with Pravastatin and Simvastatin in patients with hypercholesterolemia: a randomized, double-blind, 52-week trial. Am Heart J 2002; 144: 1036–43.
22 Schneck DW, Knopp RH, Ballantyne CM, McPherson R, Chitra RR, Simonson SG. Comparative effects of Rosuvastatin and Atorvastatin across their dose ranges in patients with hypercholesterolemia and without active arterial disease. Am J Cardiol 2003; 91: 33–41.
23 Schwartz GG, Bolognese MA, Tremblay BP, Caplan R, Hutchinson H, Raza A, *et al*. Efficacy and safety of rosuvastatin and atorvastatin in patients with hypercholesterolemia and a high risk of coronary heart disease: a randomized, controlled trial. Am Heart J 2004; 148: e4.
24 Catapano AL, Davidson MH, Ballantyne CM, Brady WE, Gazzara RA, Tomassini JE, *et al*. Lipid-altering efficacy of the ezetimibe/simvastatin single tablet *versus* rosuvastatin in hypercholesterolemic patients. Curr Med Res Opin 2006; 22: 2041–53.
25 Yamamoto A, Arakawa K, Sasaki J, Matsuzawa Y, Takemura K, Tsushima M, *et al*. Clinical effects of rosuvastatin, a new HMG-CoA reductase inhibitor, in Japanese patients with primary hypercholesterolemia: an early phase II study. J Atheroscler Thromb 2002; 9: 48–56.
26 Deedwania PC, Gupta M, Stein M, Ycas J, Gold A; IRIS Study Group. Comparison of rosuvastatin versus atorvastatin in South-Asian patients at risk of coronary heart disease (from the IRIS Trial). Am J Cardiol 2007; 99: 1538–43.
27 Kosoglou T, Statkevich P, Yang B, Suresh R, Zhu Y, Boutros T, *et al*. Pharmacodynamic interaction between ezetimibe and rosuvastatin. Curr Med Res Opin 2004; 20: 1185–95.
28 Strandberg TE, Feely J, Sigurdsson EL; DISCOVERY study group. Twelve-week, multicenter, randomized, open-label comparison of the effects of rosuvastatin 10 mg/d and atorvastatin 10 mg/d in high-risk adults: a DISCOVERY study. Clin Ther 2004; 26: 1821–33.
29 Ballantyne CM, Miller E, Chitra R. Efficacy and safety of rosuvastatin alone and in combination with cholestyramine in patients with severe hypercholesterolemia: a randomized, open-label, multicenter trial. Clin Ther 2004; 26: 1855–64.
30 Cheung RC, Morrell JM, Kallend D, Watkins C, Schuster H. Effects of switching statins on lipid and apolipoprotein ratios in the MERCURY I study. Int J Cardiol 2005; 100: 309–16.
31 Fonseca FA, Ruiz A, Cardona-Muñoz EG, Silva JM, Fuenmayor N, Marotti M, *et al*. The DISCOVERY PENTA study: a DIrect Statin Comparison of LDL-C Value — an Evaluation of Rosuvastatin therapY compared with atorvastatin. Curr Med Res Opin 2005; 21: 1307–15.
32 Bots AF, Kastelein JJ; Discovery Netherlands Investigators. Achieving lipid goals in real life: the Dutch DISCOVERY study. Int J Clin Pract 2005; 59: 1387–94.
33 Leiter LA, Rosenson RS, Stein E, Reckless JP, Schulte KL, Schleman M, *et al*. Efficacy and safety of rosuvastatin 40 mg versus atorvastatin 80 mg in high-risk patients with hypercholesterolemia: results of the POLARIS study. Atherosclerosis 2007; 194: e154–64.
34 Ballantyne CM, Weiss R, Moccetti T, Vogt A, Eber B, Sosef F, *et al*. Efficacy and safety of rosuvastatin 40 mg alone or in combination with ezetimibe in patients at high risk of cardiovascular disease (results from the EXPLORER study). Am J Cardiol 2007; 99: 673–80.
35 Asztalos BF, Le Maulf F, Dallal GE, Stein E, Jones PH, Horvath KV, *et al*. Comparison of the effects of high doses of rosuvastatin *versus* atorvastatin on the subpopulations of high-density lipoproteins. Am J Cardiol 2007; 99: 681–5.
36 Talini E, Di Bello V, Bianchi C, Palagi C, Delle Donne MG, Penno G, *et al*. Early impairment of left ventricular function in hypercholesterolemia and its reversibility after short term treatment with rosuvastatin A preliminary echocardiographic study. Atherosclerosis 2008; 197: 346–54.
37 Sviridov D, Hoang A, Ooi E, Watts G, Barrett PH, Nestel P. Indices of reverse cholesterol transport in subjects with metabolic syndrome after treatment with rosuvastatin. Atherosclerosis 2008; 197: 732–9.
38 Betteridge DJ, Gibson JM, Sager PT. Comparison of effectiveness of rosuvastatin *versus* atorvastatin on the achievement of combined C-reactive protein (<2 mg/L) and low-density lipoprotein cholesterol (<70 mg/dl) targets in patients with type 2 diabetes mellitus (from the ANDROMEDA study). Am J Cardiol 2007; 100: 1245–8.
39 Stein EA, Amerena J, Ballantyne CM, Brice E, Farnier M, Guthrie RM, *et al*. Long-term efficacy and safety of rosuvastatin 40 mg in patients with severe hypercholesterolemia. Am J Cardiol 2007; 100: 1387–96.
40 Laks T, Keba E, Leiner M, Merilind E, Petersen M, Reinmets S, *et al*. Achieving lipid goals with rosuvastatin compared with simvastatin in high risk patients in real clinical practice: a randomized, open-label, parallel-group, multi-center study: the DISCOVERY-Beta study. Vasc Health Risk Manag 2008; 4: 1407–16.
41 Underhill HR, Yuan C, Zhao XQ, Kraiss LW, Parker DL, Saam T, *et al*. Effect of rosuvastatin therapy on carotid plaque morphology and composition in moderately hypercholesterolemic patients: a high-resolution magnetic resonance imaging trial. Am Heart J 2008; 155: 584.e1–8.
42 Faergeman O, Hill L, Windler E, Wiklund O, Asmar R, Duffield E, *et al*. Efficacy and tolerability of rosuvastatin and atorvastatin when force-titrated in patients with primary hypercholesterolemia: results from the ECLIPSE study. Cardiology 2008; 111: 219–28.
43 Mazza F, Stefanutti C, Di Giacomo S, Vivenzio A, Fraone N, Mazzarella B, *et al*. Effects of low-dose atorvastatin and rosuvastatin on plasma lipid profiles: a long-term, randomized, open-label study in patients with primary hypercholesterolemia. Am J Cardiovasc Drugs 2008; 8: 265–70.
44 Pirro M, Schillaci G, Romagno PF, Mannarino MR, Bagaglia F, Razzi R, *et al*. Influence of short-term rosuvastatin therapy on endothelial progenitor cells and endothelial function. J Cardiovasc Pharmacol Ther 2009; 14: 14–21.
45 Lu TM, Ding YA, Leu HB, Yin WH, Sheu WH, Chu KM. Effect of rosuvastatin on plasma levels of asymmetric dimethylarginine in patients with hypercholesterolemia. Am J Cardiol 2004; 94: 157–61.
46 Wongwiwatthananukit S, Sansanayudh N, Dhummauppakorn R, Kitiyadisai C. Efficacy and safety of rosuvastatin every other day compared with once daily in patients with hypercholesterolemia. Ann Pharmacother 2006; 40: 1917–23.

47 Zhu JR, Tomlinson B, Ro YM, Sim KH, Lee YT, Sriratanasathavorn C. A randomised study comparing the efficacy and safety of rosuvastatin with atorvastatin for achieving lipid goals in clinical practice in Asian patients at high risk of cardiovascular disease (DISCOVERY-Asia study). Curr Med Res Opin 2007; 23: 3055–68.

48 Qu HY, Xiao YW, Jiang GH, Wang ZY, Zhang Y, Zhang M. Effect of atorvastatin *versus* rosuvastatin on levels of serum lipids, inflammatory markers and adiponectin in patients with hypercholesterolemia. Pharm Res 2009; 26: 958–64.

49 Liu JP, Chow SC. Bridging studies in clinical development. J Biopharm Stat 2002; 12: 359–67.

50 Uyama Y, Shibata T, Nagai N, Hanaoka H, Toyoshima S, Mori K. Successful bridging strategy based on ICH E5 guideline for drugs approved in Japan. Clin Pharmacol Ther 2005; 78: 102–13.

51 Othman AA, Tenero DM, Boyle DA, Eddington ND, Fossler MJ. Population pharmacokinetics of S (–)-carvedilol in healthy volunteers after administration of the immediate-release (IR) and the new controlled-release (CR) dosage forms of the racemate. AAPS J 2007; 9: E208–18.

52 Wu KH, Cui YM, Guo JF, Zhou Y, Zhai SD, Cui FD, *et al*. Population pharmacokinetics of cyclosporine in clinical renal transplant patients. Drug Metab Dispos 2005; 33: 1268–75.

Acta Pharmacologica Sinica (2011) 32: 126–132
 1671-4083/11 $32.00
www.nature.com/aps

Original Article

Effects of formoterol-budesonide on airway remodeling in patients with moderate asthma

Ke WANG[1], Chun-tao LIU[1], Yong-hong WU[1], Yu-lin FENG[1], Hong-li BAI[2], En-sen MA[2], Fu-qiang WEN[1, *]

[1]Department of Respiratory Medicine, West China Hospital, Sichuan University, Chengdu 610041, China; [2]Department of Radiology Medicine, West China Hospital, Sichuan University, Chengdu 610041, China

Aim: To evaluate the effect of inhaled formoterol-budesonide on airway remodeling in adult patients with moderate asthma.
Methods: Thirty asthmatic patients and thirty control subjects were enrolled. Asthmatic subjects used inhaled Symbicort 4.5/160 μg twice daily for one year. The effect of formoterol-budesonide on airway remodeling was assessed with comparing high-resolution computer tomography (HRCT) images of asthmatic patients and controls, as well as expression levels of cytokines and growth factors, inflammatory cell count in induced sputum, and airway hyper-responsiveness.
Results: The differences in age and gender between the two groups were not significant. However, differences in FVC %pred, FEV_1 %pred, and PC_{20} between the two groups were significant. After treatment with formoterol-budesonide, the asthma patients' symptoms were relieved, and their lung function was improved. The WT and WA% of HRCT images in patients with asthma was increased, whereas treatment with formoterol-budesonide caused these values to decrease. The expression of MMP-9, TIMP-1, and TGF-β_1 in induced sputum samples increased in patients with asthma and decreased dramatically after treatment with formoterol-budesonide. The WT and WA% are correlated with the expression levels of cytokines and growth factors, inflammatory cell count in induced sputum, and airway hyper-responsiveness, while these same values are correlated negatively with FEV_1/FVC and FEV_1%.
Conclusion: Formoterol-budesonide might interfere in chronic inflammation and airway remodeling in asthmatic patients. HRCT can be used to effectively evaluate airway remodeling in asthmatic patients.

Keywords: asthma; hyper-responsiveness; airway remodeling; high-resolution computer tomography; formoterol-budesonide; induced sputum; single-center, open-label study

Acta Pharmacologica Sinica (2011) 32: 126–132; doi: 10.1038/aps.2010.170; published online 20 Dec 2010

Introduction

Bronchial asthma is a chronic inflammatory disease of the airways that is characterized by respiratory symptoms associated with variable airflow obstruction, airway hyper-responsiveness, and airway remodeling[1]. Airway remodeling refers to airway structural alterations that likely have clinical consequences. Epithelial shedding, goblet cell and submucosal gland hyperplasia, increased accumulation of smooth muscle bundles and extracellular matrix (ECM), microvascular alterations, cartilage changes, and airway wall edema are the main histological features of asthmatic airways[2]. The ECM remains in a state of dynamic equilibrium of new synthesis and degradation due to the action of matrix metalloproteinases (MMPs) and tissue inhibitors of metalloproteinases (TIMPs)[3] as well as growth factors such as transforming growth factor β_1 (TGF-β_1)[4]. Of the MMP family, MMP-9 is one of the major proteinases involved in airway inflammation and bronchial remodeling in asthma[5, 6]. TIMP-1, the major inhibitor of MMP-9, has also been postulated to act in airway remodeling. In addition, TGF-β_1 induces ECM deposition and thus contributes critically to fibrosis in the airways and lungs[4].

High-resolution computed tomography (HRCT) has made it possible to accurately measure airway dimensions. Quantitative analysis of bronchial wall thickness (WT), airway narrowing, and bronchodilation can be performed for patients with pulmonary diseases, such as bronchial asthma, by measuring airway dimensions[7]. Numerous image analysis techniques have been developed for measurement of airway dimensions[8–10]. These techniques make it possible to accurately measure changes in airway dimensions longitudinally or after intervention by matching CT sections of the same airways in a non-invasive way.

Corticosteroids are effective in controlling asthma. Corticosteroids reduce airway eosinophilic inflammation and expres-

* To whom correspondence should be addressed.
E-mail wenfuqiang@126.com
Received 2010-07-10 Accepted 2010-09-04

sion of GM-CSF, IL-4, IL-5, IL-11, and IL-17[11]. The combination of inhaled corticosteroids (ICSs) with long-acting inhaled β_2-agonists (LABAs) has been recommended to improve the effectiveness of asthma treatment[12]. Formoterol-budesonide is preferentially delivered and deposited in the distal airways. However, it is not clear whether formoterol-budesonide deposition in peripheral airways can influence airway remodeling. The present study evaluated whether formoterol-budesonide can influence airway remodeling. To this end, we examined the expression levels of MMP-9, TIMP-1, and TGFβ_1 in the sputum of patients with asthma compared to those treated with formoterol-budesonide. Thin-section CT was used to evaluate the degree of airway remodeling.

Materials and methods

Study design

A single-center, open-label study was conducted in adult patients with moderate asthma to evaluate the effect of inhaled formoterol-budesonide on peripheral remodeling. The Ethics Committee of West China Hospital, Sichuan University, approved the study, and all subjects gave written informed consent. Patients and control subjects who met the inclusion and exclusion criteria had a baseline thin-section CT scan, an induced sputum collection, and a lung function exam. Patients were then treated with formoterol-budesonide (Symbicort, AstraZeneca, Lund, Sweden; 4.5/160 μg twice daily) for one year. After treatment for one year, another thin-section CT scan, induced sputum collection, and lung function exam were conducted. The effect of formoterol-budesonide on airway remodeling was measured by comparisons of CT images, expression levels of cytokines and growth factors in induced sputum, and airway hyper-responsiveness.

Subjects

Thirty patients were diagnosed with moderate asthma according to the Global Initiative for Asthma (GINA) 2006 [http://www.ginasthma.org], and thirty more were used as control subjects. Patients with chronic bronchitis or any major comorbid disease that might affect asthma disease activity, such as HIV, metastatic cancer, and congestive heart failure were excluded from the study. Subjects with moderate asthma had to fulfill the following criteria: daily symptoms; exacerbations that may affect activity and sleep; nocturnal symptoms more than once a week; daily use of inhaled short-acting β_2-agonist; FEV_1 or PEF 60% to 80% predicted; and PEF or FEV_1 variability >30%. Asthmatic subjects had not used any steroids within the 180 d preceding the beginning of the study. Healthy control subjects were recruited from hospital personnel who answered in a screening questionnaire that they did not have respiratory symptoms and who had FEV_1 values of more than 80% of the predicted value, PC_{20} methacholine of more than 10 mg/mL, and normal findings on simple chest radiograms. All subjects were nonsmokers or ex-smokers of at least 2 years with a smoking history of less than 15 pack-years. None of the subjects had respiratory tract infections in the 2 weeks preceding the two follow-ups.

Sputum collection and procession

Induced sputum was obtained according a previously described method, with slight modification[13]. The sputum was examined within 1 h. The entire sputum sample was inspected for salivary contamination under an inverted microscope; all portions that appeared free of salivary contamination were placed in a 15-mL polystyrene tube using forceps. Dithiothreitol (a final concentration of 1 mmol/L) was freshly diluted in distilled water equal to 4 times the sputum weight and added to the sputum sample. The mixture was vortexed for 30 s and then placed on a bench rocker and rocked for 15 min. A further 4 volumes of Dulbecco's phosphate-buffered saline was added to stop the effect of dithiothreitol and rocked for 5 min. The suspension was filtered through a 70-μm cell strainer. The resulting suspension was centrifuged at 800×*g* for 10 min and the supernatant was aspirated and stored in Eppendorf tubes at –70°C in the presence of aprotinin. All subjects produced an adequate specimen of sputum; a sample was considered adequate if the patient was able to expectorate at least 2 mL of sputum.

Total cell counts were performed in a hemocytometer and expressed as millions per milligram of selected induced sputum. The proportion of salivary squamous cells was noted. Differential cell counts were performed by counting 400 cells on May Grünwald Giemsa-stained slides. Results were expressed as a percentage of the total cell count. Slides were coded and cell counts were performed by an expert observer who did not know the clinical characteristics of the patients. Only samples with cell viability >70% and squamous cell contamination <20% were considered adequate.

TGF-β_1, MMP-9, and TIMP-1 concentrations were measured with enzyme-linked immunosorbent assay kits (R&D Systems Inc, Minneapolis, MN, USA; Bender MedSystems GmbH, Vienna, Austria; BioSource International Inc, Camarillo, CA, USA) according to the manufacturer's guidelines. The minimum detectable levels of TGF-β_1, MMP-9, and TIMP-1 in these assay systems were 1.7 pg/mL, 0.8 ng/mL, and 1 ng/mL, respectively. All results were corrected for the volume and dilution of sputum or saliva.

High-resolution computed tomography (HRCT) protocol

HRCT was performed using a multi-detector row spiral CT scanner (Sensation 16, Siemens Medical System, Erlangen, Germany) with sixteen detector arrays. Patients were scanned in the supine position during one breath hold at deep inspiration. The scans were obtained with 16×1 mm collimation at 10 mm intervals, with a table feed of 11 mm per 0.5 s scanner rotation. Scanning was performed at 120 kV and 80 mAs, regardless of patient size, using a 512×512 matrix. Images were reconstructed with a bone algorithm and a 512×512 matrix. Images were viewed at a window level of -450 HU and a width of 1500 HU. CT scans were interpreted by two radiologists who were unaware of the clinical history of the patients and control subjects.

Bronchial wall thickening was assessed as follows. All visible sections of bronchi were counted at five levels in the

pulmonary fields (right and left lungs), and all circular (complete circles or at least two thirds of a circle) and longitudinal bronchi except the hilar bronchi were included. The five levels were 1 cm above the carina (Level 1), 1 cm below the carina (Level 2), the right pulmonary vein (Level 3), 3 cm below the top of the pulmonary vein (Level 4), and above the right side of the diaphragm (Level 5). The bronchial wall thickness at these five levels was measured. The following parameters were determined with semiautomatic image-processing program: luminal area (LA), total airway area (TA), short axis of lumen (LSD), and short axis of total airway (TSD). In airways in which an adjacent vessel or a branching of a small bronchus abutted the boundary of the airway, an extrapolated line was traced. Airway wall area (WA) was calculated as TA-LA and WT was calculated as (TSD-LSD)/2. Relative WA (WA% = [WA/TA]×100) was also calculated.

Statistical analysis

All data are expressed as the mean±SEM. Statistical analyses were performed using SPSS 12.0 software. Statistical significance was analyzed with one-way analysis of variance (ANOVA) followed by the Student-Newman-Keuls test to isolate significant difference. Chi-square test and Pearson correlation analysis were also used. A P value less than 0.05 (two-tailed test) was considered statistically significant.

Results

Subjects

The sixty patients were divided into an asthma group and a control group. The patients' demographic characteristics are listed in Table 1.

Table 1. Demographic characteristic of study subjects. Data are presented as mean±SEM. $^{b}P<0.05$, $^{c}P<0.01$ compared with normal control subjects. $^{e}P<0.05$, $^{f}P<0.01$ compared with asthma group pre-treatment.

	Control group (n=30)	Asthma group pre-treatment (n=30)	Asthma group after treatment (n=30)
Age (Year)	33.3±6.80	35.2±3.16	35.2±3.16
Gender (M/F)	16/14	16/14	16/14
FVC %pred (%)	95.6±4.21	75.7±5.28^{b}	83.4±3.41^{e}
FEV_1 %pred (%)	103.2±6.95	68.3±2.86^{c}	88.2±4.12^{f}
PC_{20} (mg/mL)	>10	1.23±0.45^{c}	4.29±0.62^{f}
V_{75} %pred (%)	102.6±8.62	66.4±12.7^{c}	95.1±9.3^{e}
V_{50} %pred (%)	94.3±10.8	53.9±17.1^{c}	74.4±10.1^{e}
V_{25} %pred (%)	96.0±24.5	59.0±18.5^{c}	83.5±11.6^{f}

The differences in age and gender between the two groups were not significant. Otherwise, the differences of FVC %pred, FEV_1 %pred, PC_{20}, V_{75} %pred, V_{50} %pred, and V_{25} %pred were significant between the two groups. After treatment, asthma symptoms had been relieved, and the differences of lung function were significant.

Evaluations of cytokines in induced sputum

The levels of MMP-9, TIMP-1, and TGF-β_1 were increased, and there was a tendency for a higher MMP-9/TIMP-1 ratio in patients with asthma. After treatment with formoterol-budesonide, the levels of cytokines decreased significantly (Table 2).

Table 2. Results measured in sputum. Data are presented as mean±SEM. $^{b}P<0.05$, $^{c}P<0.01$ compared with normal control subjects. $^{e}P<0.05$, $^{f}P<0.01$ compared with asthma group pre-treatment.

	Control group (n=30)	Asthma group pre-treatment (n=30)	Asthma group after treatment (n=30)
Volume (mL)	2.7±0.6	3.2±0.8	2.5±0.5
SQU (%)	32.6±8.5	29.7±9.2	30.4±10.7
TLC ($\times10^6$/mL)	2.1±0.7	3.4±1.0^{b}	2.4±0.9^{e}
Macrophages (%)	59.7±6.8	49.2±5.3^{c}	55.0±7.7^{be}
Lymphocytes (%)	1.9±0.5	1.6±0.5	1.7±0.7
Neutrophils (%)	37.4±6.8	29.3±8.4^{c}	39.8±10.1^{be}
Eosinophils (%)	0.9±0.3	4.1±0.8^{c}	1.8±0.5^{cf}
MMP-9 (ng/mL)	66.8±12.1	184.7±23.4^{c}	120.5±14.9^{cf}
TIMP-1 (ng/mL)	129.8±34.2	275.4±69.6^{c}	208.9±59.7^{cf}
MMP-9/TIMP-1	0.47±0.11	0.69±0.18^{c}	57.4±0.14^{cf}
TGF-β_1 (ng/mL)	14.6±5.7	35.1±16.3^{c}	25.8±13.9^{be}

SQU, squamous epithelial cells; TLC, total inflammatory cell count.

HRCT evaluation

The bronchial wall thickening based on the number of bronchi counted on HRCT scans is shown in Figure 1 and Table 3. The WT and WA% in the asthma group before treatment were significantly increased compared to data from the control group. After treatment, the WT and WA% of the patients with asthma decreased, and the differences were also significant compared to the data before treatment.

Correlation analysis

The WT and WA% of patients with asthma were well correlated with hyper-responsiveness, degree of infiltration of inflammatory cells, and concentration of chemokines involved in airway remodeling, while being negatively correlated with FEV_1/FVC and FEV_1%. Importantly, the WT and WA% of patients with asthma were more correlated in the proximal airway than in the distal airway (Table 4).

Discussion

We demonstrated that FEV_1/FVC and FEV_1% decreased, while airway hyper-responsiveness, degree of infiltration of inflammatory cells, and concentration of chemokines involved in airway remodeling increased in patients with moderate asthma compared to patients in a control group. Formoterol-budesonide can interfere in the chronic inflammation and remod-

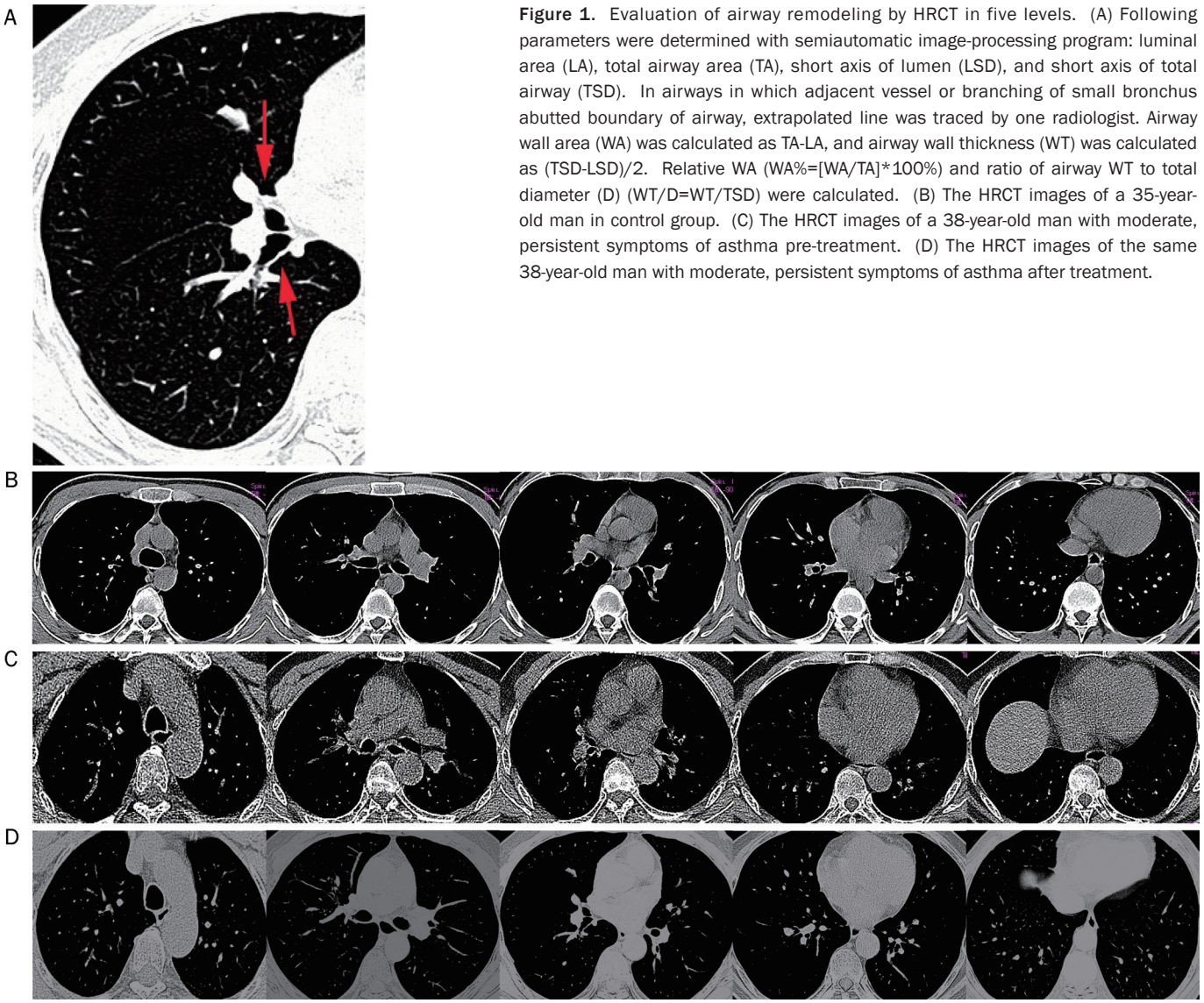

Figure 1. Evaluation of airway remodeling by HRCT in five levels. (A) Following parameters were determined with semiautomatic image-processing program: luminal area (LA), total airway area (TA), short axis of lumen (LSD), and short axis of total airway (TSD). In airways in which adjacent vessel or branching of small bronchus abutted boundary of airway, extrapolated line was traced by one radiologist. Airway wall area (WA) was calculated as TA-LA, and airway wall thickness (WT) was calculated as (TSD-LSD)/2. Relative WA (WA%=[WA/TA]*100%) and ratio of airway WT to total diameter (D) (WT/D=WT/TSD) were calculated. (B) The HRCT images of a 35-year-old man in control group. (C) The HRCT images of a 38-year-old man with moderate, persistent symptoms of asthma pre-treatment. (D) The HRCT images of the same 38-year-old man with moderate, persistent symptoms of asthma after treatment.

eling in the airway as well as relieve asthmatic symptoms. The WT and WA% in the moderate asthma group before treatment were significantly increased compared to data in the control group. After treatment, the WT and WA% of the asthmatic patients decreased. The WT and WA% of patients with asthma were well correlated with hyper-responsiveness, degree of infiltration of inflammatory cells, and concentration of chemokines involved in airway remodeling, while being negatively correlated with data of FEV_1/FVC and $FEV_1\%$. Importantly, the WT and WA% of patients with asthma were more correlated in the proximal airway than in the distal airway.

Chronic inflammation and airway remodeling is an important feature of asthma, including infiltration of eosinophils, lymphocytes, and mast cells in the airway and the structural changes of airway walls. Observing airway inflammation and airway remodeling can directly evaluate the severity of asthma and effect of treatment[14]. Biopsy or bronchoalveolar lavage through a bronchofibroscope is an invasive procedure that is risky and has poor tolerance and repeatability. The clinical administration of bronchofibroscope is limited, and it is only suitable for scientific research in patients with mild asthma. Therefore, evaluation of clinical severity and treatment effect are determined indirectly by clinical manifestations and lung function, methods that are flawed. When bronchodilators are used to improve airway reactivity, symptoms and lung function do not reflect the degree of airway inflammation at that time.

As a non-invasive technology that can objectively reflect the state of airway inflammation, induced sputum technique has been applied to study the pathogenesis and development of airway inflammatory disease[15, 16]. As a semi-quantitative technology, it is similar to biopsy of bronchial mucosa and bronchoalveolar lavage for determining the levels of inflammatory cytokines. In our study, there were increased levels of MMP-9, TIMP-1, and TGF-β_1 as well as a tendency for a higher

Table 3. HRCT measurements of airway dimensions. Data are presented as mean±SEM. [b]*P*<0.05, [c]*P*<0.01 compared with normal control subjects. [e]*P*<0.05, [f]*P*<0.01 compared with asthma group pre-treatment.

	Control group (*n*=30)	Asthma group pre-treatment (*n*=30)	Asthma group after treatment (*n*=30)
WT (mm)			
Level 1	0.15±0.02	0.31±0.03[c]	0.28±0.04[cf]
Level 2	0.12±0.03	0.24±0.02[c]	0.20±0.03[cf]
Level 3	0.10±0.01	0.17±0.02[c]	0.14±0.02[be]
Level 4	0.06±0.01	0.09±0.01[b]	0.07±0.01[be]
Level 5	0.03±0.01	0.06±0.01[b]	0.04±0.01[be]
WA% (%)			
Level 1	6.3±2.1	12.7±3.4[c]	10.5±4.2[ce]
Level 2	19.8±4.2	33.5±9.6[c]	28.9±5.7[cf]
Level 3	32.7±7.6	42.6±11.0[c]	37.4±4.5[ce]
Level 4	35.8±7.7	45.2±19.1[c]	37.3±6.4[be]
Level 5	41.3±10.4	58.6±17.3[c]	43.3±9.9[be]

Table 4A. Coefficient correlation of WT, WA% correlated with data of patients' lung function and inflammatory factors in the induced sputum. [b]*P*<0.05.

WA%	Level 1	Level 2	Level 3	Level 4	Level 5
FEV_1/FVC	-0.657[b]	-0.628[b]	-0.591[b]	-0.412[b]	-0.245
FEV_1 %pred	-0.563[b]	-0.574[b]	-0.533[b]	-0.376[b]	-0.304[b]
PC_{20}	0.578[b]	0.452[b]	0.593[b]	0.317[b]	0.294
TLC	0.312[b]	0.370[b]	0.365[b]	0.276	0.221
Neutrophils	0.449[b]	0.492[b]	0.436[b]	0.387[b]	0.339[b]
Eosinophils	0.602[b]	0.548[b]	0.559[b]	0.507[b]	0.530[b]
MMP-9	0.551[b]	0.437[b]	0.491[b]	0.354[b]	0.206
TIMP-1	0.495[b]	0.448[b]	0.467[b]	0.339[b]	0.346[b]
MMP-9/TIMP-1	0.734[b]	0.778[b]	0.692[b]	0.650[b]	0.632[b]
TGF-β_1	0.773[b]	0.702[b]	0.754[b]	0.717[b]	0.668[b]

Table 4B. Coefficient correlation of WA% correlated with data of patients' lung function and inflammatory factors in the induced sputum. [b]*P*<0.05.

WA%	Level 1	Level 2	Level 3	Level 4	Level 5
FEV_1/FVC	-0.573[b]	-0.622[b]	-0.549[b]	-0.477[b]	-0.398[b]
FEV_1 %pred	-0.448[b]	-0.493[b]	-0.404[b]	-0.376[b]	-0.382[b]
PC_{20}	0.636[b]	0.679[b]	0.682[b]	0.561[b]	0.470[b]
TLC	0.352[b]	0.394[b]	0.351[b]	0.282	0.195
Neutrophils	0.560[b]	0.533[b]	0.438[b]	0.427[b]	0.362
Eosinophils	0.599[b]	0.548[b]	0.552[b]	0.571[b]	0.496[b]
MMP-9	0.547[b]	0.449[b]	0.437[b]	0.405[b]	0.398[b]
TIMP-1	0.641[b]	0.578[b]	0.545[b]	0.548[b]	0.512[b]
MMP-9/TIMP-1	0.757[b]	0.749[b]	0.730[b]	0.782[b]	0.751[b]
TGF-β_1	0.719[b]	0.681[b]	0.655[b]	0.639[b]	0.633[b]

MMP-9/TIMP-1 ratio in patients with asthma. After treatment with formoterol-budesonide, the levels of the increased cytokines decreased significantly. The counts of neutrophils and eosinophils reflect the degree of chronic inflammation, while the levels of TGF-β_1, MMP-9, and TIMP-1 reflect the degree of airway remodeling[3–6]. TGF-β_1 is a 25-kDa homologous molecular dimer that can promote fibroblasts to differentiate into myofibroblasts, which can then secrete interstitial collagen[17]. TGF-β_1 can stimulate the synthesis and deposition of the ECM and inhibit enzymatic degradation of matrix proteins, thus regulating the expression of cell-surface matrix protein receptors. In asthmatic airways, *in situ* hybridization and immunohistochemical studies indicate that TGF-β_1 is increased and associated predominantly with submucosal and inflammatory cells, including fibroblasts, smooth muscle cells, eosinophils, macrophages, and the airway ECM, with variable expression associated with epithelial cells[18]. Matrix metalloproteinase (MMP) is the main rate-limiting enzyme that regulates the extracellular matrix[19]. In the state of asthma, too much MMP is generated, leading to an imbalance of MMP/TIMP, excessive degradation of extracellular matrix, and the imbalance of degradation/synthesis, causing structural damage to lung tissue and airway remodeling. MMP-9 and TIMP-1 are the most important factors involved in this process[19]. In our study, we found that there were increased levels of MMP-9, TIMP-1, and TGF-β_1 and a tendency for a higher MMP-9/TIMP-1 ratio in patients with asthma, as well as clinical symptoms and hyper-responsiveness in the airway. After treatment with formoterol-budesonide for one year, the increased levels of cytokines significantly decreased, as did the degree of infiltration of inflammatory cells, clinical symptoms and hyper-responsiveness in the airway.

The pathology of asthma involves both large and small airways. The traditional lung function test preferentially identifies changes in large airways, and biopsy of the small airways is very difficult to achieve. Traditional chest X-ray and CT cannot distinguish between the minute structures of the lungs. High-resolution spiral CT-ray beams go through a narrow collimator using bone algorithm image reconstruction, which can show airways 1.5 to 2 mm in diameter and identify constitutions of 100 to 200 μm[8]. Thus, HRCT has a higher resolution than traditional chest X-ray and CT in the imaging of airway and lung substance and can show narrower parts of the airways. Because of its non-invasive and intuitive features, it has been used to evaluate airway remodeling in chronic inflammatory diseases in recent years[9, 20]. Kasahara *et al*[21] measured the thickness of the epithelial reticular basement membrane (RBM) in the bronchial biopsy specimens of 49 patients with asthma and 18 healthy controls. HRCT evaluation of airway wall thickness was performed, which showed that the percentage of the airway wall area to the total airway area (WA%) and the percentage of the thickness of the airway wall to the diameter of the airway (WT%) in the asthma group were significantly higher than in the normal group; in addition, both WA% and WT% were well correlated with the thickness of the RBM while being negatively correlated with the FEV_1 of asthmatic patients. Thickening of the RBM was accompanied by airway thickening, which could lead to irreversible airflow obstruc-

tion. HRCT showed that the airway wall thickening was well correlated with thickening of the RBM as shown by bronchial biopsy, and thickening of the airway wall had a good correlation with the deterioration of pulmonary function. Gupta *et al*[22] found that HRCT scan abnormalities were present in 80% of subjects with severe asthma and often coexisted with bronchial wall thickening (62%), bronchiectasis (40%), and emphysema (8%). HRCT scans can reliably predict important bronchial wall changes. In this study, we carried out HRCT scans to evaluate airway remodeling at five levels so that the measurements of the small airways were more representative of degree of airway remodeling. The WT and WA% in the asthma group before treatment were significantly increased compared to data in the control group. After treatment, the WT and WA% of the patients with asthma decreased. The WT and WA% of patients with asthma were well correlated with hyper-responsiveness, degree of infiltration of inflammatory cells, and concentration of chemokines involved in the process of airway remodeling and were negatively correlated with FEV_1/FVC and FEV_1%. The WT and WA% of patients with asthma accurately reflected the degree of airway remodeling in patients with asthma. Reversible airway obstruction by factors such as secretions in the airway, mucus plug, bronchospasm, and edema of the airway wall could lead to the overestimation of airway wall thickness[23]. Before examination of high-resolution spiral CT, reversible obstructive factors should be reduced to a minimum. Measurement with a HRCT scan is also affected by many factors such as the subjective judgment of radiologists, window width, and window level[24]. This variability indicates that the accuracy and repeatability of direct measurement of changes in the small airway lumen should be improved. In our study, these changes were more accurate in the proximal airways than in the distal airways. A number of technical factors, including the methods of reconstruction, vision and image scanning current, and voltage, also need to be further studied.

ICS in combination with LABA inhalers are recommended for the treatment of persistent asthma. Budesonide can inhibit airway eosinophilic inflammation and reduce the number of mast cells and release of inflammatory mediators. Formoterol can stabilize the mast cell membrane, relax bronchial smooth muscle, inhibit capillary leakage, and activate sensory nerve endings. Budesonide and formoterol can complement and promote each other in the treatment of asthma[24]. Usmani *et al*[25] found that formoterol might promote glucocorticosteroid receptors transferred to the nucleus and thus play a role in anti-inflammatory activity. Budesonide can upregulate the expression of β_2 receptors and suppress the expression of GATA-3, which plays a role in the interaction between antigen-presenting cells and effect cells in the process of asthma[26]. Some earlier studies have also suggested that airway structural changes are associated with airflow limitation or airway hyper-responsiveness[27–29]. Taken together, these findings suggest that the airway structural changes can impair respiratory function and aggravate asthmatic symptoms even in patients with mild asthma. Although inhalation of steroids can inhibit airway inflammation in asthma, it is still unclear whether it can reverse airway structural changes[30]. Our research found that inhalation of budesonide-ormoterol for one year could effectively alleviate asthma symptoms, improve lung function, reduce airway hyper-responsiveness, inhibit inflammatory cell infiltration, and reverse airway remodeling in patients with asthma. These results suggest that treatment with budesonide-formoterol might be started from the early stage of even mild bronchial asthma.

In conclusion, formoterol-budesonide might interfere in chronic inflammation and remodeling in the airways as well as relieve asthmatic symptoms. HRCT and induced sputum can be applied to the evaluation of airway remodeling in asthma, which needs to be further studied.

Acknowledgements

This study was supported by a grant from Clinical Medicine Research Special Fund from Chinese Medical Association (No 08020750153).

Author contribution

Ke WANG and Chun-tao LIU designed research and wrote the manuscript; Yong-hong WU performed research; Hong-li BAI and En-sen MA analyzed data; Yu-lin FENG and Fu-qiang WEN revised the manuscript.

References

1 Busse WW, Lemanske RF Jr. Asthma. N Engl J Med 2001; 344: 350–62.
2 Bergeron C, Boulet LP. Structural changes in airway diseases: characteristics, mechanisms, consequences, and pharmacologic modulation. Chest 2006; 129: 1068–87.
3 Araujo BB, Dolhnikoff M, Silva LF, Elliot J, Lindeman JH, Ferreira DS, *et al*. Extracellular matrix components and regulators in the airway smooth muscle in asthma. Eur Respir J 2008; 32: 61–9.
4 Makinde T, Murphy RF, Agrawal DK. The regulatory role of TGF-beta in airway remodeling in asthma. Immunol Cell Biol 2007; 85: 348–56.
5 Vignola AM, Riccobono L, Mirabella A, Profita M, Chanez P, Bellia V, *et al*. Sputum metalloproteinase-9/tissue inhibitor of metalloproteinase-1 ratio correlates with airflow obstruction in asthma and chronic bronchitis. Am J Respir Crit Care Med 1998; 158: 1945–50.
6 Simpson JL, Scott RJ, Boyle MJ, Gibson PG. Differential proteolytic enzyme activity in eosinophilic and neutronphilic asthma. Am J Respir Crit Care Med 2005; 172: 559–65.
7 Castagnaro A, Rastelli A, Chetta A, Marangio E, Tzani P, De Filippo M, *et al*. High-resolution computed tomograghy evaluation of airway distensibility in asthmatic and healthy subjects. Radio Med 2008; 113: 43–55.
8 Chooi WK, Matthews S, Bull MJ, Morcos SK. Multislice helical CT: the value of multiplannar image reconstruction in assessment of the bronchi and small airways disease. Br J Radiol 2003; 76: 536–40.
9 Matsuoka S, Kurihara Y, Nakajima Y, Niimi H, Ashida H, Kaneoya K. Serial change in airway lumen and wall thickness at thin-section CT in asymptomatic subjects. Radiology 2005; 234: 595–603.
10 Marchac V, Emond S, Mamou-Mani T, Mamou-Mani T, Le Bihan-Benjamin C, Le Bourgeois M, *et al*. Thoracic CT in pediatric patients with difficult-to-treat asthma. AJR Am J Roentgenol 2002; 179: 1245–52.

11 Stock P, Akbari O, Dekruyff RH, Umetsu DT. Respiratory tolerance is inhibited by the administration of corticosteroids. J Immunol 2005; 175: 7380–7.
12 Wang K, Liu CT, Wu YH, Feng YL, Bai HL. Budesonide/formoterol decreases expression of vascular endothelial growth factor (VEGF) and VEGF receptor 1 within airway remodelling in asthma. Adv Ther 2008; 25: 342–54.
13 Duong M, Subbarao P, Adelroth E, Obminski G, Strinich T, Inman M, *et al*. Sputum eosinophils and the response of exercise-induced bronchoconstriction to corticosteroid in asthma. Chest 2008; 133: 404–11.
14 Bartoli ML, Bacci E, Carnevali S, Cianchetti S, Dente FL, Di Franco A, *et al*. Clinical assessment of asthma severity partially corresponds to sputum eosinophilic airway inflammation. Respir Med 2004; 98: 184–93.
15 Malerba M, Ragnoli B, Radaeli A, Tantucci C. Usefulness of exhaled nitric oxide and sputum eosinophils in the long-term control of eosinophilic asthma. Chest 2008; 134: 733–9.
16 Reid DW, Wen Y, Johns DP, Williams TJ, Ward C, Walters EH. Bronchodilator reversibility, airway eosinophilia and anti-inflammatory effects of inhaled fluticasone in COPD are not related. Respirology 2008; 13: 199–809.
17 Batra V, Musani AI, Hastie AT, Khurana S, Carpenter KA, Zangrilli JG, *et al*. Bronchoalveolar lavage fluid concentrations of transforming growth factor (TGF)-beta1, TGF-beta2, interleukin (IL)-4 and IL-13 after segmental allergen challenge and their effects on alpha-smooth muscle actin and collagen III synthesis by primary human lung fibroblasts. Clin Exp Allergy 2004; 34: 437–44.
18 Bottoms SE, Howell JE, Reinhardt AK, Evans IC, McAnulty RJ. TGF-bera isoform specific regulation of airway inflammation and remodeling in a murine model of asthma. PloS One 2010; 5: e9674.
19 Araujo BB, Dolhnikoff M, Silva LF, Elliot J, Lindeman JH, Ferreira DS, *et al*. Extracellular matrix components and regulators in the airway smooth muscle in asthma. Eur Respir J 2008; 32: 61–9.
20 Matsuoka S, Kurihara Y, Yagihashi K, Niimi H, Nakajima Y. Peripheral solitary pulmonary nodule: CT findings in patients with pulmonary emphysema. Radiology 2005; 235: 266–73.
21 Kasahara K, Shiba K, Ozawa T, Okuda K, Adachi M. Correlation between the bronchial subepithelial layer and whole airway wall thickness in patients with asthma. Thorax 2002; 57: 242–6.
22 Gupta S, Siddiqui S, Haldar P, Raj JV, Entwisle JJ, Wardlaw A, *et al*. Qualitative analysisof high-resolution CT scans in severe asthma. Chest 2009; 136: 1521–8.
23 Franquet T, Stern EJ. Bronchiolar inflammatory diseases: high-resolution CT findings with histologic correlation. Eur Radiol 1999; 9: 1290–303.
24 Humbert M, Andersson TL, Buhl R. Budesonide/formoterol for maintenance and reliver therapy in the management of moderate to severe asthma. Allergy 2008; 63: 1567–80.
25 Usmani OS, Ito K, Maneechotesuwan K, Ito M, Johnson M, Barnes PJ, *et al*. Glucocorticoid receptor nuclear translocation in airway cells after inhaled combination therapy. Am J Respir Crit Care Med 2005; 172: 704–12.
26 Miller-Larsson A, Selroos O. Advances in asthma and COPD treatment combination therapy with inhaled corticosteroids and long-acting beta 2 agonists. Curr Pharm Des 2006; 12: 3261–79.
27 Bouler LP, Laviolette M, Turcotte H, Cartier A, Dugas M, Malo JL, *et al*. Bronchial subepithelial fibrosis correlates with airway responsiveness to methacholine. Chest 1997; 112: 45–52.
28 Beasley R, Roche WR, Roberts JA, Holgate ST. Cellular events in the bronchi in mild asthma and after bronchial provocation. Am Rev Respir Dis 1989; 139: 806–7.
29 Chetta A, Foresi A, Del Donno M, Bertorelli G, Prsci A, Olivieri D. Airways remodeling is a distinctive feature of asthma and is related to severity of disease. Chest 1997; 111: 852–7.
30 Leigh R, Pizzichini MM, Morris MM, Maltais F, Hargreave FE, Pizzichina E. Stable COPD: predicting benefit from high-dose inhaled corticosteroid treatment. Eur Respir J 2006; 27: 964–71.

Acta Pharmacologica Sinica (2011) 32: 133–138
 1671-4083/11 $32.00
www.nature.com/aps

Original Article

Heparin responsiveness during off-pump coronary artery bypass graft surgery: predictors and clinical implications

Duk-hee CHUN[1, #], Seong-wan BAIK[2, #], So Yeon KIM[3], Jae Kwang SHIM[4], Jong Chan KIM[3], Young Lan KWAK[4, *]

[1]Department of Anesthesiology and Pain Medicine, CHA Bundang Medical Center, CHA University, Sungnam, Korea; [2]Department of Anesthesiology and Pain Medicine, Pusan National University College of Medicine, Busan, Korea; [3]Department of Anesthesiology and Pain Medicine, Yonsei University College of Medicine, Seoul, Korea; [4]Department of Anesthesiology and Pain Medicine, Anesthesia and Pain Research Institute, Yonsei University College of Medicine, Seoul, Korea

Aim: To evaluate the clinical impact of reduced heparin responsiveness ($HR_{reduced}$) on the incidence of myocardial infarction (MI) following off-pump coronary artery bypass graft surgery (OPCAB), and to identify the predictors of $HR_{reduced}$.
Methods: A total of 199 patients scheduled for elective OPCAB were prospectively enrolled. During anastomosis, 150 U/kg of heparin was injected to achieve an activated clotting time (ACT) of ≥300 s, and the heparin sensitivity index (HSI) was calculated. HSIs below 1.0 were considered reduced ($HR_{reduced}$). The relationships between the HSI and postoperative MI, cardiac enzyme levels and preoperative risk factors of $HR_{reduced}$ were investigated.
Results: There was no significant relationship between the HSI and cardiac enzyme levels after OPCAB. The incidence of MI after OPCAB was not higher in $HR_{reduced}$ patients. $HR_{reduced}$ occurred more frequently in patients with low plasma albumin concentrations and high platelet counts.
Conclusion: $HR_{reduced}$ was not associated with adverse ischemic outcomes during the perioperative period in OPCAB patients, which seemed to be attributable to a tight prospective protocol for obtaining a target ACT regardless of the presence of $HR_{reduced}$.

Keywords: heparin responsiveness; off-pump coronary artery bypass graft surgery; risk factors; myocardial infarction

Acta Pharmacologica Sinica (2011) 32: 133–138; doi: 10.1038/aps.2010.180; published online 6 Dec 2010

Introduction

Heparin inhibits thrombin generation by binding to antithrombin III (AT-III), and heparin is widely used as an anticoagulant during percutaneous coronary interventions (PCI) and coronary artery bypass graft surgery (CABG) to prevent thromboembolic complications[1–3]. However, large variability exits in individual heparin responsiveness[4, 5], and despite the theoretical possibility of increased periprocedural ischemic events associated with reduced heparin responsiveness ($HR_{reduced}$), clinical evidence is either contradictory or limited.

In patients undergoing PCIs, conflicting results exist with regard to the association between $HR_{reduced}$ and ischemic complications such as abrupt vessel closure during and after angioplasty[6–10]. In the surgical setting, only a single retrospective study has been performed to evaluate the relationship between ischemic complications in patients undergoing on-pump CABG, which found a close correlation between $HR_{reduced}$ and fatal myocardial infarction (MI)[11].

Surgical revascularization is also widely performed by off-pump coronary artery bypass graft surgery (OPCAB) during which a similar degree of anticoagulation, as used during PCIs, is sufficient. Unlike with PCIs, however, all patients presenting for OPCAB have previous exposure to heparin during coronary angiography, which is one of the well-established risk factors of $HR_{reduced}$[4, 5, 12]. Moreover, OPCAB still confers significant inflammatory responses and is associated with a postoperative procoagulant state relative to on-pump CABG[13, 14]. Concerning the possible relationship between $HR_{reduced}$ and an increased risk of ischemic events, there is still no clear recognition of patients with $HR_{reduced}$ or the clinical significance of $HR_{reduced}$ in patients undergoing OPCAB at present.

The aim of this study was to prospectively identify

# These authors contributed equally to this work.
* To whom correspondence should be addressed.
E-mail ylkwak@yuhs.ac
Received 2010-06-09 Accepted 2010-09-15

predictors of $HR_{reduced}$ and its clinical impact with regard to the incidences of MI and other major morbidity endpoints in the immediate postoperative period in patients undergoing OPCAB.

Materials and methods

Patients

This was a prospective study enrolling all consecutive patients scheduled for elective isolated multivessel OPCAB between April 2007 and March 2008 at a single university hospital. The approval of the institutional review board and patients consent were obtained. Exclusion criteria were the presence of known preoperative coagulopathy, emergency surgery or preoperative use of an intra-aortic balloon pump.

Patients demographics; preoperative medications, including anticoagulant therapy; and preoperative hematological and biochemical laboratory results, including hematocrit, total white cell count, percentage of neutrophils, platelet count, plasma protein and albumin concentrations, C-reactive protein (CRP), fibrinogen concentration, activated partial thromboplastin time, and prothrombin time, as well as levels of myocardial enzymes including creatinine kinase-MB (CK-MB) and troponin (Tn) T, were assessed. Additionally, the preoperative AT-III concentration and activated clotting time (ACT) were assessed.

All patients received standard anesthetic and surgical care according to institutional guidelines by physicians blinded to this study.

Measurement for ACT

ACT was monitored with the Hemochron® Response Whole Blood Coagulation System (International Technidyne Corp (ITC), Edison, NJ, USA) using Hemochron HRFTCA510 celite ACT tubes.

Heparin sensitivity index

Baseline ACT was determined by blood sampling immediately after the insertion of the arterial line. An initial dose of 150 U/kg of porcine heparin was injected into a central venous line just prior to Y-graft formation; the target ACT value was 300 s[15]. Ten minutes after the loading dose, the ACT was measured. An ACT of 300 s or greater was considered adequate. Then, a follow up ACT measurement was taken 30 min after the first ACT measurement. If the ACT fell below the target value of 300 s, an additional dose of heparin was administered. If the ACT was between 250 and 299 s, an additional 2000 U of heparin was administered, and if the ACT was between 200 and 249 s, then an additional 3000 U of heparin was injected. Ten minutes after the injection of additional heparin, the ACT was remeasured. Upon completion of anastomoses, the ACT was measured again, and the heparin activity was neutralized with protamine sulfate. If the ACT was greater than 300 s, 50 mg of protamine sulfate was administered. If the ACT was between 251 and 299 s or between 200 and 250 s, 30 mg or 20 mg protamine sulfate was administered, respectively. Patients were considered to have $HR_{reduced}$ if the heparin sensitivity index [HSI, HSI=(post-heparin ACT – baseline ACT)/heparin loading dose (U/kg)] was below 1.0 after the initial dose of 150 U/kg of heparin[16]. Patients with HSI≥1 were considered to have normal heparin responsiveness (HR_{normal}).

Variables assessed

Intraoperative variables such as the total amount of heparin and protamine administered, the number and nature of grafts, the amount of blood loss and the amount transfused were recorded. The amount of blood loss and blood transfused during postoperative period, the coagulation profiles and myocardial enzyme levels were recorded.

All of the patients were transferred to the intensive care unit (ICU) after surgery and treated with fentanyl-based intravenous patient-controlled analgesia for 2–3 d for pain control, and anti-platelet therapy was started within 24 h unless contraindicated.

In the immediate postoperative period, the following variables were assessed. The highest postoperative CK-MB and Tn-T levels were recorded during first seven postoperative days. Clinical diagnostic criteria for MI were defined as the occurrence of an increase in cardiac enzyme levels five times above the upper normal limit; new Q waves of greater than 0.04 mm or a reduction in R waves greater than 25% in at least 2 leads, or both; new ST elevation in at least 2 contiguous leads measuring more than 0.2 mV in leads V1–V3 or more than 0.1 mV in all other leads; or a new left bundle branch block[17]. Postoperative major morbidity endpoints were defined as permanent stroke, renal dysfunction, hemostatic re-exploration, deep sternal wound infection, and prolonged ventilation (>48 h)[18]. For clarification, renal dysfunction was defined as an acute postoperative renal insufficiency resulting in 1 or more of the following: (1) an increase in the serum creatinine level (Cr) to >2.0 mg/dL, (2) a ≥50% increase in Cr over the preoperative baseline value, or (3) a new requirement for dialysis. The development of *de novo* atrial fibrillation was also assessed. Patients were followed up for 6 months postoperatively for cardiac morbidities/mortality and restenosis, which was defined as stenosis with a cross-sectional diameter >50% at the site of bypass graft as assessed by computed tomography (CT) angiography. Cardiac morbidities included Q-wave and non-Q-wave MI and the need for repeat revascularization[19].

Statistical analysis

Statistical analyses were performed with SPSS 12.0 software (SPSS, Inc, Chicago, IL, USA). Data were expressed as the mean±SD or as the number of patients (percentage). Data were tested using the Pearson χ^2 test, Mann-Whitney U-test or Student's *t* test, as appropriate, to compare patients with $HR_{reduced}$ to patients with HR_{normal}. Factors associated with $HR_{reduced}$ with a P value <0.05 in the univariate analysis were entered into a multivariate logistic regression analysis following a stepwise, forward model. To evaluate the relationship between the HSI and changes in cardiac enzyme levels

(highest postoperative cardiac enzyme level – preoperative cardiac enzyme level), linear regression analysis was performed. We determined that at least 148 patients would be required to detect a two-fold increase in the incidence of postoperative MI in patients with $HR_{reduced}$[7] at an alpha level of 0.05 with 80% power, considering the 20% incidence of $HR_{reduced}$[16, 20] in cardiac surgical patients and the 8% incidence of postoperative MI following OPCAB in our institute[21].

Results

A total of 199 patients were enrolled during this study period. Thirty-one (15.5%) of these 199 patients met the criteria for $HR_{reduced}$ (HSI range, 0.51 to 0.99). In the HR_{normal} group, the HSI range was 1.00 to 4.04. The patient characteristics were not different between the two groups. Preoperative medications and the number of patients requiring continuous heparin use preoperatively were also similar between the groups (Table 1).

Table 1. Patients' characteristics. Data are expressed in numbers or mean±SD.

	HR_{normal} (n=168)	$HR_{reduced}$ (n=31)	P value
Age (years)	64.0±8.5	65.5±9.6	0.361
Sex: male	120 (71%)	20 (65%)	0.439
Body surface area (m^2)	1.72±0.17	1.68±0.19	0.199
MI within 1 week	6 (3.6%)	3 (9.7%)	0.149
MI within 1 month	12 (7.1%)	4 (12.9%)	0.224
Preoperative medications			
β-blockers	97 (57.7%)	14 (45.2%)	0.136
ACE inhibitors	57 (33.9%)	9 (29.0%)	0.379
ARB	48 (28.6%)	8 (25.8%)	0.470
Calcium channel blockers	72 (42.9%)	19 (61.3%)	0.058
α and β blockers	44 (26.2%)	8 (25.8%)	0.580
Sigmart	102 (60.7%)	19 (61.3%)	0.559
Aspirin	138 (82.1%)	24 (77.4%)	0.779
Clopidogrel	129 (76.8%)	25 (80.6%)	0.490
Intravenous heparin	50 (29.8%)	11 (35.5%)	0.525
LVEF (%)	56±13	53±14	0.192
LVEDD (mm)	50±5	52±7	0.064
Grade of MR ≥2	7 (4.2%)	2 (6.5%)	0.633
NYHA ≤2	152 (90.5%)	29 (93.5%)	0.744
NYHA ≥3	16 (9.5 %)	2 (6.5%)	0.744
Diseased vessel numbers	2.7±0.5	2.9±0.3	0.087

HR_{normal}, normal heparin responsiveness; $HR_{reduced}$, reduced heparin responsiveness; MI within 1 week, myocardial infarction within 1 week prior to the surgery; MI within 1 month, myocardial infarction within 1 month prior to the surgery; ACE, angiotensin converting enzyme; ARB, angiotensin receptor blocker; Intravenous heparin, preoperative intravenous heparin administration; LVEF, left ventricular ejection fraction; LVEDD, left ventricle end-diastolic diameter; MR, mitral regurgitation; NYHA, New York Heart Association Classification.

The preoperative laboratory results indicated that patients with $HR_{reduced}$ were more likely to have significantly lower Hct, plasma total protein and plasma albumin concentrations; significantly higher neutrophil percentages, platelet counts, CRP and fibrinogen concentrations; and significantly shortened partial thromboplastin times compared to patients with HR_{normal} (Table 2). In multivariate analysis, low plasma albumin concentrations (P=0.001, odds ratio 0.191, 95% confidence interval 0.073–0.498) and high platelet counts (P=0.033, odds ratio 1.006, 95% confidence interval 1.000–1.011) remained independent risk factors of $HR_{reduced}$.

Table 2. Preoperative laboratory variables. Data are expressed in mean±SD.

	HR_{normal} (n=168)	$HR_{reduced}$ (n=31)	P value
Age (years)	64.0±8.5	65.5±9.6	0.361
Hematocrit (%)	38±5	35±5	0.001
Protein (g/L)	7.0±0.7	6.5±0.8	0.005
Albumin (g/dL)	4.3±0.5	4.0±0.4	0.001
WBC count (/μL)	7325±2006	7825±2570	0.312
Neutrophil (%)	58.4±9.4	63.0±12.2	0.017
Platelet count (×10^3/μL)	239±68	275±88	0.011
CRP (mg/dL)	6.27±11.7	13.6±26.7	0.014
Fibrinogen (mg/dL)	361±92	432±124	0.001
Prothrombin time (s)	11.0±2.6	11.0±1.3	0.880
Partial thromboplastin time (s)	39.0±16.3	32.2±9.3	0.003
CK-MB (ng/mL)	3.5±2.5	4.2±3.9	0.390
Troponin T (ng/mL)	0.19±1.35	0.71±2.24	0.256
AT-III (%)	94.3±15.5	101.7±16.0	0.073
Baseline ACT (s)	142±16	148±19	0.101

HR_{normal}, normal heparin responsiveness; $HR_{reduced}$, reduced heparin responsiveness; WBC, white blood cell; CRP, C-reactive protein; CK-MB, creatine kinase-MB; AT-III, antithrombin-III; ACT, activated clotting time.

During surgery, patients with $HR_{reduced}$ received significantly larger amounts of heparin and transfused red blood cells (Table 3).

There was no significant relationship between the HSI and changes in the CK-MB and Tn-T levels (P=0.804 and 0.904, respectively). The HSI was also similar between the patients with and without postoperative myocardial infarction (1.5±0.5 *vs* 1.5±0.4, P=0.939). The incidence of perioperative MI within 7 d and the incidence of other postoperative complications were not significantly different between the two groups (Table 4). During the 6 month follow up period, none of the patients developed symptoms of ischemia except 1 patient in the HR_{normal} group who developed a symptomatic arrhythmia caused by restenosis of the venous graft to the right coronary artery and underwent PCI with a stent procedure. CT angiography was performed in 105 patients and 16 patients of the HR_{normal} and $HR_{reduced}$ groups, respectively. Sixteen patients in the HR_{normal} group met the predefined criteria of restenosis, in contrast to none of the patients in the $HR_{reduced}$ group (Table 4).

Discussion

In this prospective study evaluating the risk factors for

Table 3. Intraoperative and postoperative data. Data are expressed in numbers or mean±SD.

	HR_{normal} (n=168)	$HR_{reduced}$ (n=31)	P value
Intraoperative variables			
Total heparin (units)	10 753±2124	12 590±1832	<0.001
Total protamine (mg)	42±11	43±15	0.836
Bleeding (mL)	236±177	279±145	0.210
pRBC (pack)	0.5±1.0	0.90±1.0	0.049
FFP (pack)	0.5±1. 6	0.6±1.2	0.606
p-conc (pack)	0.3±1.5	0.1±0.7	0.543
Postoperative variables			
bleeding (mL)	1214±518	1291±453	0.440
pRBC (pack)	0.6±1.3	0.6±1.0	0.962
FFP (pack)	0.5±1.6	0.6±1.2	0.823
p-conc (pack)	0.3±1.5	0.1±0.7	0.483
Graft numbers	3.3±0.7	3.5±0.6	0.051
Arterial grafts	2.8±1.0	2.7±1.1	0.558
Vein grafts	0.45±0.87	0.74±1.2	0.183
Both arterial and vein grafts	42 (25%)	10 (32%)	0.398
Operation time (min)	249±50	266±36	0.067
Anesthesia time (min)	327±52	346±39	0.054

HR_{normal}, normal heparin responsiveness; $HR_{reduced}$, reduced heparin responsiveness; pRBC, packed red blood cells; FFP, fresh frozen plasma; p-conc, platelet concentrates.

Table 4. Postoperative outcome. Data are expressed in numbers or mean±SD.

	HR_{normal} (n=168)	$HR_{reduced}$ (n=31)	P value
Highest CK-MB	13.4±17.1	11.2±8.7	0.511
Highest Tn-T	0.47±2.29	0.63±1.47	0.715
Postoperative MI	22 (13.1%)	2 (6.5%)	0.382
Stroke	2 (1.2%)	0	0.712
Renal failure	14 (10.1%)	2 (6.5%)	0.531
Reoperation	2 (1.2%)	0	0.712
Prolonged ventilation	1 (0.6%)	1 (3.2%)	0.288
A-fib development	40 (23.8%)	7 (22.6%)	0.544
Six months follow up			
cardiac morbidities	1 (0.6%)	0	1.000
restenosis	16/105 (15.2%)	0/16 (0%)	0.126

HR_{normal}, normal heparin responsiveness; $HR_{reduced}$, reduced heparin responsiveness; CK-MB, creatine kinase-MB; Tn-T, troponin-T; MI, myocardial infarction; A-fib, atrial fibrillation; restenosis, confirmed by computed tomographic angiography.

$HR_{reduced}$ and its association with MI and morbidity endpoints following OPCAB, low albumin concentrations and high platelet counts were identified as independent predictors of $HR_{reduced}$. However, the incidences of postoperative MI and morbidity endpoints including cardiac morbidities were not increased in patients with $HR_{reduced}$.

The use of heparin during procedures involving coronary arteries requires particular attention to decrease perioperative thrombogenesis without increasing the risk of bleeding. During cardiopulmonary bypass (CPB), ACTs of less than 300 s caused coagulation in bypass circuits, and ACTs are recommended to be longer than 400–480 s[1, 22]. Accordingly, a single retrospective review evaluating the impact of heparin responsiveness on ischemic complications within the first postoperative 48 h revealed that $HR_{reduced}$ was an important risk factor for fatal MI after on-pump CABG[11]. Additionally, in patients undergoing coronary balloon angioplasty, there was an inverse relationship between heparin responsiveness and the incidence of abrupt vessel collapse during and after angioplasty[7, 8, 23]. On the contrary, other studies involving patients undergoing stent insertion reported no correlation between heparin responsiveness and ischemic complications[9, 10], although there was a case of stent thrombosis associated with $HR_{reduced}$[6].

OPCAB constitutes an important axis as a surgical revascularization technique of diseased coronary arteries, and by avoiding CPB, a reduced amount of heparin is required during surgery. Based on previous studies, ACTs between 250 and 300 s during OPCAB seem to be acceptable in many institutions[22, 24], and the majority of hospitals administered 150 U/kg heparin at the beginning of graft anastomosis for a target ACT value of approximately 300 s[15], which is similar to that for PCI. In view of the inflammation and coagulation statuses, OPCAB stands in a unique position because it is still associated with significant inflammatory responses and the activation of the coagulation and fibrinolytic systems following mid-sternotomy and cardiac manipulation, which are more pronounced in OPCAB patients than in patients undergoing PCI[2, 25]. Moreover, it has been demonstrated that OPCAB is associated with a postoperative procoagulant state related to increases in prothrombin factor and von Willebrand factor and to transient platelet dysfunction compared to on-pump CABG[13, 14]. In addition, unlike for PCI, all patients presenting for OPCAB have previous exposure to heparin during coronary angiography, which is a well-known risk factor for $HR_{reduced}$[4, 5, 12], and yet, evidence is lacking with regard to heparin responsiveness and its clinical impact on OPCAB patients. Thus, we aimed to evaluate factors affecting $HR_{reduced}$ and the relationship between heparin responsiveness and postoperative MI and morbidity endpoints.

As our results indicate, patients with HSIs<1.0 composed 16% of the study population, and low albumin concentrations and high platelet counts were identified as independent predictors of $HR_{reduced}$. However, we did not observe any relationship between the HSI and changes in myocardial enzyme levels, and the HSI was also similar between patients with and without postoperative MI. Plausible causes for these results are as follows. Although previous studies found adverse ischemic outcomes in patients with $HR_{reduced}$, these studies were either retrospective or did not prospectively manage the target ACT as in this study. In the current trial, the ACT was

closely monitored and maintained at >300 s prospectively by administering additive heparin if necessary during grafting. The ACT measured after the last heparin dose and before coronary anastomosis was above 300 s in all patients; this may be why $HR_{reduced}$ did not demonstrate any clinical relevance with respect to myocardial enzyme levels and MI during the perioperative period. This is in accordance with the results of previous studies in the PCI setting in which ACT was prospectively managed to be at least 225 s regardless of the presence of $HR_{reduced}$[9, 10]. Considering that patients with $HR_{reduced}$ seemed to be in a preoperatively hypercoagulable state and that the minimum ACT during surgery was significantly lower in patients with $HR_{reduced}$ (297±44 s *vs* 253±23 s, $P<0.001$), it still might be important to acknowledge the risk in these patients and to perform additional and frequent ACT measurements to maintain an adequate ACT level and to titrate the heparin dosage during surgery. Inflammatory markers such as CRP and the neutrophil percentages were not independent risk factors for $HR_{reduced}$. Perhaps the utilization of more distinct inflammatory markers such as interleukins could have resulted in a different outcome. Unlike previous studies of cardiac surgery, in our study, the AT-III levels were not lower in patients with $HR_{reduced}$, and only a few patients exhibited AT-III levels below 60% (4 in the HR_{normal} and 1 in the $HR_{reduced}$ group). Low AT-III activity has been reported to contribute to $HR_{reduced}$ and hypercoagulability[26, 27] and could result in major thrombotic complications after PCI and on-pump CABG[28, 29]. Considering the significant decrease in AT-III activity during on-pump CABG[30], the different results compared to the previous study may also be partly attributable to the variable AT-III activity. Although, the $HR_{reduced}$ group received a significantly larger amount of heparin and transfused red blood cells during surgery, it is difficult to establish a direct relationship between them because the $HR_{reduced}$ group initially had a lower hematocrit level.

Heparin responsiveness potentially may influence not only the periprocedural morbidity but also the long term patency of grafted vessels. Heparin inhibits the activation of the mitogen-activated protein kinase in vascular smooth muscle cells, and thus, the relative resistance to the antiproliferative action of heparin could be associated with long term graft patency[31]. In an *in vitro* study, heparin resistance in cultured vascular smooth muscle cells was a highly significant predictor of subsequent vein graft stenosis[32]. Although there have been few studies evaluating whether a population clinically characterized by $HR_{reduced}$ during vascular procedures has concurrent hyperstenotic characteristics with an increased risk of graft stenosis, more careful follow-up is required in these patients. In this study, $HR_{reduced}$ was not associated with cardiac morbidities or restenosis of graft vessels during a six month follow-up period after OPCAB.

The limitations of this study are as follows. The anti-platelet therapy consisting of aspirin and clopidogrel was started empirically 24 h after surgery as appropriate, and the inter-individual variability of clopidogrel responsiveness was not assessed, which might have affected the ischemic outcomes of the patients regardless of the HSI[33].

In conclusion, low plasma albumin concentrations and high platelet counts were identified as independent predictors of $HR_{reduced}$. Despite a strong theoretical possibility and a close relationship between $HR_{reduced}$ and postoperative MI in on-pump CABG patients, $HR_{reduced}$ was not associated with adverse ischemic outcomes during the postoperative period after OPCAB. A tight prospective protocol for obtaining a target ACT regardless of the presence of $HR_{reduced}$ seems to be of the highest importance while performing surgical revascularization.

Acknowledgements

This study was supported by a faculty research grant (6-2008-0187) of Yonsei University College of Medicine of 2008.

Author contribution

Duk-hee CHUN, Seong-wan BAIK, and Young Lan KWAK designed the study; Duk-hee CHUN, So Yeon KIM, Jae Kwang SHIM, and Jong Chan KIM performed the research; Duk-hee CHUN, Seong-wan BAIK, and Jae Kwang SHIM analyzed the data; Young Lan KWAK wrote the manuscript.

References

1 Avidan MS, Levy JH, van Aken H, Feneck RO, Latimer RD, Ott E, *et al*. Recombinant human antithrombin III restores heparin responsiveness and decreases activation of coagulation in heparin-resistant patients during cardiopulmonary bypass. J Thorac Cardiovasc Surg 2005; 130: 107–13.

2 Karmanoukian H, Attuwabi B, Nader ND. Antithrombotic controversies in off-pump coronary bypass. Semin Thorac Cardiovasc Surg 2005; 17: 59–65.

3 Levy JH. Heparin resistance and antithrombin: should it still be called heparin resistance? J Cardiothorac Vasc Anesth 2004; 18: 129–30.

4 Cloyd GM, D'Ambra MN, Akins CW. Diminished anticoagulant response to heparin in patients undergoing coronary artery bypass grafting. J Thorac Cardiovasc Surg 1987; 94: 535–8.

5 Staples MH, Dunton RF, Karlson KJ, Leonardi HK, Berger RL. Heparin resistance after preoperative heparin therapy or intraaortic balloon pumping. Ann Thorac Surg 1994; 57: 1211–6.

6 Kaku B, Katsuda S, Taguchi T, Nitta Y, Hiraiwa Y. A case of acute myocardial infarction with repetitive stent thrombosis during emergent percutaneous coronary intervention. Transient decrease in antithrombin III activity and heparin resistance. Int Heart J 2009; 50: 111–9.

7 Ferguson JJ, Dougherty KG, Gaos CM, Bush HS, Marsh KC, Leachman DR. Relation between procedural activated coagulation time and outcome after percutaneous transluminal coronary angioplasty. J Am Coll Cardiol 1994; 23: 1061–5.

8 Narins CR, Hillegass WB Jr, Nelson CL, Tcheng JE, Harrington RA, Phillips HR, *et al*. Relation between activated clotting time during angioplasty and abrupt closure. Circulation 1996; 93: 667–71.

9 Brener SJ, Moliterno DJ, Lincoff AM, Steinhubl SR, Wolski KE, Topol EJ. Relationship between activated clotting time and ischemic or hemorrhagic complications: analysis of 4 recent randomized clinical trials of percutaneous coronary intervention. Circulation 2004; 110: 994–8.

10 Tolleson TR, O'Shea JC, Bittl JA, Hillegass WB, Williams KA, Levine G, *et al*. Relationship between heparin anticoagulation and clinical out-

comes in coronary stent intervention: observations from the ESPRIT trial. J Am Coll Cardiol 2003; 41: 386–93.
11 Ranucci M, Frigiola A, Menicanti L, Cazzaniga A, Soro G, Isgro G. Risk factors for fatal myocardial infarction after coronary bypass graft surgery. Eur J Anaesthesiol 2001; 18: 322–9.
12 Chan T, Hwang NC, Lim CH. A statistical analysis of factors predisposing patients to heparin resistance. Perfusion 2006; 21: 99–103.
13 Moller CH, Steinbruchel DA. Platelet function after coronary artery bypass grafting: is there a procoagulant activity after off-pump compared with on-pump surgery? Scand Cardiovasc J 2003; 37: 149–53.
14 Mariani MA, Gu YJ, Boonstra PW, Grandjean JG, van Oeveren W, Ebels T. Procoagulant activity after off-pump coronary operation: is the current anticoagulation adequate? Ann Thorac Surg 1999; 67: 1370–5.
15 Englberger L, Streich M, Tevaearai H, Carrel TP. Different anticoagulation strategies in off-pump coronary artery bypass operations: a European survey. Interact Cardiovasc Thorac Surg 2008; 7: 378–82.
16 Ranucci M, Isgro G, Cazzaniga A, Ditta A, Boncilli A, Cotza M, *et al*. Different patterns of heparin resistance: therapeutic implications. Perfusion 2002; 17: 199–204.
17 French JK, White HD. Clinical implications of the new definition of myocardial infarction. Heart 2004; 90: 99–106.
18 Shroyer AL, Coombs LP, Peterson ED, Eiken MC, DeLong ER, Chen A, *et al*. The Society of Thoracic Surgeons: 30-day operative mortality and morbidity risk models. Ann Thorac Surg 2003; 75: 1856-64; discussion 1864–5.
19 Keeley EC, Velez CA, O'Neill WW, Safian RD. Long-term clinical outcome and predictors of major adverse cardiac events after percutaneous interventions on saphenous vein grafts. J Am Coll Cardiol 2001; 38: 659–65.
20 Avidan MS, Levy JH, Scholz J, Delphin E, Rosseel PM, Howie MB, *et al*. A phase III, double-blind, placebo-controlled, multicenter study on the efficacy of recombinant human antithrombin in heparin-resistant patients scheduled to undergo cardiac surgery necessitating cardiopulmonary bypass. Anesthesiology 2005; 102: 276–84.
21 Choi YS, Shim JK, Hong SW, Kim DH, Kim JC, Kwak YL. Risk factors of atrial fibrillation following off-pump coronary artery bypass graft surgery: predictive value of C-reactive protein and transfusion requirement. Eur J Cardiothorac Surg 2009; 36: 838–43.
22 Tanaka KA, Thourani VH, Williams WH, Duke PG, Levy JH, Guyton RA, *et al*. Heparin anticoagulation in patients undergoing off-pump and on-pump coronary bypass surgery. J Anesth 2007; 21: 297–303.
23 Bittl JA, Ahmed WH. Relation between abrupt vessel closure and the anticoagulant response to heparin or bivalirudin during coronary angioplasty. Am J Cardiol 1998; 82: 50P–56P.
24 Hansen KH, Hughes P, Steinbruchel DA. Antithrombotic- and anticoagulation regimens in OPCAB surgery. A Nordic survey. Scand Cardiovasc J 2005; 39: 369–74.
25 Raivio P, Kuitunen A, Suojaranta-Ylinen R, Lassila R, Petaja J. Thrombin generation during reperfusion after coronary artery bypass surgery associates with postoperative myocardial damage. J Thromb Haemost 2006; 4: 1523–9.
26 Na S, Shim JK, Chun DH, Kim DH, Hong SW, Kwak YL. Stabilized infective endocarditis and altered heparin responsiveness during cardiopulmonary bypass. World J Surg 2009; 33: 1862–7.
27 Lemmer JH Jr, Despotis GJ. Antithrombin III concentrate to treat heparin resistance in patients undergoing cardiac surgery. J Thorac Cardiovasc Surg 2002; 123: 213–7.
28 Matthai WH Jr, Kurnik PB, Groh WC, Untereker WJ, Siegel JE. Antithrombin activity during the period of percutaneous coronary revascularization: relation to heparin use, thrombotic complications and restenosis. J Am Coll Cardiol 1999; 33: 1248–56.
29 Loubser PG, McCarthy JJ, Attar M. Coronary thrombosis associated with antithrombin-III deficiency. J Cardiothorac Vasc Anesth 1997; 11: 756–9.
30 Hashimoto K, Yamagishi M, Sasaki T, Nakano M, Kurosawa H. Heparin and antithrombin III levels during cardiopulmonary bypass: correlation with subclinical plasma coagulation. Ann Thorac Surg 1994; 58: 799-804; discussion 804–5.
31 Sindermann JR, March KL. Heparin responsiveness *in vitro* as a prognostic tool for vascular graft stenosis: a tale of two cell types? Circulation 1998; 97: 2486–90.
32 Refson JS, Schachter M, Patel MK, Hughes AD, Munro E, Chan P, *et al*. Vein graft stenosis and the heparin responsiveness of human vascular smooth muscle cells. Circulation 1998; 97: 2506–10.
33 Patti G, Nusca A, Mangiacapra F, Gatto L, D'Ambrosio A, Di Sciascio G. Point-of-care measurement of clopidogrel responsiveness predicts clinical outcome in patients undergoing percutaneous coronary intervention results of the ARMYDA-PRO (Antiplatelet therapy for Reduction of MYocardial Damage during Angioplasty-Platelet Reactivity Predicts Outcome) study. J Am Coll Cardiol 2008; 52: 1128–33.